ULB FACULTÉ DES SCIENCES

UNIVERSITÉ LIBRE DE BRUXELLES

Subsea Permafrost Thaw in Arctic Sediments: an experimental and modeling study of its physical features and biogeochemical impacts

Thesis presented by Matteo PUGLINI

with a view to obtaining the PhD Degree in Science ("Docteur en Science")

Année académique 2019-2020

Supervisor: Prof. Sandra Arndt

Co-supervisor: Prof. Victor Brovkin

Biogeochemistry and Modeling of the Earth System

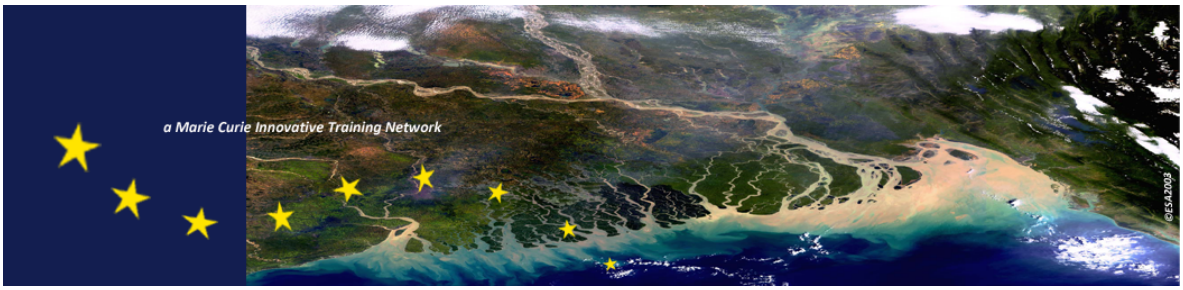

The research leading to these results has received funding from the European Union's Horizon 2020 research and innovation programme under the Marie Skłodowska-Curie grant agreement No 643052 (C-CASCADES project)

Für Andre, trotz allem die Nachtigall meiner Heide

—

RÉSUMÉ FRANÇAIS

Les plateaux continentaux de l'Océan Arctique renferment une importante quantité de carbone encore mal quantifiée sous forme de pergélisol sous-marin (SSPF, de l'anglais subsea permafrost) et d'hydrates gazeux associés. Il a été suggéré que la submersion de ces plateaux continentaux pendant la déglaciation et leur dégel progressif provoqué par le réchauffement climatique actuel, conduisent à l'activation du carbone stocké et au relarguage de méthane dans l'océan peu profond et, à terme, vers l'atmosphère. Etant donné le manque de mesures directes, nos connaissances sur le dégel du SSPF et de sa contribution au bilan de méthane et de sa contribution à la rétroaction sur le climat restent limitées. L'objectif principal de cette thèse est de faire la synthèse de résultats d'analyse en laboratoire, de modélisation et de considérations théoriques afin de fournir une vision systématique nouvelle du SSPF et d'évaluer correctement son rôle au sein du cycle du carbone global.

Dans cette thèse, j'ai considéré les résultats de deux expériences en laboratoire, les premières réalisées avec comme objectif l'étude directe du processus de dégradation dans la partie supérieure du sol gelé après un événement de submersion. L'étude montre un bon accord entre les mesures avec les résultats de modélisation et avec le profil parabolique de la limite de dégel prévue par la théorie. Cela confirme que la conduction thermique peut être considérée comme le principal mécanisme de propagation de la chaleur. Cependant le mauvais accord avec la solution de Stefan détaillée suggère que les conditions aux limites réelles et la convection doivent également être incluses. Une comparaison des taux de dégel du SSPF mesurés et modélisés met en évidence l'importance des premières phases après la submersion

J'ai ensuite analysé les résultats de la première implémentation d'une composante SSPF dans JSBACH, le module de surface continentale du modèle de système Terre de l'Institut Max Planck (MPI-ESM). Les conditions des fonds sous-marins des simulations de référence ont été obtenues à partir de simulations pré-industrielles de MPI-ESM. Les simulations avec JSBACH que j'ai réalisées en 1D au niveau du site montrent que le temps de réponse typique du SSPF à la submersion est de l'ordre du millénaire et que le dégel est contrôlé par la lente pénétration du sel dans les sédiments. Le dégel thermo-chimique est de seulement 82 cm en 1000 ans, n'impliquant aucune menace de dégradation massive. En revanche, dès que la température des eaux profondes est légèrement plus élevée que la température de dégel du SSPF, une destabilisation massive (avec des taux de dégel supérieurs à

15 cm an^{-1}) est possible. Ce scenario est compatible avec la température de fond de la mer Laptev prévu en l'an 2300 dans le cadre de RCP 8.5 ou encore avec l'augmentation observée des températures de l'eau en été dans la mer Laptev. Les simulations JSBACH ont montré également que le modèle est capable de reproduire qualitativement des caractéristiques complexes comme les taliks provoqués par la salinité, c'est-à-dire des sols non-gelés dans les régions de pergélisol.

L'objectif du dernier chapitre est l'estimation des émissions potentielles non-turbulentes de méthane par le plateau continental arctique de la Sibérie orientale (ESAS, de l'anglais East Siberian Arctic Shelf), qui héberge SSPF et hydrates gazeux. En utilisant le modèle diagénétique BRNS, j'ai trouvé que l'oxydation anaérobique du méthane est un biofiltre efficace qui consume souvent presque complètement le méthane dissout avant qu'il n'atteigne la colonne d'eau. Cependant, il a été montré que dans des configurations caractérisées par une dynamique advective rapide (taux de sédimentation élevé et/ou flux advectif) l'efflux de méthane non-turbulent peut atteindre 27 $\mu molCH_4$ cm^{-2} an^{-1} (comparable aux volcans de boue). Un flux significatif (19 $\mu molCH_4$ cm^{-2} an^{-1}) est aussi possible dans une fenêtre temporelle restreinte quand les conditions aux limites du méthane sont perturbées. Une extrapolation régionale à l'échelle de la barrière de Laptev a montré cependant que le flux d'eau-sédiment n'excède pas 0.1 $GgCH_4$ an^{-1}.

Cette dissertation constitue la première étape en vue d'un couplage entre un modèle de réaction-transport des sédiments (comme BRNS) et un modèle du système Terre (comme JSBACH), un outil préconisé depuis longtemps par la communauté de la modélisation et capable de mettre correctement en perspective le rôle du SSPF dans un cycle du carbone intégré et dans le système climatique.

ENGLISH ABSTRACT

The Arctic shelves host a large, yet poorly quantified amount of carbon, in form of subsea permafrost and associated gas hydrates. The subsea permafrost is relic permafrost which formed when the shelves, which were exposed during the glacial periods and whose subaerial conditions allowed permafrost to grow, were submerged once the sea level rose at the beginning of the Holocene. It has been suggested that shelf flooding during deglaciation and global-warming induced thawing lead to activation of stored carbon eventually releasing methane to the shallow ocean and ultimately to the atmosphere. Given the paucity of direct measurements, little is known about subsea permafrost thaw and its contribution to methane budget and to methane-climate feedback. In order to correctly frame the subsea permafrost within the carbon cycle a better understanding of its physical features and its biogeochemical effects is needed. The main goal of this dissertation is therefore encompassing laboratory results, modeling results and theoretical speculation to offer a systematic and novel view of the subsea permafrost in perspective of an integrated study of the topic.

In the thesis, I considered the results of two laboratory experiments, the first ever carried out with the aim of a direct investigation of the degradation process of frozen soil from above after a submersion event. The outcomes of such experiments were compared with the results of a numeric thermal model developed on purpose and with the theoretical expectations of a modified Stefan's problem. The study reveals a good agreement of measurements with modeling results and with the theoretically expected parabolic profile of the thawing boundary. This confirms that the heat conduction might be regarded as the main heat propagation mechanism. However the scarce agreement with the detailed Stefan's solution suggests that the real boundary conditions and convection should be also included to describe the system in the laboratory. A comparison with measured subsea permafrost thawing rates reveals a good qualitative consistency and highlights the importance of the first phases after the submersion.

Then I analyzed the results of the first implementation of a subsea permafrost component into JSBACH, the land surface model of the Earth System Model (ESM): ESM of the Max Planck Institute (MPI-ESM). The model has been developed based on the pre-existing terrestrial permafrost, which has provided the spin-up run needed to model the flooding of the permafrost and the formation of the subsea permafrost. The sea bottom boundary conditions for baseline simulations were derived from the pre-industrial runs of Ocean component of the MPI-ESM. The 1-D site-level JSBACH simulations I performed

show that the typical response time of the subsea permafrost to the submersion is of the order of the millennia, in line with other previous findings and that thawing is controlled by the slow penetration of salt into the the sediments. The thermo-chemical thawing during the interglacial condition is of only 82 cm in 1000 years, setting no threat for massive destabilization. Instead, as soon as the sea bottom water temperatures is even slightly higher than the thawing temperature of the subsea permafrost a massive destabilization (with thawing rates > 15 cm yr^{-1}) is possible. And this perspective is compatible either with projected seabottom temperature in the Laptev Sea in year 2300 according RCP 8.5 or with the observed increase in summer water temperatures in the Laptev Sea. JSBACH simulations also showed that the model is capable to qualitatively reproduce complex features like salinity-induced taliks, *i.e.* unfrozen soil in a permafrost region which can enhance heat, water and chemical transport.

The aim of the last chapter was the investigation of the potential contribution of the subsea permafrost as a methane source and the estimation of the potential non-turbulent emissions of methane from the East Siberian Arctic Shelf (ESAS), which is underlain by destabilizing subsea permafrost or gas hydrates. Using the diagenetic model BRNS, I found that in marine sediments, the (an)aerobic oxidation of methane are efficient biofilters that often consume the dissolved methane almost completely before it reaches the water column. However, it was shown that in settings characterized by fast advective dynamics (high sedimentation rate and/or advective flow) the non-turbulent methane efflux can be as high as 27 $\mu molCH_4$ cm^{-2} yr^{-1} (comparable to mud-volcanoes). Bioirrigation and quality of the organic matter may enhance this flux as well. A substantial flux (19 $\mu molCH_4$ cm^{-2} yr^{-1}) is also possible in a limited time window when the methane boundary conditions are perturbed. A regional upscale to the Laptev Shelf showed that the flux does not exceed 0.1 $GgCH_4$ yr^{-1} , a quantity not sufficiently large to support the previously published high (and debated) estimates of ESAS methane fluxes to the atmosphere.

This dissertation represents the first step in the direction of a coupling between a sediment reactive-transport model (like BRNS) and an Earth System Model (like JSBACH), a tool advocated for long by the modeling community and capable to put into the right perspective the subsea permafrost into an integrated carbon cycle and climate research.

Ice contains no future, just the past, sealed away. As if they're alive, everything in the world is sealed up inside, clear and distinct. Ice can preserve all kinds of things that way - cleanly, clearly. That's the essence of ice, the role it plays.

— *The Ice Man*, Murakami Haruki

CONTENTS

LIST OF FIGURES

LIST OF TABLES

ACRONYMS

AAT	All-At-a-Time (sensitivity study)
AOM	Anaerobix Oxidation of Methane
AeOM	Aerobix Oxidation of Methane
ALK	ALKalinity
ANME	ANaerobic MEthanotrophs
ATP	Adenosine TriPhosphate
BC	Boundary Condition(s)
BP	Before Present
BRNS	Biogeochemical Reaction Network Simulator
DIC	Dissolved Inorganic Carbon
DOC	Dissolved Organic Carbon
ESAS	East Siberian Arctic Shelf
ESM	Earth System Model
FTCS	Forward-Time Central-Space algorithm
GH	Gas Hydrate
GHG	GreenHouse Gas(es)
GHSZ	Gas Hydrate Stability Zone
H2020	Horizon 2020
IBPT	Ice-Bound Permafrost Table
JSBACH	Jena Scheme for Biosphere-Atmosphere Coupling in Hamburg
LGM	Last Glacial Maximum
LOAC	Land-Ocean Aquatic Continuum
ME	Main Effect
MG	MethanoGenesis
MPI-ESM	Earth System Model of the Max Planck Institute

MPI-OM	Max Planck Institute Ocean Model
OAT	One-At-a-Time (sensitivity study)
OM	Organic Matter
PAGH	Permafrost-Associated Gas Hydrate
PDE	Partial Differential Equation
PF	PermaFrost
POC	Particulate Organic Carbon
PT	Permafrost Table
RCM	Reactive Continuum Model
RCP	Representative Concentration Pathway
RTM	Reactive-Transport Model
S-AOM	Sulfate-mediated Anaerobic Oxidation of Methane
SL	Subsea Land
SMT	Sulfate-Methane Transition
SMTZ	Sulfate-Methane Transition Zone
SR	Sulfate Reduction
SRB	Sulfate Reducing Bacteria
SSPF	SubSea PermaFrost
SWI	Sediment-Water Interface
SWI(0)	Sediment-Water Interface at the beginning of submersion phase, the year 0
TEA	Terminal Electron Acceptor
ΣAOM	Integrated rate of Anaerobic Oxidation of Methane
ΣB	Integrated AOM-performing Biomass
ΣSR	Integrated rate of the organoclastic Sulfate Reduction

SYMBOLS

ω	Sedimentation rate
Ω	Carbonate saturation state
e	Enthalpy per unit mass
L	Latent heat per unit mass
$c_{(L/S)}$	Specific heat at constant pressure (for liquid and solid phase)
T_m	Melting temperature
k	Thermal conductivity
ρ	Density
α	In chapter 2 and 3: thermal diffusivity. In chapter 4: bioirrigation coefficient
$Z(t)$	Position of the phase boundary
q	Heat flux
A	Areal cross section
λ (or Λ)	Stefan's parameter in case of pure water (or in case of brine)
St	Stefan's number
$T_f(S)$	*Liquidus* temperature with salinity S
D	Salt diffusivity
$\Phi(\Lambda)$, $\Psi(\Lambda)$	Functions of Λ resulting from enforcing Stefan's conditions
T^*, S^*	Temperature and salinity at the interface between thawed and solid phases
φ	Porosity
φ_0	Porosity at the sediment-water interface
φ_∞	Minimum porosity at depth
$\mathcal{K}$	Eddy thermal conductivity
KT	Multiplying factor to keep track of enhanced heat transport due to convection
d_n	Numbers of grid layers between the sand-water interface and the phase interface
N	Scale factor to model space dependency of KT in Chapter 2
h	Newton's heat transfer coefficient
ζ	Exponent of the thawing according to a power law
t_{sub}	Time since submergence of the subsea permafrost
θ_i	Volumetric soil ice content
θ_w	Volumetric soil water content
K	Soil hydraulic conductivity
$\mathcal{D}$	Soil water diffusivity
ψ	Matric potential
T_w	Sea bottom water temperature
G	Geothermal gradient
ξ	Porosity for a dissolved species and solid fraction for a solid species
F_i	Total flux affecting the concentration of the i-th species
D_i	Effective diffusion coefficient for the i-th species
S_i	Sources/sinks affecting the concentration of the i-th species
D_b	Bioturbation coefficient
c_0	Length scale for modeling sediment compaction
v_{up}	Upward water flow velocity

α_0	Bioirrigation coefficient at the sediment-water interface
z_{irr}	Bioirrigation attenuation depth
a	Average lifetime of reactive organic matter
ν	RCM parameter
g_0	Shape factor of RCM
μ_g	Biomass growth rate
B	AOM-performing biomass
R	Gas constant
χ	Number of electrons transferred per mole of ATP
F_K	Kinetic factor of AOM bioenergetic formulation
F_T	Thermodynamic factor of AOM bioenergetic formulation
μ_d	Biomass decay rate
$K_m^{\mathrm{CH_4}}$	Half-saturation constant of $\mathrm{CH_4}$
$K_m^{\mathrm{SO_4^{2-}}}$	Half-saturation constant of $\mathrm{SO_4^{2-}}$
γ	Activity coefficient
ΔG_r	Difference in Gibbs free energy of a reaction
ΔG_{BQ}	Minimum energy needed to support biomass growth
SD	Conversion factor solid/dissolved species
$D_{a_{MG}}$	Damköhler number of methanogenesis
$D_{a_{AOM}}$	Damköhler number of AOM
η	AOM efficiency
$[\mathrm{CH_4}]_-$	$\mathrm{CH_4}$ at the bottom of the sediment column
k_{AOM}	reaction constant in AOM bimolecular formulation
$m_{\mathrm{CH_4}}$	Molecular mass of $\mathrm{CH_4}$
m_{C}	Molecular mass of carbon
$\epsilon_{\mathrm{CH_4}}$	methanogenic production coefficient

1 INTRODUCTION

The Arctic Ocean

The Arctic Ocean has a comparatively small volume with respect to other oceans (1% of global ocean water, Lammers et al., 2001) and it might be conceived as a macroscopic "estuary" (McClelland et al., 2012) in consideration of its size, its strong riverine input ($10-11\%$ of global runoff, Lammers et al., 2001; Shiklomanov et al., 2000; Fichot et al., 2013) and its huge and shallow continental shelf. The Arctic Shelf (fig. 1.1) covers about 53% of Arctic Ocean's area (Bates et al., 2009) and it includes the Siberian Shelf which is the most extensive continental shelf in the world ($\sim 3 \cdot 10^6$ km^2, Wegner et al., 2015). It is subdivided in its Western portion, corresponding to the Kara shelf, and in its Eastern portion, known as East Siberian Arctic Shelf (ESAS) (Romanovskii et al., 2001; Shakhova et al., 2010b) spreading over $\sim 2.1 \cdot 10^6$ km^2 with a mean depth of ~ 45 m (James et al., 2016) and underlying the Laptev Sea, the East Siberian Arctic Sea and the Russian portion of the Chukchi Sea. Other relevant Arctic shelves are the Beaufort shelf, the Lincoln shelf and the Barents shelf.

Riverine input in the Arctic Ocean

Because of large shelf area, the Arctic Ocean is particularly sensitive to riverine input of freshwater, heat (Whitefield et al., 2015), alkalinity, mineral debris (McClelland et al., 2016) and organic carbon (Holmes et al., 2012; Wegner et al., 2015; McClelland et al., 2016). The 65% of aggregated discharge (McClelland et al., 2012) in the waters of the Arctic Ocean is ascribable to the "Big Six", *i.e.* Ob, Yenisey, Lena, Kolyma, Yukon and Mackenzie rivers. Their role in moving and delivering mineral particulates as well as terrigenous carbon to the Arctic Ocean is particularly relevant since overall they drain about 67% of the permafrost[1] region.

Carbon in the Arctic shelves

The ESAS and the other Arctic shelves sediments are characterized by a high organic carbon content (Stein et al., 1994) varying between 1.51% and 5.7% (Rachold et al., 2004; Jorgenson et al., 2005; Ping et al., 2011; Vonk et al., 2012) with an average of 1.76% (Wegner et al., 2015). Such values put the Arctic Ocean and its continental shelves as rightful components of the carbon cycle with a potentially pivotal role which has been poorly studied so far and has only recently been framed into a global perspective, with an increasing interest in scientific community rising in the last decade.

Recent measurements

Such interest has been driven by recent measurements of biogeochemical properties of the Arctic waters and by the growing understanding of the processes occurring in high latitudes. Monitoring of

1 Permafrost (PF) is defined as soil/rock that is continuously cryotic, *i.e.* whose temperature is below 0 °C, for at least two consecutive years (Tarnocai et al., 2009)

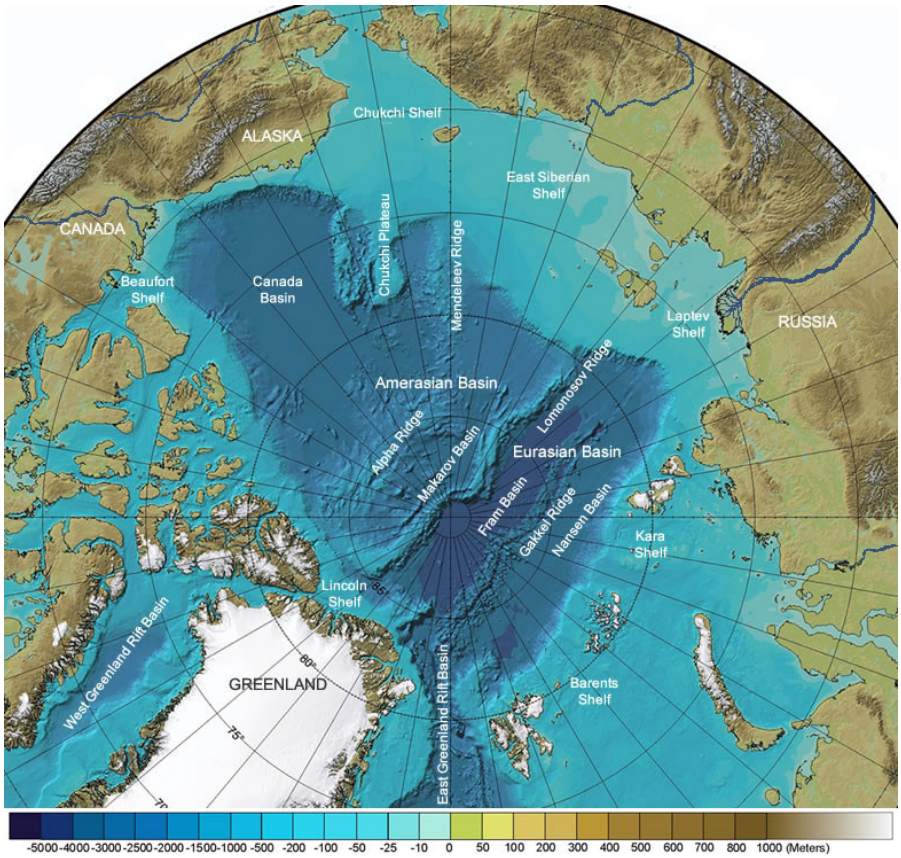

Figure 1.1: Bathymetric Chart of the Arctic Ocean annotated with the names of seafloor features. Five of the Big Six rivers can also be seen. (Redrawn from Jakobsson et al., 2012).

water pCO_2, dissolved inorganic carbon (DIC), alkalinity (ALK), carbonate saturation state (Ω) and methane concentration has offered the possibility to investigate aspects of the Arctic carbon cycle that have been largely overlooked as yet.

Acidification: a land-ocean link

The Arctic waters represent sometimes a really productive setting (Raymond et al., 2007) with consequent carbon fixation and reduction of pCO_2. Nevertheless Ocean acidification is particularly emphasized in cold waters, because of the increase in solubility of CO_2 due to low temperatures (Guinotte et al., 2008; Bates et al., 2009). Acidification has been globally ascribed to anthropogenic increase of CO_2 in the atmosphere (ACIA, 2005; Orr et al., 2005; Hoegh-Guldberg et al., 2010) but in the ESAS the detected undersaturation for aragonite (Qi et al., 2017) appears to be driven more by degradation of terrestrial organic carbon than by uptake of CO_2 from atmosphere (Semiletov et al., 2012; Vonk et al., 2012; Semiletov et al., 2016; Tanski et al., 2016). Given the large amount of PF-derived terrestrial carbon in waters of Siberian rivers (Semiletov et al., 2011; Semiletov et al., 2012; Vonk et al., 2013; Vonk et al., 2014) and the presence of PF in coastal deposits (Vonk et al., 2012; Sparkes et al., 2015), the link between PF and acidification

suggests a more general link between processes on land and offshore shelf processes.

Shelves exposed at the LGM

Such a connection is even tighter considering the specific trait of the Beaufort shelf and even more of the ESAS. Because of their gentle slope, these shelves were above the sea level several times over the glacial cycles (at the Last Glacial Maximum (LGM) - 26.5 kyr before present - the sea level was 120 m below the current one, Fleming et al., 1998; Bauch et al., 2001) and their subaerial conditions and lack of ice cap (Clark et al., 2002) allowed PF to aggrade. Eustatic sea transgression started at the end of the Pleistocene ($\sim 12 - 13$ kyr ago, Bauch et al., 2001) and lasted till 5 kyr ago when the sea level reached the 30 m isobath, after which further coastal retreat happened at the lower rate set by the erosion-based processes of thermo-denudation[2] and thermo-abrasion[3] (Shakhova et al., 2017).

The SSPF

This means that the coastline retreated between $300 - 800$ km southwards in ESAS (Soloviev, 1981; Overduin et al., 2007) since the LGM, submerging the PF at that time and forming the so-called Subsea Permafrost (SSPF). Since then the SSPF sediments have experienced diagenetic changes, as well as an increase in temperature and salinity intrusion due to seawater. Temperature changes have been particularly far-reaching: while terrestrial PF underwent an increase in temperature by about $6 - 7$ °C with respect to the LGM (Frenzel, 1992), SSPF has warmed up of about 17 °C in the last 12 kyr (Brigham et al., 1983; Soloviev et al., 1987; Kim et al., 1999; Romanovskii et al., 2001; Gavrilov et al., 2003; Romanovskii et al., 2005; Weingartner et al., 2005; Taylor et al., 2013; Shakhova et al., 2014), a difference which is displayed for instance in

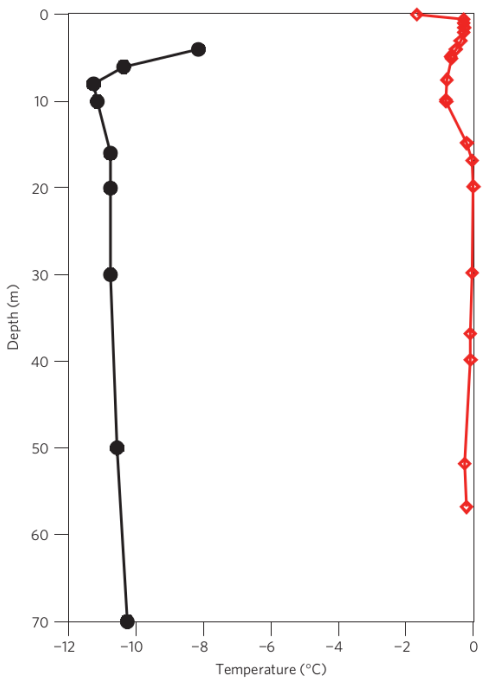

Figure 1.2: Comparison of temperature vertical profile of terrestrial PF (black) borehole in Chay-Tumus (Grigoriev, 1986), south of Lena delta, and a SSPF boreholes (red) in Buor Khaya Bay, Laptev sea. From Shakhova et al., 2014

2 Destabilization of PF bluffs and coastal PF due to insulation and heat flux.

3 Destruction of the coastal PF due to combined action of thermo-mechanical effects of seawater and wind.

Fig. 1.2, reporting a terrestrial and a submarine PF temperature profile. Such warming has reduced mechanical strength of the sediments and increased temperature to a value close to the thawing, which would then make the organic carbon available to microbial activity.

Sediments have also accumulated during the Holocene on top of the submerged PF, summing up to $\sim 4.3 \cdot 10^6$ Tg[4] (Stein et al., 2004) and making the Siberian shelf the largest sedimentary basin in the world (Gramberg et al., 1983) with sediment columns predicted to reach up to 15 km in thickness (Khain et al., 2009).

1.1 THE PERMAFROST AND THE CARBON CYCLE

PF appears clearly to be the distinguishing feature of the region, both on land and on the shelf.

1.1.1 *The terrestrial and coastal permafrost*

Carbon in terrestrial PF

Fig. 1.3 shows that PF is found in about $\sim$ 25% of the Northern Hemisphere ($\sim 17.8 \cdot 10^6$ km^2, Hugelius et al., 2014) and that practically most of current PF area has experienced subzero temperatures for millennia with the consequent accumulation of a vast amount of organic carbon because of reduced bacterial degradation. PF on land is thought to store $\sim$ 1300 PgC[5] altogether (Hugelius et al., 2014), corresponding to $\sim$50% of global terrestrial soil carbon or almost twice the amount of carbon currently held in the atmosphere (Schaefer et al., 2014; Hugelius et al., 2014). The large rivers draining the vast permafrost-affected plains of Eurasia and America represent therefore a considerable link between the land and the Arctic waters and form a substantial part of the so-called Land-Ocean Aquatic Continuum (LOAC) (Regnier et al., 2013), the continuous and widespread set of aquatic connections that capillarily drains the land, mobilizing, transporting and processing material and chemical species from land to ocean. Holmes et al., 2012 estimated that 34 TgC yr^{-1} of dissolved organic carbon (DOC) and 5.8 TgC yr^{-1} of particulate organic carbon (POC) have been supplied by rivers to the Arctic Ocean, thus constituting a tight link between hydrological and carbon cycle.

The LOAC

The coastal PF

Another relevant component, at the boundary of the LOAC, is the long coastline of the Arctic Ocean ($>$ 101000 km, World Vector Shoreline, Soluri et al., 1990), especially its Siberian portion, which sums up to 53.8% of the total shore alone. The Arctic coast, particularly the one corresponding to the ESAS, is characterized by tall (up to $\sim$ 40 m thick and an average of 25 m, Vonk et al., 2012) bluffs of Yedoma/Ice-Complex deposits. These are outcropping of Pleistocene origin, whose formation is still debated (Zimov et al., 2006; Schirrmeis-

4 Teragram. 1 Tg $= 10^{12}$ g.

5 Pg: petagram. 1 Pg $=$ 1 Gt $= 10^{15}$ g.

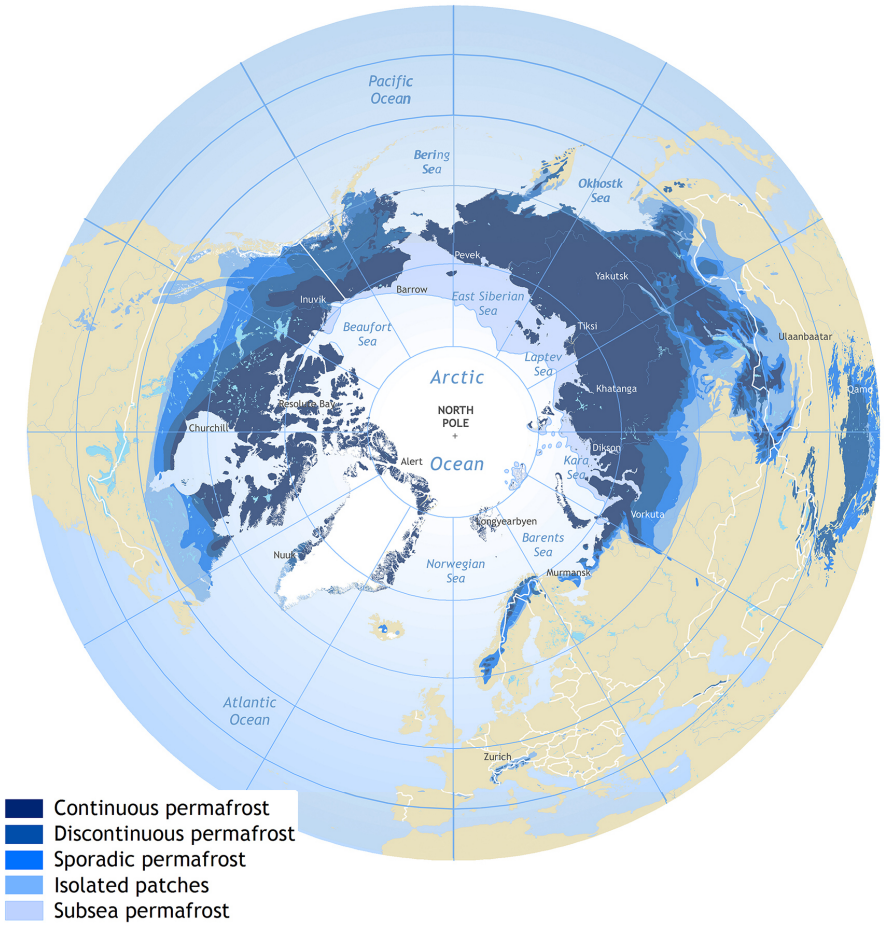

Figure 1.3: Map of permafrost in the Northern Hemisphere. The Permafrost is classified as continuous, discontinuous, sporadic and isolated. The extent of subsea permafrost has been set by the maximum theoretically possible, corresponding to 100 m isobath. From Brown et al., 1997.

ter et al., 2011; Schirrmeister et al., 2013; Grosse et al., 2013; Strauss et al., 2017) and which present a high carbon content ($1-5\%$, Zimov et al., 2006; Schirrmeister et al., 2011) and a high ground ice content (up to 85%, average 20%), usually under form of syngenetic ice-wedges (Grosse et al., 2013). Ice-rich coasts are affected by a high erosion rate with extreme values of 20 m yr^{-1} (Vonk et al., 2012) up to 80 m yr^{-1} (Semiletov et al., 2012), although highly variable in space and time (Semiletov, 1999; Rachold et al., 2000; Lantuit et al., 2011; Overduin et al., 2016; Tanski et al., 2016; Shakhova et al., 2017) . The coastal erosion, also consequence of the diminishing sea ice covering (Screen et al., 2010; Forbes, 2011), causes a flow of terrigenous particulate carbon of about 22 TgC yr^{-1} (Vonk et al., 2012) to the ESAS alone with an amount of $14-20$ TgC yr^{-1} reaching the seabed (Vonk et al., 2012; Wegner et al., 2015).

1.1.2 *The subsea permafrost*

Unlike its terrestrial counterpart, the carbon content of the SSPF is very much unconstrained in consequence of the uncertainty regarding SSPF area and physical conditions.

Carbon partition in Arctic sediments

The carbon of the Arctic shelves could be split into four reservoirs: upper sediment, subsea permafrost, SSPF-associated gas hydrates and deep free gas. The form and the partitioning of carbon is debated but, given the environmental conditions, it is agreed that deep carbon is stored as frozen organic matter or in form of methane. Estimates report that the proper SSPF if the ESAS may contain up to 500 PgC (Zimov et al., 2006; Shakhova et al., 2010a), gas hydrates about 540 $PgCH_4$ and free gas deposits further 360 $PgCH_4$ (Gramberg et al., 1983; Soloviev et al., 1987). These numbers solely would correspond to about 1200 PgC in ESAS. Estimates by McGuire 2009 indicate instead a lower carbon content: $2 - 65$ $PgCH_4$ ($1.5 - 49$ PgC) in the whole Arctic Ocean Gas Hydrates deposits and an extra 9.4 PgC in upper sediments, but no estimate has been provided for the proper submerged permafrost alone.

Within the carbon cycle, SSPF is thought to play a triple role (Overduin et al., 2015b):

1. sequestrating frozen carbon (Grosse et al., 2011);
2. acting as a roof preventing free gas from below to seep through (Ruppel, 2011; Ruppel et al., 2017);

Role of the SSPF

3. creating the thermodynamic conditions for shallow gas hydrates (O'Connor et al., 2010; Ruppel et al., 2017; Dean et al., 2018). Gas hydrates are a structure, naturally occurring under certain conditions, able to store large quantity of gas (*e.g.* methane)[6].

Possible climate feedback

Warming and thawing of the SSPF affects these roles and positive feedback exacerbates the SSPF destabilization even further. The aspect of major concern is the climatic feedback of methane, which is expected from destabilizing gas hydrates, free gas and also as aftermath of the degradation of the organic matter stored in the SSPF, available to microbial activity once it thaws. Possible climate feedback associated to this methane has not been assessed yet, considering that a climate model encompassing the SSPF and related features in its components is currently missing.

CH_4 as a GHG

Methane (CH_4) is the third most important greenhouse gas (GHG) after water vapor and CO_2 and is the second major anthropogenic GHG after CO_2. A positive radiative forcing of ~ 1 W m^{-2} can be attributed to CH_4 alone from 1750 (Myhre et al., 2013). Although the current concentration in the atmosphere is 1850 ppb (only 0.45% of CO_2 concentration), its global warming potential is 28 over 100 years

6 See section 1.3.3.1 for more.

and 84 over 20 years (Myhre et al., 2013), namely it is 28-fold or 84-fold more efficient than CO_2 as GHG. If one takes additionally in consideration feedback effects on climate and on the presence of other GHGs (especially the water vapor, and ozone, as byproduct of reaction with hydroxyl radical) the global warming potential of CH_4 is overall estimated to be even higher: 34 for 100 years and 86 for 20 years. Its role in the climate system is clearly relevant and therefore cannot be overlooked.

1.1.2.1 *Methane fluxes from the Arctic Ocean*

A series of measurements carried out in summer as well as winter seasons in the last decade (Shakhova et al., 2007; Shakhova et al., 2010b; Shakhova et al., 2014) have drawn the attention of the scientific community on the waters of the ESAS and encourage a better understanding of the link between their CH_4 content and the underlying SSPF. CH_4 concentrations in the Laptev Sea are indeed anomalously high, up to 500 nM, while normal CH_4 concentration in water column of other oceans is about 5 nM (Damm et al., 2008). A first estimate (Shakhova et al., 2010b) of venting flux from the ESAS summed up to $\sim$ 8 $TgCH_4$ yr^{-1} and it was then updated (Shakhova et al., 2014) to the amount of 17 $TgCH_4$ yr^{-1}, taking into account hotspots, storm-induced ventilation and ebullition, the latter being the most important component of methane flux (230 $\mu molCH_4$ cm^{-2} yr^{-1} – 1.4 $mmolCH_4$ cm^{-2} yr^{-1}).

CH_4 fluxes from the ESAS

Such estimates have fostered a lively discussion (Shakhova et al., 2019) about the origin of this methane (Shakhova et al., 2014; Overduin et al., 2015b; Sapart et al., 2017; Shakhova et al., 2017) its biogeochemical role, the role of bubbles (McGinnis et al., 2006; Thornton et al., 2016) and the physics and status of subsea permafrost and associated clathrates (Soloviev et al., 1987; Kvenvolden, 1988; Ruppel et al., 2017; Shakhova et al., 2019). The highest estimate of CH_4 flux has however found no general validation via alternative and complementary ways (AMAP, 2015; Berchet et al., 2016; Lorenson et al., 2016; Myhre et al., 2016; Reum, 2019).

The ongoing CH_4 increase in the atmosphere, its potent effect as GHG and the relative weight that emissions from Arctic Ocean might have with respect to the whole global oceanic sources call therefore for a better awareness of the processes involving CH_4. Such understanding would be necessary to reduce the uncertainty in CH_4 emissions from the SSPF and assess its associated potential climate feedback.

The Arctic warms faster

This is specially relevant in a setting like the Arctic, whose warming has been occurring at a rate and intensity almost as double as elsewhere in the world (Trenberth et al., 2007; Bekryaev et al., 2010; Overland et al., 2011; Christensen et al., 2013; Jeffries et al., 2012; AMAP, 2015) and which has been projected to continue relentlessly through-

out the 21^{st} century (Collins et al., 2013; AMAP, 2015) as effect of the polar amplification (Masson-Delmotte et al., 2006; Pithan et al., 2014).

Monitoring has also shown that oceanographic changes have been occurring in the Arctic Ocean, in terms of currents and thermal/salt features. Waters of Atlantic origin (warmer and saltier) have been growing in volume entraining a phenomenon of "Atlantification" (Carmack et al., 1995; Zhang et al., 1998; Maslowski et al., 2000; Barton et al., 2018) and recently it has also been estimated that the inflow of Pacific waters through the Bering Strait has been rising (Qi et al., 2017). Atlantic waters, carried along the West Spitsbergen Current are thought to have caused an increase in temperatures up to 1 °C with respect to pre-1999 mean in the Makarov basin (Walczowski et al., 2006) and have affected air-sea fluxes of CO_2 and methane (Wåhlström et al., 2016). Although these changes appeared at first not to happen along the Russian Arctic coast (Biastoch et al., 2011), Dmitrenko et al., 2011 showed that the shallowest (< 10 m) bottom waters of Laptev Sea and East Siberian Arctic Sea actually have been warming by 2.1 °C during summer since mid-1980s, probably because of variations in the atmospheric circulation. A year-round under-ice temperature measurement in central Laptev Sea (water depth $30 - 50$ m) exhibited an episodic warming of $+0.6$ °C in sea bottom in winter 2012/2013. Supposedly this is a consequence of the joint contributions of sea ice retreat, enhanced Lena water heat transport and lagged effects of summer solar radiation (Janout et al., 2016), proving evidence that warming might not be limited just to summer months.

Oceanographic changes in the Arctic Ocean

1.2 CURRENT KNOWLEDGE ABOUT THE SUBSEA PERMAFROST: AN OVERVIEW OF THE PHYSICAL PROCESSES

History of the SSPF exploration

The first mention of the Arctic SSPF dates back to 1880 when a pioneer, Adolf Erik Nordenskiöld, reported that the sandy bottom of a bay of Chukchi Sea appeared to be cemented by ice. This observation remained just a curiosity, confirmed by Vize, 1946 (reported in Vigdorchik, 1980) and Ponomarev, 1940 and it drew scientific interest only later in 1950s and especially 1960-1970s, in connection with the stability of offshore oil structures (Terzaghi, 1952; Black, 1957; Lachenbruch, 1962; Mackay, 1972; Molochushkin, 1973; Lewellen, 1974; Brewer, 1975; Hunter et al., 1976; Osterkamp et al., 1976). The first drilling campaigns in ESAS date back to the initiative of N. F. Grigoriev (Grigoriev, 1962; Grigoriev, 1966), V. A. Usov (Usov, 1965), M. S. Ivanov (Ivanov, 1969) and the first extensive research by E. N. Molochushkin (Molochushkin, 1973), who found both frozen and unfrozen sediments with cryotic temperature. Other campaigns were launched later (Fartyshev, 1993) but measurements have been sparse throughout the Arctic Shelves and this has for long hindered our knowledge of physical and biogeochemical aspects of the SSPF. Only during the last

decade more systematic observational data have been retrieved (Shakhova et al., 2017; Shakhova et al., 2019) but still most of our current knowledge about the SSPF is based on modeling results. In the Siberian shelf, drilling has been limited to few and and shallow boreholes in water depth < 10 m (Slagoda, 2004; Overduin et al., 2007; Rachold et al., 2007; Grigoriev, 2008; Winterfeld et al., 2011). Data from Canadian part of the Beaufort shelf (Hu et al., 2013) and the US portion (Harrison et al., 1978; Sellmann et al., 1980; Osterkamp et al., 1989) are a bit more spread, but still do not represent a comprehensive set of observations.

From the physical point of view the SSPF could be regarded as a frozen porous medium in salty environment. Despite this seemingly simplicity the physics of the SSPF and its theoretical understanding remains poorly understood and represents a challenge for further investigation.

1.2.1 *The subsea permafrost: extension, degradation processes and thawing regime*

Observation of the SSPF extension

The first rough estimate of the SSPF extension is the one shown in Fig. 1.3 by Brown et al., 1997, that is simply based on the maximum possible SSPF extension down to the 100 m isobath. In the Beaufort Sea Brothers et al., 2012 and Brothers et al., 2016 showed however that SSPF extends only to $20 - 25$ m isobath, in Khara sea Portnov et al., 2014 confirmed that boreholes found SSPF mainly between 0 m and 20 m isobath. This calls for models capable of taking into account these differences. Many models (*e.g.* Romanovskii et al., 2005, Nicolsky et al., 2010, Nicolsky et al., 2012, Angelopoulos et al., 2019) of different complexity have been developed over the years, including more and more features to keep up with the increasing evidences resulting from measurements. Up until now modeling and theoretical considerations agree that SSPF evolution after inundation has been affected by:

Factors affecting SSPF current state

- Thermal, ice state and thickness before the submersion (Harrison et al., 1978; Nicolsky et al., 2012; Shakhova et al., 2017);
- Presence of thermokarst lakes before the submersion (Romanovskii et al., 2001; Romanovskii et al., 2005; Overduin et al., 2008; Nicolsky et al., 2010; Nicolsky et al., 2012; Shakhova et al., 2017);
- Duration of the submersion (Romanovskii et al., 2001; Overduin et al., 2008);
- Coastline retreat rate (Shakhova et al., 2017; Angelopoulos et al., 2019);
- Sea bottom water temperature and salinity (Delisle, 2000; Romanovskii et al., 2001; Romanovskii et al., 2005; Nicolsky et al., 2012; Angelopoulos et al., 2019);

- Geological features (rocks, layering, geothermal heat flux) (Soloviev et al., 1987; Romanovskii et al., 2001; Nicolsky et al., 2012).

The theoretical understanding of how the thawing occurs, once sea transgression has happened, is however incomplete. If it is glaring that sea water acted as thermal buffer for submerged permafrost (Angelopoulos et al., 2019), there are still many open questions about the overall processes as well as transient and local features.

Two are the basic mechanisms of SSPF degradation included in most of the current models, the upward and downward degradation (Romanovskii et al., 2005; Nicolsky et al., 2012; Shakhova et al., 2017).

SSPF degradation mechanisms

- *Upward*: it occurs under the effect of the geothermal heat flux coming from below. It is predicted to happen everywhere - although it is more accentuated in fault lines, while the low geothermal heat flux of cratons makes it rather slow - and to be the most important (Drachev et al., 2003; Drachev, 2000; Drachev et al., 1999; Drachev et al., 1995; Romanovskii et al., 2001; Romanovskii et al., 2005) form of SSPF degradation. In spite of this, such degradation is however the least interesting one in a climatic perspective, as:
  i. it is due to internal factors, and it is not consequently altered because of changes of the environmental/climatic conditions;
  ii. it happens from below and, although relatively quick, the effects of ensuing thawed SSPF are unlikely to be noticed in centennial time scale.
- *Downward*: it occurs under the joint action of two effects
  i. The chemical thawing due to the presence of salt, which lowers the freezing point. When salty waters are in touch with fresh frozen soil at 0 °C, the latter is thermodynamically out of equilibrium and it can thaw in spite of cryotic seawater temperature. Considering that the average bottom water temperatures of the Arctic Ocean are below 0 °C (Nicolsky et al., 2010; Dmitrenko et al., 2011), thawing of the SSPF is expected to take place mainly because of this salinity-induced effect. This chemical thawing, although happening everywhere, is however usually not explicitly included in most of the SSPF models, which do not consider salt diffusion from above in the submerged PF and merely implement salt effect (if any) by lowering the thawing temperature of a constant value.
  ii. The thermal thawing due to positive sea water temperatures at the top of the SSPF, typically occurring below large water bodies such as big rivers (Delisle, 2000; Nicolsky et al., 2010), an effect which is enhanced by sea-ice loss

(Shakhova et al., 2014) or influence of warmer waters coming from other Oceans. Since all the SSPF models are in first order heat transfer models, such a thermal effect is generally explicitly considered, as long as top temperature boundary conditions include the aforementioned warming.

Downward degradation process, being on the limit of thermodynamic equilibrium, is sluggish but, unlike the upward degradation from below, is more sensitive to climatic changes. Furthermore its aftermaths can theoretically affect the climate itself due to emissions which alter atmospheric CH_4 and CO_2 concentrations.

Model results

Thermal models for the the ESAS (Romanovskii et al., 2001; Romanovskii et al., 2005; Nicolsky et al., 2012) predict the SSPF down to the 60 m isobath and a thicker and shallower SSPF in correspondence of the coast and the Siberian islands, fact that highlights how the top of the SSPF is linked to the time of submergence. It has been generally shown (Osterkamp et al., 1989; Brothers et al., 2012; Overduin et al., 2015a; Overduin et al., 2016; Shakhova et al., 2017; Sherman et al., 2017) how the top of SSPF table deepens with increasing distance from the coast. This feature is expected not only on the basis of common sense but also of theoretical considerations.

1.2.1.1 *Stefan's problem*

Description of the Stefan's problem

The problem of thawing SSPF from above can be indeed roughly simplified and traced back to the general problem of a phase boundary moving with time during a phase change, the so called *Stefan's problem*. The problem takes its name from the physicist Jozef Stefan who first introduced this class of problems in relation to ice formation already in 1891 (Stefan, 1891). Its well-posedness and solutions have been studied under a large variety of boundary conditions over a century but its application to the SSPF is more complicated, because of the extreme simplification needed to employ the analytical solution of Stefan problem in case of a eutectic system (like saline water), not to mention the difficulties related to reconstruction of past boundary conditions, the forms of heat and chemical transports that should be taken into account as well as inhomogeneities of the medium and the erosion.

An analytical solution of the Stefan problem for SSPF was proposed in 1978 by Harrison et al., 1978 to explain SSPF conditions in the Prudhoe Bay (Alaska) with a reasonable success. In spite of this, their approach was not applied in other contexts or verified elsewhere and with alternative tools, although shorefaces of the Arctic Ocean have been suggested to be the "natural laboratory" for the study of SSPF dynamics (Are, 2003).

A benchmark for theoretical models could be the investigation of thawing regimes (*i.e.* the evolution of the top of SSPF over time) since each thawing regime is characterized by a thawing rate. With a *space-for-time* substitution the thawing rate can be also inferred from spatial observations and coast retreat rate. It has been well established that thawed layers at the seabed thickens seawards (Hunter et al., 1976; Osterkamp et al., 1989; Overduin et al., 2015a; Overduin et al., 2016) with a deepening of the top of the SSPF table. Stefan's solution predicts a thawing rate which is inversely proportional to the square root of the thawing time, but other regimes have been suggested. For instance Portnov et al., 2014 brings back an idea by Sharbatyan, 1974 and proposes a two-stage thawing regime where only the second phase follows a Stefan solution, while Osterkamp et al., 1989 observes a three-zonal thawing where again only the last one behaves according to Stefan's. In spite of the empirical relationship identified by Overduin et al., 2016, which relates thawing rate to depth of the SSPF and submersion time and which implicitly hints at a general validity of Stefan-like solution, an explicit association is still missing.

Thawing rate is a key quantity

1.2.1.2 *Time response and thawing rate*

SSPF response time

The time response of the SSPF and annexed structures has been numerically investigated in several studies (Romanovskii et al., 2005; Nicolsky et al., 2012; Razumov et al., 2014; Hunter et al., 2013; Portnov et al., 2014; Razumov et al., 2014; Malakhova et al., 2017). If it is clear that the time scale of heat propagation in submerged and frozen sediments is slow and of the order of thousands of years, it is also obvious that a precise quantification is still lacking with literature estimates range from 3 kyr (Dmitrenko et al., 2011), $5-7$ kyr (Romanovskii et al., 2005), to $10-20$ kyr (Malakhova et al., 2017). Time response to warming is certainly an important parameter, as it sets the climatic effects on the SSPF, it is thus important to reduce its uncertainty, although an accepted definition of *SSPF time response* is currently missing.

Debate about SSPF response time

Because of this poor quantifications a debate has arisen whether current SSPF degradation - and possibly related methane release to the water column - might be a response to recent climate change (Shakhova et al., 2009; Shakhova et al., 2010b) or merely the lagging natural response to deglaciation and submergence. If long time scales hint indeed at the latter (Harvey et al., 1995; Hunter et al., 2013; Kretschmer et al., 2015; Malakhova et al., 2017), recently submerged ($<<$ 1 kyr ago) PF that has already been thawing Rachold et al., 2007; Shakhova et al., 2014hints in the direction of the former.

Measured thawing rates in the Laptev Sea

The only direct comparative measurement of thawing rate available in Laptev Sea (Shakhova et al., 2017) are consistent with a predominant influence of the current climate on the thawing of the SSPF. High ($\sim$ 14 cm yr^{-1} in the last $\sim$ 30 yr) and increasing values with respect

to the thawing rate of 30 years ago (5.7 cm yr^{-1}) suggest an abrupt acceleration of the response of the SSPF to changing climatic conditions not compatible with the long-standing response. The linear thawing rate that can be inferred by the same measurements would be instead $\sim$ 7 cm yr^{-1}. All these values, together with the rate of 5.3 cm yr^{-1} (Overduin et al., 2015b), fall anyway in the wide range of $1 - 15$ cm yr^{-1} estimated for 12 sites near the coast (< 10 m) of Laptev Sea and reported in Overduin et al., 2007.

1.2.2 *SSPF Taliks*

Definition of taliks

Another controversial point of our knowledge on SSPF regards the existence of taliks and how they develop. A talik is a portion of unfrozen ground within a zone of frozen PF. Depending on its features it can be open (if connected with the top of the PF table), closed (if surrounded by frozen PF) or through (if it pierces the full thickness of PF). The latter are thought to possibly play an important role as they vertically connect sub- and supra-PF waters, enabling the transport of chemical species and material which would otherwise be just trapped below the bulk of compact SSPF.

Talik formation

With the processes currently implemented in SSPF models, taliks are predicted only in specific conditions: under large river bodies (Delisle, 2000; Frederick et al., 2014) and in correspondence of fault zones as consequence of the high geothermal heat flux (Romanovskii et al., 2001) - the so called tectono-genetic taliks (Shakhova et al., 2017). Drillings have however shown that taliks can be found also in other settings and conditions.

Thermokarst

Taliks can for instance evolve as a follow-up stage of thaw lakes (Shakhova et al., 2015). The latter are shallow lakes, often underlain by taliks (Romanovskii et al., 2000; Gavrilov et al., 2003), which originated from thawing of terrestrial PF when coastal plain began to warm at the end of Pleistocene, giving rise to a phenomenon known as thermokarst. The fate of these thermokarst-induced featured after submergence is debated: it is both thought that cryotic sea temperature might have hindered further talik development (Romanovskii et al., 2000; Romanovskii et al., 2004; Overduin et al., 2007) but there is evidence (Shakhova et al., 2015; Shakhova et al., 2017) that salt might have prevented thermokarst lakes from freezing determining a growth of underlain taliks.

Salt-induced taliks

Modeling results by Nicolsky et al., 2010 showed that taliks can also open because of the combined effect of salty sediments and geothermal heat flux. Such taliks can be through or closed in a "wafer-like" structure, *i.e.* frozen-unfrozen-frozen layers, proving that even models are able to reproduce taliks outside the fault lines or in areas not affected by warm riverine waters. These salinity-induced features are

compatible with findings by Osterkamp et al., 1989 and Baker et al., 1989.

CryoGRID2

The action of salt is rarely included in SSPF models, in spite of the examples above showing its pivotal importance. One of the few models endowed with a parallel heat and salt diffusion scheme is CryoGRID2 (Westermann et al., 2013; Westermann et al., 2016; Westermann et al., 2017) which has been recently applied to the study of SSPF in Buor-Khaya Bay in Laptev Sea (Angelopoulos et al., 2019). Its results have highlighted the prominent role of the chemical erosion in thawing from above and therefore are very useful for further SSPF modeling and for comparison with theoretical analytical solution.

1.3 METHANE IN THE ARCTIC SHELVES

1.3.1 *Methane as GHG: the global budget*

CH_4 in the atmosphere is currently increasing at a rate of 10 $TgCH_4$ yr^{-1} corresponding to about 10 ppb yr^{-1} (see Fig. 1.4).

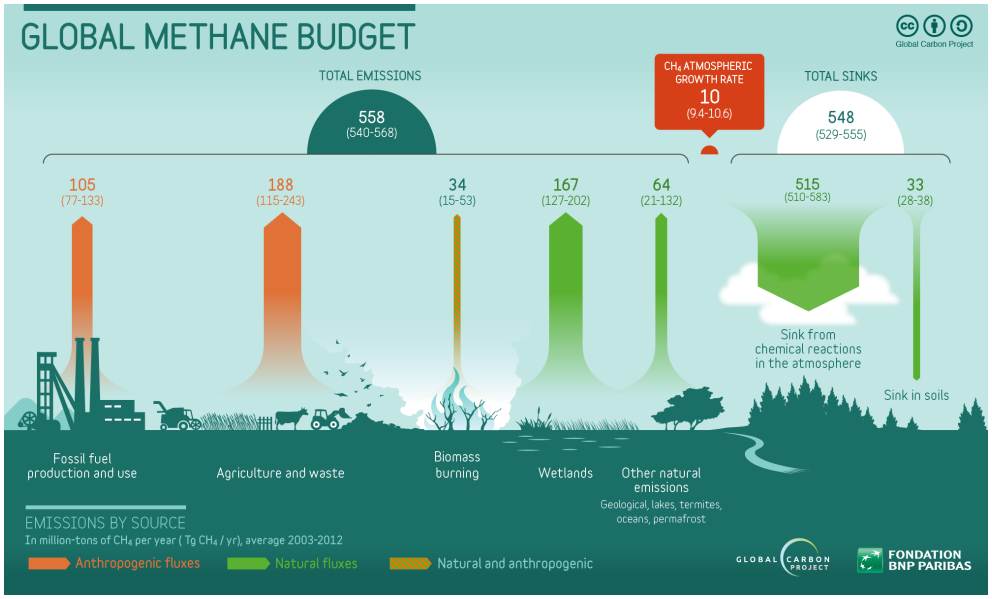

Figure 1.4: Global methane budget with natural and anthropogenic emissions and natural sinks. From Le Quéré et al., 2018.

Sources of CH_4 increase in the atmosphere

The anthropogenic sources account for the 46-67% of the increase in the atmosphere from 1980, while natural sources contribute for 33-54% (Kirschke et al., 2013). The main anthropogenic sources are agriculture and waste (188 $TgCH_4$ yr^{-1}, Saunois et al., 2016) and fossil fuel (105 $TgCH_4$ yr^{-1}, Saunois et al., 2016). The largest natural sources are by far wetlands (167 $TgCH_4$ yr^{-1}), followed by freshwater systems (Saunois et al., 2016; Dean et al., 2018).

The role of terrestrial and subsea permafrost remains instead uncertain. Current CH_4 emissions from land permafrost is estimated to

be only up to 1 $TgCH_4$ yr^{-1} (Saunois et al., 2016) with the potential of increasing sensibly however in the next century (Gao et al., 2013; McCalley et al., 2014; Schneider von Deimling et al., 2015; Dean et al., 2018).

Although the emissions from oceanic sources, including the SSPF and methane hydrates, are generally accepted to represent a small contributor to global budget (Ehhalt, 1974; Kirschke et al., 2013; Saunois et al., 2016), they lie in a relatively wide range of $1 - 35$ $TgCH_4$ yr^{-1} (Rhee et al., 2009; Anderson et al., 2010; Etiope, 2015; Saunois et al., 2016). It is moreover striking that out of this amount, up to 17 $TgCH_4$ yr^{-1} might derive from the ESAS waters only (Shakhova et al., 2014). This in turn implies that much of the uncertainty originates from the uncertainty of the CH_4 budget from the ESAS, which is then to be reduced, especially in perspective of projections for future scenarios.

CH_4 from oceanic sources

1.3.2 *Methane biogeochemistry*

While the general knowledge of the SSPF is rather broad and coarse, the biogeochemistry of CH_4 is much better known, although several gaps are still open. The difference in the state-of-the-art of the research on the SSPF and on CH_4 implies an intrinsic difference in how the current knowledge is exposed and the level of the research questions. Concerning the physical aspects of the SSPF, the scientific investigation arises from the lack of answers to basic questions and the research is, accordingly, rather general. Considering instead the biochemistry of CH_4, the open issues originate mainly from a lack of understandings of some of the details of the processes involved or some very specific aspects. This implies that the description of the current knowledge has to go much deeper into the topic in order to expose the gaps which are still to be addressed. The following sections will be therefore intrinsically more detailed than Section 1.1.2 in order to properly illustrate present research questions.

Difference between current knowledge about the SSPF and CH_4 biogeochemistry

1.3.2.1 *Methane production*

CH_4 originate mainly by processes affecting the organic matter[7], it means hence that sediments, and especially continental margins, represent a productive environment for methanogenesis, considering a global flux of organic matter to the sea floor of $40 - 191$ TmolC yr^{-1} (Dunne et al., 2007; Boetius et al., 2013). The CH_4 originating from organic matter can be thermogenic and biogenic[8]. Thermogenic methane is produced at the high temperatures and pressures of deep

CH_4 comes from OM

7 Abiotic methane can be originated, for instance, by serpentinization of olivines in presence of CO_2 (Etiope, 2017), but its global weight in hydro-, bio- and atmo-sphere is marginal with respect to organic-derived CH_4.

8 Pyrogenic methane, *i.e* originating from combustion, also exists but, for obvious reasons, it is not considered here given the submarine setting.

strata and therefore it is the most important source of natural gas. It can be of microbial or inorganic origin and is characterized by a $\delta^{13}C$ in the range between $-50‰$ and $-20‰$ (Whiticar, 1999). Biogenic methane represents by far the largest portion of methane in sediments originating in the superficial sediments affected by SSPF and is also sensitive to climatic perturbation.

CH_4 formation and anoxia

A crucial condition to permit methanogenesis is usually the absence of O_2. There is however evidence of CH_4 production in oxic environments, which for instance gives rise to the so-called "Ocean Methane Paradox" (Kiene, 1991), for which many solutions have indeed been proposed (Angelis et al., 1994; Kiene et al., 2000; Stefels, 2000; Karl et al., 2008; Carini et al., 2014). But except for these peculiar cases, anoxic conditions are necessary for methane production since, in presence of oxygen even the most thermodynamically stable carbon substrate is rapidly oxidized to CO_2.

OM degradation and redox ladder in the sediments

Methanogenesis is generally the final reaction in the complex multistep process (Arndt et al., 2013) represented by microbial degradation of organic matter (OM). Micro-organisms exploit electronic cascades to provide energy along a chain of enzyme- mediated biochemical redox reactions. Carbon in the OM plays the role of electron donor, getting oxidized, and the energy yield of the full redox reaction ultimately depends on the terminal electron acceptor (TEA) which overall acts as an oxidant, getting reduced. This entails a preferential sequence of how the OM gets mineralized by micro-organisms along different metabolic pathways with different TEAs according to the energy gain ladder. First the oxidant which provides the highest energy profit (i.e. O_2) is used, and then, once that is depleted, all the other ones - in the order NO_3^-, Mn(IV), Fe(III), SO_4^{2-} - down till the least energy-yielding one, *i.e.* the organic matter itself via fermentation which results in the production, among the others, of acetate (CH_3COO^-), CO_2 and H_2. These processes determine the typical vertical zonation of the TEAs and byproducts of organic matter decomposition throughout the sediment column according to the redox sequence (Claypool et al., 1974; Froelich et al., 1979; Stumm et al., 1996) and displayed in Fig. 1.5.

Methanogenesis

Methanogenesis is the energy-yielding metabolism typical of a group of archaea known as methanogens. All the methanogenic pathways have in common the conversion of a methyl group ($-CH_3$) in CH_4 (Lessner, 2009) but the origin of this methyl group is variable. Methane production can occur mainly along two pathways[9]:

1. *Hydrogenothrophic* pathway, via reduction of CO_2 according to the reaction:

$$4\,H_2 + CO_2 \longrightarrow CH_4 + 2\,H_2O. \tag{1.1}$$

9 A third one, the dismutation of methanol or methylamines is also possible but its importance in sediments is irrelevant

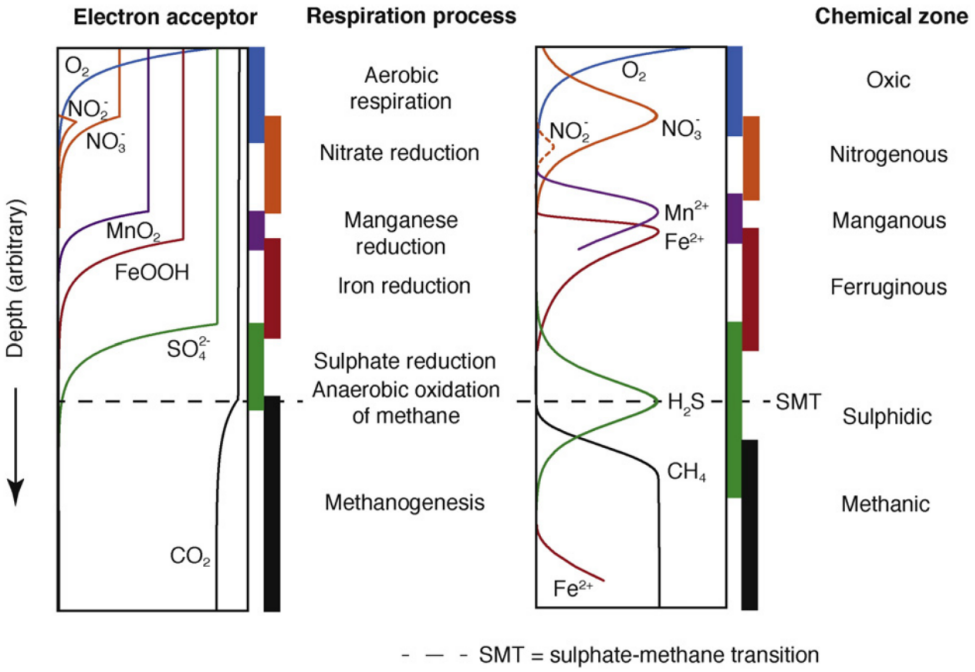

Figure 1.5: Typical vertical zonation of chemical species in sediment porewater according to redox ladder. From Roberts, 2015.

In spite of being common to all the seven orders of methanogens known[10], only 30% of biogenic methane derives from this pathway (Lessner, 2009).

2. *Acetoclastic* pathway, according to the reaction:

$$CH_3COO^- + H_2O \longrightarrow CH_4 + HCO_3^-. \tag{1.2}$$

Even if only the order of *Methanosarcinales* are able to use acetate, this pathway is thought to produce the 70% of biogenic methane (Lessner, 2009).

Acetoclastic CH_4 has an isotopic signature in the range $\delta^{13}C = [-40‰, -70‰]$ and is associated more to freshwater environments, while hydrogenothrophic CH_4 has an even lighter isotopic signature ($\delta^{13}C = [-60‰, -90‰]$) and has been associated with marine environments (Whiticar et al., 1986).

Methanogenic budget

The estimated methane production within the marine sediments is conspicuous and ranges between 26 and 61 $TgCH_4\ yr^{-1}$ (Boetius et al., 2013; Egger et al., 2018), while for comparison, the total annual primary production of the oceans is $30 - 59$ PgC (Berger et al., 1989; Hedges et al., 1995) but only a small fraction ($1 - 0.1\%$, Zabel et al., 2006) reaches the sea floor and is therefore available to anaeroboic degradation which ends up, if OM is enough, into methanogenesis.

10 *Methanosarcinales, Methanomicrobiales, Mathenopyrales, Methanocellales, Methanobacteriales, Methanomassiliicoccales*

The global CH_4 production is approximately 1.9 $PgCH_4$ yr^{-1} (Thauer et al., 2008).

Newly discovered methanogens

The aforementioned zonation of pore water chemical species has been challenged by the discovery of a second phylum of methanogens (Evans et al., 2015; Lang et al., 2015; Vanwonterghem et al., 2016) which could coexist with sulfate-reducing bacteria (SRB) and this might lead to methane production also in a zone overlapping the sulphidic zone, although its contribution to CH_4 is unknown so far (Dean et al., 2018).

Expected change in methanogenesis

Temperature increase of waters of ESAS (Dmitrenko et al., 2011), thawing at faster rate of SSPF and remobilization of old, and likely more labile (Drake et al., 2015b; Spencer et al., 2015), carbon at deeper levels might be associated with a more intense bacterial activity throughout the sediment column (degrading also more recently accumulated organic matter) which could enhance then methanogenesis.

The accumulation of methane in sediments horizon has to take into account not only CH_4 production but also its consumption since, at last, it is the (im)balance of these two processes that enables the build-up of CH_4 at depth.

1.3.2.2 *Methane consumption in marine ecosystems*

Role of microbial CH_4 consumption

Microbial CH_4 consumption is the largest sink of CH_4 on Earth after photochemical reactions in the troposphere (James et al., 2016). CH_4 consumption occurs according to two processes: aerobic methane oxidation (AeOM) and anaerobic oxidation of methane (AOM). The latter being is by far the most relevant process (Hinrichs et al., 2002; Reeburgh, 2007; Egger et al., 2018) for marine environments, removing up to 90% of CH_4 of the sediments (Hinrichs et al., 2002).

AEROBIC OXIDATION OF METHANE (AEOM) AeOM is performed by aerobic methane oxidizing bacteria (MOB) in presence of oxygen, namely in the upper oxic sediment zone or in the water column, according to the following reaction (Boetius et al., 2013):

AeOM

$$CH_4 + 2\,O_2 \longrightarrow CO_2 + 2\,H_2O \tag{1.3}$$

which, releasing CO_2, can contribute to sediment or water acidification (Biastoch et al., 2011) and/or water anoxia (Dickens, 2003; Elliott et al., 2011).

MOB are ubiquitous and the main lineages are $\alpha-$ and $\gamma-$Proteobacteria (Hanson et al., 1996; Op den Camp et al., 2009). The former thrive in terrestrial environments and therefore are not of interest in marine ecosystem. The latter are typical for terrestrial as well as marine environments, need high CH_4 concentration (larger than atmospheric one) and utilize CH_4 both for assimilation (*i.e.* biomass production) and energy yielding (Hanson et al., 1996).

ANAEROBIC OXIDATION OF METHANE (AOM) AOM was firstly predicted on the base of mass balance calculation already in the 1970s (Reeburgh, 1976; Panganiban et al., 1979) but for years there were only indirect evidences of the process. Over time, increasingly more proofs and details were collected and a series of biogeochemical measurements has provided strong indications for a sulfate-dependent AOM according to the reaction:

AOM

$$CH_4 + SO_4^{2-} \longrightarrow HCO_3^- + HS^- + H_2O \tag{1.4}$$

This reaction can become thermodynamically favorable (*i.e.* with a negative Gibbs free energy) in sediments but providing only little energy (varying between -16 kJ mol^{-1} and -33 kJ mol^{-1}), at the lower limit of energy needed to support ATP formation. In ideal conditions this minimum energy is ~ 50 kJ, but for some inevitable inefficiency a more realistic estimate is $60 - 70$ kJ (Schink, 2002). Usually 3-4 protons are used for a single ATP molecule (Van Walraven et al., 1996; Schink, 1997; Van Walraven et al., 1997; Stock et al., 1999), which means that each proton has to provide roughly 15 kJ mol^{-1} (Caldwell et al., 2008). In spite of this tight energetic constraint and low rate measured in the field (Schink, 1997; Hoehler et al., 2001; Jørgensen et al., 2001; Jackson et al., 2002) - indicating that AOM operate close to the thermodynamic limit - a large amount of aggregates of archaea and sulfate reducing bacteria was actually found (Boetius et al., 2000) at the horizon of CH_4 consumption and SO_4^{2-} reduction. This horizon is a relatively narrow zone of sediments which takes the name of Sulfate-Methane Transition Zone (SMTZ, SMT in Fig. 1.5).

Energetic considerations about the AOM

SMTZ

Such observations suggest that a synthrophic consortium of anaerobic methanotrophic archaea (anaerobic methanotrophs, ANME) and SRB might actually mediate the AOM (Boetius et al., 2000; Orphan et al., 2001; Niemann et al., 2006b; Knittel et al., 2009) and narrows down the energetic constraint even more as each proton needs to provide approximately the double of the aforementioned energy to sustain ATP formation. Field experiments (Hoehler et al., 1994) had previously that a low H_2 concentration (< 0.3 nM) is the necessary condition for AOM to occur. This finding together with the observation of the ANME-SRB consortia have offered a hint to unravel the AOM mechanism. It is now thought that AOM relies on the interspecies hydrogen transfer between ANME, producing H_2 according to the reaction[11]

Suggested AOM mechanism

$$CH_4 + 2\,H_2O \longrightarrow CO_2 + 4\,H_2 \tag{1.5}$$

and SRB, consuming H_2 in the reaction

$$SO_4^{2-} + 4\,H_2 + H^+ \longrightarrow HS^- + 4H_2O. \tag{1.6}$$

At pH$=7.0$, temperature $T = 298$ K, and pressure of 1 bar, the Gibbs energy of reaction (1.5) is $\Delta G = 135.4$ kJ mol^{-1}, the one of reaction

11 Which is exactly the reverse of reaction (1.1)

(1.6) is $\Delta G = -152.3$ kJ mol^{-1} and this gives a net (negative) Gibb's energy of $\Delta G = -16.9$ kJ mol^{-1} (Dale et al., 2006), in line with theoretical expectations.

Since the proposed mechanism for CH_4 oxidation is the reverse hydrogenothrophic methanogenesis, it is apparent that only one of the two reaction is possible, given the environmental conditions. Considering then that SRB compete with methanogenic archaea for H_2 (Lovley et al., 1988) and are instead synergetic with ANME, AOM only occurs when SRB consume enough H_2 to make AOM thermodynamically viable (Hoehler et al., 1994; Hoehler et al., 1998; Dale et al., 2006; Dale et al., 2008c). Finally it must be stressed that since most of the cellular reactions are aqueous-phase reactions, in case the methane enters in step (1.5) in gaseous phase, AOM is limited to the gas-liquid surface and therefore limited in rate and also in energy production (Caldwell et al., 2008). For this reason microbes are considered to have access only to dissolved methane, where the energy yield might also be higher (Caldwell et al., 2008).

Observational evidence of AOM mechanism

To date no ANME has ever been isolated but transfer of electrons between CH_4 and sulfates (Iversen et al., 1985; Hoehler et al., 1994) and strongly depleted ^{13}C archaeal biomarkers (Elvert et al., 1999; Hinrichs et al., 1999; Thiel et al., 2001; Knittel et al., 2009) robustly back the suggested dynamics. Other alternative pathways and electron transfer have been proposed, too (Valentine et al., 2000; Sørensen et al., 2001; Caldwell et al., 2008; Milucka et al., 2012; McGlynn et al., 2015; Wegener et al., 2015). Three main marine clades of sulfate ANME have been identified (according to their biomarkers) so far: ANME-1a/b, ANME-2a/b/c and ANME-3 (Knittel et al., 2009).

AOM global budget

A recent investigation (Egger et al., 2018) suggests that $45 - 61$ $TgCH_4$ are globally oxidized annually at the SMTZ, a budget which corresponds to the $15 - 20\%$ of the previous estimate of 305 $TgCH_4$ yr^{-1} (Hinrichs et al., 2002; Reeburgh, 2007) but not far from the numbers found by Boetius et al., 2013 (67 $TgCH_4$ yr^{-1}, see Fig. 1.6). If compared to the amount of CH_4 entering the SMTZ ($\sim$ 80 $TgCH_4$ yr^{-1}, Boetius et al., 2013, see Fig. 1.6) an efficiency between 56% and 76% can be inferred. The 80% of AOM occurs in shelf environment (Egger et al., 2018) and is accompanied by a sulfate reduction of 5.3 $TmolSO_4^{2-}$ yr^{-1}, corresponding to 7% (Jørgensen et al., 2006) or 47% (Bowles et al., 2014) of the total global SO_4^{2-} reduction occurring in the seabed.

Alternative AOM pathways

Other possible pathways for anaerobic oxidation of methane, which use other chemical species as oxidants instead of SO_4^{2-}, have been discovered in the last years: iron (Beal et al., 2009; Crowe et al., 2011; Sivan et al., 2011; Norði et al., 2013), manganese (Beal et al., 2009), nitrite (Ettwig et al., 2010) and nitrate (Raghoebarsing et al., 2006; Haroon et al., 2013). Iron- and manganese-coupled AOM pathways might be important for other biogeochemical cycles (*e.g.* phosphorus,

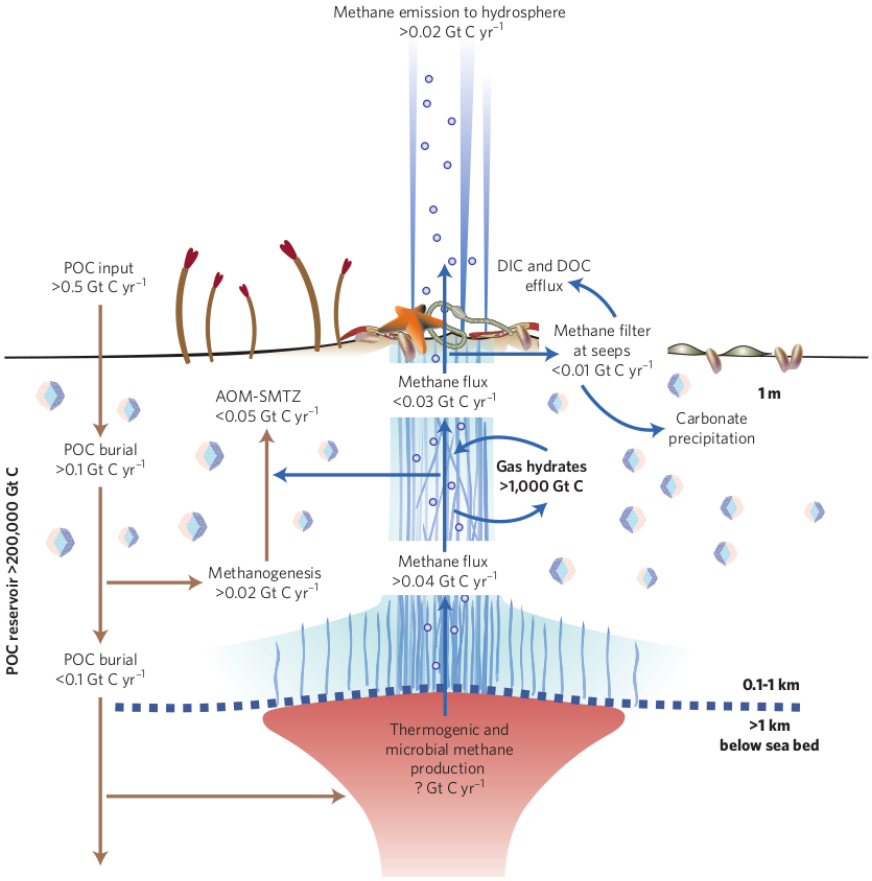

Figure 1.6: Scheme of methane (in carbon equivalents) and carbon fluxes at continental slope according to the assumptions and analysis of Boetius et al., 2013. From Boetius et al., 2013.

Rooze et al., 2016), but they are expected not to be globally efficient contributors to CH_4 removal (Sivan et al., 2011; Egger et al., 2014), even if their role on Arctic shelves is not clear (Winkel et al., 2018). Nitrate-coupled AOM is instead more typical of freshwater environments (Ettwig et al., 2010; Ettwig et al., 2012; Vaksmaa et al., 2016; Welte et al., 2016) although some species have been detected in marine environments, too (Li-dong et al., 2014; Chen et al., 2015; Padilla et al., 2016).

1.3.3 *Current knowledge of methane in the Arctic Shelves: subsea permafrost, hydrates and the role of AOM*

CH_4 fluxes from the ESAS

The degradation of the SSPF and the destabilization of the hydrates have been pointed out as the main drivers (Shakhova et al., 2014; Shakhova et al., 2015; Shakhova et al., 2017) of the oversaturation in methane of the ESAS waters and hence as the processes at the origin of the relevant CH_4 flux ($8 - 17$ $TgCH_4$ yr^{-1}, Shakhova et al., 2010b;

Shakhova et al., 2014) from the ESAS waters only[12]. It is remarkable though that this comparatively high flux might originate from such a tiny portion of global waters. In fact the CH_4 flux could be comparable with the total CH_4 emission of Northern tundra, *i.e.* $\sim$ 19.5 $TgCH_4\ yr^{-1}$ (McGuire et al., 2012) and even larger than the global emissions from artificial water reservoirs ($\sim$ 13 $TgCH_4\ yr^{-1}$, Deemer et al., 2016), from Arctic freshwaters (13 $TgCH_4\ yr^{-1}$, Bastviken et al., 2011) or from estuaries ($\sim$ 7 $TgCH_4\ yr^{-1}$, Borges et al., 2011). These considerations and the uncertainty of the estimation call for a new assessment of the CH_4 venting from the ESAS.

Measurements do not support high CH_4 flux from the ESAS

Whilst high emissions have been confirmed locally along water leads and polynyas[13] by airborne observations (Kort et al., 2012), the integrated annual flux sum up only to 0.3 $TgCH_4\ yr^{-1}$. Alternative methods, as the atmospheric constraints of Berchet et al., 2016 or, more recently, of Reum, 2019, have offered new estimates of CH_4 emissions, which do not agree with the high values reported in Shakhova et al., 2014 nor in Shakhova et al., 2010b. A revised CH_4 flux (Berchet et al., 2016) from Arctic waters suggests a value of $0 - 4.5$ $TgCH_4\ yr^{-1}$. A work by Thornton et al., 2016 further reduced the estimate of the maximum to 2.9 $TgCH_4\ yr^{-1}$ and downsized the role of methane bubbles, while Lorenson et al., 2016 constrained the emission in the range $0.02 - 2.24$ $TgCH_4\ yr^{-1}$ and Reum, 2019 to $0.4 - 1.5$ $TgCH_4\ yr^{-1}$.

Unknown CH_4 benthic-pelagic flux in the ESAS

Global marine seepage sums up to $\sim 27 - 65$ $TgCH_4\ yr^{-1}$ (Anderson et al., 2010; Boetius et al., 2013) but CH_4 flux at Arctic seabed is unknown as well as it is unknown the methane production in the sediments, the one related to SSPF or to hydrate destabilization. The latter constitute a peculiar and shelf-specific feature that is worth a zoom-in.

1.3.3.1 *Methane hydrates*

Definition of GH

A large portion of the carbon stored in the Arctic Shelves is thought to be preserved in the form of methane hydrates. Gas hydrates (also known as clathrates) are a specific state of matter (optically similar to ice, see Fig. 1.7) in which low molecular weight gas (mainly CH_4) is trapped in a "cage" of water molecules (Sloan Jr et al., 2007). Depending on the symmetry of the cage, three clathrates have been identified (structure I, structure II, and structure H, Fortes et al., 2010). Hydrates are a highly-concentrated form of methane: 1 m^3 of hydrates sequesters a maximum of 180 m^3 of gaseous methane at standard temperature and pressure (Ruppel et al., 2017). This feature is also at

12 It is however worth stressing that a high concentrations of CH_4 in the water not necessarily imply a high methane outgassing as Myhre et al., 2016 and even more remarkably the BP Deepwater Horizon blowout in 2010 showed (Kessler et al., 2011; Yvon-Lewis et al., 2011).

13 Laptev Sea hosts for instance the Great Siberian Polynya

the origin of its high latent heat: $52 - 60$ kJ $(\text{molCH}_4)^{-1}$ (Handa, 1986; Zhang, 2015) whereas the latent heat of water is only ~ 6 kJ mol^{-1}.

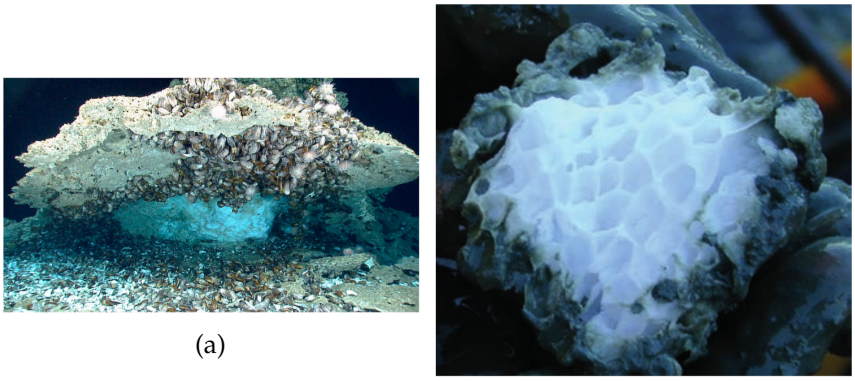

(a) (b)

Figure 1.7: *a.* Gas hydrate (white material) formed beneath mussel-coated carbonate rock on the seafloor of the Gulf of Mexico as photographed by NOAA's Deep Discoverer remotely operated vehicle in 2014. From Ruppel et al., 2017. *b* Methane hydrate block from the subduction zone off Oregon (Pacific Northwest, USA) at a depth of about 1200 m in the upper meter of the sediments. From AMAP, 2015.

Methane hydrates represent the stable thermodynamic form of methane in presence of water under certain conditions of pressure (p), temperature (T) and salinity (S) provided that water is saturated in CH_4 (Xu et al., 1999; Mestdagh et al., 2017). These p-T-S conditions define the (Gas) Hydrate Stability Zone (GHSZ) and occur globally at the majority of ocean depths but the lack of methane at saturation level normally prevents formation of clathrates.

Definition of GHSZ

Uncertainty in CH_4 concentrations explain the high variability of the estimates of CH_4 stock, as many assessments rely on the evaluation of the GHSZ and on looser assumptions on the methane water concentration (Dean et al., 2018). Recent estimates range in $400 - 2500$ PgC (Milkov et al., 2003; Archer, 2007; Archer et al., 2009; Boswell et al., 2011; Burwicz et al., 2011; Denisov et al., 2011; Wallmann et al., 2012; Piñero et al., 2013) but much larger estimates have been proposed as well in earlier studies ($>$ 10000 PgC, Kvenvolden, 1988; MacDonald, 1990). For hydrates in Arctic Ocean the values vary: $30 - 170$ PgCH_4 (McGuire et al., 2009), 116 PgC (Kretschmer et al., 2015), 500 PgC (Kvenvolden, 1988) and 900 PgC (Biastoch et al., 2011).

CH_4 stock in GH

Given the required p-T-S conditions, GHSZ occurs in two cases:

1. In submarine conditions where the top of the GHSZ lies between a depth of 300-500 m and the lowest boundary usually lies a few hundreds meters beneath the seafloor (Hester et al., 2009; Ruppel et al., 2017). 99% (Ruppel et al., 2017) of the gas hydrates belongs to this type. Because of the aforementioned me-

thane constraint, they occur generally in continental margins where carbon delivery to the seafloor is high enough to enable methanogenesis.

Occurrence of GHs

2. Inside or below the PF at shallower depths because colder temperatures provide stability conditions for hydrates at lower pressure. These hydrates are defined as Permafrost-Associated Gas Hydrates (PAGH) and only $\sim$ 1% of global gas hydrates is thought to belong to this type (Ruppel et al., 2017).

Almost all the methane trapped in clathrate is biogenic (Archer, 2007; Ruppel, 2011; Wallmann et al., 2012) and therefore characterized by a light ^{13}C signature.

GHs associated to the SSPF

A specific type of PAGH is the one occurring below the SSPF, as it is determined by PF presence but in a submarine environment which, by itself, would not provide the necessary condition to create a GHSZ. McGuire et al., 2009 estimated a methane content in SSPF-hydrates of $2-65$ $PgCH_4$ while estimates by Shakhova et al., 2010a, just limited to ESAS, are of $\sim$ 540 $PgCH_4$ (based on Gramberg et al., 1983). The latter is however highly debated (Ruppel et al., 2017).

GHs after sea transgression

SSPF-hydrates are unique as they are the only shallow marine hydrates, namely hydrates existing in subsea settings with water depth $<$100 m (Shakhova et al., 2019). After the inundation of the shelf area and the formation of the SSPF, sediment temperature increased and this led to a new quasi-stationary condition that also triggered the destabilization of SSPF-hydrates. Temperature, more than pressure, causes the largest destabilization of this type of gas hydrates (Makogon et al., 2007; Archer et al., 2009; Mestdagh et al., 2017; Chuvilin et al., 2018), with exceptions at the edge boundary of the GHSZ where slight pressure changes (also induced by storms) can cause partial release of gaseous CH_4. After the submersion some of the hydrates were preserved under new p-T conditions, some gaseous CH_4 migrated to the Sediment-Water Interface (SWI) and another portion was reconverted back to gas hydrate (conceivably at a different level) in a metastable relic form, due to a phenomenon known as "self-preservation" (Yershov et al., 1991; Chuvilin et al., 2000; Istomin, 2006). Such a phenomenon[14] also allowed hydrates to survive on longer time-scales and, very likely, to partially persist during previous sea trans- and re-gression cycles. Earlier glacial cycles have however always been shorter ($1-2$ kyr) than the current one ($>$5 kyr) (Fleming et al., 1998) and this makes the present stage particularly critical for the current state of the SSPF-hydrates since they are covered by an increasingly thinner SSPF layer.

14 Self-preservation is not fully explained, but is thought to be caused by local features of the sediments (Kwon et al., 2008; Chuvilin et al., 2011; Hachikubo et al., 2011; Prasad et al., 2019) and a coupling between the mass-transfer resistance and the heat transfer resistance (Bai et al., 2015)

Considered that sediments permeability is determined by the frozen water content, the amount of relic SSPF is a discriminant for the possible release of CH_4 from below. Moreover the gas hydrates themselves have been thought to act as a cap for gas seepage, though with an incomplete seal (Naudts et al., 2006).

Role of GHs as a cap for migrating CH_4

CH_4, possibly originating from gas hydrates has been considered the plausible cause of the Paleocene-Eocene Thermal Maximum, a climate warming event ($+5-8$ °C) which took place rapidly (in less than 2000 yr) (Dickens et al., 1995; Dickens et al., 1997). It means that in the past hydrate-originating CH_4 fluxes might have been conspicuous while the current estimates are rather low: $2-10$ $TgCH_4$ yr^{-1} (Ciais et al., 2013; Kirschke et al., 2013; Etiope, 2015; Saunois et al., 2016). These amounts rely on the hypothetical values by Cicerone et al., 1988 with no new measurements performed to assess the global hydrates contribution to atmospheric CH_4, let alone contribution from SSPF-associated hydrates. Gas hydrates are expected to respond slowly ($>$ 100000 yrs, Dean et al., 2018) to change of boundary conditions due to the slow thermal transfer in the sediment, high latent heat and self-preservation (Xu et al., 1999; Archer et al., 2009; Hunter et al., 2013; Mestdagh et al., 2017; Ruppel et al., 2017). In case of PAGH, the release of CH_4 lags the thawing of corresponding PF (Ruppel et al., 2017).

CH_4 emissions from GHs

Degrading SSPF-hydrates have been invoked as the cause of the oversaturation in methane of ESAS waters, together with thawing SSPF. A number of models has attempted to assess the potential release of CH_4 from hydrates to the water column to check for their role (Reagan et al., 2009; Westbrook et al., 2009; Biastoch et al., 2011; Reagan et al., 2011; Thatcher et al., 2013; Kretschmer et al., 2015). 473 $TgCH_4$ have been estimated to be emitted from hydrates to the Arctic Ocean in the next 100 years (Kretschmer et al., 2015), namely 4.73 $TgCH_4$ yr^{-1}, resulting in a practically null flux to atmosphere once the microbial oxidation in the water column occurs. This model result is also in line with a new measurement based on radiocarbon (Sparrow et al., 2018), which has recently proven that the CH_4 from the thawing SSPF and from gas hydrates currently is not contributing to marine CH_4 emissions to the atmosphere (Dean et al., 2018). This revised weight of emissions however does not mean that CH_4 release from ESAS sediments might be without consequences as, for instance, the CH_4 released to the Arctic waters in the last 30 yr (Westbrook et al., 2009) is thought to have had repercussions on water acidification due to AeOM (Biastoch et al., 2011).

Role of GHs in CH_4 flux from the Arctic Ocean

1.3.3.2 *Dissolved methane and free gas: the AOM and the role of bubbles*

Recent numbers found by Egger et al., 2018 have downsized the global estimates of AOM but have stressed the major role of shelves for the AOM itself. In this light the Arctic shelves represent thence an

AOM occurs mainly in shelf areas

even more relevant environment to be studied, in particular the ESAS, being it the largest continental shelf.

Hypothesis 1: CH_4 *in ESAS waters comes from the SSPF and GHs*

The debate about the origin of the high CH_4 concentration in ESAS waters is open. Shakhova and her collaborators on several occasions (Shakhova et al., 2010b; Shakhova et al., 2014; Shakhova et al., 2015; Shakhova et al., 2017; Shakhova et al., 2019) reiterated that the thawing SSPF and the associated hydrates are the origin of CH_4 emissions to the water, via diffusion or ebullition. Bubbles of CH_4 would also cause the high estimated CH_4 flux to atmosphere[15]. Sapart et al., 2017 partially backed the theory about the origin of the CH_4 based on a triple isotopes analysis of ESAS waters and sediment cores, which confirmed the biogenic (and not thermogenic) origin of the CH_4 although the ^{14}C analysis prevented a unique explanation of the data.

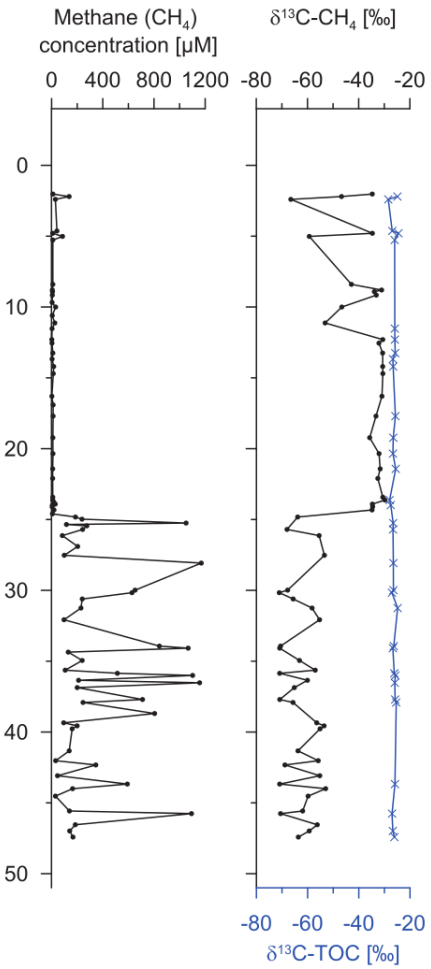

Figure 1.8: Vertical profile of CH_4 concentration (*left*) and $\delta^{13} - CH_4$ (*right*) in a subsea permafrost core. The y-axis reports the meters below sea floor. The abrupt drop of CH_4 and increase in $\delta^{13} - CH_4$ at 24.75 m, corresponding to the the Ice-Bonded Permafrost Table, have been interpreted as evidence of methane oxidation. From Overduin et al., 2015b

Hypothesis 2: CH_4 *in ESAS waters cannot come from the SSPF and GHs*

However several other measurements and modeling results have challenged this interpretation. As previously stated, direct atmospheric observations do not support the estimated sea-air CH_4 flux and the role of bubbles has been also heavily reduced (Thornton et al., 2016). Furthermore, evidence has been found of an efficient sulfate-mediated AOM in the thawed layers of the SSPF: a strong decrease of CH_4 concentration and increase of $\delta^{13}C$ at top of the PF table (Fig. 1.8) not accompanied by methanogenesis that might replace the oxidated CH_4 (Overduin et al., 2015b). Winkel et al., 2018 has discovered

15 The estimate of about 17 $TgCH_4\ yr^{-1}$ (Shakhova et al., 2014) is in fact not directly measured but is based on upscaling the volumetric fraction of bubbles in the water column.

a thriving community of ANME with isotopic indications of AOM coupled to sulfate but also to iron, manganese and nitrate. Marine and terrestrial clades of ANME have been detected both in frozen and unfrozen SSPF confirming what was expected, *i.e.* the occurrence of an efficient (72-100%) AOM also in correspondence of the SSPF. The potential AOM associated with SSPF environment has been estimated to be $0.0001 - 1.1889\ TgCH_4\ yr^{-1}$.

Bubbles can reconcile the diverging hypotheses

Bubbles could represent a partial solution for the debate reconciling the existence of an efficient AOM barrier in the SSPF sediments and a high CH_4 concentration in the water. Bubbles are difficult to be properly measured and upscaled (given the episodic and random character of ebullition phenomena) and are tricky to be modelled both from the physical (McGinnis et al., 2006; Leighton, 2007) and biogeochemical (Mogollón et al., 2009; Regnier et al., 2011; Boudreau et al., 2015) points of view. They are usually detected locally with optical images and with hydro-acoustic techniques (Shakhova et al., 2014; Leifer et al., 2017; Shakhova et al., 2017). Some acoustic anomalies in seismic surveys (Shakhova et al., 2017) also hint at the presence of moving free gas accumulated beneath the ESAS sea floor in some locations (see Fig. 1.9). Such trapped gas can be directly unroofed for instance by ice-scouring, a process in which icebergs can dig furrows up to 4 m deep and several kilometers long in the top sediment. This action mechanically destroys the upper sediments, resuspend the material and liberates trapped gas (Brooks, 1974; Cherkis et al., 1992; Clark et al., 1998; Shakhova et al., 2017). Therefore free gas, which forms in the sediments, may in theory have the chance to bypass the several biofilters in the sediments (Haeckel et al., 2007; Regnier et al., 2011) and in the waters, since it is unaccessible to methanotrophs, and finally make it to the atmosphere,

Details of bubble dynamics and chemistry

While rising, bubbles exchange gas with surrounding water and this process may determine the collapse of the bubbles themselves or the replacement of gas inside them (McGinnis et al., 2006; James et al., 2016). For such a reason, flares of CH_4 bubbles - detected all over the world, *e.g.* in the Black Sea (McGinnis et al., 2006) or the Gulf of Mexico (Yvon-Lewis et al., 2011) - manage to reach the sea surface only in shallow waters, like the ESAS waters. However their composition could eventually be completely different once they get to the surface. The gas replacement while rising might be at the origin of the measured high water CH_4 concentration.

A series of other aspects complicate nevertheless this picture. CH_4 oxidation, although slow and inefficient, happens actually also at surface of bubbles and this process may cause the collapse of the bubbles. If CH_4 bubbles are emitted in the GHSZ another phenomenon occurs: a coat of CH_4 hydrate forms on the bubble (Maini et al., 1981; Topham, 1984; Gumerov et al., 1998; Rehder et al., 2002). On one hand, it protects the bubbles and inhibits gas exchange (Rehder et al., 2002) on the

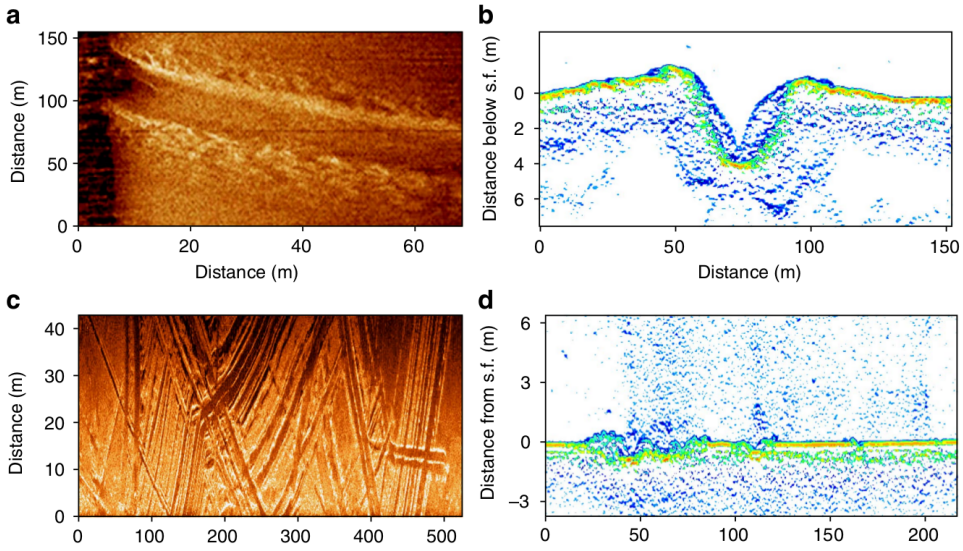

Figure 1.9: High resolution sonar image of sea floor showing a in ice scour *a* and vertical profile of the ice scour itself **b**. *c* reports several furrows on ESAS sea floor and *d* shows the the furrows and bubble plumes evading from the altered sediments. From Shakhova et al., 2017.

other hand it utilizes part of the methane and this might eventually cause the collapse of the bubbles itself, if not big enough (McGinnis et al., 2006).

All these aspects are therefore compatible with the presence of bubbles in ESAS waters, high water CH_4 concentration but also with an active AOM filter in the sediments and a small CH_4 flux to the atmosphere[16].

The processes affecting CH_4 production and migration introduced so far are schematically reported in Fig. 1.10.*a*. Fig. 1.10.*b* shows the methane stores in the Arctic and the sources of their potential emissions to ocean and atmosphere.

1.3.3.3 *Other biogeochemical aspects of methane-affected sediments*

Anoxia and acidification

CH_4 presence in the sediments has also other biogeochemical effects. Besides the already mentioned potential for the formation of hypoxic/anoxic zones due to AeOM (Yamamoto et al., 2014) and possible acidification (Biastoch et al., 2011; Boudreau et al., 2015), CH_4 interacts also with other chemical cycles: sulfur, iron and carbonate the most important ones.

SO_4^{2-} consumption

Egger et al., 2018 has recently highlighted that, in spite of stoichiometric ratio of 1:1 (reaction 4.3), the measured mean ratio of sulfate and methane flux at SMTZ is 1.41:1. It suggests that only 70% of the

16 According to Archer, 2015 considering a piston velocity of 3 m d^{-1} and a methane concentration of 50 nM, the CH_4 annual flux of an ice-free ESAS would be only 0.4 $TgCH_4$ yr^{-1} and the flux due to bubbles only 0.02 $TgCH_4$ yr^{-1}.

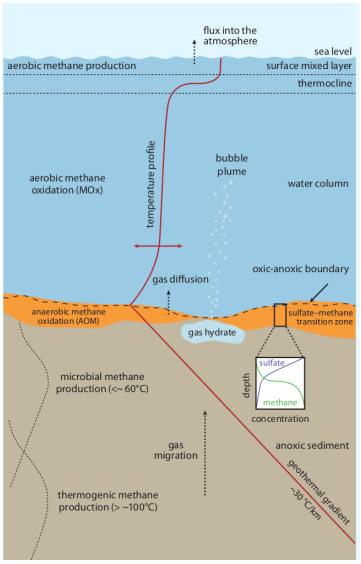

(a) Typical areas of methane production, accumulation, oxidation and migration within ocean sediments and waters. The AOM process and SMTZ is highlighted.

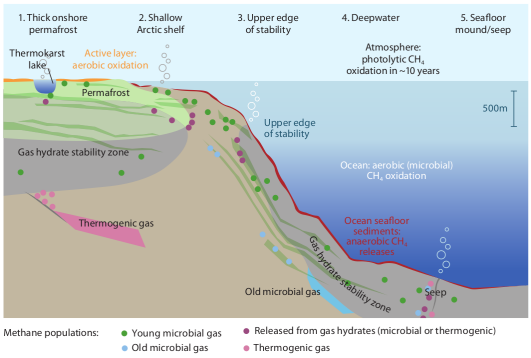

(b) Terrestrial and shelf stores of methane with the sources of potential emissions to the Arctic ocean. In PF and SSPF regions (left of graphic) the GHSZ occurs at shallower depth because of temperature effects. GHSZ does not imply that gas hydrates are actually present in the same area. Redrawn from Ruppel, 2011.

Figure 1.10: From AMAP, 2015.

sulfate consumed in correspondence of the SMTZ can be ascribed to AOM process as we know it. This leaves room open for a possible role of organoclastic sulfate reduction (Regnier et al., 2011; Komada et al., 2016) as well as other processes (*e.g.* like a concurrent recycling of CH_4 in the SMTZ, Beulig et al., 2017) or a combination of multiple ones (Egger et al., 2018).

Alkalinity production and authigenic carbonates

Another peculiar characteristics of AOM reaction (eq. 4.3) is the local production of alkalinity, unlike AeOM. Such production may drive the precipitation of authigenic carbonates (mainly aragonite and dolomite) at the SMTZ (Aloisi et al., 2000; Luff et al., 2005; Pierre et al., 2012; Crémière et al., 2016b; Crémière et al., 2016a) and have an impact on sediment column carbonate saturation state Ω. Authigenic carbonates, originating by AOM alkalinity production, are usually characterized by very low $^{13}\delta C$ ($< -70‰$), as result of a process involving many biological step and therefore several isotopic fractionation in favor of lighter carbon. Even the most extremely ^{13}C-depleted carbonates ever reported ($-125‰$, Drake et al., 2015a) are thought to be AOM-induced. The study of authigenic carbonate sometimes enables to reconstruct scenarios of past CH_4 seepage and the movement of the SMTZ, offering in turn some constraints to the models.

Interaction with iron

The impact of AOM on the carbonate system and alkalinity is strictly connected to the fate of byproducts of reaction 4.3, especially H_2S and its interaction with iron (Rickard et al., 2007).

If hydrogen sulfide reaches oxic area, it gets oxidized in sea water according to the reaction:

$$HS^- + 2\,O_2 + HCO_3{}^- \longrightarrow SO_4{}^{2-} + CO_2 + H_2O \tag{1.7}$$

the net reaction of (4.3) and (1.7) would end up giving the same products as if methane underwent directly the AeOM (1.3).

The other pathway that sulfides might follow, would be the reaction with reduced iron, not a rare eventuality in the ESAS and Beaufort shelves which receive high benthic iron fluxes due to glacial contribution of iron oxides (Raiswell et al., 2006; Thuróczy et al., 2011) and from sea-ice melting (Wang et al., 2014). The reaction reads

$$Fe^{2+} + HS^- + HCO_3{}^- \longrightarrow FeS_{(m)} + CO_2 + H_2O \tag{1.8}$$

and precipitates iron (II) monosulfide, mainly in the form of mackinawite ($FeS_{(m)}$) a still rather soluble compound. Also in this case the ALK units produced in (4.3) are consumed. Some of the $FeS_{(m)}$ produced in reaction 1.8 may however react with an extra hydrogen sulfide produced in reaction 4.3, and the following step would occur:

$$FeS_{(m)} + HS^- + H^+ \longrightarrow FeS_{2(p)} + H_2 \tag{1.9}$$

This would lead to precipitation of pyrite ($FeS_{2(p)}$) and therefore to an irreversible alkalinity production within the sediments, considering that $FeS_{2(p)}$ is (practically) insoluble (Rickard et al., 2007). Such a process has been so far overlooked in assessment and considerations about CH_4 oxidation, acidification effects and budget of benthic-pelagic flux of DIC and ALK.

Knowledge gaps in the ecology of AOM communities

Finally the ecology of AOM-performing microbial communities, especially at high latitudes, is not well understood (James et al., 2016) and this of course interferes with a deeper comprehension of the process itself. This is especially true in a dynamic setting like SSPF-affected areas, where labile carbon might also come from thawing SSPF fostering CH_4 production and AOM. Even the prediction of future effects and possible climate feedback is hindered by such limited knowledge of how the ecosystem might react (James et al., 2016; Dean et al., 2018). It is well assessed that even at great depths (*i.e.* pressures, D'Hondt et al., 2004; Parkes et al., 2005) and low temperature (Niemann et al., 2009) microorganism remain active and therefore their activity can be assumed to be ubiquitous. It is known, for instance, that the doubling time of ANME-2 consortia is ~ 7 months (Nauhaus et al., 2007) and that an efficient biofilter requires typically $> 10^{10}$ cells cm^{-3} (Lösekann et al., 2007; Knittel et al., 2009), but general studies

on the importance of AOM at low temperatures are missing (Dean et al., 2018). The bioenergetics of the AOM-performing communities (Q_{10}, growth dynamics, microbial population shift) is also poorly understood and investigated and this inevitably limits the trustworthiness in simulation of the processes.

1.4 RESEARCH OBJECTIVES AND DISSERTATION OUTLINE

Goal of the thesis: SSPF physics and microbiogechemistry

The thesis is designed to investigate the two macro-areas of the SSPF-related research which can be identified on the basis of the prevailing knowledge gaps exposed in the previous sections: the physical state of the SSPF and its biogeochemistry, with a specific focus on the effects of CH_4 possibly deriving from the SSPF. The dissertation is outlined to examine the structural and physical features of the SSPF first and the biogeochemical aspects later, since the former lay down in principle the constraints for the latter.

Systematic approach

Aim of the research presented here is a systematic study of the SSPF in a multi-sided way encompassing several approaches: laboratory results, modeling results and theoretical analysis in order to give an integrated and novel view of the SSPF and its role in the Arctic carbon cycle.

1.4.1 *Chapter 2. The subsea permafrost in a box: laboratory experiments, modeling results and comparison with the Stefan's problem*

Content of Chapter 2: laboratory experiments

Chapter 2 describes the results of some idealized laboratory experiments, aiming at having an insight how the heat transfer occurs in subsea permafrost, simplified in its constituents as a frozen porous medium underlain by warmer salty water. A simplified model solving heat equation is also presented and critically compared to the the results of the laboratory experiment for validation and possible employment with other boundary conditions. A comparison with the mathematical hypothesis of the Stefan's problem is carried out for movement of the phase boundary and thawing regimes. A final connections to measurements of real subsea permafrost is also considered.

Research questions of Chapter 2

Research questions:

Q2.1 *Is the numerical model able to reproduce the movement of the phase boundary?*

Q2.2 *How do the laboratory and model results compare to theoretical expectations?*

Q2.3 *How do the model results compare with field observations?*

1.4.2 *Chapter 3. The subsea permafrost enters an Earth System Model: the case of JSBACH*

Content of Chapter 3: JSBACH simulations

Chapter 3 shows the first integration of a SSPF component within a large-scale model, part of an Earth System Model (ESM). It reports the results of the implementation of the SSPF in JSBACH, the land component of the ESM of the Max Planck Institute for Meteorology. Based on the already present permafrost module, a physical 1-D model of the SSPF - from spin up, to submergence and thawing- is implemented taking into account heat transport and salt effect (in a heuristic way). The outcome of several simulations enable the exploration of idealized as well more realistic setups. A special care is given to the analysis of the thawing process in the aftermath of submergence, to the capacity of the model to reproduce (at least qualitatively) the formation of taliks and to the evaluation of the role of salt. The SSPF thawing rate is also assessed since it represents the key quantity needed for the desired coupling between a large scale model of the SSPF (like in JSBACH) to a reaction-transport model (like BRNS, the diagenetic model employed in the microbiogeochemical analysis of Chapter 4). Such an integrated model would represent a novel tool able to systematically study the impact of degrading SSPF on carbon at a larger scale. This chapter represents a first step towards this accomplishment.

Research questions of Chapter 3

Research questions:

Q3.1 *How does submergence affect the permafrost in JSBACH? What is the SSPF time response to change of upper boundary conditions from land to submarine?*

Q3.2 *How does the SSPF modeled in JSBACH compare to observations, other studies and to theoretical expectations?*

Q3.3 *Under which conditions is an extensive destabilization of the SSPF possible?*

Q3.4 *Is JSBACH capable to model complex features like taliks?*

Q3.5 *What are the current limitations present in JSBACH for modeling the SSPF?*

1.4.3 *Chapter 4. Assessing the potential for non-turbulent methane escape from the East Siberian Arctic Shelf: the employment of BRNS*

Content of Chapter 4: investigation with BRNS

Chapter 4 is devoted to exploring the AOM and potential methane flux of methane-affected sediments with the avail of 1-D reaction-transport diagenetic model (BRNS). With this model the porewater profiles of two case studies (boreholes) are firstly reproduced for validation. Secondly a thorough one-at-a-time steady-state sensitivity analysis is performed on an idealized sediment column, designed

to reproduce the typical setting of the ESAS sediments. An underlying source of methane is also considered to account for the degrading SSPF and/or destabilizing methane hydrates. Analysis of simulations enables the identification of the main drivers of the AOM, an assessment of its efficiency on a wide range of parameters (with special attention to the transferability of the model in other settings) and the detection of environmental conditions which allow a large non-turbulent methane flux to be released to the water column. A simple all-at-time sensitivity analysis permits the evaluation of synergies among the different parameters. A first order geographical study of the methane flux in the Laptev sea accompanies these results.

Other unclear aspects of the AOM in such settings are also tackled, as the link between sulfate fluxes and AOM at the SMTZ, or the connection of AOM with organic matter delivery.

Finally a series of transient simulations examines the dynamics of methane, AOM and AOM-performing biomass in the aftermath of a change of boundary conditions, as it would occur because of the thawing SSPF and/or degrading hydrates. Idealized future scenarios are considered, too.

Research questions:

Research questions of Chapter 4

Q4.1 *How much* CH_4 *could be emitted from Arctic sediments?*

Q4.2 *How efficient is the AOM biofilter? Which are the most important environmental controls on the efficiency of the AOM itself?*

Q4.3 *Under which condition is a high* CH_4 *escape possible?*

Q4.4 *How does the AOM affects the relation between* CH_4 *and* SO_4^{2-} *in the Arctic sediments?*

2

THE SUBSEA PERMAFROST IN A BOX: LABORATORY EXPERIMENTS, MODELING RESULTS AND COMPARISON WITH THE STEFAN'S PROBLEM

2.1 INTRODUCTION

Numerous phenomena within the Earth system involve the water solid-liquid phase change. The range of typical space and time scales where water phase change plays a main role goes from pico- (Caleman et al., 2008) and milli-second (Schremb et al., 2017) to millennial, from few Ångstrom typical of molecular activity (Vrbka et al., 2005) to thousands of kilometers of large continental scale.

Introduction to the Stefan's problem

The freezing-melting phase change is challenging even without demanding to describe its details at a microscopic level, in spite of it being a common and familiar phenomenon. It is the prototype of first order phase transition (being the entropy and the volume discontinuous at the transition) and it is intrinsically nonlinear. The first mathematical formulation of the liquid-solid phase change dates back to the seminal work by Stefan (Stefan, 1891), hence the problem is widely known as *Stefan's problem*. Since the position of the interface separating liquid and solid phase is unknown the problem takes also the name of *moving boundary problem*.

Many mathematical tools have been developed to solve the original simplistic Stefan's problem as well as other more complicated setups involving *e.g.* materials different from water (Tien et al., 1967), arranged in a more complex geometry (Myers et al., 2007; Mitchell et al., 2010), stagnant as well as flowing fluids (Epstein et al., 1983) or showing other "exotic" properties (Alexiades et al., 1981)[1].

Role of water phase change in PF soils

Water phase plays a conspicuous role in permafrost areas since ice-bonded or ice rich soils have different physical properties (porosity, thermal diffusivity, heat capacity, stress-strain characteristics, *etc.*) compared to the dry ones. Understanding how the phase change determines soil features overall is important not only from a speculative point of view, but also because of the practical consequences it may have to tackle geological, biological and geotechnical problems (*e.g.* Terzaghi, 1952; Molochushkin, 1973; Hunter et al., 1976; Osterkamp et al., 1976). Ice presence within the soil has a paramount effect on the biogeochemical activity. It indirectly affects the thermophysical and connective properties of the soil matrix and directly prevents (or at least reduces strongly) microbial activity and this allows carbon to

1 For a comprehensive overview see Alexiades et al., 1993.

be sequestered and stored for long periods. Over the millennia this process has enabled the formation of the boreal permafrost, whose carbon stock on land is thought to be $\sim$ 1300 PgC (Hugelius et al., 2014).

Challenge of the SSPF

A further challenge for the research is represented by the formation of the SubSea Permafrost (SSPF) following the submergence of terrestrial permafrost and the ongoing submersion of the coastal permafrost in aftermath of the retreat of the Arctic coast (Lantuit et al., 2011). This challenge arises because the system encompasses the simultaneous presence of a frozen soil (*i.e.* a porous medium, tricky to be modeled) and salty water. Solutes alter the properties of pure water shifting the equilibrium between the phases and therefore changing the freezing/melting temperature[2].

Role of salt

Many processes relating to water phase change in soils are still poorly covered, *e.g.* the movement of the moisture (Hoekstra, 1966; Hoekstra, 1967) and salt and ions (Brouchkov, 2000) under presence of temperature and concentration gradients. Most of the open questions concern the interwoven role of salt and temperature in causing destabilization of the SSPF which has been diffusively observed. Since the mean annual sea bottom temperature is below zero (Dmitrenko et al., 2011), salt is expected to play a key role in determining dissolution of pore ice in the submerged permafrost (Harrison et al., 1978; Angelopoulos et al., 2019). Salt appears therefore to be strictly linked to the SSPF stability and, potentially, to the release of the stored carbon, with consequent possible feedback on the climate system (Schuur et al., 2015).

Parabolic shape of the phase boundary: Stefan's solution?

Previous measurements (MacAulay et al., 1977; Harrison et al., 1981; Osterkamp et al., 1982; Harrison et al., 1978; Hutter et al., 1999; Overduin et al., 2016) and models (Sidhu, 1991; Angelopoulos et al., 2019), as reported in Fig. 2.1, show that the phase boundary between the frozen and the thawed regions of the SSPF deepens with time at an increasingly slowing down rate. Moreover the phase boundary is characterized by a parabolic shape and a uniform salinity in many cases. Assuming a "space-for-time" substitution and a constant coastal retreat[3], the parabolic shape in space implies a movement of the phase boundary that deepens with the square root of the time of submergence ($\propto \sqrt{t}$) and a decrease in the thawing rate of the form $\propto 1/\sqrt{t}$. Such a trend would be characteristic of the classical solution of the Stefan's problem, in its typical formulation with unrealistic constant boundary conditions and uniform thermal properties. For such reasons, without further qualifications, the fact that the SSPF might follow a Stefan or Stefan-like profile is purely conjectural and worth further investigation (Hutter et al., 1999).

2 In addition to the freezing point depression due to adhesion forces and soil retention effect, which is however usually small and can be neglected.

3 The latter assumption is rarely true but can be easily relaxed.

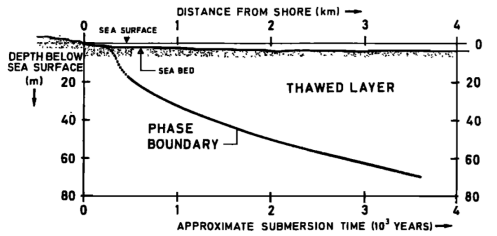

(a) Estimated position of the SSPF top table at the Prudhoe Bay, Alaska. The phase boundary is dashed where its details are not well known. From Hutter et al., 1999.

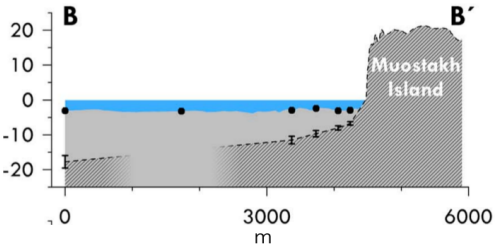

(b) Top of the ice-bonded SSPF table on the Muostakh Island in the Buor-Khaya Bay (Laptev Sea) as resulting from seismic noise analysis. From Overduin et al., 2015a.

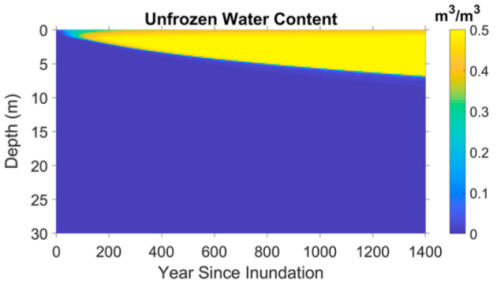

(c) Modeled unfrozen water content of the SSPF for the simulation representative of general conditions of the ESAS in Angelopoulos et al., 2019.

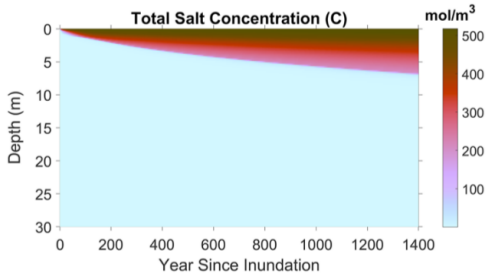

(d) Modeled salt content of the SSPF for the simulation representative of general conditions of the ESAS in Angelopoulos et al., 2019.

Figure 2.1: Measured (*a* and *b*) and modeled (*c* and *d*) profile of top of the SSPF phase boundary. The parabolic profile is apparent in measurements and models. Model results point out the strict correlation between salt penetration and phase boundary.

Transport regimes in the SSPF

The coupled role of salt and heat transfer in the thawing of the SSPF can give rise to several transport regimes: i) a diffusive heat and salt transport ; ii) a convective heat and salt transport; iii) a mixed regime with diffusive heat and convective salt transport[4]. The regimes might evolve from one into the other: for instance a non-steady double-diffusion Bénard convection (Hutter et al., 1999) might establish between the salt penetrating from the sea floor and the upgoing fresh water originating from melting pore ice at the phase interface. Such a phenomenon would induce a convection described with the Oberbeck-Boussinesq approximation of the Darcy's law (Hutter et al., 1999). Besides buoyancy, a convective flow can also be induced by the ocean pump (Hutter et al., 1999), namely the suction effect of ocean circulation at the bottom of the sea floor.

An overlooked process

This variegate picture shows how complex the physics of the SSPF is. Although important, heat and salt transport processes and their physical implications have been largely overlooked, receiving surprisingly little attention, with only a few studies dating back to the late 1970s but no recent further investigation. The tight link between thawing

4 Given the difference in diffusivity of salt and heat, with salt diffusivity up to 4 orders of magnitude smaller than heat diffusivity (Harrison et al., 1978).

and salt has emerged again recently in the modeling study of Angelopoulos et al., 2019 (Fig. 2.1.*c-d*). However, the limited observational data have hindered a deeper understanding of the processes actually taking place: most of theoretical conclusions are limited to a description of possible scenarios based on speculative assumptions while most of modeling premises are left to common sense.

Laboratory setups

In this chapter I show the results of two laboratory experiments, which were performed to offer extra observational evidence in a research area poor of direct measurements and to take a further step towards the modeling of the physics of submerging permafrost. Laboratory results were also compared with a purely diffusive numerical model. To my knowledge, no lab experiments aiming at investigating the thawing of frozen sediments under marine conditions had ever been performed in the past.

The experimental design included two simplified settings:

i. Pure ice overlaid by a warmer salty water, in order to calibrate the transport parameters of the numerical model;

ii. A frozen sand sample saturated with pure ice and overlaid by warm salty water, a setup whose aim was reproducing the SSPF in its basic constituents: an ice-bond porous medium overlain by warmer marine water.

In both cases the main quantity under observation has been the phase boundary between ice (or frozen sand) and water (or unfrozen sand).

Research questions of chapter 2

The goal of this chapter is getting a better understanding of the submergence process of the permafrost tackling the following research questions:

Q2.1 *Is the numerical model able to reproduce the movement of the phase boundary?* In other terms, assuming the numerical implementation of the heat diffusion scheme is well stated[5], I could rephrase the question asking whether and under which circumstances the modeling hypotheses are compatible with the laboratory results.

Q2.2 *How do the laboratory and model results compare to theoretical expectations?* As stated, the movement of the phase boundary is theoretically described by the solution of the Stefan's problem. A direct comparison of experimental outcomes with theoretical predictions and a discussion about the limitations is therefore needed.

Q2.3 *How do the model results compare with field observations?* A direct comparison between the sparse and rare field measurements of thawing subsea permafrost and the model and laboratory

5 A discussion on the numerical solution of the heat equation is beyond the scope of this study

results is complicated by the difference spatial and temporal scales between the two settings. However, a basic and rough juxtaposition is useful to grasp the vicinity of the model results and laboratory measurements with the real object of the research, namely the SSPF. The quantity more suitable for comparison is the thawing rate. On one hand, the thawing rate characterizes the thawing regimes, on the other hand it quantifies the divergence from the Stefan's solution. A collection of thawing rates obtained with different methods (geoelectric sounding and direct boreholes) by Overduin et al., 2016 provides a good basis for comparison.

2.2 THEORETICAL APPROACH

The theoretical problem of thawing dates back to Stefan and can be essentially considered as a non-linear problem of heat conduction complicated by the salt presence.

2.2.1 *The Stefan's problem: a moving boundary problem*

Stefan's problem (Stefan, 1891) deal with the description of the temperature distribution and the position of the moving boundary of a homogeneous material undergoing a phase change, *e.g.* ice-water phase change.

A moving boundary problem

The presence of a moving boundary whose position is not known *a priori* is what makes the solving of this type of problem difficult. The presence of an interface introduces non-linearities and discontinuities in the solution of the partial differential equations (PDEs), which describe the system.

Let us assume a homogeneous medium undergoing a phase change under constant pressure. The natural quantity describing the heat transfer in this condition is the enthalpy which, in absence of a change volume[6] is also a measure of internal energy.

The sensible heat

The heat accompanying a temperature increase is called *sensible heat* and its infinitesimal expression is given by

$$de = c_p dT \tag{2.1}$$

with e: enthalpy (thermal energy) per unit mass, c_p: specific heat at constant pressure and T: temperature. The energy needed to increase the temperature from a reference temperature T^* to a certain temperature T is therefore given by integrating Eq. 2.1. In a context of a phase change problem, the natural reference temperature is given by

6 And of other isochoric work

the phase-change temperature of the material T_m[7] and so the sensible heat per unit mass is given by

$$e(T) = \int_{T_m}^{T} c_{L/S}(\mathcal{T}) d\mathcal{T} \tag{2.2}$$

where $c_{L/S}$ is the liquid(L) or solid (S) specific heat at constant pressure for $T > T_m$ and $T < T_m$ respectively.

The latent heat

At $T = T_m$ a jump in the enthalpy distinguishes the material since the liquid phase contains the latent heat. The enthalpy[8] then reads:

$$\begin{cases} e_S(T) = \int_{T_m}^{T} c_S(\mathcal{T}) d\mathcal{T} & \text{for } T < T_m \\ e_L(T) = L + \int_{T_m}^{T} c_L(\mathcal{T}) d\mathcal{T} & \text{for } T > T_m \end{cases} \tag{2.3}$$

where L: latent heat per unit mass, also called enthalpy of fusion.

The system is then described by a set of PDEs which consists of the heat equation in the homogeneous liquid phase, the heat equation in the homogeneous solid phase and then the interface condition, also known as Stefan's condition. The heat equation reads[9]

The heat equation

$$\rho c \frac{\partial T(\vec{r}, t)}{\partial t} = \nabla \cdot (k \nabla T(\vec{r}, t)) \tag{2.4}$$

with ρ: density of the homogeneous medium, c: specific heat, k: (isotropic) thermal conductivity. In case of a constant thermal conductivity, constant density and constant specific heat, it can be rewritten as a parabolic PDE:

$$\frac{\partial T(\vec{r}, t)}{\partial t} = \alpha \nabla^2 T(\vec{r}, t) \tag{2.5}$$

with $\alpha = k/(\rho c)$: thermal diffusivity.

2.2.1.1 *The Stefan's condition*

The Stefan's condition: a form of conservation of energy

The interface condition can be retrieved invoking the energy conservation law. In the traditional Stefan's problem the interface is considered dimensionless and sharp and the difference between densities of liquid and solid phase is neglected[10].

By conservation of energy, the difference between heat flux leaving the interface and heat flux entering the interface is used to melt the medium, a melting which causes a movement of the phase boundary.

Derivation of Stefan's condition in 1-D

Let us derive Stefan's condition in 1-D, leaving the generalization in the 3-D to specific references (Alexiades et al., 1993). Consider a

7 Assuming it is constant.

8 With convention that $e = 0$ for solid at $T = T_m$

9 Dropping dependence on time t and position $\vec{r}$ on the parameters for simplicity of notation, considering only heat conduction described by Fourier's law and no additional volumetric heat source or sink

10 More realistic case where $\rho_S \neq \rho_L$ can also be treated.

slab of solid material with constant cross section A and length $[0, l]$. Assume heat is then provided at, say, $z = 0$ causing a liquid phase moving towards face at $z = l$. At a certain time t, liquid is found from $0 \leq z < Z(t)$, $Z(t)$ is the sharp interface and solid is found from $Z(t) < z \leq l$. The total enthalpy is given applying Eq. 2.3:

$$E(t) = A \left\{ \int_0^{Z(t)} [\rho c_L (T(z,t) - T_m) + \rho L]\, dz + \int_{Z(t)}^{l} \rho c_S (T(z,t) - T_m) dz \right\}. \tag{2.6}$$

with ρ: the common value of the density. Global energy balance requires that

$$\frac{dE(t)}{dt} = A\,[q(0,t) - q(l,t)] \tag{2.7}$$

where $q(0,t)$ is the heat flux into the slab and $q(l,t)$ is the heat flux out of the slab. Using then Leibniz's rule for the total derivative under the integral sign yields:

$$\begin{aligned} \frac{1}{A}\frac{dE(t)}{dt} = \rho c_L [T(Z(t),t) - T_m]\dot{Z}(t) + \rho L \dot{Z}(t) + \int_0^{Z(t)} \rho c_L \frac{\partial T(z,t)}{\partial t} dz + \\ + \int_{Z(t)}^{l} \rho c_S \frac{\partial T(z,t)}{\partial t} dz - \rho c_S [T(Z(t),t) - T_m]\dot{Z}(t). \end{aligned} \tag{2.8}$$

Considering that $T(Z(t),t) = T_m$ by definition, employing the heat equation 2.4 and integrating the quantity gives:

$$\begin{aligned} \frac{1}{A}\frac{dE(t)}{dt} = \rho L \dot{Z}(t) + k_L \frac{\partial T}{\partial z}(Z(t)^-, t) - k_L \frac{\partial T}{\partial z}(0,t) + \\ + k_S \frac{\partial T}{\partial z}(l,t) - k_S \frac{\partial T}{\partial z}(Z(t)^+, t) \end{aligned} \tag{2.9}$$

where the superscript $+/-$ stand for the right and left derivative respectively. Enforcing Eq. 2.7 and considering that

$$-k_L \frac{\partial T}{\partial z}(0,t) = q(0,t) \quad \text{and} \quad -k_S \frac{\partial T}{\partial z}(l,t) = q(l,t)$$

the Stefan's condition in 1-D can finally be derived:

$$\rho L \dot{Z}(t) = -k_L T_z(Z(t)^-, t) + k_S T_z(Z(t)^+, t) \tag{2.10}$$

where the subscript z denotes the partial derivative with respect to that variable. As expected, results would have not changed if a different reference temperature had been chosen instead of T_m.

General Stefan's condition

Eq. 2.10 is the 1-D for of the more general Stefan's condition given by

$$\rho L v = \vec{q} \cdot \hat{n}|_L - \vec{q} \cdot \hat{n}|_S \tag{2.11}$$

where v: velocity of the interface (perpendicular to the interface itself), $\vec{q}$: the heat flux, $\hat{n}$: the unit versor normal to the moving surface and $|_{L/S}$ denotes the limiting value calculated on the liquid or solid phase respectively (Alexiades et al., 1993).

2.2.1.2 *One and two-phase Stefan's problem*

With the introduction of Stefan's condition, I can now define the Stefan's problem. Let us consider a slab, $0 \leq z \leq l$, initially solid at a temperature $T_i < T_m$, and let us assume that the temperature at the left end is then suddenly set to $T_L > T_m$ while the right end, at $x = l$, is kept insulated. The solution of Stefan's problem consists in finding the position of the phase interface $Z(t)$ and the temperature distribution in each phase.

System for the two-phase Stefan's problem

The associated Cauchy problem is mathematically described by the following set of differential equations, boundary conditions and initial conditions[11]:

$$T_t = \alpha_L T_{zz},\ 0 < z < Z(t) \text{ liquid region} \tag{2.12a}$$

$$T(Z(t), t) = T_m, \tag{2.12b}$$

$$T_t = \alpha_S T_{zz},\ Z(t) < z < l \text{ solid region} \tag{2.12c}$$

$$L\rho \dot{Z}(t) = -k_L T_z(Z(t)^-, t) + k_S T_z(Z(t)^+, t), \text{ Stefan's condition} \tag{2.12d}$$

Initial conditions

$$Z(0) = 0 \tag{2.12e}$$

$$T(z, 0) = T_i < T_m,\ 0 < z < l \tag{2.12f}$$

Boundary conditions

$$T(0, t) = T_L > T_m \tag{2.12g}$$

$$-k_s T_z(z, l) = 0, \text{ insulating boundary} \tag{2.12h}$$

and it defines the two-phase Stefan's problem, because both the two phases (solid and liquid) are present and "active".

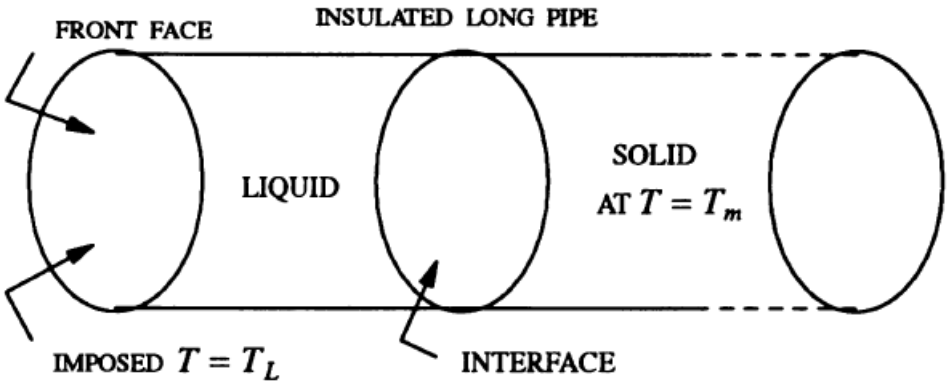

Figure 2.2: Slab of phase changing material. It depicts the system described by the one-phase Stefan's problem. From Alexiades et al., 1993.

For sake of simplicity the one-phase Stefan's problem can be defined, too. In this case only one phase (let's say liquid) is "active" while the other phase is kept at the constant temperature of phase

11 Not writing explicit dependence on space z and time t.

change T_m. In such a situation, only the liquid temperature has to be found. The system is schematically described in Fig. 2.2 and can be mathematically stated as:

System for the one-phase Stefan's problem

$$T_t = \alpha_L T_{zz},\ 0 < z < Z(t) \text{ liquid region} \tag{2.13a}$$

$$T(Z(t), t) = T_m, \tag{2.13b}$$

$$L\rho\dot{Z}(t) = -k_L T_z(Z(t)^-, t) \tag{2.13c}$$

Initial conditions

$$Z(0) = 0 \tag{2.13d}$$

Boundary conditions

$$T(0, t) = T_L > T_m \tag{2.13e}$$

As the second end plays no role, the slab can be practically considered semi-infinite $[0, \infty]$.

Non-linearity of the Stefan's problem

The non-linearity of the system can be intuitively grasped considering that two different temperatures $T_{L,1}$ and $T_{L,2}$ would correspond to two different interface positions and two different temperature distributions at a given time t. It means that, if a T_L given by the sum of the two temperatures were considered, *i.e.* $T_L = T_{L,1} + T_{L,2}$, the solution would not be equal to the sum of the each individual solution for $T_{L,1}$ and $T_{L,2}$. In other words then the "superposition principle" does not hold (Landau, 1950).

The non-linearity can be mathematically highlighted considering the equations 2.13 and the fact that T_m is assumed to be constant[12]. Setting the total derivative of T_m to zero results in:

$$0 = \frac{dT_m(Z(t), t)}{dt} = \frac{\partial T(Z(t), t)}{\partial z}\dot{Z}(t) + \frac{\partial T(Z(t), t}{\partial t} \tag{2.14}$$

and then replacing Eq. 2.13a and Eq. 2.13c in Eq. 2.14 yields

$$T_{zz} = \frac{c_L}{L} T_z^2 \tag{2.15}$$

an equation which explicitly shows the non-linearity of the problem.

Whilst the well-posedness of a Stefan's problem has been proved under reasonably general assumptions (Cannon et al., 1974; Cannon et al., 1975), an analytic solution in closed form is possible only under very restrictive conditions of semi-infinite slab, constant temperatures at the boundary and constant thermal properties (Alexiades et al., 1993).

The solution in this case is the so called Neumann similarity solution and reads (see appendix A.1 for the derivation):

12 A general proof of the non-linearity can be drawn also releasing the assumption of a constant T_m.

Neumann's similarity solution

Position of the phase interface

$$Z(t) = 2\lambda\sqrt{\alpha_L t} \tag{2.16a}$$

Temperature in liquid region $0 \leq z < Z(t)$

$$T(z,t) = T_L + \frac{T_m - T_L}{\operatorname{erf}\lambda}\operatorname{erf}\left(\frac{z}{2\sqrt{\alpha_L t}}\right) \tag{2.16b}$$

Temperature in solid region $z > Z(t)$

$$T(z,t) = T_i + \frac{T_m - T_i}{\operatorname{erfc}(\lambda\nu)}\operatorname{erfc}\left(\frac{z}{2\sqrt{\alpha_L t}}\right) \tag{2.16c}$$

with T_i: initial temperature as reported in Eq. 2.12f, $\nu = \sqrt{\alpha_L/\alpha_S}$, "erf" is the error function and "erfc" is the complementary error function. The adimensional parameter λ has to satisfy the following transcendental equation:

$$\frac{St_L}{e^{\lambda^2}\operatorname{erf}\lambda} - \frac{St_S}{\nu e^{(\nu\lambda)^2}\operatorname{erfc}(\nu\lambda)} = \sqrt{\pi}\lambda \tag{2.17}$$

where St_L and St_S are the Stefan's number defined as:

$$St_L = \frac{c_L(T_L - T_m)}{L} \tag{2.18}$$

and

$$St_S = \frac{c_S(T_m - T_S)}{L}. \tag{2.19}$$

Interpretation of the Stefan's number

Stefan's number, being the ratio between the sensible heat $c_L(T_L - T_m)$ (or $c_S(T_m - T_S)$) and latent heat, gives an idea whether the bulk of the heat in the process is dominated by the phase change or by the heat conduction. For melting ice/freezing water, given the high latent heat, the Stefan's number rarely exceeds 1, let alone in cases where external temperatures T_L is very close to the melting temperature T_m, which is what occurs in case of subsea permafrost conditions. It means therefore that the majority of heat stored or released is in form of latent heat at the phase boundary[13].

The solution (Eq. 2.16) of the Stefan's problem applies also in case of a freezing problem, just interchanging the subscripts S and L and the latent heat L by $-L$.

2.2.1.3 *Stefan's problem with an eutectic solution*

The Stefan's problem, as described in the Section above, can be extended in case of a presence of a solution, whose freezing/thawing

13 For sake of curiosity, waxes have Stefan's numbers similar to water and other non metallic materials. Metals have Stefan's numbers of the order of $1 - 10$ and it means that latent heat and sensible heat are usually comparable. Other materials like silicates have very large Stefan's numbers, which means that sensible heat dominates on latent heat.

characteristics are affected by the colligative properties of the solute. The solution considered is the salty water. The solution of salt and water is the prototype of an eutectic system[14], *i.e.* a solution that melts (solidifides) at a temperature which is lower than the melting (freezing) temperature of each constituent.

The eutectic solutions

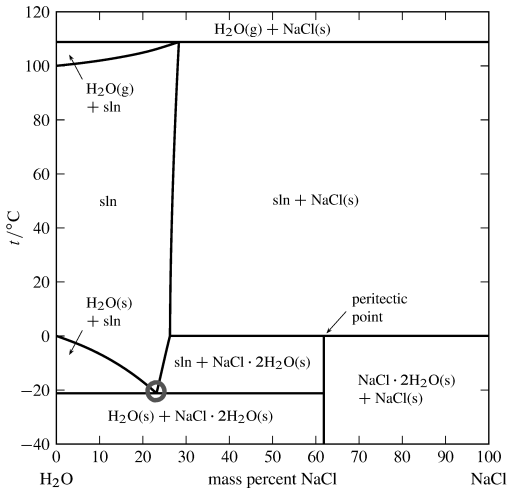

Figure 2.3: Phase diagram of the NaCl and water solution. The eutectic composition (circle) of about 23.3% of concentration has a temperature of −21.1 °C: it is the lowest temperature at which solid and liquid salty water can coexist at the equilibrium. The curve between "sln(solution)" and "sln(solution)+H_2O(s)(ice)" is the *liquidus*, representing the temperature at which a binary solution of a given composition is in equilibrium between the solid and the liquid phase. From Cohen-Adad et al., 1991.

Phase diagram of solution $H_2O + NaCl$

The phase diagram is shown in Fig. 2.3. My focus is on its lowest-left section, the portion of interest in consideration of the typical salinity of sea water. When saltwater with a certain salinity $\bar{S}$ starts freezing, temperature and composition follow the *liquidus* curve. It represents the temperature at which ice and brine are in thermodynamical equilibrium and has a a cusp minimum at the eutectic composition and temperature (circle of fig. 2.3). Below the eutectic temperature the system is solid and both crystallized ice and salt are present separately (in form of lamella or grains).

The *liquidus* curve for seawater (at constant pressure of 1 bar) can be expressed by (Millero, 1978):

$$T_f(S) = -0.0575S + 1.710523 \cdot 10^{-3} S^{3/2} - 2.154996 \cdot 10^{-4} S^2 \quad (2.20)$$

with S: salinity. In case of low concentration, the curve is usually approximated via the linear relationship:

$$T_f(S) = T_m - m \cdot S \quad (2.21)$$

with $T_m = 0$ °C: melting temperature of pure water and $m = 0.06$ °C psu^{-1}.

In order to treat salinity in Stefan's problem, let us assume again the pure ice slab considered earlier, $0 \leq z \leq l$, at the initial temperature T_i brought into contact with salty water with a temperature T_L,

14 From Greek ϵv=*well* and $\tau\eta\xi\iota\varsigma$=*melting* and therefore "easy to melt".

higher than the *liquidus* temperature associated with the concentration of the solution S_L, *i.e.* $T_f(S_L)$.

Salt presence requires two extra equations: one to take into account diffusion of salinity and one to describe the conservation of mass of the solute at the boundary. Unlike the Stefan's problem of Section 2.2.1.2, in this case the interfacial temperature T^* is given by Eq. 2.20 (or 2.21) with salinity S^*, *i.e.* $T^* = T_f(S^*)$, which represents an unknown varying quantity to be determined as well.

Stefan's condition for the solute

Assuming that the salt concentration in the ice phase S_S is constant (at most null) and that salt does not move inside the solid, salt diffusion in the liquid phase ($0 \leq z < Z(t)$) is given by:

$$\frac{\partial S(z,t)}{\partial t} = D\frac{\partial^2 S(z,t)}{\partial z^2} \tag{2.22}$$

with D salt diffusion coefficient in water, which is usually $10^{-2} - 10^{-3}$ the thermal diffusivity.

Invoking the conservation of the mass M of the solute:

$$M = \int_0^{Z(t)} S(z,t)dz + S_S \cdot (l - Z(t)) \tag{2.23}$$

and imposing therefore that its time derivative is equal to zero, I get:

$$(S^* - S_S)\dot{Z}(t) = -DS_z(Z(t)^-, t) \tag{2.24}$$

which is the additional Stefan's condition for concentration at the interface.

PDE system for phase-changing solution

The system is then described by following set of PDEs:

Transport equations for $0 < z < Z(t)$

$$T_t = \alpha_L T_{zz} \tag{2.25a}$$

$$S_t = DS_{zz} \tag{2.25b}$$

Transport equations for $Z(t) < z < l$

$$T_t = \alpha_S T_{zz} \tag{2.25c}$$

$$S_S(z,t) = 0 \tag{2.25d}$$

Conditions at the interface

$$T(Z(t),t) = T_f(S^*), \tag{2.25e}$$

$$L\rho\dot{Z}(t) = -k_L T_z(Z(t)^-, t) + k_S T_z(Z(t)^+, t) \tag{2.25f}$$

$$(S^* - S_S)\dot{Z}(t) = -DS_z(Z(t)^-, t) \tag{2.25g}$$

Initial conditions

$$Z(0) = 0 \tag{2.25h}$$

$$T(z,0) = T_i, \quad 0 < z < l \tag{2.25i}$$

$$S(z,0) = 0, \quad 0 < z < l \tag{2.25j}$$

Boundary conditions

$$T(0,t) = T_L \tag{2.25k}$$
$$-k_s T_z(z,l) = 0 \tag{2.25l}$$
$$S(0,t) = S_L \tag{2.25m}$$
$$S(z,l) = 0 \tag{2.25n}$$

As the form of the equations for salinity (Eq. 2.25b and 2.25g) are in the same form as the ones for temperatures (Eq. 2.12a, 2.13a, 2.12d, 2.13c) the solution for salinity has also the same form and requires an additional constraint on the Stefan parameter Λ[15]. The solution for salinity and temperature reads (Harrison et al., 1978):

Neumann's solution for a phase-changing solution

Position of the phase interface

$$Z(t) = 2\Lambda\sqrt{Dt} \tag{2.26a}$$

Temperature in liquid region $0 \leq z < Z(t)$

$$T(z,t) = T_L + \frac{T^* - T_L}{\operatorname{erf}(\Lambda/\beta)} \operatorname{erf}\left(\frac{z}{2\beta\sqrt{Dt}}\right) \tag{2.26b}$$

Temperature in solid region $z > Z(t)$

$$T(z,t) = T_i + \frac{T^* - T_i}{\operatorname{erfc}(\Lambda/\gamma)} \operatorname{erfc}\left(\frac{z}{2\gamma\sqrt{Dt}}\right) \tag{2.26c}$$

Salinity in liquid region $0 \leq z < Z(t)$

$$S(z,t) = S_L + \frac{S^* - S_L}{\operatorname{erf}\Lambda} \operatorname{erf}\left(\frac{z}{2\sqrt{Dt}}\right) \tag{2.26d}$$

with $\beta = \sqrt{\alpha_L/D}$, $\gamma = \sqrt{\alpha_S/D}$.

Plugging the equations above in the Stefan's condition for temperature gives the following transcendental equations for Λ (Harrison et al., 1978):

$$\frac{1}{\Phi(\Lambda)+1} = \frac{\frac{T_L}{T_f(S_L)} + \delta\left(\frac{\beta}{\gamma}\right)^2 \frac{\Phi(\Lambda/\beta)}{\Psi(\Lambda/\gamma)} \frac{T_i}{T_f(S_L)} + \epsilon\beta^2\Phi(\Lambda/\beta)}{1 + \delta\left(\frac{\beta}{\gamma}\right)^2 \frac{\Phi(\Lambda/\beta)}{\Psi(\Lambda/\gamma)}} \tag{2.27}$$

with $\delta = k_S/k_L$, $\epsilon = [L\rho D/(-k_L T_f(S_L))$, $\Phi(x) = \sqrt{\pi}xe^{x^2}\operatorname{erf}(x)$ and $\Psi(x) = \sqrt{\pi}xe^{x^2}\operatorname{erfc}(x)$.

Substituting Eq. (2.26d) in Eq. (2.25g), with $S_S = 0$ as in pure fresh ice, it yields:

$$\frac{S^*}{S_L} = \frac{1}{\Phi(\Lambda)+1}. \tag{2.28}$$

In order to close the solution the third equation needed is the one connecting T^* and S^*, *i.e.* Eq. (2.20) or (2.21).

15 I use the capital Λ to distinguish it from the parameter λ that appeared in the previous equations when salinity was not considered, in which case $\lambda = \Lambda$

With three equations (Eq. 2.20/2.21, 2.27 and 2.28) and three unknowns (Λ, T^* and S^*), the problem is closed and solution is given by Eq. 2.26. It can also be analytically solved, if one assumes the proportion $S^* : S_L = T^* : T_f(S_L)$ to hold (Harrison et al., 1978).

2.2.2 *Stefan's problem and submergence of permafrost*

The Stefan's problem and the SSPF

The system described by Eq. 2.25 can be used to represent submergence of permafrost under marine water. Let us assume that z is now a downward vertical coordinate and that the initial condition (*i.e.* permafrost before submergence) might be described by a porous medium (the soil) saturated with fresh ice and with temperature T_i. Sudden submergence with marine water at a constant temperature T_L and salinity S_L is then described by the system of Eq. 2.25, as the gravity and its effects are anyhow neglected. The region above the frozen interface ($0 \leq z < Z(t)$) is simply the thawed region while the region below the interface $z > Z(t)$ is the one still bound by ice. The interface $Z(t)$ is the so called Ice-Bound Permafrost Table (IBPT).

Thermal properties of soils

Thermal properties of the two regions are dependent on the hydrological state of the soil (porosity, ice and liquid water fraction) and standard parametrizations can be employed. The weighted arithmetic mean is used for the heat capacity and the weighted geometric mean is used for thermal conductivity, which should take into account the real geometry of the soil [16]. Namely:

In thawed (t) region: $0 < z < Z(t)$

$$c_t = c_m(1-\varphi) + c_w\varphi \qquad k_t = k_m^{(1-\varphi)}k_w^{\varphi} \qquad \rho_t = \rho_m(1-\varphi) + \rho_w\varphi \tag{2.29a}$$

In frozen (f) region: $z > Z(t)$

$$c_f = c_m(1-\varphi) + c_i\varphi \qquad k_f = k_m^{(1-\varphi)}k_i^{\varphi} \qquad \rho_f = \rho_m(1-\varphi) + \rho_i\varphi \tag{2.29b}$$

where φ: porosity, the subscript m stands for soil matrix, w for water and i for ice.

Equations representing the phase boundary in case of pure water (Eq. 2.16) and in case of the presence of salty water (Eq. 2.26a) have the same form which goes $\sim \sqrt{t}$. It implies that melting front moves further from its original position over time but at an increasingly slower rate provided by its derivative: $\sim 1\sqrt{t}$ and whose magnitude is set by λ (or Λ) and D.

16 This is because the weighted geometric mean is the half-way between the weighted harmonic mean, which would be right in case the heat flux would occur mostly "in series", and the weighted arithmetic mean, which would be right in case the heat flux would occur mostly "in parallel" (*e.g.* Dassargues, 2018)

2.2.3 *Diffusion vs. convection*

Convection

Density driven double diffusion and/or ocean pump can trigger instabilities of the diffusive regime and lead to the onset of convection. Analysis of the details of the convection regime and its effects are beyond the scope of this work but two aspects should however be stressed.

Salt and heat transports can differ

The first aspect is that temperature and salinity do not have to be transported in the same way because of the difference in diffusivities between salt and heat. It can happen that salt motion is driven by convection while heat transport follows diffusion. As shown above both temperature an salt contributes to the thawing and, in case of subzero temperatures, the limiting factor for the thawing is the rate at which salt is provided at the interface (Harrison et al., 1978; Hutter et al., 1999).

Motionless solution is the baseline solution

The second aspect is that a motionless solution for the interstitial water - namely a solution with no convection - can be considered to be the basic state for a more complex perturbative expansion (Hutter et al., 1999). This solution, corresponding to the solution shown in Section 2.2.1.3, is characterized by a vertically changing salt and temperature profile as well as by a moving sharp boundary interface. Such a solution exists provided that the density change under phase change is ignored. Density change induces a velocity at the interface due to the contraction/expansion of the liquid. Considering the sensible difference between water and ice density, this condition would never theoretically hold and motion should always be affected by convection. However the motionless solution can reasonably be considered legitimate when the thawing is slow and motion is additionally hindered by the soil matrix.

2.3 EXPERIMENT DESIGN

In this section I will describe the design of the experiments performed to study two idealized and simplified thawing setups. The experiments took place in the sea ice laboratory of the Max Planck Institute for Meteorology in Hamburg[17].

Table 2.1: Initial conditions of the two experiments

Experiment	Water temperature before pouring	Water height	Salinity at the beginning[a]	Height ice/sand
1: pure ice	4.5 °C	30.0 cm	35.8	9.1 cm
2: frozen sand	14.0 °C	26.5 cm	33.0	7.9 cm

a HQ40D Hach Portable Multi Meter. Uncertainty: 0.01

17 The experiments were thought in concert with Dr. Dirk Notz and performed with help of Niels-Jakob Fuchs.

2.3.1 *Pure ice and salty warm water*

(a) Tank with the ice layer at the bottom and the frame holding the ruler and the temperature sensors.

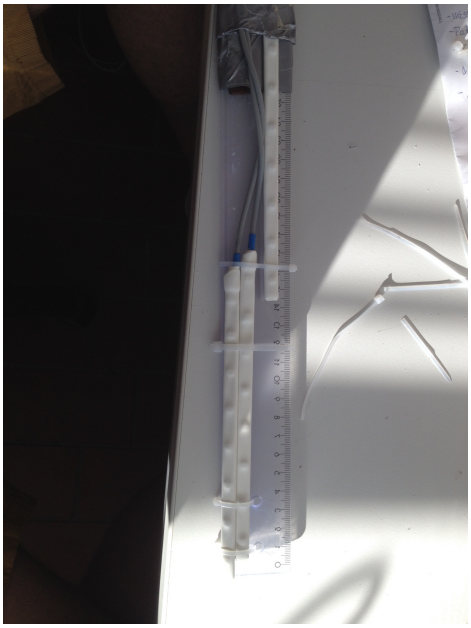

(b) The three temperature sensors sticks. The two lowermost are arranged in order to have a sensor every 1 cm, while the uppermost one has a sensor every 2 cm.

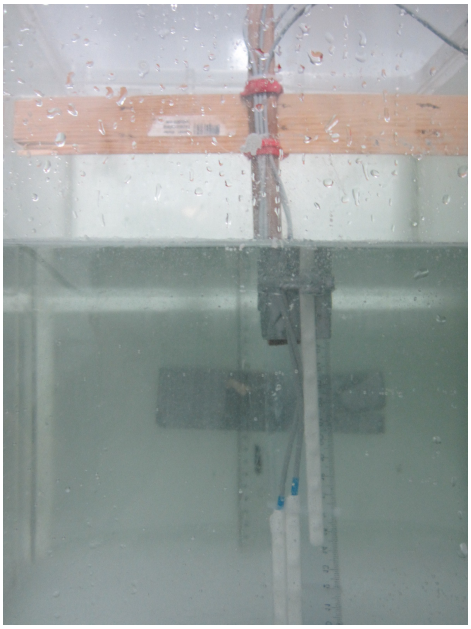

(c) Tank with the ice layer at the bottom and with salty water on top.

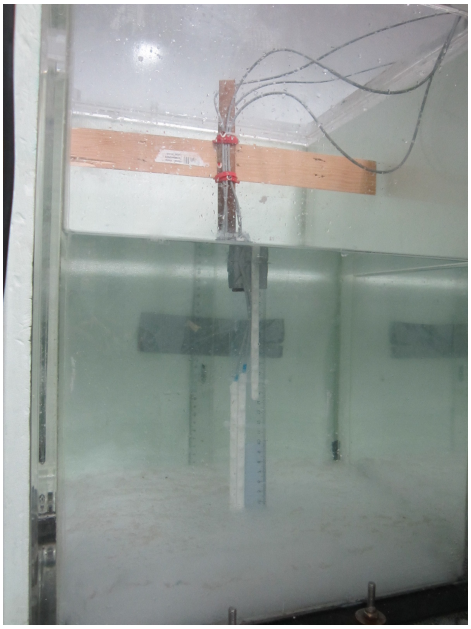

(d) Tank with the ice layer at the bottom and with salty water on top at the end of the experiment. The uneven surface of the ice can be easily detected.

Figure 2.4: Laboratory setup for the first experiment, aimed at describing the thawing of pure ice under the influence of warmer salty water.

A tank of about $30 \times 30 \times 50$ cm is located in a cold room, endowed with a thermostat and a temperature sensor measuring room temperature every 15 s so that the effect of any fast variations can be in case considered in the analysis. The refrigerating room is big enough such that the opening of the door does not affect considerably the temperature of the experimental setup. In order to reduce temperature variations induced by external disturbances the tank is surrounded by an insulating coat of polyurethane foam.

Design of the first experiment: ice-water

In the tank an ice layer is grown with the help of a cooling plate, freezing the ice from below up to a thickness of 9 cm (fig. 2.4.*a*). A frame holding three sticks with 8 temperature sensors each[18] and a ruler[19] is placed in the tank (fig. 2.4.*b*).

The room temperature is kept at roughly a constant value of about 3 °C. A solution of water and NaCl at 35.8 psu and at 4.5 °C is poured on top of the ice, whose temperature is −1.62 °C (fig. 2.4.*c*). The height reached by water is 30 cm. The system is not stirred and the thawing process is observed for the next 72 hours, during which the height of the ice at different points of the surface and salinity is directly measured. The temperature inside the bucket is measured by the stick sensors every 3.45 minutes.

This setup was designed to investigate how the thawing of pure ice proceeds as consequence of the double effect of temperature and chemical action of salt without the extra complication of a porous medium. It enables also an estimate of the model parameters (see Section 2.4).

2.3.2 *Frozen sand and salty warm water*

Design of the second experiment: frozen sand-water

This experimental setup is the one which is supposed to resemble the SSPF in its idealized form of an ice-bond soil submerged by salty water.

I have chosen to use sand to mimic the subsea permafrost, based on the availability of the material for the experiment and on observational evidence (Shakhova et al., 2017; Wild et al., 2018). In the same bucket as in the experiment above, a volume of sand is then saturated with fresh water and frozen from below. A layer 7.9 cm thick of frozen sand is so formed (see fig. 2.5.*a*).

A saline solution (33 psu) at 14 °C is then slowly poured on top of the frozen sand reaching eventually a height of 26.5 cm. Also in this case the system is not stirred. In such a setting the measurement of the height of the left ice-bond sand is done by difference, using a ruler to measure the thawed sand. The thawing is measured twelve times in about 47 hours, the room temperature every 15 seconds and the temperature inside the bucket every 3 seconds.

18 Accuracy: < 0.1 °C.
19 Resolution: 0.1 cm.

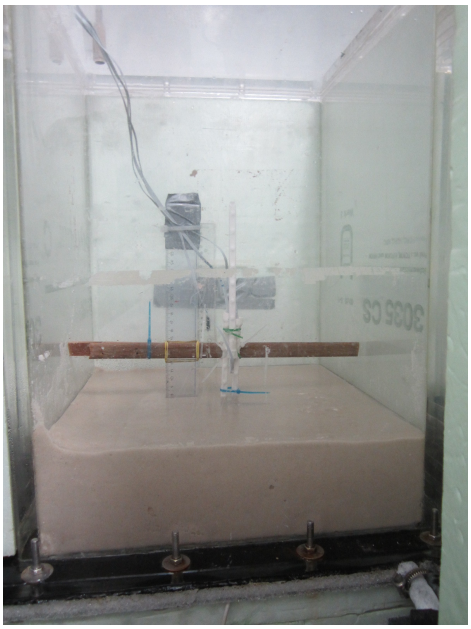

(a) Tank with the frozen layer of sand at the bottom and the frame holding the ruler and the temperature sensors before salty water is poured.

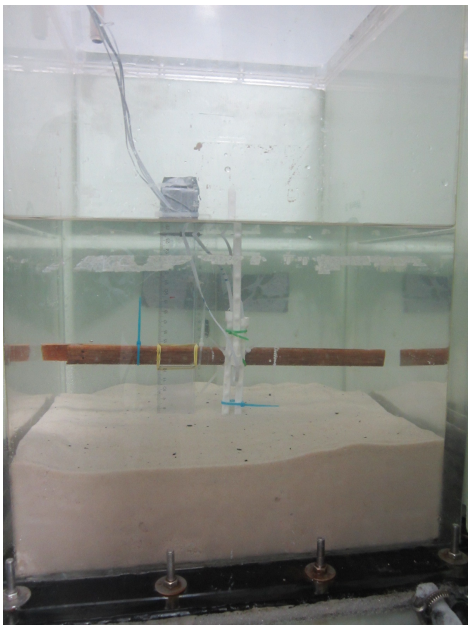

(b) Tank with frozen layer of sand at the bottom and warmer salty water poured on top at the beginning of the experiment.

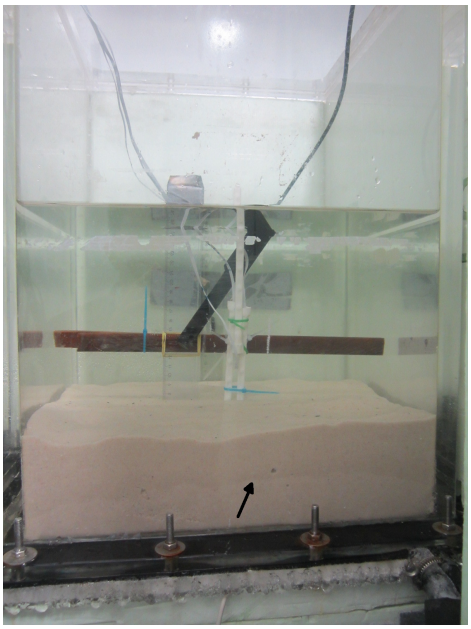

(c) Tank with frozen layer of sand at the bottom and warmer salty water poured on top at the end experiment. The arrow points at the interface between still frozen and thawed sand.

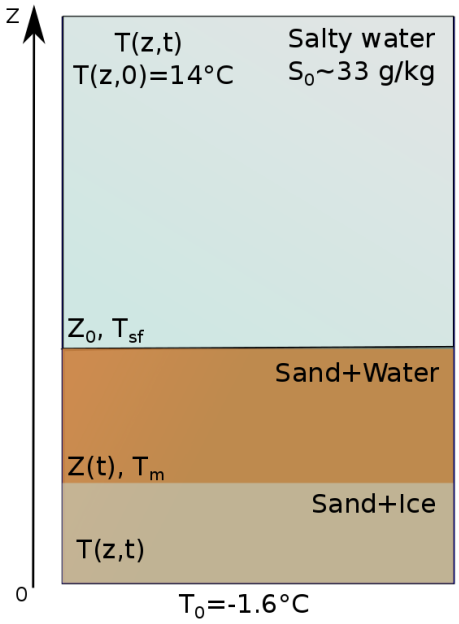

(d) Sketch of the setup

Figure 2.5: Laboratory setup for the second experiment, aimed at describing the thawing of frozen saturated sand under the influence of warmer salty water.

Porosity measurement

A sample of the sand is also used to estimate its average porosity.

The void volume V_V can be estimated with two measurements of volume:

1. one measurements of the bulk volume $V_b = V_m + V_V$, with V_m volume of the sand matrix;
2. one measurements of the total volume V_t, after having mixed the sand with a known amount of water V_w. The total volume $V_t = V_w + V_m$

V_V reads then $V_V = V_b - (V_t - V_w)$. Porosity φ is finally given by $\varphi = V_V / V_b$.

2.4 NUMERICAL MODEL

The aim of the developed numerical model is solving systems of PDEs with initial and boundary conditions as the ones described in Section 2.2.1.

FTCS scheme to solve the heat propagation

I implemented a numerical scheme for heat diffusion based on the well-known forward-time central-space (FTCS) scheme (*e.g.* Anderson et al., 2016) with an equally-gapped vertical grid in space. Such a scheme is an explicit scheme in time that uses the central difference in space and the forward Euler method in time. Von Neumann stability condition requires that

$$\Delta t \leq \frac{(\Delta z)^2}{2\alpha} \tag{2.30}$$

with Δt: time step, and Δz: space of the grid.

Algorithm of the model

The algorithm for the update of the interface position, temperature and salinity follows the steps below:

1. The time derivative of the the interface is evaluated using Stefan's condition for heat (Eq. 2.25f).
2. Temperature is updated above and below the phase interface. The temperature is calculated in each "homogeneous" region applying the FTCS scheme described above: it means that in the case of the *ice-water* experiment the heat equation is solved for the water and for the ice. In the case of the *frozen sand-water* experiment, the heat equation is solved in the water, in the thawed sandy region and in the frozen sand (according to the sketch reported in Fig. 2.5.*b*).
3. The boundary conditions are enforced.
4. Salinity is update on average, computing how much fresh water is released at the phase interface at each time step and dilutes then the salt content.

5. The interface temperature is set equal to the the freezing temperature corresponding to the updated salinity (according to Eq. 2.20).

6. In case of the *frozen sand-water* experiment, the temperature at the thawed sand-water interface is determined requiring that heat fluxes on both sides of interface are the same.

7. Go to the following time step.

As evident from step 4, salinity field is not model in favour of an average quantification and a simplified numerical implementation.

Taking into consideration the experimental realization, the equations describing the processes in Sections 2.2.1.2 and 2.2.1.3 need some modifications to adapt to the practical realization in the laboratory.

2.4.1 *Turbulent motion: the multiplying factor KT*

Convection arises

Whilst the water in the experiments is not actively stirred with a pump[20], it can be thought that a series of processes might however induce a convective regime in the water, *e.g.* the pouring of the water and the difference in density between salty water and freshwater being released at the phase interface. This convection should be somehow incorporated in the equations described so far.

Convection-affected heat equation

Considering convection, the heat equation in the liquid phase (Eq. 2.25a) modifies as follows:

$$T_t = \mathcal{K}(T, S, \cdots) T_{zz} \tag{2.31}$$

with $\mathcal{K}$: eddy thermal conductivity[21]. The same modification would be required for the salt field but, as stated above, I chose not to model it explicitly.

The Stefan's condition (Eq. 2.25f) also needs to consider the turbulent heat flux. A way would be following the approach suggested by Notz et al., 2003, where the Stefan's condition become:

$$L\rho\dot{Z}(t) = k_S T_z(Z(t)^+, t) + \rho_L c_L \langle w'T' \rangle \tag{2.32}$$

with $\langle w'T' \rangle$: Reynolds average turbulent heat flux, expressed in term of friction velocity[22] (Notz et al., 2003). This approach would however be too complicated to model as it would require either an explicit computation of the velocity field in the bucket (a task way beyond the scope of this work) or assumptions on the friction velocity.

The multiplying factor KT

For this reason the model is simplified considering only an en-

20 A stirred experiment was also run but brought no meaningful results.

21 Depending on temperature, salinity and a set of other quantities or combination of quantities which affect the transport locally, like density and velocity field.

22 The fluctuating part of the velocity field.

hanced diffusion for the heat transport. This approach is in theory inherently wrong, given the deep difference in nature between conduction and convection. Nevertheless it is worth being employed and tested in systems characterized by a slow advective dynamics, like the ones under examination. The heat conductivity of the water is hence multiplied by a numerical factor KT, not necessarily constant in space and time, which is supposed to take into account the more efficient heat transport in a turbulent motion. In all the equations where k_L appears (*e.g.* Eq. 2.25a and 2.25f) it is to be replaced by $KT(t) \cdot k_L$.

$KT(t)$ is meant to consider convection in a rough approximation: this implies that $KT(t)$ should also account for the effects of the thawed layer of sand in the second experiment, since it is thought to reduce the convective heat transport at the phase boundary. The saturated sand below the sand-water interfaces slows down the density driven motion and thickens the region where mixing occurs, determining a better mixed solution and, therefore, a less intense turbulence. For this reason, for the *frozen sand-water* experiment, an exponential damping factor is added to KT to model how it diminishes with depth:

$$KT((t), z) = (KT(t) - 1)e^{-\frac{d_n}{N}} + 1 \tag{2.33}$$

where d_n: the numbers of grid layers between the sand-water interface and the phase interface and N: a scale factor equal to $2 - 3$. The choice of an exponential damp relies just on a commonly used functional form for an attenuating factor.

2.4.2 *The top boundary condition at the water-air interface*

Newton's condition

While the bottom boundary condition for temperature is provided by the temperature of the cooling plate, the uppermost boundary condition requires assumptions of how the heat is transferred from the water mass to the air. I used Newton's condition, a common hypothesis for the heat transfer. It postulates that heat loss is directly proportional to the difference in temperature between the water and the air in the room. Mathematically it reads:

$$-\mathcal{K}T_z(L, t) = h(T(L, t) - T_{air}) \tag{2.34}$$

with L: coordinate of the water-air interface, and T_{air} air temperature, h: heat transfer coefficient (W m^{-2} K^{-1}) and t: time. Since the air temperature is measured every 15 seconds while the model time step $\Delta t << 15$ s, the T_{air} considered is the one closest to the considered time step. The heat transfer coefficient h depends on local properties of the fluid and degree of "pureness" of the heat transfer regime (whether conduction, convection or radiation is predominant) and

must be usually evaluated case by case. Using again the KT parameter of the previous Section, Eq. 2.34 reads:

$$-KT \cdot k_L T_z(L,t) = h(T(L,t) - T_{air}). \tag{2.35}$$

The *ice-water* experiment is aimed at determining the range of applicability of the model described above and at calibrating the parameters ($KT(t)$ and h) to better fit the experimental setup and the outcomes.

Transferability of the model parameters

The quantities set with the *ice-water* experiment are then supposed to be used to model the *frozen sand-water* experiment. Of the two quantity to be varied ($KT(t)$ and h), the heat transfer coefficient h is expected to lie in almost the same range for both the experiments since the conditions at the water-air interface are reasonably similar for both the setups. $KT(t)$ is instead a rough and simplistic approximation to take into account the convection and therefore it is more prone to relevant fluctuations and changes due to the motion of the freshwater from the phase interface to the sand-water interface and due to the details of convective dynamics in a porous medium. For such a reason the employment of the $KT(t)$ found in the *ice-water* experiment is expected not to be not optimal to model the *frozen sand-water* experiment.

2.5 RESULTS AND DISCUSSION

2.5.1 *Pure ice and salty warm water*

The set of measurements starts immediately after warm salty water is poured in the bucket, on top of the ice layer.

Relative error increases over time

The measured thawing is shown in Fig. 2.6 by the experimental data, whose relative error that grows from 3% of the initial measurements to the ∼13% of the last measurement. This increase is due to the the thinning of the ice layer on one hand and the increasingly more uneven ice surface that develops over time (Fig. 2.4.*d*) as a consequence of all the disturbances and and the intrinsic phenomena whose effects pile up over time (adhesion effects, boundary effects, disturbances due to direct measurements with ruler and consequent induced turbulent motion, temperature instability).

Answering Q2.1

2.5.1.1 *KT follows a relaxation dynamics*

A first sensitivity study was performed considering KT merely as constant fit parameter (Fig. A.1): several simulations were run keeping h fixed and varying KT ($6 - 8 - 10 - 12 - 20 - 30 - 90$). The heat transfer coefficient is a quantity with a large variability in natural and artificial phenomena and for air and water it varies between $5 - 3000$

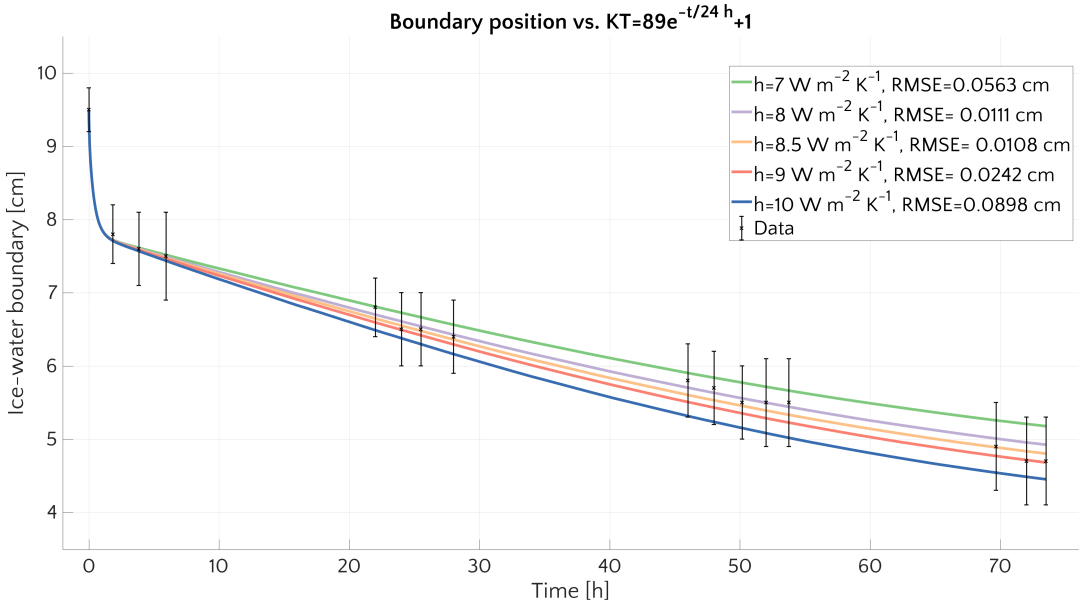

Figure 2.6: Melting of ice over time after warm salty water has been poured on top of the fresh ice volume in the bucket. Experimental values (black error bars) and model output in case of the hypothesis of an exponentially decaying $KT(t)$ with several values of the heat transfer coefficient h.

W m^{-2} K^{-1} [23] with, for instance, measures for lakes between $20 - 30$ W m^{-2} K^{-1} (Williams, 1963). I varied h between 5 and 12 W m^{-2} K^{-1}, given the range reported in literature.

KT changes over time

From this set of simulations it appears that, for a given value of h, different values of KT are suitable to reproduce the measurements at different times: higher values of KT (~ 90) perform well at the beginning of the experiment - right after the warmer water was poured - and smaller values of KT ($8 - 10$) fit better at the end of the experiment. This behaviour suggests two points: i) that values for h considered are in a good range to reproduce measured ice evolution; ii) that a KT decreasing with time is expected to better reproduce the data.

A relaxation dynamic

Another set of simulations with KT linearly varying between 90 and 8 - and same h as above - was then attempted but gave odd results, probably ascribable to the physical meaning of KT, which turns out to have a scientific meaning and to be something more than a mere fitting parameter. Since it represents the enhanced heat transfer due to turbulent convection, a linear decrease with time is actually rather unphysical. A better guess would instead be a typical relaxation dynamics, described in its simplest form by an exponential decay with a characteristic time. Relaxation physics for KT is supported by the idea that the turbulent movements require some time before they decrease after the water is poured and a quasi-stationary state

23 https://www.engineersedge.com/heat_transfer/convective_heat_transfer_coefficients__13378.htm

settles. Nevertheless a real steady state is never reached because of the density-driven change due to the melting ice.

In light of these considerations and of the results shown in Fig. A.1, I tested an exponential decay of KT over time in the form of:

$$KT(t) = 89e^{-\frac{t}{\tau}} + 1 \tag{2.36}$$

with τ typical time scale. Considering how KT had varied in the previous sensitivity study reported in Fig. A.1, I guessed a relaxation time τ of roughly 24 hours.

I finally ran a sensitivity study using this exponential model for KT and with different h in the range already explored. The results are shown in Fig. 2.6. The hypothesis of a relaxation dynamics for KT is underpinned by the generally good agreement between measurements and model. The value of $h = 8.5$ W m^{-2} K^{-1} corresponds to the smallest root mean squared error (RMSE) of 0.0108 cm and, based on this, it is the best value to be used.

Answering Q2.2

2.5.1.2 *Comparison with Stefan's results*

A comparison among measurements, simulations and theoretical expectations offers the chance to investigate the validity of the assumptions behind the thawing scheme and to discuss the proximity to the Stefan's solution.

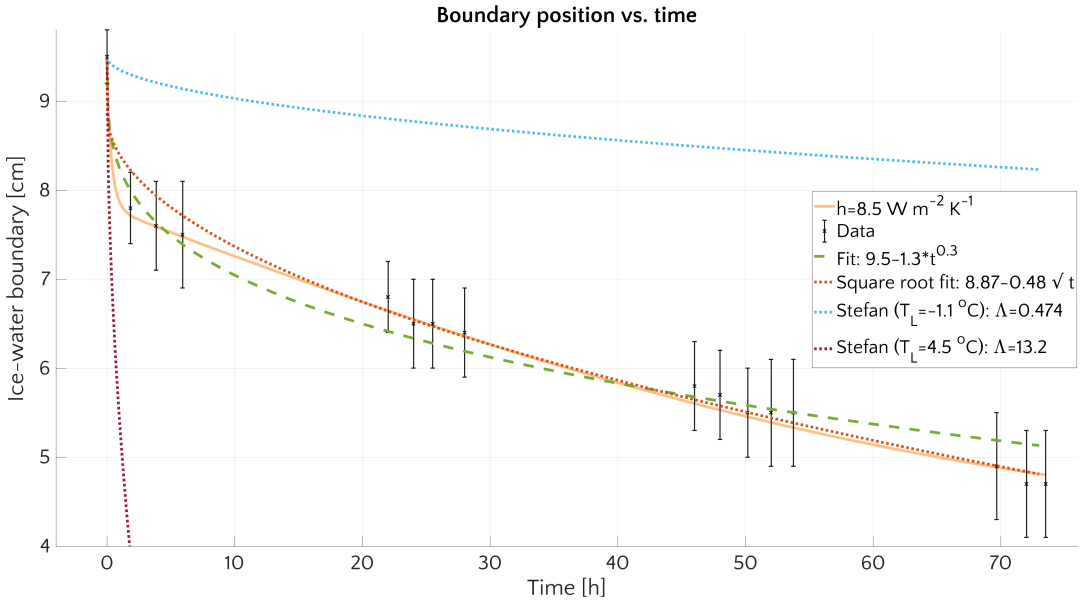

Figure 2.7: Melting of ice over time. Measurements (black). Best model results, with exponential decaying KT and $h = 8.5$ W m^{-2} K^{-1} (orange). Power law fit (green, dashed). Square root fit (red, dotted). Stefan fit according to two different values of T_L: $T_L = 4.5$ °C, the initial value of water poured into the tank (dark red, dotted) and $T_L = -1.1$ °C, the average value of the water temperature in the bucket throughout the experiment (blue, dotted).

Good agreement between model and data

Fig. 2.7 shows in black the experimental results. The simulated values (in orange) appears to be capable of reproducing the quick drop that occurs right after the salty water is poured in the tank. Such a swift response shows that the period right after the submergence of the ice represents the moment with the fastest thawing rate and therefore the most sensitive one as it sets the bottom line for the following thawing, which later happens instead at a smaller pace.

Power-law exponent: 0.3

Hypothesizing that the thawing follows a power law, the best fit enables a quantification of the "vicinity" to the Stefan's solution, which follows a power of 0.5. The fit shows that the best exponent is 0.3. It says that the effective thawing is actually non-Stefan and that the short times (*i.e.* the first moments of the experiment) are even more relevant than in a typical Stefan scheme: at small times the thawing corresponding to a 0.3 power is larger than for a power of 0.5.

The experiment setup does not correspond to an idealized Stefan's setting, as it is affected by relevant turbulent components, varying boundary conditions (see Fig. 2.9) and size limitations which do not belong to Stefan's idealized problem. Therefore it comes with no surprise that the thawing does not strictly follow Stefan's solution. However results suggest that the system is either not that far from the theoretical Stefan's formulation.

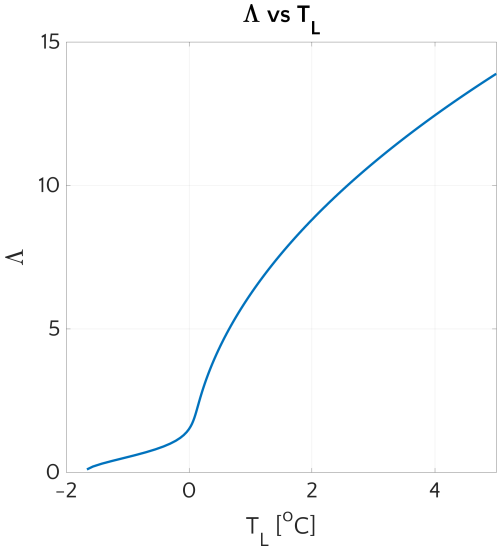

Figure 2.8: Plot of the implicit function Λ versus T_L resulting from Eq. 2.27 with S_L - used to evaluate $T_f(S_L)$ - equal to 31.2 psu: the average salinity measured throughout the experiment duration.

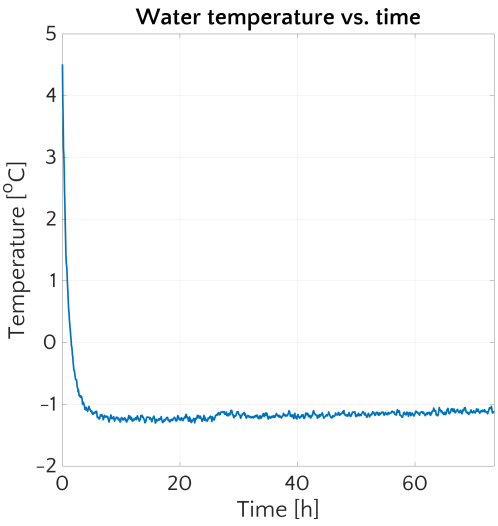

Figure 2.9: Evolution of the temperature of the water poured on top of ice over time, which represent the upper boundary condition for the ice layer.

Good agreement between a $\sqrt{t}$ trend and data

It is hence worth exploring further and comparing the laboratory outcomes with a "Stefan-like" solution, *i.e.* with a solution according to which the ice melting is proportional to $\sqrt{t}$. A simple fit to a square root trend (Fig. 2.7, bright red dotted curve) overlaps with

the simulated results, except for the thawing in the first 20 hours. It suggests therefore that the general thawing behavior might actually be well grasped by a Stefan-like solution and that the deviation from the expected 0.5 exponent might be due to the thawing occurring at the beginning.

A direct application of the theoretical results derived in Section 2.2.1.3 is instead not that successful. Using as S_L the average salinity measured throughout the experiment and employing the *liquidus* relation (Eq. 2.20), the implicit value of Λ (Eq. 2.27) can be found and plotted (Fig. 2.8). Employing the values of Λ corresponding to the initial water temperature ($T_L = 4.5$ °C, $\Lambda = 13.2$) and to the average water temperature ($T_L = -1.1$ °C, $\Lambda = 0.474$), two degradation curves (according to Eq. 2.26a) are plotted respectively in Fig. 2.7. Both these curves fail capturing the experimental results and define the limits within which the measurements, the simulation result, the power-law fit and the square root fit are contained. Such disagreement is a strong suggestion that the hypothesis behind the derivation of the Stefan's parameter, based on idealized setting, are indeed not met in the experimental setup, as for instance shown in Fig. 2.9. It displays how rapidly the temperature of the water on top of the ice drops after it was poured. It is obvious that this water is far from being considered a thermal reservoir, one of the conditions under which the discussion in Section 2.2.1.3 is carried out.

Poor agreement between Stefan's solution and data

Possible explanation

2.5.1.3 *Temperature evolution*

The modeled heat transfer is purely diffusive but the results above clearly show that in the bucket there are some important non-diffusive contributions taking place. This aspect implies that the measured vertical temperature profiles and temperature evolution are not expected to be well captured by the simulated temperature. However this does not exclude that a direct comparison between measured and modeled temperature might be informative.

Model vs. reality

Fig. 2.10 shows the vertical temperature profile at 6 different times (at $0 - 3.83 - 25.5 - 46 - 53.75 - 72$ hours after the beginning of the experiment), when the interface position has also been measured. As it can be seen from Fig. 2.10.*a*, the initial temperature within the ice is not as uniform as assumed. The temperature of the water is instead rather uniform and equal to the initial value of about 4.5 °C.

The situation changes however quickly as shown in panel 2.10.*b*. The bottom temperature is lower than the one recorded at the cooling plate at first, probably due to an intrinsic instability of the device. The value of the modeled temperature within the water is striking: in only 3.83 hours[24] the expected temperature has dropped of almost 6 °C. As the profile at the phase interface shows, the salinity-induced

Fast drop of water temperature

24 The profile is roughly the same after 1.8 hours, although not shown

temperature imposed at the phase boundary, drives a cooling faster than it really is. The small slope of the modeled water temperature is however in good agreement with the small slope of the measured water temperature.

As the experiment continues and the thermal model runs, the gradient of the modeled water temperature grows steeper as expected from the implemented diffusive scheme, whose equilibrium solution would be a simple linear profile. However a comparison with the sensor measurements shows that the profile of the measured water temperature is generally rather vertical, independently of time. This feature hints at the fact that the water inside the bucket is generally well mixed because of convection. Moreover, the water temperature evolves towards the *liquidus* temperature corresponding to its salinity.

Water is well mixed: convection

The only level within the bucket whose temperature differs substantially from the other levels is indeed the shallowest level, *i.e.* the one closer to the air-water interface. One can actually expect that this level, being so shallow (2 cm in the water), is the level which is affected most by the heat transfer with the air in the room.

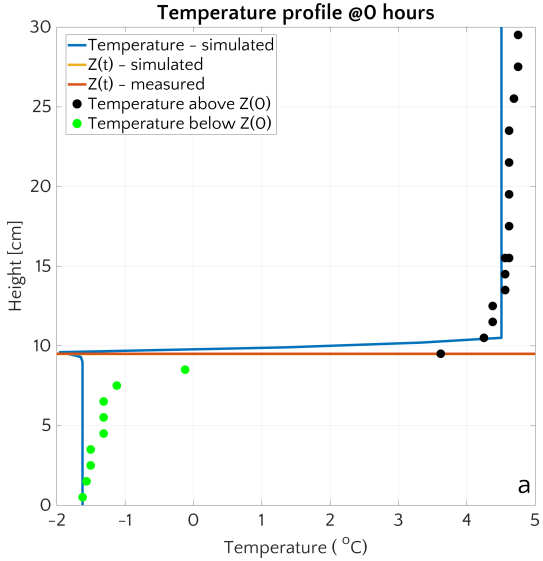
Temperature profile @0 hours
Temperature - simulated
Z(t) - simulated
Z(t) - measured
Temperature above Z(0)
Temperature below Z(0)
Height [cm]
Temperature (°C)
a

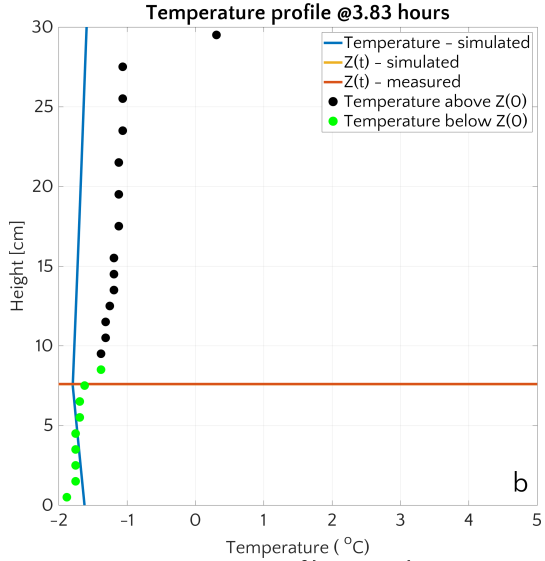
Temperature profile @3.83 hours
Temperature - simulated
Z(t) - simulated
Z(t) - measured
Temperature above Z(0)
Temperature below Z(0)
Height [cm]
Temperature (°C)
b

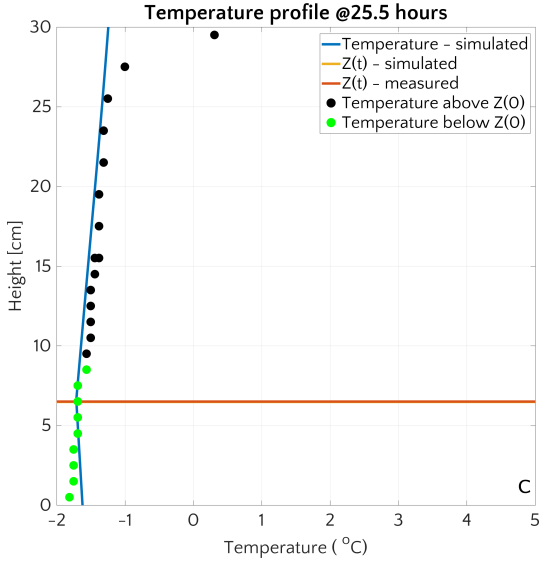
Temperature profile @25.5 hours
Temperature - simulated
Z(t) - simulated
Z(t) - measured
Temperature above Z(0)
Temperature below Z(0)
Height [cm]
Temperature (°C)
c

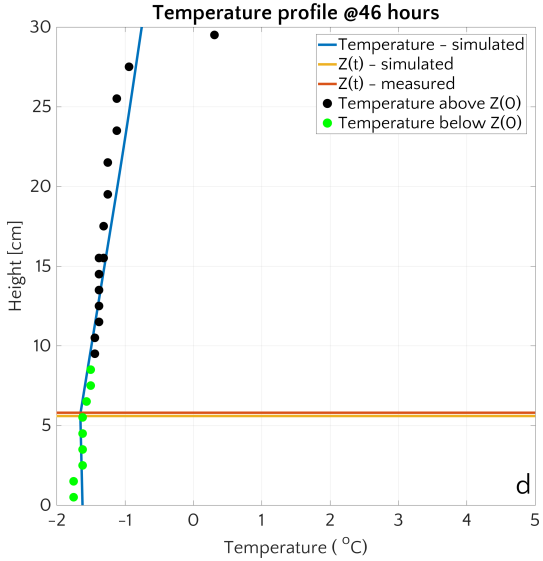
Temperature profile @46 hours
Temperature - simulated
Z(t) - simulated
Z(t) - measured
Temperature above Z(0)
Temperature below Z(0)
Height [cm]
Temperature (°C)
d

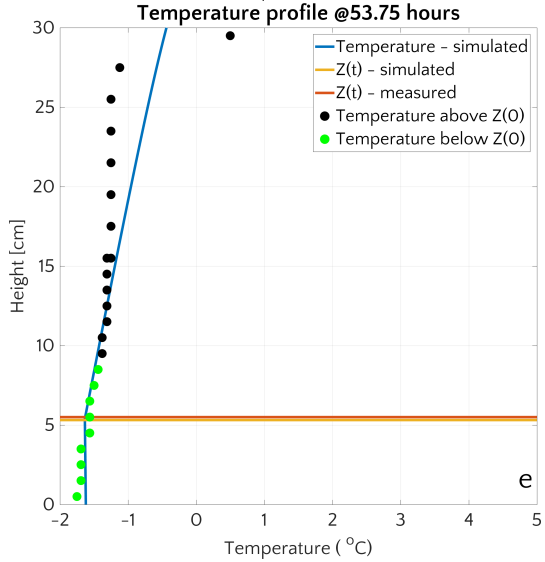
Temperature profile @53.75 hours
Temperature - simulated
Z(t) - simulated
Z(t) - measured
Temperature above Z(0)
Temperature below Z(0)
Height [cm]
Temperature (°C)
e

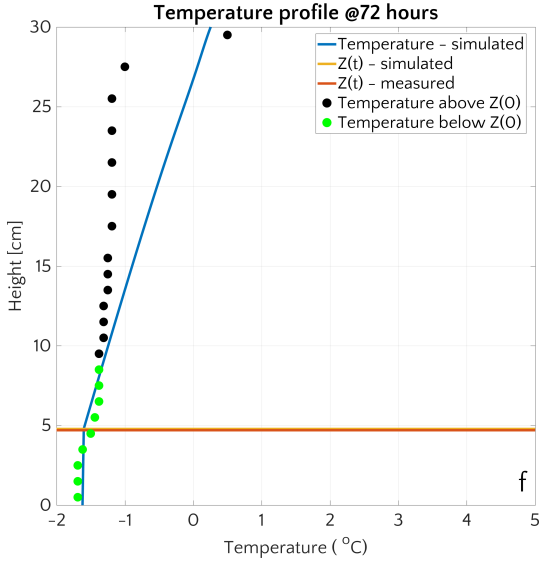
Temperature profile @72 hours
Temperature - simulated
Z(t) - simulated
Z(t) - measured
Temperature above Z(0)
Temperature below Z(0)
Height [cm]
Temperature (°C)
f

2.5.2 *Frozen sand and salty warm water*

The analysis for the second experiment, the one involving frozen sand and warmer salty water, follows the same steps shown in the Section 2.5.1, with the extra step of the evaluation of the porosity needed for the model.

POROSITY AND DENSITY MEASUREMENTS In a graduated cylinder I measured a volume $V_b = 95$ mL of sand and in another cylinder a volume $V_w = 100$ mL of water. After pouring the water into the cylinder containing the sand, and having stirred the mixture, the volume of the mixture resulted being $V_t = 155$ mL. Employing the formula of Section 2.3.2, porosity resulted being $\varphi = 42\%$. This is the value employed in the numeric model.

$\varphi = 42\%$

2.5.2.1 *Thawing experiment*

Answering Q2.1 and Q2.2

In consideration of how this second experiment was conceived, I could have used some of the results determined for the *ice-water* experiment: for instance, the heat transfer coefficient $h = 8.5$ W m^{-2} K^{-1} could have also been employed to model the *frozen sand-water* experiment. Nevertheless it turns out that a direct transferability of the parameters is naive, besides being meaningless. A trivial application of the parameters found in the *ice-water* experiment is hindered by a series of factors: the higher initial temperature of the salty water poured in the *frozen sand-water* experiment, the water dynamics slowed by the presence of the sand and the higher mixing area between salty water and fresh interface. These features are altogether expected to increase the stratification of the water, to reduce the mixing inside the water and to reduce the multiplying effect of turbulence, as the sand thaws. Therefore, in light of these considerations, a lower value for h and for KT is supposed to better reproduce the experimental results for the second experiment.

Debate about transferability of the parameters

This guess is confirmed in Fig. 2.11. Using the same investigation carried out in the previous Section 2.5.1, the values of the parameters better reproducing the data are indeed corresponding to a smaller h (0.2 W m^{-2} K^{-1} being the best fit) and a maximum $KT = 4$, just the 4% of the $KT_{max} = 90$ found for the *ice-water* experiment. Not only the maximum values, but also its relaxation time scale τ is largely reduced to roughly 1 hour. This reduction can be ascribed to the milder way the water was poured on the frozen sand and to the enhanced stratification, *i.e.* stability, of the water at the beginning.

Smaller values for KT and h

However none of the model runs seems capable to reproduce the fast thawing occurring in the first hours.

A comparison between the best model results (with $h = 0.2$ W m^{-2} K^{-1}), a power-law fit and theoretical models is carried out and shown in Fig. 2.12. Once again the best fit follows the same power-law as in

Power-law exponent: 0.3

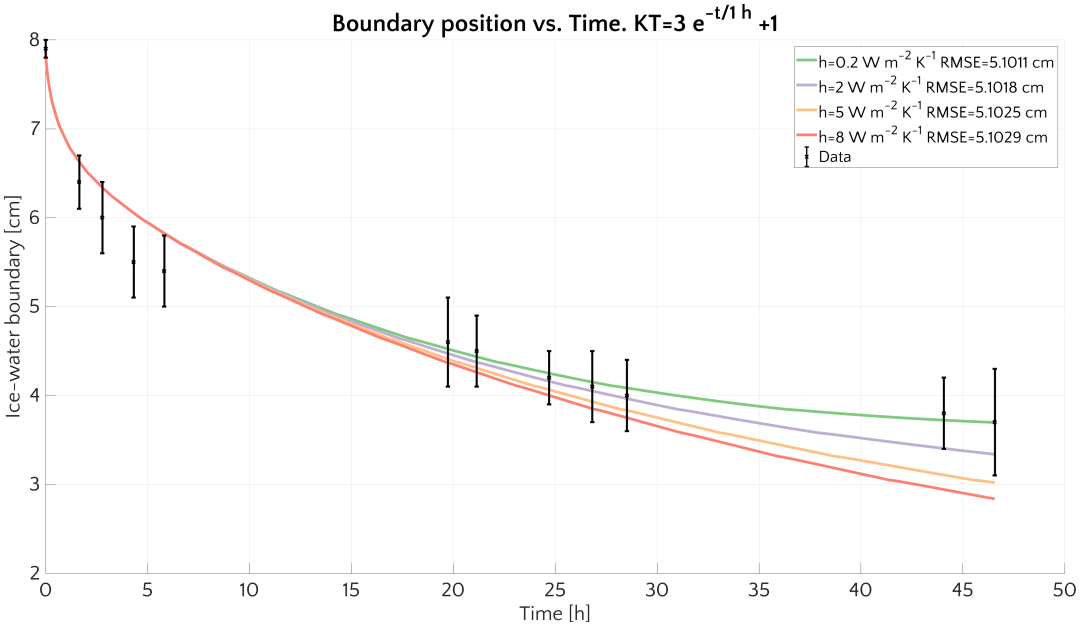

Figure 2.11: Thawing of frozen interface over time after the warmer salty water has been poured on top of the frozen sand layer in the bucket. Experimental values (black error bars) and model output in case of the hypothesis of an exponentially decaying $KT(t)$ with several values of the heat transfer coefficient h.

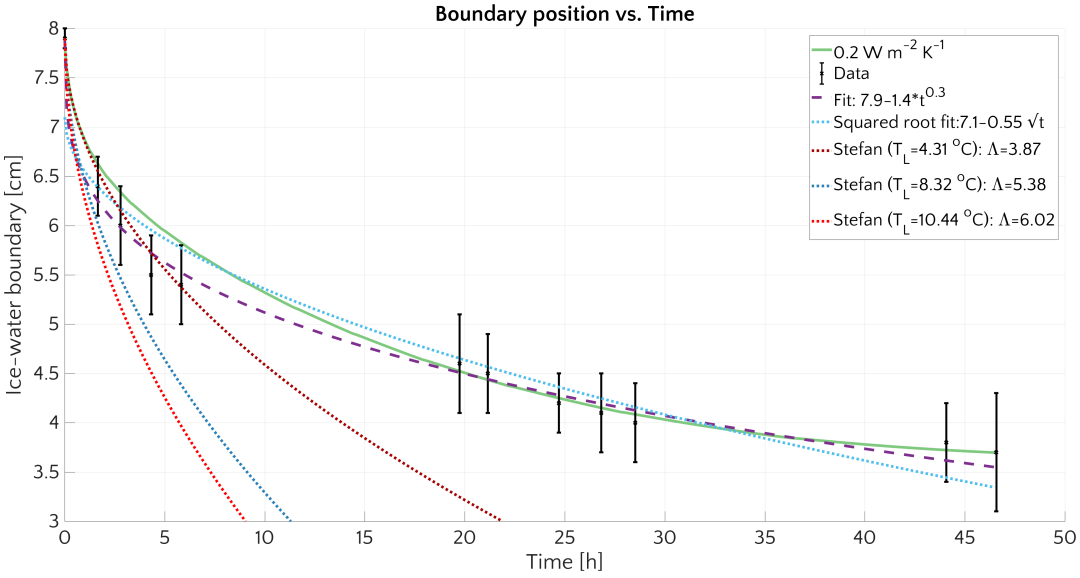

Figure 2.12: Thawing of frozen sand over time. Measurements (black). Best model results, with exponential decaying KT and $h = 0.2$ W m^{-2} K^{-1} (green). Power law fit (purple, dashed). Square root fit (light blue, dotted). Stefan fit according to three different values of T_L: $T_L = 4.31$ °C, the lowest temperature measured in the water right after pouring (dark red, dotted), $T_L = 8.32$ °C, the average value of the water temperature right after pouring (dark blue, dotted) and T_L: $T_L = 10.44$ °C, the highest temperature measured in the water right after pouring (light red, dotted).

the *ice-water* experiment: namely the phase interface moves like $\propto t^{0.3}$. This trend allows the power-law fit to better capture the drop occurring right after the warm salty water is poured in the tank, a drop which is so pronounced that not even the square-root fit manages to reproduce.

The distance of observational results from the Stefan-like square-root fit and the model results, gives indication that in this experiment the thawing regime is actually heavily driven by relevant "spurious" effects, even more than in the previous experiments. These effects shift the experimental setup away from the theoretical assumptions, which are therefore scarcely met.

Poor agreement between Stefan's solution and data

The distance from theoretical expectations is even more stressed if the theoretical Stefan's solution is shown. Three curves, corresponding to three different T_L, are reported and all of them lie way off the experimental results. If other values for T_L - *e.g.* the average temperature in the water column at a later stage of the experiment - were employed, however the results using Eq. 2.26a would not give a thawing profile compatible with experimental values.

Considered that in the experiment the temperature of the water T_L changes with time, it might be that different Stefan profiles, following Eq. 2.26a and corresponding to different Λ (*i.e.* an different T_L) might add up and provide a reasonable agreement with data. This kind of stratagem is however not the aim of the research, whose task was to assess if a theoretical formulation could provide solutions compatible with observations and, if possible, easy to upscale and generalize for such a tricky system.

2.5.3 *Comparison of thawing rate trends*

Answering Q2.3

Upscaling is not meaningful. Comparison is useful.

As stated, comparing the result I obtained in the laboratory and modeled with an *ad hoc* model with the SSPF observations would be pretentious if not disingenuous given the practical and logical impossibility of:

1. upscaling a $30 \times 30 \times 50$ to the Arctic ocean;
2. demanding that a frozen sand is sufficient to properly simulate the SSPF, even only on its physical aspect.

The experiments however, as a practical realization of idealized scenarios, are expected to grasp some of the fundamental aspects inherent the real SSPF and to study them.

Bearing this in mind, in this Section a comparison of the thawing rate measured in the field and the thawing rates derived in the two lab experiments is carried out. The thawing rate[25] represents a specific quantity characterizing the SSPF and a simple phase changing

25 Known also as *degradation rate*

system. For the SSPF it was noticed (Overduin et al., 2016) that the thawing rate r is directly proportional to the depth of the IBPT (z_{IBPT}) and inversely proportional to the submergence time (t_{sub}), *i.e.*:

$$r = \frac{z_{IBPT}}{t_{sub}}. \tag{2.37}$$

Thawing rate $\sim 1/t^{\zeta}$

If, according to Stefan's hypotheses, one assumed that $z_{IBPT} \propto \sqrt{t_{sub}}$, then the observational relation 2.37 would be perfectly compatible with Stefan's theoretical degradation rate, *i.e.* $r_{Stefan} \propto 1/\sqrt{t_{sub}}$. However other possible power laws, with exponent < 1, cannot be excluded either. Fig 2.13.*a* actually shows that the overall thawing rate has to decrease inversely to a positive power of the submergence time.

$\zeta = 0.5 - 0.8$ *for the SSPF*

A power-law fit of the observed SSPF reported in Overduin et al., 2016 degradation rate shows that it follows a steeper decrease, $\propto 1/t^{0.8}$, which would then imply that $z_{IBPT} \propto t_{sub}^{0.2}$. However it cannot even be excluded that the Stefan-like square-root fit is compatible with observational results, especially given the sparseness of the three measurements which allows an exploration of the times $t_{sub} > 60$ years. The SSPF thawing rate appear to be particularly high (even larger than 80 cm yr^{-1}) in the first years of the submergence, a fact which stresses the pivotal role of the period right after the submergence to catch the main degradation. This confirms on the field what experimental results also show.

$\zeta = 0.6$ *for the lab experiments*

Fig. 2.13.*b* reports the overall experimental thawing rates for both the experiments I performed. The qualitative trend does not differ much from the measurements of Overduin et al., 2016 (although the scales are very different), and both the behaviors are comparable. According to a power-law fit, degradation goes like $\propto 1/t^{0.6}$, with would imply a movement of the phase boundary like $\propto t^{0.4}$. This is in rather good agreement with what found in Section 2.5.1 and 2.5.2, where the phase boundary was estimated to move $\propto t^{0.3}$ (Fig. 2.7 and 2.12).

If I considered the asymptotic value of the thawing reached in the lab after few hours (which I might consider as a steady-state thawing rate), *i.e.* < 0.1 cm h^{-1}, it would lead to an yearly thawing of about 8 m, way beyond the already relevant value of about 80 cm yr^{-1} which has been measured But, as already said, this discrepancy is not surprising or alarming, since experimental setups were not meant to reproduce, in a small spatial scale, the SSPF conditions and thence a naive upscale of the results is not meaningful. It shall also be regarded that the experimental degradation rates could have decrease considerably, getting closer to SSPF data, if longer experiment had been run.

2.6 CONCLUSIONS

In this chapter I analyzed the results of two experiments I ran with the aim to investigate the physics of the thawing of the SSPF in a simplified setting.

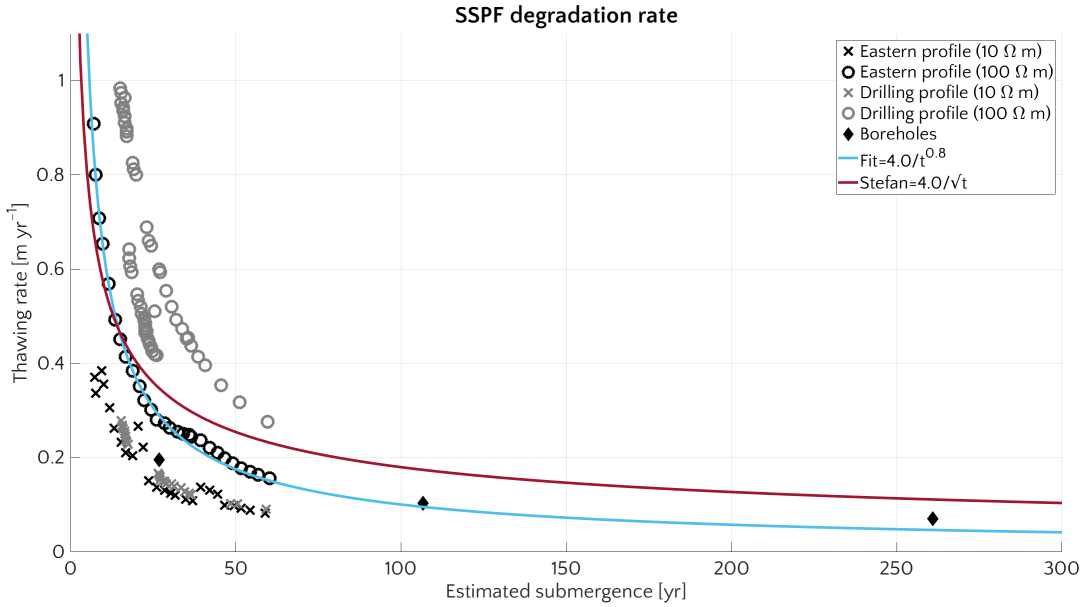

(a) SSPF degradation rates estimated from geoelectric soundings - for 10 Ωm and 100 Ωm - in two areas (eastern and drilling) reported in Overduin et al., 2016). A power-law fit (blue) and square-root fit (dark red) has been derived, too. Data are from Overduin et al., 2016.

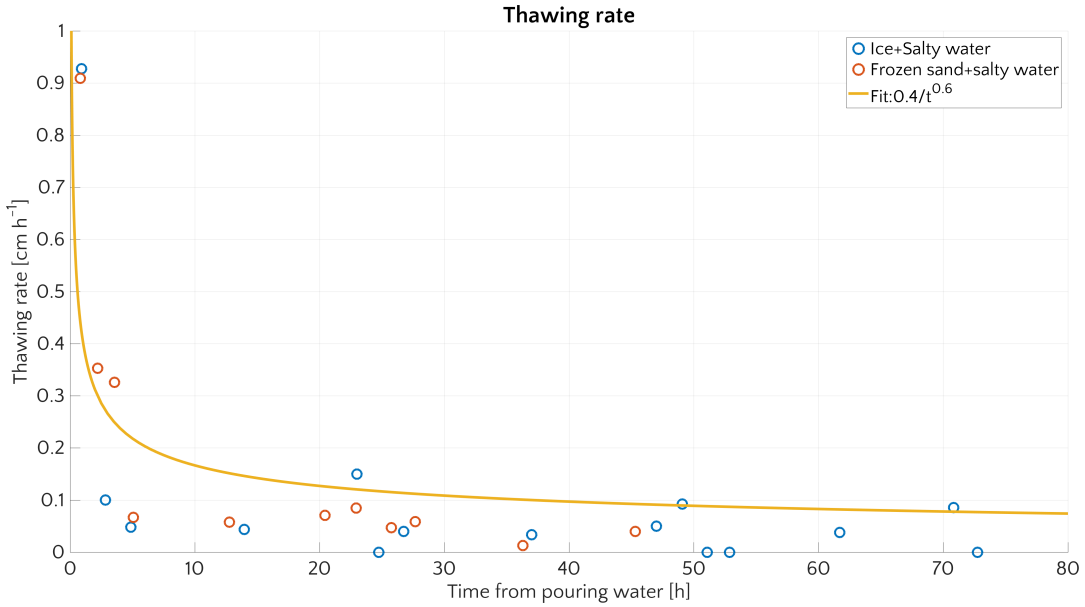

(b) Thawing rates for both the experiments I ran: the *ice-water* (blue circle) and the *frozen sand+water* (red circle). A power-law fit (yellow) is reported.

Figure 2.13: Thawing rates. Data from Overduin et al., 2016 and laboratory results.

Movement of the phase boundary

Both experiment consist in checking how a the phase interface - in a sample of pure ice and in a sample of frozen sand respectively - moves downwards under the influence of the warmer salty water which is poured on top. The experiment involving frozen sand is

designed to model the SSPF in the simplest way possible: as an ice-bound porous medium overlaid by warmer water. The results of the experiments are also compared with the results of a simplified thermal model, developed *ad hoc*, and with the analytical solution of the Stefan's problem.

Experimental limitations

It must be stressed that the experiments are not intended to simulate the Arctic sediments and the evolution of the SSPF on a smaller scale. The goal of their design is to shed some light on the mechanisms behind the thawing/melting process and to check how the assumptions employed in developing the numerical model and in deriving the theoretical results hold and in which limits.

In the experiments convection does matter

One of the main hypotheses for the theoretical derivation of Stefan's solution as well for developing the model, is that the heat transfer occurs only via diffusion. This assumptions is blatantly violated in the experimental setups because of the buoyancy-induced instability due to density difference between freshwater and salty water at the phase interface. In order to keep track of this aspect in the model, I introduced a multiplying factor KT aimed at considering an enhanced heat transfer, though without explicitly modeling the turbulent heat transfer. Assuming that KT follows an exponential relaxation dynamics, the model results are in good agreement with experimental outcomes, especially in the case of the *ice-water* experiment. This comes with no surprise considering the complexity that goes along with the presence of a porous medium (sand) and considering the extra assumptions needed on KT in the case of the *frozen sand-water* experiment. In this latter case KT has also to keep track of a damped turbulent heat exchange in thawed sand layers.

Heat diffusion is the bottom line transport mechanism

The overall good agreement between the laboratory results and the model results however suggests that the heat conduction is sufficient to grasp the main thawing/melting mechanisms, once it is properly modified to consider convection.

Discrepancy between Stefan's solution and data

A comparison between lab results, numerical fits and theoretical solutions shows a more complicated picture. In case of both the experiments, a straightforward application of the Stefan's solution has failed in reproducing the laboratory outcomes. This could be unexpected considering that the hypotheses behind the numerical model and the theoretical results are the same and that the model works rather well in reproducing the observations. Plausibly the origin of such a discrepancy does not lie in the background assumptions but in the fact that Stefan's solution does not take at all into account the turbulent heat transfer, unlike the numerical model. The generally good agreement between the laboratory outcomes and the square-root fits, *i.e.* the fit with the same trend expected in Stefan's theoretical solution, further on suggests that the system can still be basically described by a Stefan's solution. However the theoretical derivation of the coefficients appears to be flawed having neglected convection. At

Possible explanation

the current state, this represents such a shortcoming that a pure application of the theoretical formulations is not useful to predict what the thawing would be given a certain set of boundary conditions. On the contrary the run of numerical model is more trustworthy. Improvements of the theoretical solutions are an open challenge to further investigation.

Thawing rate $\sim 1/t^{\zeta}$

Comparing the thawing rate derived from the laboratory outcomes and the set of the observational thawing rates collected by Overduin et al., 2016 shows an immediate resemblance. In both cases, in spite of the very different scale in space and time, the thawing rate decreases quickly as the inverse of a power of the submergence time. In both cases the decrease is however faster than the one predicted by Stefan's, which would go like $\propto 1/\sqrt{t}$. This comparison shows that the laboratory setup is able to reproduce, at least qualitatively, one of the main features of the natural occurring subsea permafrost and stresses the relative importance of the first stages of the submergence. Finally it advocates for a deepening of the theoretical analysis of the thawing rate and for a better comparison with a larger number of observational data.

3

THE SUBSEA PERMAFROST ENTERS AN EARTH SYSTEM MODEL: THE CASE OF JSBACH

3.1 INTRODUCTION

Terrestrial PF vs. frozen soil

Subsea permafrost (SSPF) refers to permafrost (*i.e.* ground which is cryotic for at least two consecutive years (Woo, 2012) located beneath current sea level. It is worth stressing that *cryotic* does not imply that the ground is frozen, *i.e.* ice-bearing or ice-bonded (Osterkamp, 2001), although much literature still mixes up the two terms and consider permafrost as perennially frozen ground. The aforementioned definition of permafrost includes also the bedrock lying beneath the regolith, as long as its temperature is below 0 °C and even if it contains no frozen water. This differentiation between frozen and cryotic ground also takes into account the fact that only pure water[1] on a planar surface and at standard pressure freezes at 0 °C, while in reality adhesion forces (*e.g.* capillarity) and colligative properties (*e.g.* presence of solutes) lower the water freezing point. The freezing point depression in terrestrial system is not that significant because:

- the effects of the matric potential are high in pores with small radii and deeply affect the freezing process only in the vicinity of matrix particle surfaces;
- concentration of solutes (mainly salt) is restricted to specific regions and limited areas.

Therefore on land, the freezing point of pore water is only slightly less than 0 °C and the definition of permafrost as perennially frozen soil is not that misleading and surely more immediate to grasp. Furthermore it can be strictly associated to the most relevant biogeochemical feature of permafrost, namely the large amount of organic carbon (Hugelius et al., 2014) which is preserved from remineralization due to the sub-zero temperatures and consequent small availability of liquid water, a necessary condition for microbial activity.

The SSPF is submarine frozen soil

The situation is however different in the marine context. Salt prevents water from freezing even at temperatures below −1 °C: *e.g.* the freezing point of seawater at 30 psu is about −1.8 °C (Millero, 1978) and highly concentrated brines can have a freezing point as low as −10 °C (Pollard et al., 1999). Salinity induces furthermore the dissolution of fresh ice whose temperature is above the *liquidus* temperature

1 Actually perfectly pure water can be (super)cooled down below 0 °C if crystal nucleations are drastically reduced, but this aspect goes beyond the terms of this introduction.

of the seawater (Chapter 2). For this reason a more practical definition should be used in the case of submarine conditions, considering also that the average seawater temperature of the Arctic Shelf is anyway below 0 °C and therefore marine sediments would be considered "permafrost" in any case if a definition purely based on temperature were enforced. I will regard as subsea permafrost (unless stated differently) the marine sediments which are frozen, *i.e.* ice-bearing or ice-bound[2].

SSPF as relic submerged PF

The SSPF is relic permafrost (Osterkamp, 2001): it formed on land while present Arctic shelves were exposed and was subsequently flooded when the sea level rose between 12 and 5 kyr before present (BP), during the Holocene transgression (Bauch et al., 2001). Over the last glacio-eustatic cycles the sea level was several times below the current one and during the late Pleistocene cold period (Nicolsky et al., 2012), it reached about 120 m below the present value. The Beaufort shelf and the Siberian shelf thus bore subaerial conditions and were not glaciated, allowing aggradation of permafrost up to hundreds of meter thick (Lachenbruch et al., 1982). The Holocene glacio-eustatic sea transgression (which halted $\sim$ 5 kyr BP at current $\sim$ 30 m isobath) and the high coastal erosion rate (Shakhova et al., 2017) then submerged a large portion of these shelves.

SSPF warmer than land PF

Since the flooding occurred, ocean waters have been altering the thermodynamic conditions of the (once) land permafrost determining its warming, thawing and degradation. The relatively warm ocean waters have increased the temperature of the former tundra by as much as $17 - 20$ °C (Brigham et al., 1983; Soloviev et al., 1987; Kim et al., 1999; Romanovskii et al., 2001; Gavrilov et al., 2003; Romanovskii et al., 2005; Weingartner et al., 2005; Nicolsky et al., 2012; Taylor et al., 2013; Shakhova et al., 2014) and water has acted as temperature buffer isolating the submerged soil from harsh climatic atmospheric conditions of the region. Such insulation has weakened the permafrost structure, reducing the soil ice content and heating it up to a temperature close the thawing threshold. Per contra terrestrial permafrost has experienced an increase of the mean annual temperature of only $6 - 7$ °C compared to the Last Glacial Maximum (Frenzel, 1992) as Fig. 1.2 shows. Ocean waters and sea ice have also contributed to the mechanical erosion of the upper part of the flooded soil as well as of the shoreline. The Arctic coasts have been retreating as an effect of the joint contribution of the higher temperature of the sea water (*i.e.* thermal abrasion) and the marine mechanical abrasion (Are, 2003; Gavrilov et al., 2003; Grigoriev et al., 2003; Günther et al., 2015).

SSPF degradation mechanisms

Because of the increase in the top boundary condition, the SSPF tapers mainly upward from below as geothermal heat flux is no

2 In case of subsea bedrock instead the standard definition based on temperature will be applied as bedrock is expected to hold no water, even if strictly speaking this is not always true but it is surely widely valid.

more in equilibrium with top mean temperature (Mackay, 1972; Romanovskii et al., 2001; Nicolsky et al., 2012). However it degrades at the same time from the top downwards. Until recently, only the downward degradation below warmer large rivers had been investigated (Delisle, 2000), but lately the role of chemical erosion due to salt has been put into perspective, in consideration of the fact that the average subzero water temperatures of the Est Siberian Arctic Shelf (ESAS) cannot explain the thawing of the SSPF (Angelopoulos et al., 2019).

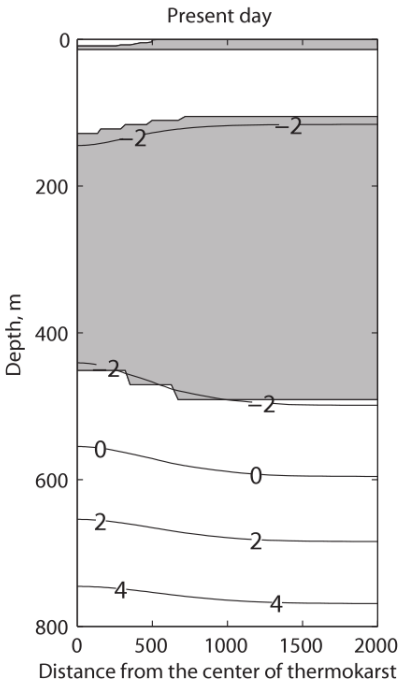

Figure 3.1: Present day SSPF and ground temperature as modeled by (Nicolsky et al., 2010). The ground material is assumed to be saline (35‰) and the geothermal heat is assumed to be 50 mW m^{-2}. The gray area represents the frozen ground. A "wafer-like" structure is represented by the sequence at the top.

Few models consider salt

Although the importance of salt had already been highlighted in the past (*e.g.* Harrison et al., 1978; Nixon, 1986; Osterkamp et al., 1989), more comprehensive SSPF models encompassing salt intrusion into the submerged permafrost have been developed only in the last decade (Nicolsky et al., 2010; Nicolsky et al., 2012). Models which implement an explicit parallel transport of heat and salt are even more recent (Angelopoulos et al., 2019).

Salt and taliks

The role of salt is considered to be decisive in preserving thaw-lake taliks after the submersion (Baker et al., 1988; Nicolsky et al., 2012; Shakhova et al., 2017) and in forming closed taliks (Nicolsky et al., 2010; Nicolsky et al., 2012) outside the zones which have traditionally been hypothesized to be possibly hosting taliks: fault lines (Kholodov et al., 1999; Romanovskii et al., 2005, see Fig. 3.3.*b*) and the SSPF in correspondence of large rivers[3] (Kholodov et al., 1999; Delisle, 2000; Frederick et al., 2014). The closed taliks hypothesized by Nicolsky et al., 2010 would be characterized by a frozen-unfrozen-frozen structure

3 A connection between rivers and their influence on talik presence had previously been guessed by Mackay, 1972 studying the area of the Beaufort shelf in the vicinity of the mouth of McKenzie.

with a thin layer of frozen material on top of the unfrozen level (see Fig. 3.1). Such "wafer-like" formation was actually detected, among the others, by (Soloviev et al., 1987; Osterkamp et al., 1989; Rachold et al., 2007).

Direct investigation of the SSPF

Until recently (Stocker et al., 2013) submarine permafrost features had not been investigated except in drilling campaigns. Drilling can provide much information on the structure and on geology, but its main drawback is that a borehole is by definition a local measurement and does not offer a larger scale perspective. With the employment of new geophysical techniques a deeper knowledge of SSPF extent has made possible. Active (Hinz et al., 1998; Brothers et al., 2012; Brothers et al., 2016) and passive (Overduin et al., 2015a) seismic methods, ground-penetrating radar (Stevens et al., 2009) and other geoelectric methods (Overduin et al., 2016; Sherman et al., 2017) have been used to study the SSPF both in the Beaufort Shelf and in the ESAS. Yet all these methods are intrinsically affected by the principle they rely on: detecting a difference in structural properties of the material. For instance, seismic methods are based on the difference of propagation velocity of P- and S-wave in frozen-consolidated and unfrozen-unconsolidated sediments layers while geoelectric methods rely on the abrupt change of resistivity of the sediments associated with the unfrozen water content. This implies that the methods are generally suitable to detect the Ice-Bound Permafrost Table (IBPT) but are incapable of identifying the SSPF based on temperature (*e.g.* in the case of bedrock). These methods are moreover highly dependent on salinity,

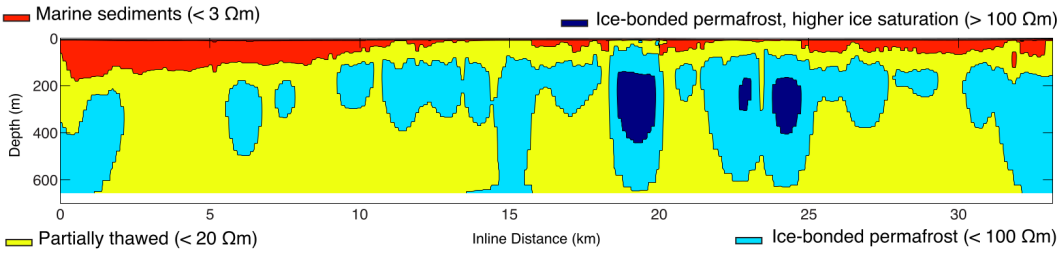

Figure 3.2: Permafrost and subsea permafrost reconstruction from a surface towed electromagnetic investigation along a transect offshore the Prudhoe Bay (Alaska). From Sherman et al., 2017.

porosity grain size and uncertainty affecting the constitutive/observational relationships the analysis of the data is based on Overduin et al., 2012; Kang et al., 2015. Finally, most of the seismic methods cannot even investigate the bulk properties of the frozen SSPF or detect its lower boundaries since seismic energy bounces back at the top boundary of the SSPF (Brothers et al., 2012). This implies that geoelectric methods remain the most appropriate SSPF mapping methods (Angelopoulos et al., 2019), even if affected by the aforementioned inherent bias (see Fig. 3.2 for an example).

SSPF extension

Direct and indirect observations have challenged the first "educated guess" of the SSPF extent down to the 100 m isobath, which represents the maximum theoretical limit set by the shelf exposed at the LGM (Brown 1997). For the Beaufort Sea, seismic reflection data are compatible with the presence of the SSPF only down to $20 - 25$ m isobath (Brothers et al., 2012; Brothers et al., 2016, Fig. 3.3.*c*). Models of the Kara Sea describe maximal SSPF extent to the 100 m isobath but offshore gas release and boreholes delimit its occurrence to the shallower $17 - 20$ m isobath (Portnov et al., 2014, Fig. 3.3.*a*). Romanovskii et al., 2005 model ice-bearing SSPF in the largest part of the shelf to the 60 m isobath, with thicker SSPF in proximity of the islands, where PF has been submerged for a shorter period (Fig. 3.3.*b*). The study by Romanovskii et al., 2005 is the first model investigation which, explicitly considering geological features like grabens and horsts and geothermal heat flux, emphasizes their role in the resulting SSPF distribution. This approach was then refined by Nicolsky et al., 2012 with the introduction of a salt-bearing SSPF, thermokarst lakes and Yedoma Ice-complex deposits and degradation in the extremely specific regional context of the Laptev Sea.

SSPF temporal response

The time response of the SSPF to submersion and a change of climatic condition has also been a controversial point. Different timescales have been suggested (Romanovskii et al., 2005; Dmitrenko et al., 2011; Malakhova et al., 2017) but a widely-agreed value is still lacking in absence of a precise definition of the time response. It is still unclear to what extent the SSPF has to be thermally affected (and in case how) in order to establish that the SSPF has responded to a change of the boundary conditions.

As stated in Chapter 2, a comprehensive understanding of the submergence process of PF is missing, and this significantly hinders past, present and future study of the SSPF, its associated features and its potential biogeochemical effects.

SSPF, a possible benchmark for different models

The modeling community has for years called for a better trade-off between models able to perform well both on the physical and on the (micro)biogeochemical side since usually only one aspect is preferred over the other (Arndt et al., 2013). A coupling between diagenetic models and regional/global Earth system models has been also advocated (Regnier et al., 2011), although this coupling is hampered by the difference in space and temporal scale the models must cope with.

Implementation of SSPF in JSBACH

In this chapter I take a first step in this direction, applying JSBACH to model the submergence of PF and the ensuing SSPF thawing. JSBACH is the land surface component of the broader MPI-ESM, the Earth System Model (ESM) developed at the Max Planck Institute for Meteorology. Whereas until today SSPF research has always been based on *ad hoc* geological-thermal models, I implemented a SSPF component for the first time in a model developed for a general land/climate study like

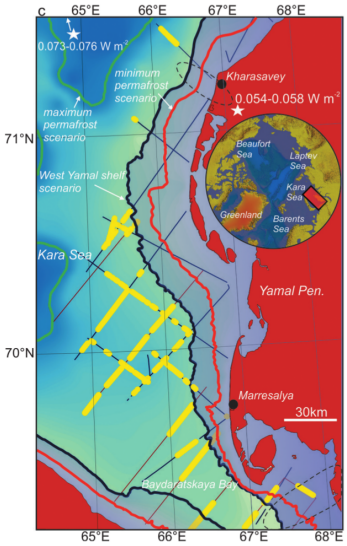

(a) Green (maximal) and red (minimal) lines extent of the SSPF at the West Yamal shelf. Yellow lines: the distribution of gas flares in the water column (Portnov et al., 2013), dashed black ovals: drilling areas (GEOS, 1997). White stars: measured geothermal heat flux (Khutorskoy et al., 2010). From Portnov et al., 2014.

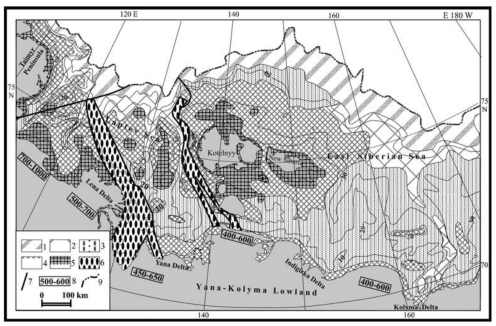

(b) Map of the modeled SSPF in Laptev sea by Romanovskii et al., 2005. Ice bearing permafrost thickness, (m): 1 discontinuous, $\leq$ 100; continuous 2 (100 – 200); 3 (200 – 300); 4 (300-400); 5 (400 – 600); 6 (100 – 600) in rifts with open taliks); 7 fault lines; 8 coastal permafrost thickness; 9 Arctic Shelf boundary.

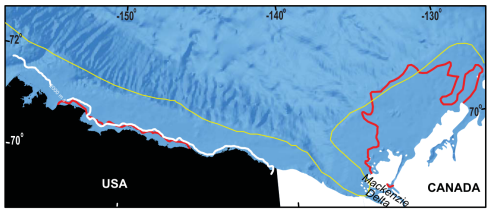

(c) Yellow line: proposed boundary for the SSPF based on the isobath (Brown et al., 1997). Red lines: seaward extent of the SSPF determined by seismic refraction analysis (Hunter et al., 1978; Pullan et al., 1987; Brothers et al., 2012). White line: line of 2000 m s^{-1} contour, used as a proxy for seaward SSPF extent. From (Brothers et al., 2016).

Figure 3.3: Modeled (*a* and *b*) SSPF extent in the Siberian Shelf. *c* Estimated and measured SSPF extent in Beaufort Sea.

JSBACH. I modified the permafrost module already present in JSBACH to account for PF formation on land and submergence under saline warmer water environment. Given the exploratory character of the research, I limited the investigation to a 1-D vertical setup, leaving the development of an integrated 3-D model to a later study. The aim of the research presented here is the modeling and the analysis of the physical consequences of the abrupt submergence of permafrost affected soil under submarine conditions to simulate SSPF formation at a site-level. I did this by running JSBACH through a spin-up phase in order to build up a terrestrial permafrost profile. Submergence is implemented by a sudden change of the boundary conditions and the switch-on of modules to account for accumulation of sediments, water saturation and transport of salinity-induced effects. Several submerging scenarios have been run to investigate their effects of the movement of the SSPF table, the SSPF ice content and temperature evolution.

Research questions of Chapter 3

More specifically I address the following specific questions:

- **Concerning permafrost submergence and SSPF formation**

  Q3.1 *How does submergence affect the permafrost in JSBACH? What is the SSPF time response to change of upper boundary conditions from land to submarine?*
  The study of movement of SSPF upper boundary, its thawing rate, its ice and thermal state, with a focus on its temporal evolution, enables a deeper insight into overlooked thawing processes and the evolution after the submersion of PF in an Earth System Model.

  Q3.2 *How does the SSPF modeled in JSBACH compare to observations, other studies and to theoretical expectations?*
  Analogies and contrasts with some measurements, with the most recent site-level model (CryoGRID2 in the version used in Angelopoulos et al., 2019) and with Stefan's problem are offered. This investigation offers a complementary view with respect to results of Chapter 2 which are based on idealistic and simplified setups and on a model explicitly developed to solve the problem of a moving boundary in the case of the experiments, unlike JSBACH.

- **Concerning thawing of the SSPF**

  Q3.3 *Under which conditions is an extensive destabilization of the SSPF possible?*
  A sensitivity study permits the evaluation of the role of salt, layering, internal parameters and boundary conditions in the thawing process from above, shedding light on the mechanisms behind it. I investigate further how the geothermal heat flux affects the overall thermal state of the sub-

merged sediments and finally provide an outlook of future evolution under simplified assumptions.

- **Concerning JSBACH modeling performance**

  Q3.4 *Is JSBACH capable of modeling complex features like taliks?*
  Taliks represent an open matter for the current SSPF research and a challenge for models. A study of their formations in the frame of simulations I ran is performed.

  Q3.5 *What are the current limitations present in JSBACH for modeling the SSPF?*
  This study represents also a technical tool for the evaluation of JSBACH: the comparison of its results with observations and other simulations as well as the investigation of its limitations serves as a starting point for further development.

3.2 METHODS

In this Section, JSBACH is described in the simplified version used here. The modeling strategy of the simulations is explored in two parts: the terrestrial permafrost spin-up phase and the submergence phase, when thawing occurs from above.

3.2.1 *JSBACH setup*

1-D simulation on a coastal grid

JSBACH is the land surface component (Brovkin et al., 2013a; Brovkin et al., 2013b; Reick et al., 2013; Schneck et al., 2013) of the Max Planck Institute Earth System Model (MPI-ESM) (Giorgetta et al., 2013) which is employed in this study. I use an offline setup endowed with a permafrost module (Ekici et al., 2014) and perform a 1-D simulation on one coastal grid-cell centered at 129.375° E, 71.811° N and in T63 resolution (1.875° × 1.865° at the point considered, *i.e.* 219.6 km×131.3 km). The choice of this grid point, roughly corresponding to the Bykovsky peninsula (north-west of Buor-Khaya bay, in Laptev Sea), is motivated by interest in studying effects of submergence and degradation of a permafrost affected coastal area in the East Siberian Arctic Shelf. The bedrock at the considered point lies at 1.11 m depth, according to the map employed by MPI-ESM (Hagemann et al., 2015).

Description of JSBACH

JSBACH simulates photosynthesis, biogeophysics and biogeochemistry of land, as well as terrestrial physical and hydrological processes. Although it now posses a soil carbon model based on YASSO (Liski et al., 2005; Thum et al., 2011; Goll et al., 2015), it is not used here, despite a recent application in the context of permafrost soil organic carbon accumulation and development across the Holocene (Schneider Von Deimling et al., 2018). The main topic of my study is the SSPF, with a specific attention in this chapter to its physical properties and

its thawing rate, aspects which would be only marginally affected by taking different soil carbon features into account.

JSBACH: soil grid

An extended vertical structure with 12 soil layers of increasing thickness is considered for JSBACH hydrology (Hagemann et al., 2015), reaching a depth of 199.6m. The choice of such a depth represents a trade-off between the scheme of increasing soil thickness (a geometric sequence with a common ratio of 2) and the depth of interest. Permafrost must be deep enough to check how it reacts to the change in upper boundary conditions on a climate time scale of 2-3 centuries, but there is no need to simulate geological permafrost in its full depth (which can reach down to $700 - 800$m, *e.g.* Fartyshev, 1993; Romanovskii et al., 2005; Nicolsky et al., 2010).

Only upper part of the SSPF is considered

Several studies (*e.g* Romanovskii et al., 2001; Romanovskii et al., 2004) highlight that the most of the SSPF thaws upward because of the geothermal heat flux, but it is unlikely that the carbon activated at the bottom of the permafrost column manages to seep through the consolidated permafrost on top and affect the upper part of the sediments, let alone the water column or the atmosphere. For this reason the potential SSPF feedback on carbon cycle and climate lies mainly in the possible vulnerability of the top of the SSPF itself. Through-taliks[4] might challenge this view but current knowledge restricts the chance of having through-taliks to fault zones (occupying roughly 5% of the ESAS, Nicolsky et al., 2012) or a specific combination of saline permafrost and geothermal heat flux (Nicolsky et al., 2010). Given these peculiar conditions I have neglected the case of possible through taliks in my study.

3.2.1.1 *Permafrost module*

An overview of JSBACH permafrost module is described here. A more detailed model explanation can be found in Ekici et al., 2014.

JSBACH: the heat balance

In the heat balance of the soil/sediments only heat conduction is considered as a heat transfer process. On land, surface temperature is evaluated by considering incoming solar radiation and surface albedo. The properties of the first soil layers on-land are dependent on the forest cover fraction of the grid. A snow scheme is implemented, too. This means that in the snow season, the uppermost snow layer is forced with incoming solar radiation and the bottom snow layer sets the upper boundary conditions for the soil layers. Lower boundary conditions are set by imposing a zero heat flux at the bottom of the last soil layer. The 1-D heat equation reads:

$$c\frac{\partial T}{\partial t} = \frac{\partial}{\partial z}\left(k\frac{\partial T}{\partial z}\right) + L\rho_i\frac{\partial \theta_i}{\partial t} \tag{3.1}$$

4 Taliks running through the entire depth of permafrost connecting the unfrozen ground beneath the frozen soil with the ground or sediment surface

where T: soil temperature (K), t: time (s), z: soil depth (m), c: volumetric heat capacity (J m^{-3} K^{-1}), k: heat conductivity (W K^{-1} m^{-1}), L: ice latent heat of fusion (J kg^{-1}), ρ_i: ice density (kg m^{-3}), θ_i: volumetric soil ice content (m^3 m^{-3}). The heat equation 3.1 is solved for each layer using a Richtmyer and Morton (Richtmyer et al., 1967) method and each time step is divided in two sub-steps. In the first step, the heat conduction (first term on the right-hand side of Eq. 3.1) is solved to give the soil-layer temperature. In the second step, soil temperature is updated considering the heat exchanged in the water phase change (second term on the right-hand side of Eq. 3.1).

JSBACH: soil hydrology

Soil hydrology is meant to describe the change of soil water content above the bedrock layer. Water transport is described by a 1-D Richards equation, which can be written as:

$$\frac{\partial \theta_w}{\partial t} = \frac{\partial}{\partial z}\left(\mathcal{D}\frac{\partial \theta_w}{\partial z}\right) + \frac{\partial K}{\partial z} + S \tag{3.2}$$

with θ_w: volumetric soil water content (m^3 m^{-3}) for layer above the bedrock, t: time (s), z: soil depth (m), S: sources and sinks (s^{-1}). K is the soil hydraulic conductivity (m s^{-1}), the same quantity entering the Darcy's law. $\mathcal{D}$ is finally the soil water diffusivity (m^2 s^{-1}), defined as a quantity dependent on the saturation state itself (hence on θ_w) as

$$\mathcal{D}(\theta_w) = \frac{d\psi(\theta_w)}{d\theta_w} K(\theta_w) \tag{3.3}$$

with $\psi(\theta_w)$: the matric potential (a.k.a. suction head). In JSBACH, D is parametrized according to formulation by Clapp et al., 1978. Richards equation describes the local change of soil moisture as a vertical diffusion-like motion (first term) and gravitational drainage (second term)[5]. Note that drainage occurs only when soil moisture is above the wilting point.

The hydrology is solved considering first water input/output (precipitation, evapotranspiration), then the phase change routine updates the liquid and frozen content. Finally, liquid water is vertically displaced.

The system also considers for supercooled liquid water formation according to the formulation by Niu et al., 2006. The presence of unfrozen water below the freezing point reflects a physical fact, is crucial for the vegetation (before submergence) and, taking into account the freezing point depression, can consider the effect of salinity and its role for an improvement in modeling the SSPF (Nixon, 1986; Nicolsky et al., 2012).

5 Richards equation in terms of moisture content θ_w can be interpreted as an advective-diffusion equation where the advection field $V(\theta_w)$ reads $\partial_{\theta_w} K(\theta_w)$, where the subscript means the partial derivative with respect to that variable. With this notation 1-D Richards equation becomes: $\partial_t \theta_w = \partial_z \left(\mathcal{D}(\theta_w)\partial_z \theta_w\right) + V(\theta_w) \cdot \partial_z \theta_w + S$.

Volumetric heat capacity c and soil heat conductivity are dependent on the hydrological state of the soil (saturation state, ice and liquid water fraction) and standard parametrization is employed in the scheme (Ekici et al., 2014). As in Chapter 2, the weighted arithmetic mean is employed for extensive quantity (like the heat capacity) and weighted geometric mean is employed for a connectivity feature which should take into account the real geometry of the soil (like heat conductivity).

JSBACH: soil thermal properties

The snow scheme is made of up to 5 snow layers (with the bottom snow layer which is in touch with the first soil layer and which can grow in size to account for increasing snow depth). Snow thermal properties are considered constant and snow layers are hydrologically inert since they are assumed to hold no water. The water from snowmelt can infiltrate in the first soil layer, though.

JSBACH: the snow scheme

3.2.1.2 *Geothermal heat flux*

JSBACH in standard configuration does not include any geothermal heat from below, a component which would be necessary to model a full geological permafrost in its entire width. In the setup employed here, the possibility of a geothermal flux was nevertheless introduced in order to study possible sensitivity to this factor, even if no major changes are expected in the permafrost, which might respond in the aforementioned climate time scale of two to three centuries.

Implementation of geothermal flux in JSBACH

The area of interest of the ESAS and especially the Laptev Sea has been object of studies with multichannel seismic reflection devices to infer its structural and stratigraphic elements as well as major rifts and faults (Drachev et al., 1999; Sekretov, 1999; Sekretov, 2000; Franke et al., 2001), the SSPF depth and extent (Overduin et al., 2015a) and geothermal heat flux (Kholodov et al., 1999). According to Romanovskii et al., 2001; Romanovskii et al., 2005 and Nicolsky et al., 2012 the geothermal heat flux can be parametrized according to the structural characteristics of the area with values of $40 - 80$ mW m^{-2} for undisturbed rocks of the tectonic platforms, 100 mW m^{-2} for active fault lines (Duchkuv et al., 1985; Duchkuv, 1985; Lysak, 1988) and $85 - 117$ mW m^{-2} along the continental slope (Drachev et al., 2003). This last value is thought to be high enough to determine the absence of the SSPF in correspondence of the shelf break. The temperature gradients associated with these values of the geothermal heat flux are in the range of $2 - 0.4$ °C/100 m (Romanovskii et al., 2005; Nicolsky et al., 2012).

Measured geothermal heat flux

3.2.1.3 *Sediment accumulation and role of salinity*

The other main modification implemented in the model is the sediment accumulation during the submergence phase along with a simplistic scheme to take into account salinity diffusion into the sedi-

ments. This ensures that the freezing point depression is considered with ensuing non-trivial effects such as the "chemical erosion" (Nicolsky et al., 2010), *i.e.* permafrost thawing due to salt presence.

Implementation of sediment accumulation scheme

First of all, a nomenclature clarification is needed. Since after sea transgression both the submerged soil and sediments accumulating after the submersion are called "sediments", for the sake of clarity in this Section I will keep the name *subsea land* (SL) for the soil layers which were previously exposed to atmospheric conditions on land and then submerged. I will use *sediments* strictly to refer to the layers accumulating during underwater phase. The term *sediment column* refers to both components: SL and sediments.

Constant sedimentation rate

In order to account for sediment accumulation I consider a constant sedimentation rate of 0.123 cm yr^{-1}, evaluated according to the formulation by Burwicz et al., 2011 considering a water depth of 40 m[6]. The snow scheme, switched on during the spin-up subaerial phase, has been modified into an accumulation scheme to consider for the sediment thermal and physical characteristics. The sediments are thus treated as external layers accumulating on top of the SL with new layers adding on with time (see Fig. 3.4 for a scheme). The width of the layers increases following the sequence: $5 - 10 - 10 - 20 - 20 - 20 - 40$ cm. The first layer in computation appears when the accumulated sediments exceed 1 cm. In a 1000-year long simulation, the years when the sediment layers are added to the underwater column are: the 9th, the 41st, the 122nd, the 203rd, the 366th, the 529th and the 692nd.

Saturation of accumulating sediments

Given the submarine conditions, the sediments have been considered fully saturated in marine water and the temperature of top layer of the sediment columns is set equal to the water temperature of the sea bottom and is always unfrozen. The thermal properties of the sediment soil matrix are the same as the thermal properties of the mineral soil used to model the land component. Exactly as on land, ice can form (or melt) over time in sediment layers if temperature changes and drops below (or rises above) the melting temperature of the pore water of the corresponding layer.

Determination of thawing temperature

The determination of the pore water freezing temperature is the trickiest point because an explicit calculation would need to take into account the freezing point depression due to the cohesive forces of the pores and, even more importantly, due to salt infiltration in the sediments. The melting of pore ice would then freshen the layer in touch with the thawing horizon, causing a difference in buoyancy which might lead to a complicated double-diffusion process described by a coupled Bénard convection (Hutter et al., 1999). Modeling and resolution of this type of convection is beyond the scope of my study, since

6 This same value is used in baseline simulations of Chapter 4.

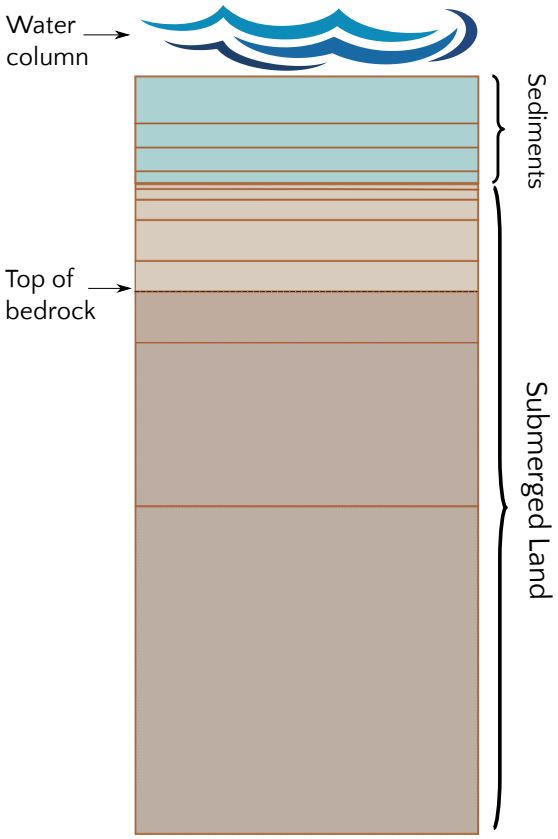

Figure 3.4: Scheme of the sediment column with sediment accumulation (not in scale and without reporting all the layers).

I am interested in a broad picture and not in solving the detailed diffusion-convection scheme in the sediment.

Another complication arises due to the forcing files used to drive the thawing process from above. I use the MPI-OM (Max Planck Institute Ocean Model, Marsland et al., 2003) simulations of sea bottom water temperature to set the upper boundary condition of the temperature of the sediment column (Giorgetta et al., 2013). In these simulations the phase change temperature of water is not dependent on salinity: freezing temperature is set constant at -1.8 °C and melting temperature of ice is set constant at 0 °C. This difference between freezing/melting point is designed to consider within MPI-OM the complicated effects of salinity in a simpler way instead of coupling it with the phase change temperature.

Salinity is not coupled to freezing point in MPI-OM

Because of this mismatch between salinity and water freezing temperature, inconsistencies would arise, if a simplified diffusion scheme were implemented to model salinity intrusion from the forcing files.

Many studies (Nixon, 1986; Osterkamp et al., 1989; Delisle, 2000; Nicolsky et al., 2010; Angelopoulos et al., 2019) have however shown that salinity is the main element affecting pore water freezing tem-

Thawing due to salinity is crucial

perature and cannot be neglected in light of the fact that the SSPF temperature is much closer to its thawing temperature than land permafrost and hence more prone to destabilization and structural weakness which unfrozen salty water might cause (Nicolsky et al., 2012; Shakhova et al., 2014).

The heuristic transport of the freezing point depression

In order to overcome these difficulties and still retain a more physical-based approach, a new heuristic method is developed based on the determination of the freezing temperature according to sea bottom water temperatures. The main assumption is that when water temperature is below 0 °C, its salinity is exactly the one needed to keep it unfrozen and, thus, the sea water temperature is at the freezing temperature. As this water percolates into the sediment column it also affects the thawing temperature of the saturated subsea soil/sediments. In other words, subzero sea water temperature plays the role of the freezing temperature: it is not the salt which is transported downcore but its effect on the water freezing point[7].

Algorithm of determination of the freezing point

As sea floor water temperatures changes rapidly a method has to be conceived to: 1) account for the diffusion within the sediment column of the salt-induced freezing point depression at a pace set by salinity intrusion and 2) average the rapid change in temperature at the top of the sediment column as its influence propagates downwards. The main steps of the employed algorithm are:

- The SL freezing temperature is initially set equal to the mean sea bottom water temperature of the first 12 month of the simulation. This allows the model to consider the seasonal variability (the change in salinity throughout the year usually determines a variation of freezing point of ~ 0.7 °C Dmitrenko et al., 2011). If any of the monthly temperatures considered for the calculation of the yearly mean happens to be higher than 0 °C, the salinity of the forcing file is used to compute the corresponding freezing point depression (according to the formulation by Millero, 1978). For the SL layers below the bedrock the freezing temperature is set to 0 °C, as its water content is supposed to be zero.

- The temperature of the first layer of the sediment column (the one in contact with the sea water) is at each time-step set equal to the sea water temperature and always unfrozen.

- To evaluate how the freezing point depression propagates downwards with diffusing salinity from above and affects the layers beneath, the typical salt diffusion time scale τ_S is considered. It is given by $\tau_S \simeq x^2/D_S(\theta)$, where x: distance between the mid points of two consecutive layers, $D_S(\theta)$: salt diffusion coefficient corrected for tortuosity θ and equal to $0.4 \cdot 10^{-2}$ m^2 yr^{-1}

7 I neglected the micro effects due to cohesive and surface forces in changing the freezing temperature as they are just minor corrections.

for $\theta = 1$ (Harrison et al., 1978). For each pair of layers the τ_S is computed and only when it has elapsed, the salinity-induced change in freezing point affects the layer beneath. Its updated freezing temperature is calculated as the mean of the freezing temperatures of the upper layer during the whole τ_S. Once the freezing temperature of a layer is changed, the process starts again.

- If a sediment layer is added on top, the layers already present are simply shifted downcore: the new sediment layer is the one in touch with the sea water and the freezing temperature of the former first layer (now second) is set equal to the freezing temperature of the former second layer (now third). A new τ_S for the extra sediment layer is also computed.

Concerning the phase change, computation the permafrost module with the sediments follows the same procedure as the original permafrost module.

3.2.2 *Modeling strategy*

Goal of modeling: insight on submergence and thawing

Although submergence of the coastal permafrost and ensuing SSPF formation can be observed in reality, only the use of models allows for an overview of the general processes occurring and the evolution of the thermal state of sub-marine permafrost on a long time scale. Given the long times involved, such a task would be difficult to achieve with measurements even if they were abundant and adequate - and this is not the case for the SSPF. If it is true that SSPF formation is still occurring because of thermal abrasion of the coast and retreat of coastline, it is also true that the most important formation stage, *i.e.* the rapid early Holocene sea level rise, happened between 11 and 8.9 yr BP (Bauch et al., 2001) and hence its physical consequences and effects cannot be probed by direct measurements in any case. Therefore the models have the aim of filling this knowledge gap.

Thawing rate: the quantity to couple ESM and RTM

The derivation of some peculiar features of the system under examination, such as the salinity penetration and thawing rate, besides being interesting on their own, offers a view on other characteristics and processes such as the mobilization of old organic matter sequestered in frozen soil or the opening of taliks. Finally, quantities like thawing rate may serve as necessary input for other models and for comparison with field measurements.

Simulation protocol

The simulations consist of a spin-up phase followed by the brisk imposition of warmer saline marine water as upper boundary conditions (*i.e.* submergence phase) and the ensuing thawing of the SSPF from above. In the following, a detailed description of the model setups for the two phases is presented.

3.2.2.1 *Spin-up phase*

The original soil moisture of the initialization file - resolution T63, 11 tiles, 5 soil layers, corresponding to the pre-industrial (PI) state (`jsbach_T63GR15_11tiles_5layers_1-850.nc`) - was firstly redistributed within the extended soil scheme of 12 layers. Each layer is constructed in order to have an increasing thickness according to a geometric sequence, namely the width d of the $n-$th soil layer $d(n)$ is given by $d(n) = 2^{n-1} \cdot 0.065$ m, where the first layer has a width of 6.5 cm and the last one 133.12 m. Such a file sets the initial state at the beginning of the spin-up phase.

Increase of soil layers

Spin-up of the upper PF

Because of the interest in the submerging process, the goal of the spin-up was to aggrade a permafrost thick enough for the climatological purpose of the experiment without the need to built up a permafrost-affected soil entirely compatible with late Pleistocene/LGM climatic conditions. To this end, forcing data from the PI control simulation with MPI-ESM-1.1.00 at T63 resolution and with a time step of 1800 s were used. Considering the slow time scale of heat propagation within soil[8], the spin-up had to be long enough to produce a steady-state temperature profile down to the chosen soil depth. Therefore the spin-up was run for 155 years, randomly picking forcing files from the pool of forcing files between 1850 and 1900. Only the forcing files in this interval were considered in order to limit the time frame of anthropogenic-affected forcing. The strategy of random sampling helped account for the inter-annual variability of the climate without the drawback of having to repeat a 50-year cycle, which might bias the outcome of the spin-up.

Initialization of soil temperatures

According to JSBACH initialization routine, the temperatures of soil layers were set in relation to the soil depth and the distance in time from the maximum surface temperature in the first year of simulation according to the following formulation:

$$T(z_i) = \bar{T}(0) + \frac{\Delta T}{2} e^{-\frac{(z_i - z_{ref})}{\sqrt{\alpha_h \cdot \mathtt{T}}}} \cos\left[2\pi\left(\frac{t_{max}}{\mathtt{T}} - \frac{z_i - z_{ref}}{\sqrt{\alpha_h \cdot \mathtt{T}}}\right)\right] \quad (3.4)$$

where $T(z)$: temperature (°C) at depth z_i of the i-th soil level; $\bar{T}(0)$: mean surface temperature (°C); ΔT: difference between maximum and minimum surface temperature (°C); $z_{ref} = 0.07$ m is the offset soil depth at which soil surface temperature is set; t_{max} is the point in time of the year corresponding to the maximum surface temperature (s); $\alpha_h = 7.5 \cdot 10^{-7}$ m^2 s^{-1} is a typical soil thermal diffusivity; and $\mathtt{T}$ is the duration of a year (s).

8 Remind that typical thermal diffusivities (α_h) of solid rocks is $\sim 3 \cdot 10^{-6}$ m^2 s^{-1} while for soil it is typically much lower $\sim 6 \cdot 10^{-7}$ m^2 s^{-1}. Using the relation that links time and length in diffusive-drive processes, *i.e.* $\ell \sim \sqrt{\alpha_h \cdot \tau}$, the time τ needed for instance for a thermal perturbation to propagate down in the soil for a quantity $\ell \sim 10$ m is roughly $\tau \sim 5$ yr.

3.2.2.2 *Submergence phase: thawing from above*

Sudden submergence

The submergence phase is modeled as a sudden change of temperature boundary conditions and the switch-on of the sediment accumulation module, imposed on the state resulting from the spin-up. Different experiments have been run to address still open questions relating the SSPF degradation process and the mechanism behind its thawing. The variety of experiments allows me to also for the first time the capability of JSBACH to model such a system.

Characteristics of submergence

The submergence phase is characterized, besides a change in temperature boundary conditions, by a change in saturation state of soil layers. The new accumulating sediment layers are considered saturated in water while the submerged land layers (above the bedrock) become saturated according to the following scheme:

- If the layer ice content is $< 60\%$ of pore space then marine water percolates downwards
- If the layer ice content is $> 60\%$ of the pore space then marine water infiltrates to the layer but does not percolate any deeper, until the pore ice melts, clearing the way for water to permeate the layers.

In consideration of the fact that submerged layers get fully saturated, no soil hydrology module is considered in the thawing phase, unlike in the spin-up phase (as described by Eq. 3.2).

Forcing files from MPI-OM simulations of the ESAS area

The baseline simulations are forced with boundary conditions which are derived from MPI-OM outcomes (Giorgetta et al., 2013) for the years $1850 - 1950$. Corresponding forcing files are generated by extracting the sea bottom values of salinity and temperature (*i.e.* the value of the deepest level simulated by MPI-OM) for an area roughly correspondent to the Eastern Laptev Sea (129.38°−136.88° E and 73.68°-75.54° N) and then calculating the monthly average over the full area. For each forcing file, 12 values (one per month) representing the sea bottom salinity and temperature are obtained and can be applied as yearly boundary conditions of the 1-D vertical system investigated here.

Set A: baseline thawing simulations

A set of 10 baseline simulations (set *A*) has been run - each for 1000 years - with the aim of determining a range of uncertainty for the experiment outcomes. Each run has been forced with a different randomization of the 101 forcing files available to take into account the interannual variability and avoid model artifacts. A restriction of the forcing years to the pool $1850 - 1950$ is backed by the interest in modeling submergence under conditions as more similar as possible to the PI conditions, in order to limit possible anthropogenic effects.

Other thawing runs

Other simulations have been run to perform sensitivity analyses:

B. Ten simulations with the same year sequences of the set *A* but whose temperature has increased of 10 °C.

C. Three simulations of idealized experiments to check the thawing process from above without considering the variability of the random climatology:

   i Sea bottom temperature $T_w = 0$ °C, phase change temperature for SL and sediments $T_m = -1.8$ °C.

   ii Sea bottom temperature $T_w = 1$ °C and phase change temperature for SL and sediments $T_m = 0$ °C.

   iii Freezing temperature $T_f = -1.8$ °C, thawing temperature $T_m = 0$ °C and sea bottom temperature T_w slightly above 0 °C (namely $T_w = 0.001$ °C). This offers a simulation with melting/freezing conditions similar to the ones considered in MPI-OM setup.

D. One simulation using similar conditions employed in Agelopolous 2019, *i.e.* a sea bottom water temperature of $T_w = -0.7$ °C, the average value of Angelopoulos et al., 2019. When the sea bottom temperature is constant the method described in Section 3.2.1.3 is flawed and so I set the freezing temperature to $T_m = T_f = -1.8$ °C, as corresponding to a salinity of 30 psu like the one considered in Angelopoulos et al., 2019 itself.

E. Two experiments runs (1000 yr long) to evaluate the effect of the geothermal heat flux coming from below, imposing a heat flux at the bottom according to the values considered in Romanovskii et al., 2005, Nicolsky et al., 2012 and Portnov et al., 2014.

   i A geothermal gradient $G = 2$ °C/100 m (corresponding to a flux of 40 mW m^{-2})[9].

   ii A geothermal gradient of $G = 3.5$ °C/100 m (corresponding to a flux of 70 mW m^{-2}).

F One simulation (200 yr) in which summer (June-September) sea bottom temperature increases of 0.09 °C yr^{-1} as found by Dmitrenko et al., 2011. The simulation length in this case is shorter to limit temperature increase to a reasonable amount. Only summer months are mainly affected because of seasonality of riverine discharge and lack of sea ice insulation effects.

Idealized thawing runs

The simulations of the set B and C.i-ii, in their idealized form, aim at assessing the SSPF response time scale to changing boundary conditions after submergence. Such an evaluation might help to tackle the open problem of identifying whether expected permafrost failure and degradation, with supposedly consequent high methane release in water column, is originated by ongoing climate change and sea water warming (as Shakhova et al., 2009 and Shakhova et al., 2010b

9 Remind that the thermal conductivity of bedrock in the model is 2 W m^{-2} K^{-1}

claim) or it is just the ongoing process of long run response to glacial termination (Anisimov et al., 2014; Malakhova, 2016; Malakhova et al., 2017).

3.2.3 *Limitations of the model*

Answering Q3.5

Many aspects of the SSPF formation and degradation are neglected or parametrized or simply inaccurate, especially in a land surface model like JSBACH which is designed to be integrated in a larger ESM, whose aim is obviously not a geologically accurate reproduction of subsea - as well as terrestrial - permafrost.

Besides the intrinsic model limitations of the permafrost module itself (see Ekici et al., 2014 about this) in producing the initial configuration before submergence, in the following I report the limitations with respect to those aspects which are more likely to affect and misreproduce submarine results[10], including:

- The lack of an independent salinity diffusion scheme within the soil parallel to the water percolation within the sediments and the employment of an heuristic approach. The absence of a brine rejection mechanism.
- The discretization of the sediment layering, which creates artifacts in growing sediments, especially when thicker sediments layers are added. The uppermost sediment layer, and not only the lowermost one, should be thinner, to avoid introducing a larger thermal inertia that is not able to keep track of the fast change of the sea bottom water temperature.
- The uniformity of the soil/sediment layers, whose heterogeneity is not resolved in 1-D. This hinders a resolution of ground structure and does take into account the potential effects of elements internal to the sediments (such as the presence of patches or clogs) and geometry and hence overlooks the role of soil topology (which is actually relevant for the evaluation of some thermal properties) and tortuosity, which is deeply affected by ice presence (Fortier et al., 1994).
- The unresolved geology of the layers, which cannot include macroscopic features like cracks and chimney.
- The lack of Yedoma Ice Complex - described as a relief - which would slow down SSPF degradation.

10 Although generally such considerations are reported after the exposition of model results, I have decided to move them here as, with these limitations in mind, it is more straightforward to correctly frame simulation outcomes which will be presented and to put them in the right perspective.

- The presence of a uniform, shallow, bedrock, which affects porosity and thermal/connectivity properties of the soil and prevents water/ice beneath.
- The lack of a module aiming at resolving methane production and escape[11], *i.e.* considering bubble formation and migration within the porous medium with the ensuing mechanical deformation of the sediment structure itself.
- The lack of groundwater discharge, whose role is unclear whether it might increase (Grandpré et al., 2012) or decrease (Frederick et al., 2015) the SSPF thawing rate.
- The lack of lateral heat and water transport, as well as the lack of other forms of heat transport than diffusion. This is particularly inaccurate in sediments heavily affected by salt intrusion, salt fingering and convective salt transport (Harrison et al., 1978; Baker et al., 1988; Osterkamp et al., 1989) or more turbulent phenomena like ice scouring (Brooks, 1974; Cherkis et al., 1992; Clark et al., 1998; Shakhova et al., 2017). Additionally the representation of a mushy layer[12] is missing.
- The absence of a dynamic scheme to take into account volume effects of melting pore ice and the consequent subsidence.
- The absence of sea ice (and related phenomena) which can grow till fastening to the sea bottom, thus affecting the temperature of the sediments (Bogorodskii et al., 2018).
- The lack of gradual submersion with a plausible coastal retreat (Angelopoulos et al., 2019).
- The neglect of features like thermokarst lakes that might have affected coastal permafrost before submergence.

Only some of the factors known to be important are included in JSBACH

Six factors are acknowledged to influence the SSPF evolution over time (Shakhova et al., 2017): the thermal and ice state of PF before submergence, the duration of submergence, the sea bottom water and salinity, the geological features, the presence of thermokarst lakes before submersion and the coastline retreat rate. Of these six factors only the first three are fully included in the model, with a simplified version of the fourth one and a total absence of the last two.

11 Although a more recent JSBACH version includes methane production and transport (Kaiser et al., 2017).

12 A layer where freezing occurs on an extended thickness instead of at a sharp interface

3.3 RESULTS

3.3.1 *Spin-up phase*

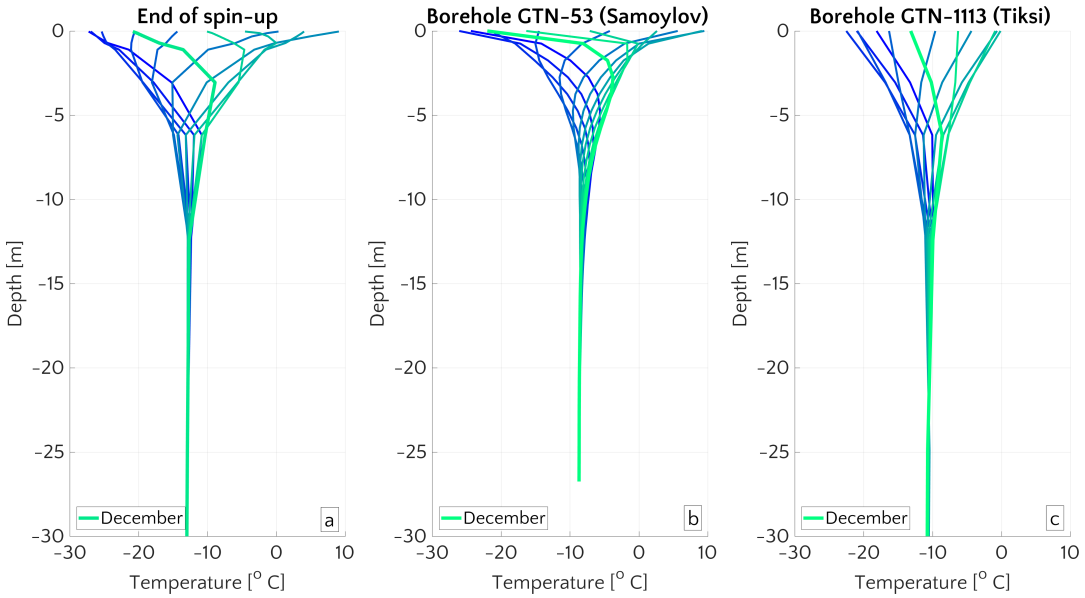

Figure 3.5: *a.* Monthly temperature profiles for the last year of the spin-up phase. For comparison, monthly average temperatures for two boreholes have been also reported. *b.* GTN-53 on Samoylov island, years of measurement: 2006 – 2015. *c.* GTN-1113 near Tiksi, years of measurement: 1993 – 2015 (the surface temperature for this borehole has been extrapolated as there are no associated measurements). The thicker line represents December and, for the spin-up simulation, it sets the initial condition of the submergence phase.

Temperature profile of the spin-up and comparison with land PF

The temperature profile resulting from the spin-up phase is shown in Fig. 3.5, reporting the temperature vertical distribution for the simulated permafrost at the end of the spin-up phase. For comparison the monthly temperature profile of two boreholes in coastal areas is also displayed. The borehole GTN-53[13] is located on the Samoylov Island (72.369555°N, 126.475111°E, elevation: 11 m), in the Lena river delta. It has a depth of 27 m and the recordings span the period 2006 – 2015. The borehole GTN-1113[14] digs instead a tundraic eluvium (71.586731°N, 128.777346°E, elevation: 46.6 m) not far from Tiksi and goes down to 30 m. The data collected are relative to the period 1993 – 2015. The profiles plotted for both the boreholes are the mean values, for each month, calculated considering all the values taken during the entire measurement time (hourly for GTN-53 and already monthly aggregated for GTN-1113).

Good agreement

The average deep temperature (−13 °C) of JSBACH-simulated permafrost at the end of the spin-up phase corresponds to the mean

13 http://gtnpdatabase.org/boreholes/view/53
14 http://gtnpdatabase.org/boreholes/view/1113

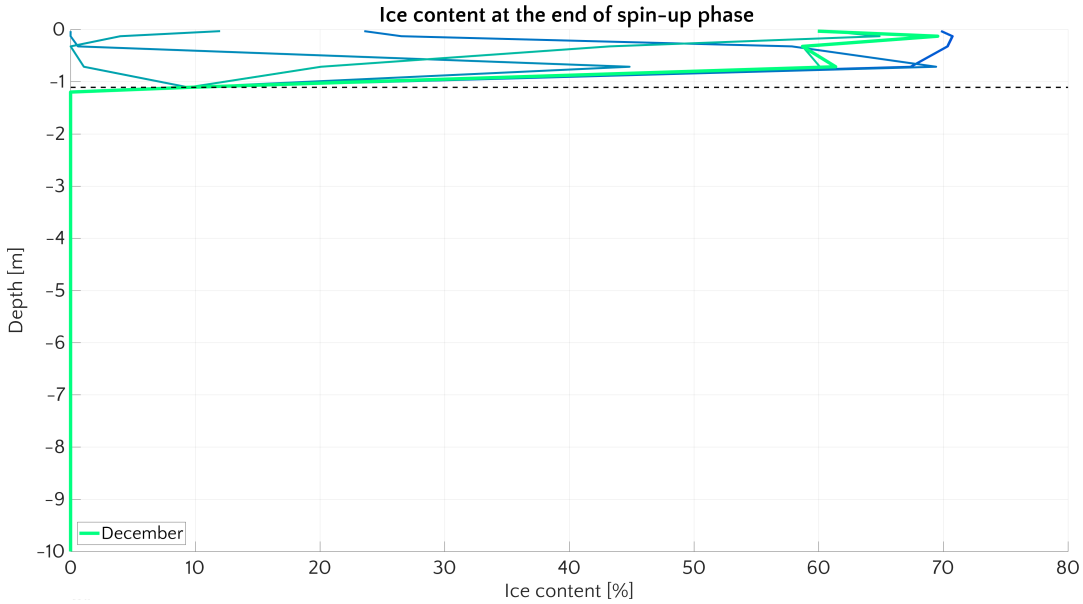

Figure 3.6: Profiles of the monthly averaged ice content (in %) for the last year of the spin-up phase. The thicker line represents December and therefore it describes the initial condition of the submergence phase. The horizontal dashed line represents the top of the uniform bedrock.

temperature of the forcing and does not deviate much from the values measured in the boreholes: -8.7 °C for GTN-53, (Fig. 3.5.*b*) and -10.8 °C for GTN-1113 (Fig. 3.5.*c*). The depth of the simulated seasonal fluctuation is also in agreement with measurements and lies at about $12 - 13$ m.

Discrepancy due local variability and long-term climate trend

The differences between simulations and measurements is ascribed to the local variability and the employment of a forcing that just repeats the pre-industrial conditions without taking into account the climate trend of the last century. The profiles of the temperature for borehole GTN-53 show warmer temperatures that reflect down to the deep temperature on one hand and to the steepest, asymmetric temperature gradients at the surface on the other hand. The maximum surface temperature for Samoylov is 9.1 °C which is the same as the simulated one during the spin-up, while the borehole of Tiksi shows overall colder conditions (maximum summer temperature -0.1 °C) and a less pronounced seasonality.

Ice profile of the spin-up

Fig. 3.6 displays the monthly-averaged vertical profile of ice content (in percentage) at the end of the spin-up. Since water cannot percolate within the bedrock no ice can form below that very same threshold. As we infer from Fig. 3.5.*a* the active layer (on the basis of temperature) goes well below the 1.11 m depth represented by the bedrock. This fact explains the high seasonal variability of ice content that drops to 0% and can reach 70% in winter months within the first meter of soil. Such values for ice contents are plausible and typical of a geological structure known as Ice Complex, a soil characterized by a

high ice content - up to 80% (Gavrilov et al., 2003; Schirrmeister et al., 2013; Strauss et al., 2017) - often aggregated in wedge-like structures, which are however only slightly affected by seasonality (Matsuoka et al., 2018). On one hand, the elevated ice percentage in the soil could be considered the signature of the formation of such structures in the model, on the other hand its strong seasonality might be an artifact due to the shallow bedrock and the lack of soil heterogeneities.

According to the procedure described in Section 3.2.2.2, the initial water content is set by the ice content with seawater not percolating any deeper than the second submerged soil layer (0.195 cm). Seawater will then also be able to saturate pore space beneath this level but at a much slower pace, since the ice clogging this level - and preventing percolation - has to melt first. Considered the average cryotic sea water temperature the melting proceeds mainly driven only by salinity intrusion and its ensuing chemical effects, which occur at a slower rate compared to the seasonal variability of the subaerial temperatures.

3.3.2 *Movement of Permafrost Table*

Answering Q3.1

Definition of the top of the SSPF table

The depth of the top of the permafrost table (PT) is reported in Fig. 3.7 for the simulations of submergence under the pre-industrial conditions (the set A of Section 3.2.2.2). The top of the PT is defined according to temperature: a comparison between the temperature T and the freezing/thawing temperature T_m is carried out for each layer and each month. The lowermost layer (throughout the year) whose temperature is above the freezing/thawing point then sets the top of the PT [15]. The freezing/thawing temperature is 0 °C for bedrock and dynamically changing according to the algorithm described in Section 3.2.1.3 for the portion above the bedrock.

Factors affecting the depth of the PT

The depth to the top of the PT is affected by two factors: i) the sediment accumulation on top of the sediment column (which adds up to 1.23 m in 1000 years of the simulation length) and ii) the thermal and chemical thawing from the top due to temperature and salt propagation. Fig. 3.7 shows the PT depth calculated from the Sediment-Water Interface (SWI) and therefore keeps track of both the aforementioned processes. The depth of the PT, average of runs resulting from the different randomization of the forcing, shows a general decrease down to the value of 2.05 m after 1000 years. The overall trend of the PT is descending, as expected, but some features are worth a deeper analysis.

15 Indeed an interpolation is considered. The actual top of the PT is determined as the intersection depth of two straight lines: the one describing temperature $T(z)$ and the one describing the freezing/thawing temperature $T_m(z)$, both connecting the center of the lowermost layer whose $T \leq T_m$ and the center of the layer immediately below.

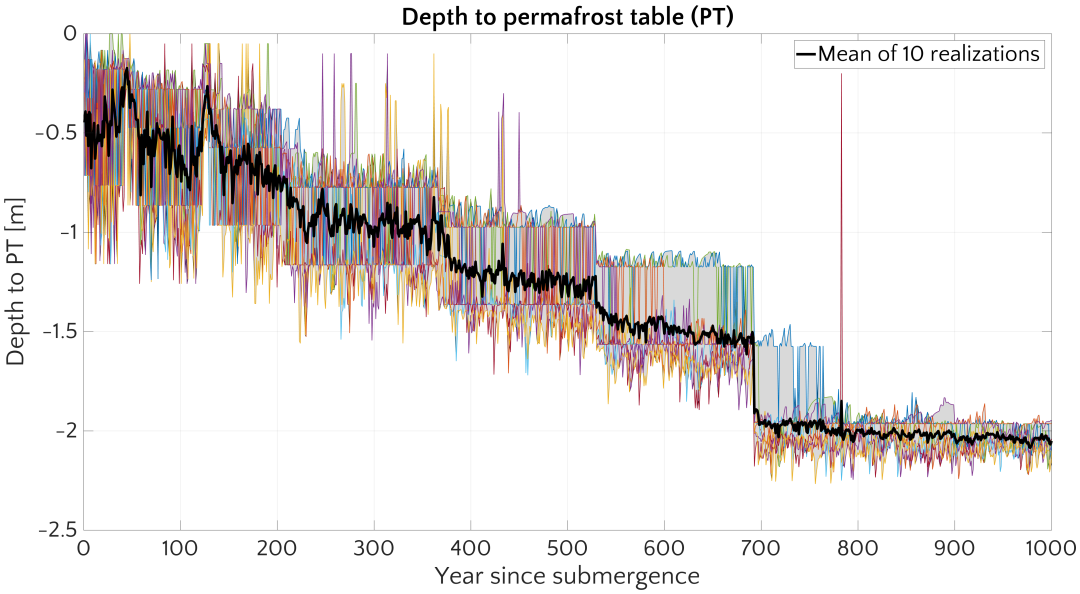

Figure 3.7: The depth to the top of subsea permafrost table (PT) over time. Each coloured line represents one of the 10 realization of the runs of the set *A*, with a different randomization of the forcing files. The black line represents the average of the 10 runs. After 1000 years the mean value of the depth of the top of the PT is 2.05 m.

Sediment discretization causes jumps in PT. PT relative to SWI(0)

The discretization of the sediment accumulation on top of the submerged soil is responsible of the step-like aspect of the value of simulated PT. When an extra layer of sediments is accounted for in the model, this leads to an abrupt decrease of depth of the PT from the SWI equal to the thickness of the added layer (thickness which increases with the number of sediment layers). Assuming this were the only reason, such an effect should not be present if the movement of the PT relative to the SWI at the beginning (SWI(0)) were considered. Fig. 3.8 shows however spikes at the years corresponding to the increase in the number of layers also in the case of the thawing relative to the SWI(0). And this brings into play the change in thermal properties, an unavoidable consequence of the dynamic increase in the number of layers on top of the column. Sediments of growing thickness augment the thermal inertia of the upper layers and this induces the abrupt change of the terms considered in the Richtmyer and Morton numerical scheme. Such an effect of the intrinsic discretization of the model explains the brisk variations of the movement of the top of PT alone with respect to SWI(0) and shall be taken into consideration to discriminate between genuine physical behavior and model artifacts.

Effect of sea bottom temperature variability

Although the general trend of the top of PT is decreasing, its up- and down-core movements reflect a real process, due to the temperature variability in time, a feature which affects the top of the PT especially at the beginning of the simulation. Directly after submergence, the top of the PT lies very close to the SWI and is therefore more prone to the effects of the swift changes of the temperature over time

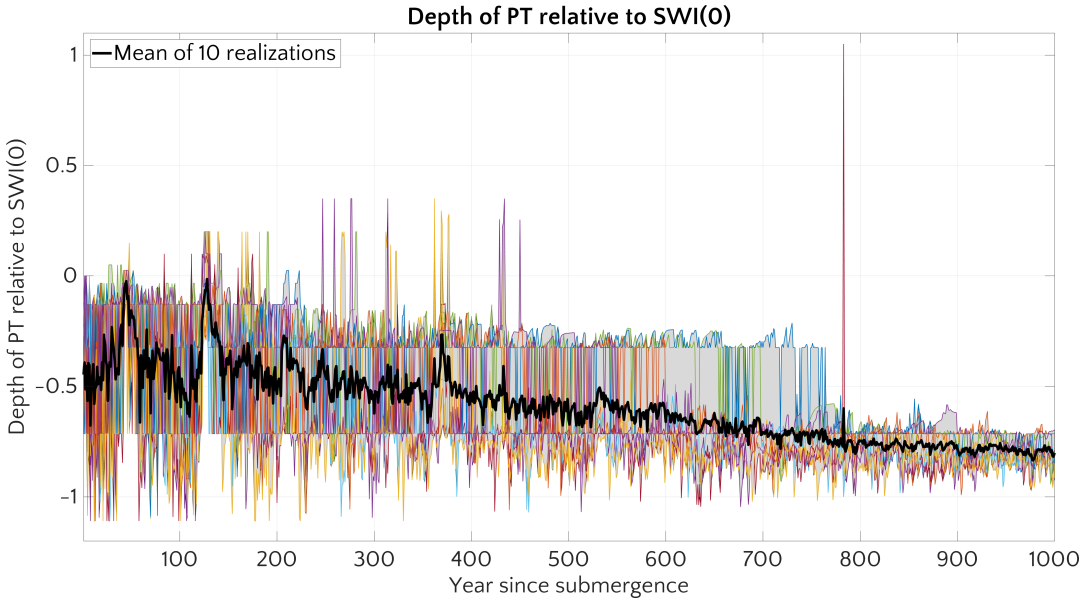

Figure 3.8: The depth to the top of the permafrost table (PT) over time relative to the SWI at the beginning of the simulation (SWI(0)). Each coloured line represent one of the 10 realization of the runs of the set *A*, with a different randomization of the forcing files. The black line represents the average of the 10 runs. This figure shows the overall downcore movement of the top of PT without considering the shift due to sediment accumulation on top. After 1000 years the mean value of the decrease of the top of PT is 0.8 m below the the SWI(0).

and salinity intrusion. Since I determined the top of the PT based on temperature, quick changes in temperatures are able to propagate promptly downwards in the sediments and also affect the position of the top of the PT. It variability, as can be noticed in Fig. 3.8, diminishes with time for two main reasons: i) the deepening of the position of the top boundary of the permafrost to depths less sensitive to the rapid changes happening at the SWI; ii) the penetration of the salinity effect on the freezing temperature which, gradually lowering the T_m as it diffuses downwards, makes the upper layers less prone to freeze back once they have been thawed, even in case of a temperature drop at the SWI.

It is worth noting that the standard deviation reduces from 23 cm to 6 cm over time and therefore while much of the movement at the beginning is affected by this variability, the depth reached at the end is actually a sound result of JSBACH simulations.

Total depth of PT after 1000 years

Bearing these considerations in mind, the final depth of the PT after a millennium of submergence lies at 2.05 ± 0.06 m below the SWI, according to the simulations. Of these 1.23 m are directly due to the sediment accumulation on top of the submerged column.

Linear thawing rate

This result only describes the possible response of the submerged permafrost to the sudden transition from land to subsea conditions in

pre-industrial setting. Although a sudden submergence is idealized, the procedure has been employed in other modeling studies and settings by Portnov et al., 2014; Razumov et al., 2014. From Fig. 3.7 and 3.8 I can infer that the submerged PT responds slowly to the change of the temperature boundary conditions, even though paramount and up to even $17 - 20$ °C (Soloviev et al., 1987; Gavrilov et al., 2003; Nicolsky et al., 2012; Shakhova et al., 2014). The linear deepening of the PT in JSBACH simulations is of ~ 2 mm yr^{-1} while the results from Romanovskii et al., 2005 fall in the range $\sim 6 - 14$ mm yr^{-1}, if the periods of the sea transgression of their simulation are considered as reference. A substantial agreement is therefore met, in spite of the several differences between the models.

Role of accumulating sediments

Based on simulation results, I can also conclude that the sediment accumulation is a process whose importance is not negligible, both in affecting the thermal properties of the permafrost itself and in burying it. On the long scale it contributes to the PT movement in roughly the same order of magnitude as the mere chemical-thermal thawing, which is however the process leading to weakening of the permafrost and eventually to its thawing, with the consequent physical and biogeochemical effects. In some runs, *i.e.* with a specific randomization of the forcing, the thawing in the first two centuries can lead to a PT level well below SWI(0) even down to 1.1 m, the bedrock level. These rapid movements of the top of PT, although temporary, may cause the activation of the frozen carbon stored in the permafrost and therefore play a role in fostering microbial activity.

Analysis of significance of the movement of the SSPF table

In consideration of the spurious effect due to sediment layers, it is worth considering whether the trend is statistically significant for each chunk with a given number of sediment layers. For this purpose I perform a non-parametric Mann-Kendall trend test (at 5% significance) to detect the general tendency of each segment. All the portions show a significant monotonic decreasing trend (with p-value≤ 0.0015) except for the first chunk, before the first layers of extra sediment is added to the model. In this case the movement of top of the PT is not sufficient to justify a statistically significant trend (the null hypothesis of an absence of a trend cannot be rejected with a p-value$= 0.47$). It should be noted that the chunk corresponding to the growth of the sediments from 1 to 5 cm ($9 - 40$ years) is showing a statistically significant increasing trend (p-value$= 0.0013$) instead of decreasing. This behaviour is nevertheless plausible and is due to the combined effect of subzero seabottom water temperatures and the lag behind of salt effect. Salt needs time to penetrate into the (partially frozen) submerged soil where it lowers the freezing point of the pore water. Thus, in the time that salt takes to penetrate deeper, the properties of submerged soil are still more akin to land than to a marine setting. This is particularly true for the thawing temperature which is only slightly affected by salt at first. Such combination of factors

implies that the subzero water temperature at the SWI tend to drive a shallowing instead of a deepening of the PT in the first place. This behavior holds as long as the freezing point depression in deeper sediment is not sufficiently low to enable an overall thawing in spite of the cryotic sea water temperatures, a condition which holds for roughly the first 40 years considering the low salt diffusivity.

Salt causes the thawing

Finally it should be emphasized that salt is the *condicio sine qua non* for the thawing from top of the SSPF. As the Fig. 3.9.*b* clarifies, the mean annual temperature at the SWI is always negative with a minimum value of -1.41 °C and a maximum of -0.23 °C. It is thus only the chemical effect of the freezing point depression due to salt which allows not only the thawing of the first layers but also prevents a general shallowing of top of PT (*i.e.* growth of SSPF). This effect has been also verified by Angelopoulos et al., 2019 in the model CryoGRID2. It turns out therefore that the salinity and its movement into the submerged sediments represent key processes, which cannot be neglected in order to model the physical behaviour of the SSPF.

Salinity dishomogeneities

It should however be stressed that the salinity of some submerged pockets can vary substantially. There are vast areas of nearly fresh water layers in continental shelves that have been submerged for millennia (Post et al., 2013) and which are compatible with a flushing action of fresh groundwater when water table is higher than the sea level in stadial phases (Archer, 2015). Such freshwater aquifers determine the sediment horizons where the cryotic sediment temperature can easily grow ice clogs. The opposite happens in layers where, because of successive freezing/thawing cycles and the consequent brine rejection, salt concentration can be higher than bottom water salinity, from 40 to 65 psu (Overduin et al., 2008) with high ($\sim 100\%$) unfrozen pore water fraction down to a temperature of -10 °C or less (Pollard et al., 1999). This heterogeneity in the salinity of the submerged soil is however not accounted for in JSBACH.

3.3.2.1 *Variation of thawing rate*

Importance of the thawing rate

A quantity which can give extra insight on the thawing mechanism and which is one of the *desiderata* of JSBACH simulations is the thawing rate. It is calculated, for each year, as the difference between the PT (with respect to the fixed reference SWI(0)) and its value of the previous year. Such a variable can serve as an input for a diagenetic-transport model as that quantity which sets the pace at which frozen organic material from below is made available for the microbial activity (see Chapter 4). As other advective quantities, like the sedimentation rate (ω) and the flow velocity (v_{up}), the thawing rate might play a substantial role for the biogeochemistry of the submerged column.

Thawing rate and thawing regime

The thawing rate of the SSPF represents also a key variable defining the thawing regimes, which might change over time (Osterkamp et al.,

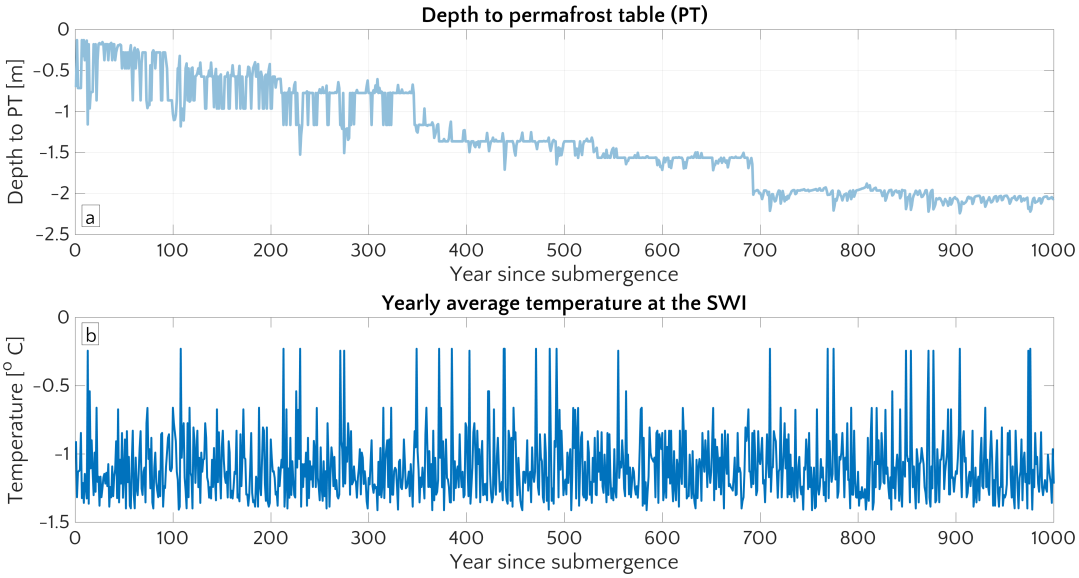

Figure 3.9: *a.* Movement of the top of the PT for run 1 of the set *A*. *b.* Corresponding yearly mean temperature at the SWI, *i.e.* the upper temperature boundary condition.

1989; Portnov et al., 2014) and offer a good variable for comparison between theoretical evaluations and model results.

Slow net thawing

As Fig. 3.10.*a* shows the thawing rate is small (0.8 mm yr^{-1} if sediment accumulation on top is not considered) for a continuous balance between deepening and shallowing of the top of the PT: negative values (*i.e.* effective thawing) are roughly counterbalanced by positive values (*i.e.* re-freezing). This is due to the variability of the boundary conditions and only the slow process of downcore diffusion of the salinity-induced freezing point depression determines the long-term deepening of the top of the PT. The transport of the colligative property, in JSBACH moving at a pace set by the small salt diffusivity, is therefore the real bottle-neck of the thawing process.

Slow thawing is theoretically expected

This goes along the lines of the analytical considerations described in Chapter 2, following Harrison et al., 1978 (Section 2.2.1.3). In spite of the fact that the Eq. 2.26 do not hold strictly for runs in the set *A*, because of the varying boundary conditions and because of the sediment accumulation (which also impacts the thawing with respect to SWI(0), as showed above), I can nevertheless draw some general conclusions on the velocity of the thawing based on discussion of Section 2.2.1.3. In the JSBACH scheme, the freezing temperature of the water at the seabed ($T_f(S_L)$) is set, by definition, equal to the temperature at the seabed (T_L, see Eq. 2.25k). The thawing scale parameter Λ (Eq. 2.26a and Fig.2.8) approaches zero and this means a slow thawing rate in a regime limited by the small value of the salt diffusivity.

Temporal variability of the thawing rate

Because of the change in the order of magnitude of the thawing rate over time, it is instructive to look at its variability in a log-log scale, as displayed in Fig. 3.10.*b*, where the absolute value of the average

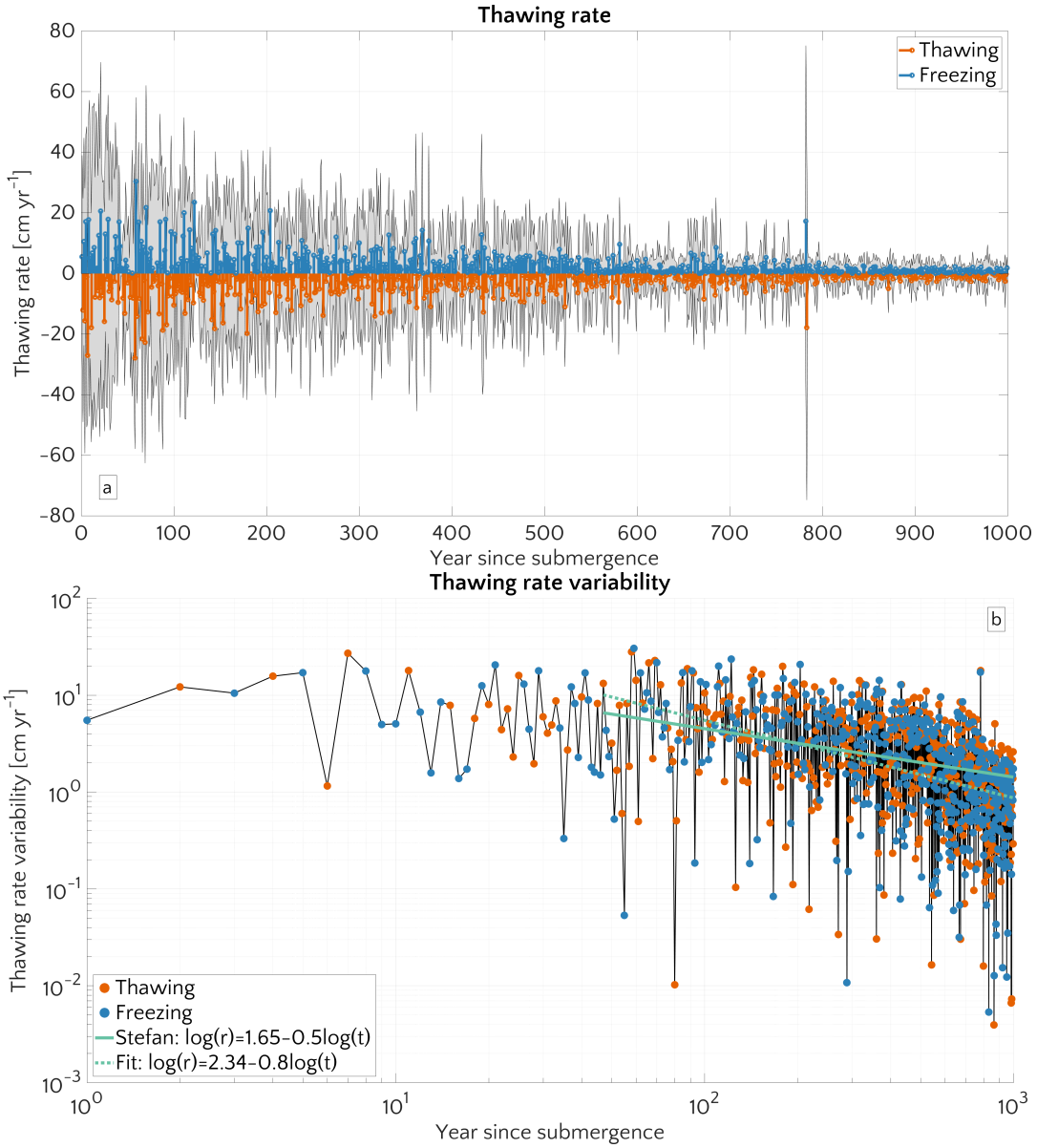

Figure 3.10: *a.* The thawing rate for simulations of the set *A*. The *red* values represent a thawing (*i.e.* a deepening of the PT), *blue* values represent a freezing (*i.e.* a shallowing of the PT) and the grey shading represents the standard deviation. *b.* The variability -*i.e.* absolute value- of the mean value of the thawing rate in a log-log scale. For the values after 40 years the *Stefan* fit (*i.e.* power law of $-1/2$) is reported (solid line) together with a best fit with power law of -0.8 (dotted line).

thawing rate is reported. Red dots indicate actual thawing while blue dots indicate a freezing. As already mentioned in Section 3.3.2, in the first 40 years the movement of the top of PT is indeed an upward movement with a net freezing process going on. This happens with jerks of the top of the PT, whose position varies of about 20 cm yr^{-1} in the first 10 years of simulations. The rate (of thawing as well freezing) lines up in the first 40 years on a level of about 8.5 cm yr^{-1}, which

is a considerably fast rate. After this first phase the absolute value of the thawing/freezing rate decreases, as well as its uncertainty among the different realizations. A fit (at the first order in the log-log) shows that the decrease of the absolute value of the thawing follows a power law $\sim 1/t^{0.8}$, with t: time. For comparison the theoretical decrease of thawing rate ($\sim 1/\sqrt{t}$) according to a merely thawing system that follows Stefan's law, as described in Chapter 2, is reported. A direct analogy is not possible, because of the alternating movement of the top of the PT, but it shows anyhow that the decrease in the rate of movement of the PT follows also a power law and it is slightly faster than a Stefan law with a change that is ± 0.9 cm yr^{-1} at the end of the simulation.

Comparison of modeled and measured thawing rates

Such values (at least for thawing) are comparable with the few measurements and model results available for the thawing rate of the SSPF. Overduin et al., 2008 showed that after a time span of a millennium, the thawing rate of the SSPF in Western Laptev sea is < 1 cm yr^{-1}. Geoelectric methods (Overduin et al., 2016) infer a thawing rate up to 40 cm yr^{-1} for 60 years after the submersion while JSBACH thawing rates are of the order of $\sim$ dm yr^{-1} for the first $40 - 50$ years of simulation. Interestingly, the trend of the absolute value of the thawing follows the same power law which is found for the thawing rates of Overduin et al., 2016 (see Fig. 2.13.*a*).

However a comparison of the results of idealized scenarios, when only thawing occurs, can be more compelling (see Section 3.3.5.1) and give more indications of the possible shift in thawing regimes.

3.3.3 *Temperature state and ice content*

The evolution of the thermal state of the SSPF gives indications of the thawing, the time response of the SSPF and the weakening of mechanical strength of the sediments, forasmuch as temperature is correlated with the ice content.

Temporal evolution of temperature depth profile

The Fig. 3.11.*a* shows that the submersion acts as a buffer capable of modifying the overall temperatures at a relatively quick rate, with an increase of about 11 °C at a depth of 20 m in $\sim$ 150 years. Once the temperature is higher than the threshold of -3 °C and more homogeneous throughout the thickness of the sediment column, the warming rate decreases as a consequence of the decrease of the temperature gradient. This leads to an almost zero-gradient temperature which is the main feature of the SSPF response to the change of the upper boundary conditions.

The contour line corresponding to higher temperatures in the upper parts of the soil appears to be more wiggly (Fig. 3.11) than the ones deeper in the soil and identifying colder temperatures. Such behavior is mainly due to the higher variability of the upper boundary

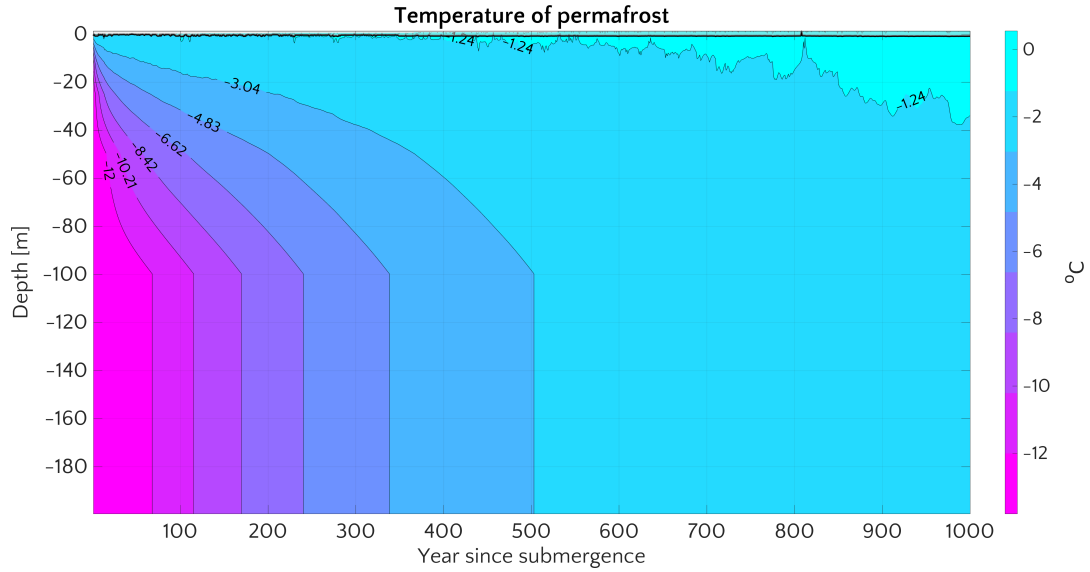

(a) Temperature profile in September for simulation 1 of the set *A*.

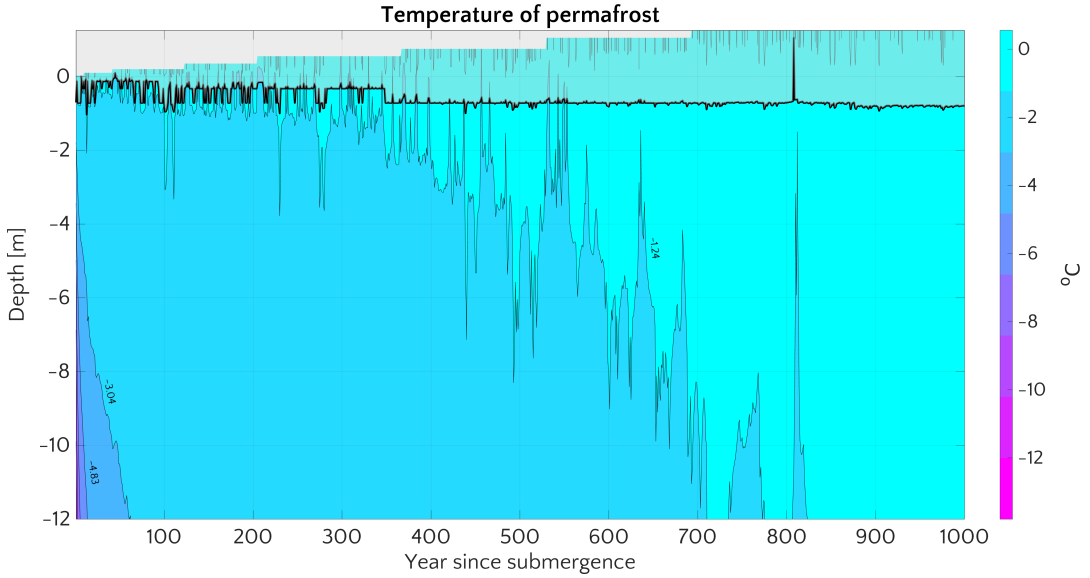

(b) Upper temperature profile in September for simulation 1 of the set *A*.

Figure 3.11: The evolution of September temperature profile for simulation 1 of the set *A*. The black line represents the top of the SSPF table while the area shaded in gray represents average thawed portion.

conditions over a limited range of values close to each other, highly affecting the top layers of the sediment column.

In spite of the relevant increase of almost 14 °C in 1000 years, sediment temperature nevertheless remains below the thawing temperature for the largest portion of sediments. This condition is true for all the other runs of the set *A*, as for instance Fig. B.1.*a*-*b* shows.

14 °C increase in 1000 years

The trend in temperature reflects in the corresponding temporal evolution of the ice content. Fig. 3.12.*b* shows the temporal evolution of September ice content for the same run whose temperature is dis-

played in Fig. 3.11. I chose values of September as they are expected to be the minimum values within the year and therefore to represent the point in time when the SSPF is the least cemented. Ice concentration is high up to 60% right after the submersion for roughly a century. In the upper part, salt penetration and thawing cause the complete melting of the September ice content and a decrease down to 25% of lower layers in about 100 years. This quantity further decreases to 10% showing an alternating behavior where ice-less years are followed by new ice formations. Ice finally completely disappears once that the SSPF table corresponds to the bedrock level. The range of ice content from 60% to 0% is in agreement with the values found by direct measurements (Osterkamp et al., 1989; Overduin et al., 2008), geophysical methods (Brothers et al., 2012; Brothers et al., 2016) and model results (Angelopoulos et al., 2019).

Connection between ice content and temperature evolution

A comparison of the residual September ice (Fig. 3.12.*b*) with the movement of the PT (Fig. 3.9.*a*) shows that the ice is present in proximity of the PT itself (also above) and goes down to the level of the bedrock. The presence of ice above the line that the defines the top of the PT is only partially an artifact of the discretization of the model[16]. It indeed means that the deepest thawing not necessarily occur in September and that seasonal re-freezing tends to start from the bottom of the seasonally thawed layer rather than from the top. This is especially true after a century from the submergence, when ice is roughly the half of the initial value and the downward degradation of the SSPF is deep enough such that the effect of the colder temperature of the layers which are still frozen overcomes the effect of the seasonal cooling coming from the sea floor.

Seasonal refreezing starts from the bottom

Fig. 3.12.*b* shows that ice lenses can form in the accumulated sediments and linger there for some years $(5 - 10)$ before disappearing and they can be highly concentrated in ice ($\sim$60%). The presence of a layer of ice, overlaying an ice-less level, overlaying in turn ice can hints at a seasonal talik (see Section 3.3.4).

Formation of ice lenses

A comparison between Fig. 3.12.*b* and the corresponding temperature trend in Fig. 3.11.*b* shows the effect of presence of ice on temperatures: as long as the ice is present in large quantities (with cores $> 25\%$) temperatures do not increase and, until $\sim$ 350 years after the submersion, the contour corresponding to the -1.24 °C wavers at about the same depth of the ice. Afterwards, the ice in the sediments decreases and temperature evolution shows an increase which is even faster once the ice is completely melted, which occurs about 600 years after the submersion. Such a behavior is due to the latent heat needed to melt away the pore ice. It is a sort of prolonged SSPF "zero-curtain effect" (Kelley et al., 1969), spread on many years: only when the ice

Extended SSPF "zero-curtain" effect

16 The top of the SSPF table is defined via an interpolation procedure and therefore it can also lie in between the centers of the layers defined in the model, while the evolution of September ice is a contour plot based on the ice content at the center of each layer, which is linearly interpolated for graphical reasons.

content of the pore space is very small, the temperature of the sediment can increase. The correlation of temperature with presence of ice is also detectable considering the times when ice lenses form in the accumulated sediments (at about 750 years and after 800 years from the submersion), points in time which are characterized by an upward movement of the colder temperature.

General validity of the results

Aforementioned results are not only specific of a certain run of the set *A* but are general, as for instance shown in Fig. B.1.*c*.

Evolution of the ice content

Fig. 3.12.*a* shows how the yearly average of the vertically integrated ice changes over time for the simulations of the set *A*. The relatively small value (14%) already at the beginning of the simulation, right after the submersion, is due to the fact the that these are values integrated along the entire height of the sediment column and the ratio is given to the pore space along the height of the column itself.

The ice content drops quickly by 6% in the first $\sim$ 15 years after the submersion, a period which corresponds to a thinning of the ice from below and from above, followed by the formation of ice in the upper sediments and a decrease of the concentration in the lowest part, the one in touch with the bedrock (see Fig. 3.12.*b* and B.1.*c*). This unexpected tapering from below might be related to a feature of the internal temperature gradient: ice formation in the upper part releases latent heat which determines a local increase in temperature which causes in turn a partial melting of the ice in the layers beneath.

Successive general ice decrease occurs much more slowly and it takes about 680 years for a further reduction of 4%. The lack of ice and the low temperature gradients are responsible for the slow response in time. It is worth stressing that the final value of overall 4% of ice content is not surprising since the quantity reported is the yearly mean of the integrated ice content, which is still present in winter months.

Temporal response of the SSPF

The sudden submersion implemented in JSBACH simulation enables the definition of a time response of the SSPF to the change of the boundary conditions after sea transgression. A clear definition of the temporal response is missing and a direct comparison with results of other models is not straightforward because of different boundary conditions, spin-up, inundation scheme, sedimentation scheme and resolution. However, in consideration of the climatic interest of the current research, a reasonable time scale can be defined as the moment after the submersion when the upper part of the sediment is significantly affected. Only the top sediments can play a significant climatic feedback role and can be influenced in turn by the modification of sea water temperatures on centennial time scales.

Time response is about 1000 yr

With this in mind, a comparison of Fig. 3.11.*a* and B.1.*a* hows clearly that, even at the end of simulation (after 1000 years), most of the sediments are well below the thawing temperature. Taking the limit of 40 m as a reference depth level to assess the change of temperature, the

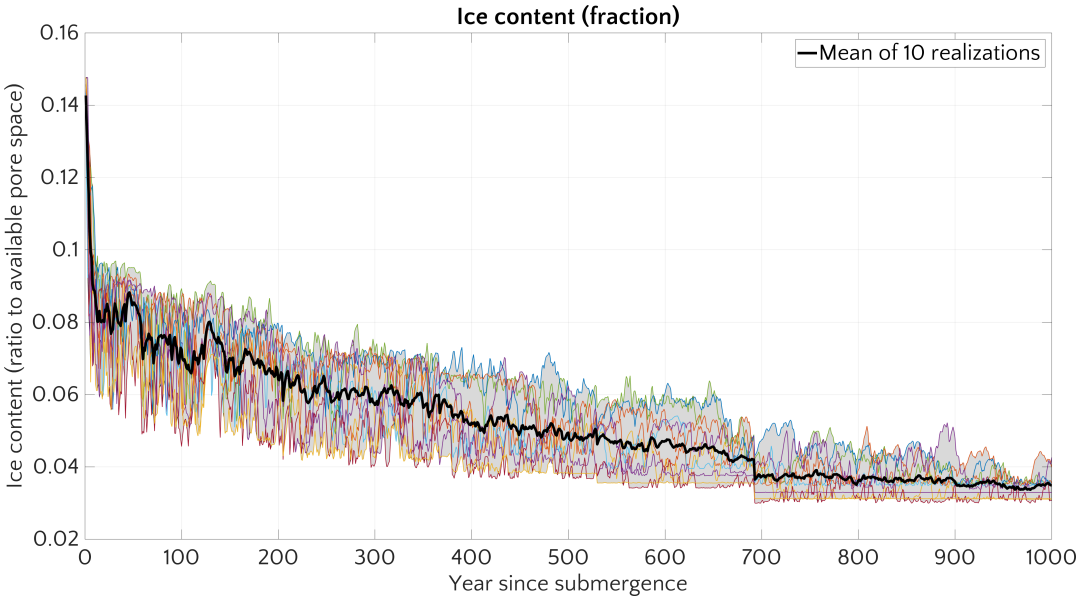

(a) Time average of integrated vertical ice content as fraction of the integrated pore space. Each coloured line represents one of the 10 realizations of the run of the set *A*, with a different randomization of the forcing files. The black line represents the average of the 10 runs. The sharp jump at 692 years is an artifact of the sudden increase of the number of sediment layers, with the adding of the thickest last sediment layer of 40 cm.

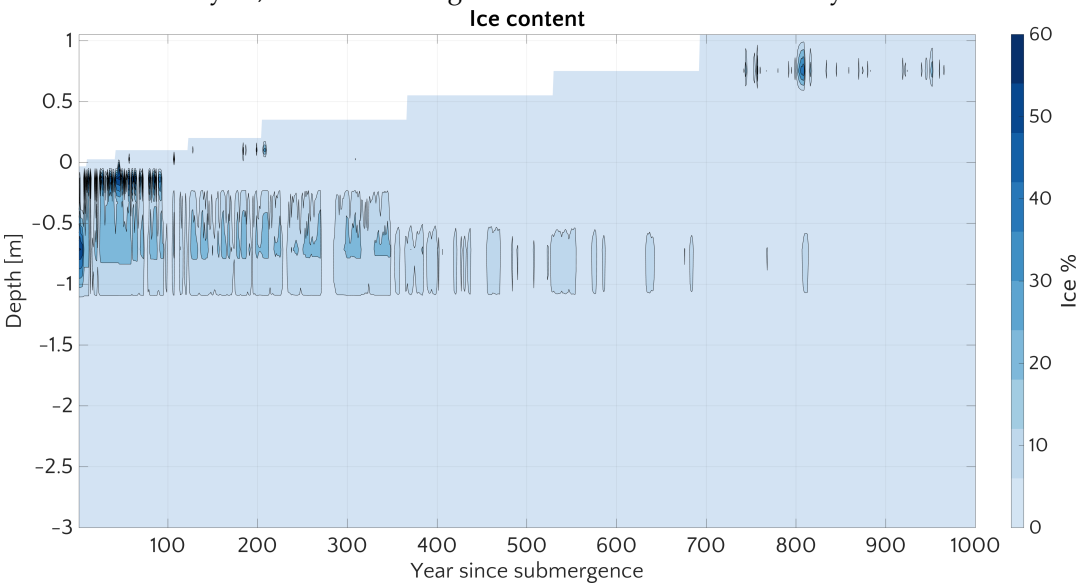

(b) Evolution of September ice content (in percentage of the pore space) for simulation 1 of the set *A*. Only the upper part of the sediments is shown, where ice can form. Bedrock lies at 1.11 m from the SWI(0).

Figure 3.12: Ice content time evolution for set *A*

temperature exceeds -1.5 °C[17] only after about $900 - 950$ years from

17 I can roughly assume that a major destabilization of the SSPF and a reduction of its ice content occurs above this temperature

the submersion, which is the same time when ice content stabilizes at its lowest level (as Fig. 3.12 and Fig. B.1.*c* suggest).

This same time scale is also suggested by considering when the top of the SSPF table reaches the bedrock level (Fig. 3.7). It is at this time that the carbon pool available in JSBACH is completely released and the lack of cementing ice weakens the structure of the sediments.

Agreement of time response with previous estimations

The slow response of the PT (see Section 3.3.2) is in agreement with the few quantitative studies on SSPF time response, such as Romanovskii et al., 2005 and Malakhova et al., 2017, both indicating that the lag in submarine permafrost response to perturbation of temperature boundary conditions is at least of the order of 7 kyr (Romanovskii et al., 2005) or even 10 kyr (Malakhova et al., 2017).

It is however reasonable assuming that with a different geological structure of JSBACH layering, ice could have also formed deeper in the sediments. This would have implied a longer time needed for its complete melting but also a concomitant deepening of the PT (this will be discussed in more detail in Sec 3.3.5.1).

3.3.3.1 *Comparison with CryoGRID2 simulations (Angelopoulos, 2019)*

Answering Q3.2

The simulation of SSPF thawing performed with CryoGRID2 (Angelopoulos et al., 2019) represents the first and only modeling study of a SSPF settings where salinity is dynamically included in the model. It offers thus the natural point of comparison with JSBACH modeling (see Table 3.1). The most suitable runs in Angelopoulos et al., 2019 to be compared with JSBACH outcomes is the "scenario C", which simulates the SSPF evolution under current typical Arctic water conditions (average temperature -0.7 °C) in a 4.6 m water depth setting.

CryoGRID2 as term of reference

Table 3.1: Differences between JSBACH and CryoGRID2 (Angelopoulos et al., 2019)

Model	Explicit salt diffusion into the sediments	Freezing temperature and salinity	Upper boundary conditions
JSBACH	No (heuristic)	Uncoupled	Monthly varying (set *A*)/ constant at −0.7 °C (set *D*)
CryoGRID2 ("scenario C")	Yes	Coupled	Varying (average −0.7 °C)

General agreement of the temperature range

The temperatures at the end of JSBACH simulations of the set *A* fall in the range [−1.38 °C,−0.8 °C] (Fig. 3.11 for an example) and are well comparable with the outcomes of the simulations by Angelopoulos et al., 2019, in the range [−1.8 °C,−0.8 °C] (Fig. 3.13). The difference of the lower limit is very likely due to the difference in the forcing temperatures and to the minimum seawater temperature possible in MPI-OM. Although a direct comparison of time dynamics is not immediate (Angelopoulos et al., 2019 show the temperature and ice profiles in April and not in September), it is apparent that the response in time

Slower JSBACH dynamics

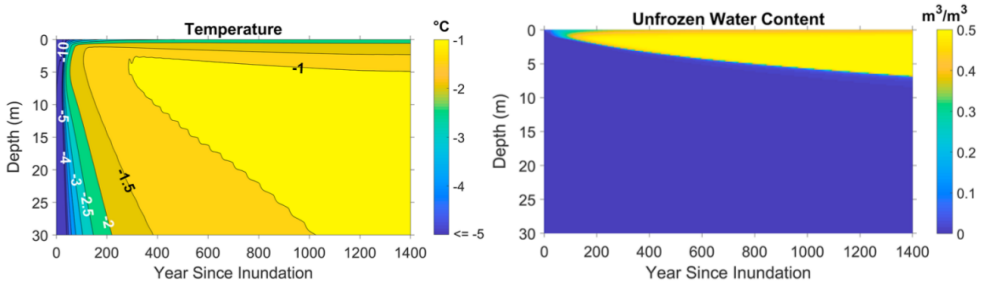

(a) Evolution of temperature at the end of April.

(b) Evolution of unfrozen water (ratio to bulk volume) at the end of April. Average porosity: 0.5.

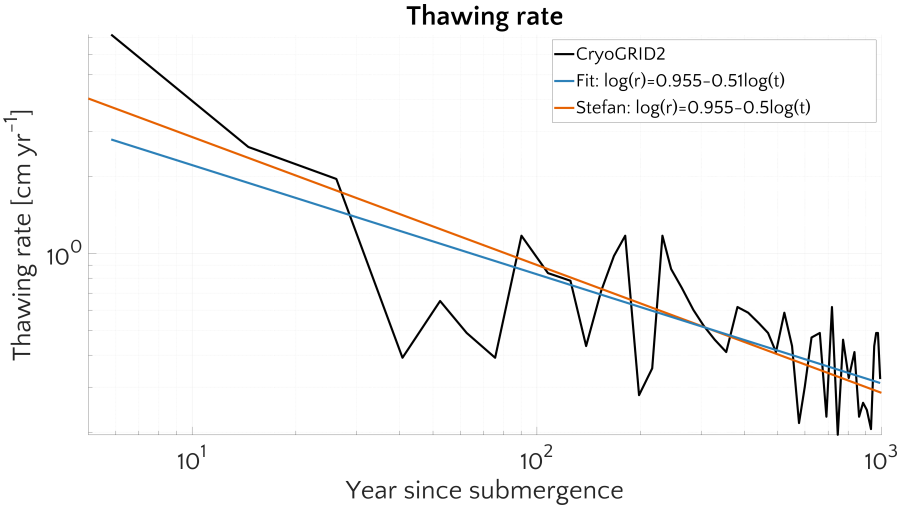

(c) Thawing rate. A linear (blue) and Stefan's (red) fit are also plotted.

Figure 3.13: From simulation of "scenario C" (typical Arctic seawater conditions) by Angelopoulos et al., 2019

of JSBACH is much slower: the complete ice melting down to 1.11 m (the bedrock) happens in more than 800 years in JSBACH, while the thawing to the same depth occurs in about 107 years in simulations with CryoGRID2 and reaches 5.75 m in 1000 years.

However both exhibit the presence of ice formation in the vicinity of the SWI. But while it never exceeds about the 20% of pore space (Angelopoulos et al., 2019), in my case it can also reach saturation state (see Fig. B.1.*c*).

Comparison of the thawing rates

Finally the evaluation of the thawing rate (Fig. 3.13.*c*) shows that CryoGRID2 follows a Stefan's rate. For JSBACH outcomes, as shown by Fig. 3.10, the alternating freezing and thawing hampers a comparison with a theoretical model. The thawing rate at the end of the simulation is, however, 0.9 cm yr^{-1}. Quantitatively it is of the same order of magnitude as the average thawing of "scenario C" in CryoGRID2 (0.8 cm yr^{-1}) and even higher than the thawing at the end of the simulation after 1400 years ($1 - 2$ mm yr^{-1}). However this agreement does not account for the freezing rate and net movement of the PT.

3.3.3.2 *Comparison with boreholes in the Laptev Sea*

Answering Q3.2

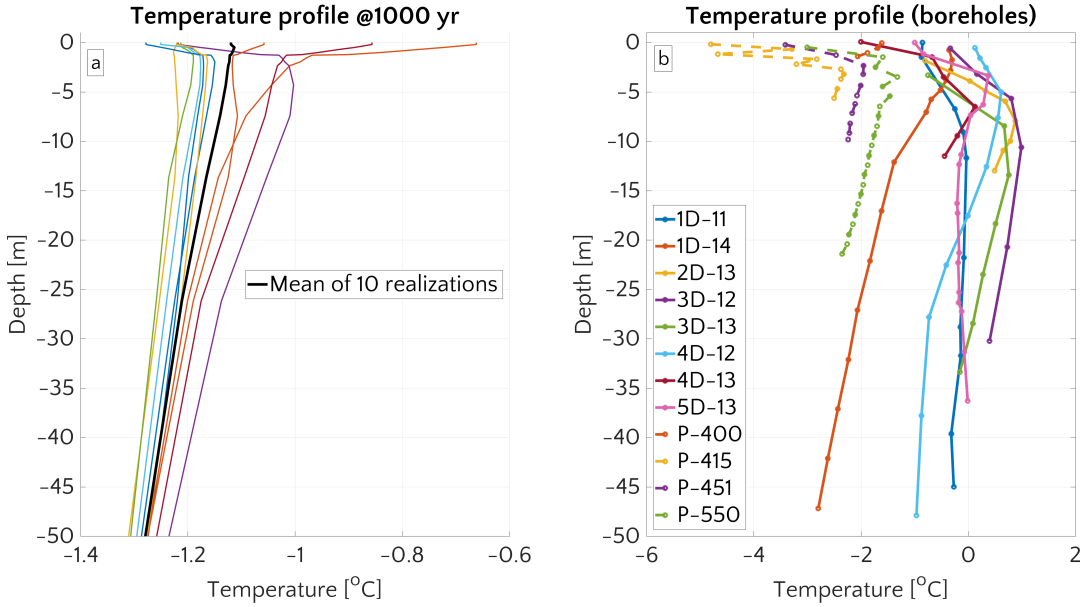

Figure 3.14: *a.* Vertical temperature profile of yearly average for each member of simulation the set *A* (coloured lines) and their mean value (black line). *b.* Vertical temperature profiles of boreholes measurements available. Continuous lines are from Shakhova et al., 2017 and references there in. The boreholes were drilled in the Bour Khaya Bay in the Laptev sea. Distance of the boreholes from the coast varies from less than 1 km to 3 km and water depth from 2.5 m to 3.4 m. Dashed lines are the average values (May and November) of the measurements done in the Prudhoe Bay (Alaska) on the Beaufort Shelf and reported in Osterkamp et al., 1989. The numbers in the names of the boreholes stand for offshore distance and water depth is less than 2.4 m.

Caveats about comparisons between modeled and measured SSPF profiles

As previously stated, JSBACH simulations are not designed to reproduce the current SSPF state: the model is not spun up to reproduce thick geological permafrost (down to $800 - 1000$ m) at the end of the Pleistocene, when the sea transgression happened. Nor have I employed forcing files derived from historical runs of the Holocene sea bottom water temperature, nor considered the gradual increase of the sea level to eustatic changes and coastal erosion. On the contrary, I force the model with pre-industrial conditions with the aim of identifying the processes and the characteristics of the thawing of submerged permafrost. For this very same reason a comparison between JSBACH temperature output at the end of the simulations and vertical temperature profiles of boreholes must not be taken as a strict model validation test but simply as a useful tool to identify the overall behaviour of the simulated SSPF with respect to local results and to quantify how model shortcomings might affect the outputs.

Fig. 3.14.*b* shows the temperatures profile from the Laptev Sea area (continuous lines) and from the Beaufort Sea (dashed lines). Keeping in mind spatial and temporal variability, I note that the boreholes in

the Beaufort Shelf are consistently colder than the ones in Buor Khaya Bay (maybe because of the warm influence of the large Lena River).

Modeling results reproduce gentle gradient well

It is nevertheless remarkable that the temperature of the sediments varies on a narrow temperature intervals: 3.4 °C for the Beaufort boreholes and 3.8 °C for the Laptev boreholes. The Siberian drills are also especially close to the threshold of 0 °C with a considerable numbers of profiles whose deep layers actually lie above it. This characteristic is a sign of unconsolidated sediments or a permafrost weakly bound and mechanically loose. The results of JSBACH simulations are able to reproduce the gentle gradient (on a temperature span of 0.7 °C) with comparatively high temperatures. Such a distinguishing feature is even clearer in Fig. 3.15, where the almost vertical (namely almost zero-gradient) temperature profile at the end of the simulation well matches the temperature profile of the borehole C2 reported in Rachold et al., 2007 and Overduin et al., 2008. Since it is the furthest of the boreholes drilled offshore Cape Mamontov Klyk (Laptev Sea), it is the one submerged earlier. It had more time to equilibrate and this explains its almost zero-gradient temperature profile, as well as the vicinity of its temperature to the freezing point.

Good agreement with older profiles

Heat conduction is probably the main heat transfer mechanism

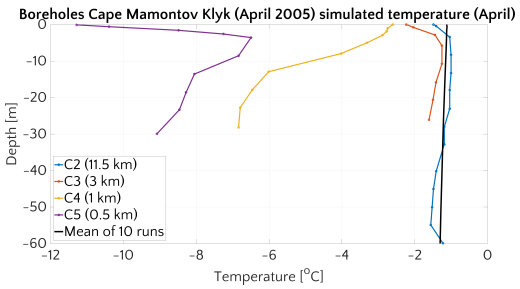

Figure 3.15: Vertical temperature profiles. Mean for April of the 10 members of the set *A* after 1000 years simulation (black line), and temperature profiles of the boreholes close to Cape Mamontov Klyk, in the Western portion of the Laptev Sea, and reported in Rachold et al., 2007 (measurements taken at the end of April 2005). The distance in parenthesis indicates the offshore distance of the boreholes and water depth goes from 1.5 m (for C5) to 6 m (for C2).

The linear vertical trend of the measurements for C2 and its compatibility with the results of diffusive heat equation (the only heat transfer considered in JSBACH) suggests therefore that, for the SSPF, the conductive heat transfer is indeed the main mode of transport of the heat at large scales and once the broad picture is considered - namely after a full submergence has happened and the sediments have had enough time to equilibrate. This rules out instead the role that a convective heat transport (mediated by an interstitial water flow) might have and suggests that it is absent or, if present, not relevant for the determination of the thermal state of the submerged sediments.

Fast-bottom sea ice is neglected in JSBACH

The profile C5 (Fig. 3.15), with its very low temperature (−11.3 °C) at the top of the sediments can be solely explained with the effect of fast-bottom sea ice. It connects the top of the sediments to the at-

mosphere, allowing the cold air temperatures to penetrate down to the submerged sediments, delaying *de facto* the effects of the submersion of the sediments and the water, that acts as a temperature buffer. Such an effect is however not considered in JSBACH: it would be complicated to model and, moreover, it is only temporary and comes to an end when the water depth is high enough to prevent fast ice to form (water depth $> 2 - 3$ m) (Bogorodskii et al., 2018).

Four boreholes in the Dmitri Laptev Strait (Soloviev et al., 1987) present frozen layers with even higher temperatures: between -0.5 °C and -0.3 °C, down to 40 m depth. These values in the upper end of the temperature range are still in agreement with JSBACH simulations.

Measurements hint at higher salinity

Temperatures that are colder than the equilibrium temperatures corresponding to the standard salinity of 30 psu have been detected at the top of the SSPF table. Osterkamp et al., 1989 measured a nearly constant temperature of -2.41 °C, a value in equilibrium with water with a salinity of 43.5 psu. Such a high concentration is explained with salt movements and consecutive concentration cycles, which occur when sea-ice does not freeze to the SWI and a layer of unfrozen water is preserved between the bottom of the ice cover and the SWI. In this condition, under-ice circulation is weak and, at the moment of sea ice formation, salt is rejected to water below. This allows the water to be in phase equilibrium with colder sea ice but still remain unfrozen. In such a situation, the top of the sediments can freeze but the downward propagation of salt is also enhanced. This effect is neglected in JSBACH as well, mainly due to the fact that in MPI-OM water temperature and salinity are not connected to each other.

3.3.4 *Taliks*

Answering Q3.4

Definition of taliks

One of the striking successes of the model has been its capability, in spite of its large scale and broad assumptions, to reproduce taliks, at least qualitatively. Taliks are one of the most interesting features in permafrost environments as they can be determined by a variety of reasons (anomalies in thermal, hydrological, hydrogeological, or hydrochemical state, Van Everdingen, 1985; Everdingen et al., 1998) and are particularly important where infrastructures (both on- and off-shore) are located, since they alter the mechanical properties of the permafrost. Although a unique definition is missing, taliks are defined on basis of frozen/unfrozen condition and not on a thermal criterion, and so they can be (Zhang, 2011):

- Noncryotic: with temperatures > 0 °C
- Cryotic: with temperatures < 0 °C and therefore formally belonging to permafrost.

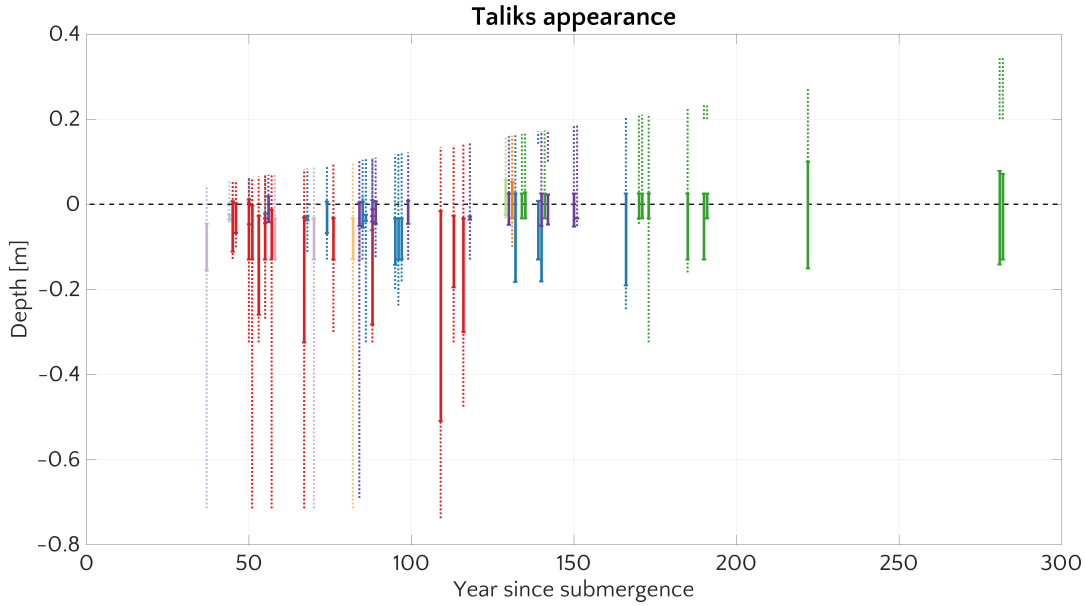

Figure 3.16: Modeled taliks in the simulations of the set *A*. Each color reports the results of a specific simulation. 9 out of 10 runs simulate talik formation. Solid lines represent the thickness of the talik while dotted lines represent the maximum extent of the active layer. Years with no lines correspond to years where no closed talik could be detected. Dashed horizontal black line represents the level of SWI(0).

According to the structures, they can be open, through and closed. Given the 1-point version of JSBACH that I use, the only taliks that can be modeled are closed taliks or through-taliks.

A copious permafrost literature is dedicated to taliks and, surprisingly, also many of the rare papers focused on the SSPF treat them, since there is no general consensus about some of the mechanisms behind their formation (Shakhova et al., 2017).

Modeled taliks

Fig. 3.16 displays the taliks reproduced by JSBACH during the simulations of the set *A*. Given the setup of the model, I identified solely the closed taliks, defined by the layers which remain thawed throughout the year and are enclosed between two frozen layers at least in winter. The dashed lines represent the maximum depth of the thawing from the SWI, which defines the top of the SSPF table previously analyzed.

JSBACH models salinity-induced taliks

The development of closed taliks clusters in the first 200 years and does not appear approximately year 40 of the simulations. This timing can be explained by the deepening of the top of the SSPF table and the freezing/thawing of active layer. In the first years after submergence, thawing from the SWI occurs (even down to 1 m, as Fig. 3.7 shows) but it is only a seasonal process. Over time, salt penetrates into the SL and saline sediments accumulate on top, allowing the conditions for formation of taliks to develop. Indeed seawater temperature may seasonally sink below the freezing temperature of the first layer(s) of sediments, causing them to freeze. Simultaneously the

temperature of lower sediments, which is already affected by salinity, is higher than or equal to the corresponding freezing temperature. When this occurs, a closed talik forms. Qualitatively this is the same salinity-induced talik described by Osterkamp et al., 1989 and arising in the model of Nicolsky et al., 2010. JSBACH can simulate such a situation only when salinity has affected a minimum numbers of layers: the layer corresponding to the SWI is by definition thawed, then at least the second one (from the top) must freeze and the third one has to be kept unfrozen due to the freezing point depression.

JSBACH models taliks in the first 200 *years*

The upper time limit for talik formation is about 200 years (there are only three later occurrences in the set A). This upper limit arises due to the combination of an increasingly deeper influence of the freezing point depression in the lower sediments and an increasingly thicker width of the thawed layers. This latter fact increases in fact thermal inertia as well as the time that the freezing point depression needs to propagate downwards. Considering that the freezing point of accumulated sediments is already rather low (since they are saline), prolongated freezing of the upper layers happens with decreasing frequency. Then a point is reached when the seasonal freezing merely occurs in correspondence with the SSPF table and no longer affects the upper layers, preventing closed taliks from forming.

Given the dynamics of the propagation of the freezing point depression, a multiple "wafer-like" structure, as modeled by Nicolsky et al., 2010 with layers of different saline sediments, is not possible in JSBACH.

Possible sensitivity to layering

Finally it is nevertheless expected that a finer layering might contribute to taliks forming for a longer period after submergence: the width of deeper layers is the factor that slows down the update of the freezing point (as described in Section 3.2.2.2) while a higher resolution would cause layers to update their freezing temperature more quickly and this would imply that more levels meet the conditions for taliks for a longer period.

As one member of the ensemble shows (the one reported in dark green in Fig. 3.16) it can also happen that features like cryopegs (layer of hypersaline brines) form. In the JSBACH case, hypersaline translates just into a layer with lower freezing point depression, which means that the talik is not just a portion of the active layer, but lies below it.

Modeled structures agree with observation. Sizes do not

Although the explanation behind these formations is the same invoked for measured active layers and taliks (Osterkamp et al., 1989) and simulations of this phenomenon (Nicolsky et al., 2010), the size and temporal evolution is different. The thickest talik modeled by JSBACH is 49 cm, much smaller than the ones simulated by Nicolsky et al., 2010 ($\sim$ 100 m). This could be explained by the fact that they start the simulations with prescribed alternate layers of salty sediments and fresh ice-complexes in the order of ten meters (15-30 m) instead

of starting "ab initio" as in my case, and this necessarily alters the outcome of the simulations.

Taliks are qualitatively reproduced

My results compare better with the boreholes studied by Osterkamp et al., 1989 or Rachold et al., 2007. They measured an active layer $0.2 - 1.4$ m thick, not far from the active layers I report. One of their samples is described as a closed talik "wafer-like" structure showing frozen sediments down to $0.2 - 0.3$ m, then unfrozen till 1.3 m and then frozen again beneath, with a talik of roughly 1 m. Although the size is roughly the double of the thickest talik simulated by JSBACH, the order of magnitude is the same. Discrepancies might also be due to the different temperature detected by Osterkamp et al., 1989 (down to -4.03 °C), which is in phase equilibrium with a much more saline seawater (64.8 psu).

The disappearance of closed taliks evolving into thawed PF is in rough agreement with measurements from the Prudhoe Bay (Osterkamp et al., 1989) which see a decrease of seasonally frozen active layer for the furthest borehole drilled or, invoking a "space-for-time" substitution, the one submerged for the longest period. But this is in strong disagreement with taliks simulations by Nicolsky et al., 2010, in which the taliks thicken over time, perhaps again due to different simulation setups at initiation.

Answering Q3.1 and Q3.4

3.3.4.1 *Seasonal cycle*

Fig. 3.17 shows how a talik (as described above) evolves seasonally. The temperature and ice profiles for simulation 5 of set *A* at year 110 after submersion is chosen as an example because it corresponds to the largest talik that JSBACH has modeled, although the dynamic is the same for all the other taliks.

Seasonal evolution of a talik

Fig. 3.17.*a* shows that the uppermost level, in contact with the sea water, is by definition always thawed. Colder winter temperatures of January (-1.49 °C) start penetrating into the sediments but the drop in temperature is slowed by the lag of the influence of slightly warmer waters of the previous December (-1.29 °C), which caused a thawed layer at the beginning of the year. Once temperatures go below the freezing point, an ice lens forms. Fig. 3.17.*b* shows that it lingers in the sediments till late July with an ice-content , of up to 60%, thence cementing and stabilizing a layer of frozen sediments about 10 cm thick. Underneath this layer, the sediments remain above the freezing temperatures, affected by temperatures of lower layers - the legacy of previous months. This condition gives rise to the talik. The frozen ice cap of the winter-spring months thaws in mid-late summer: a lag that is due to time that heat needs to reach the sea floor (with sea bottom temperature reaching its year maximum, -0.58 °C, only in August) and by the seasonal "zero-curtain effect".

Comparison with seasonal dynamics in CryoGRID2

The summer temperature wave propagates down for about 80 cm and thaws extra frozen layers, determining the depth of the top of

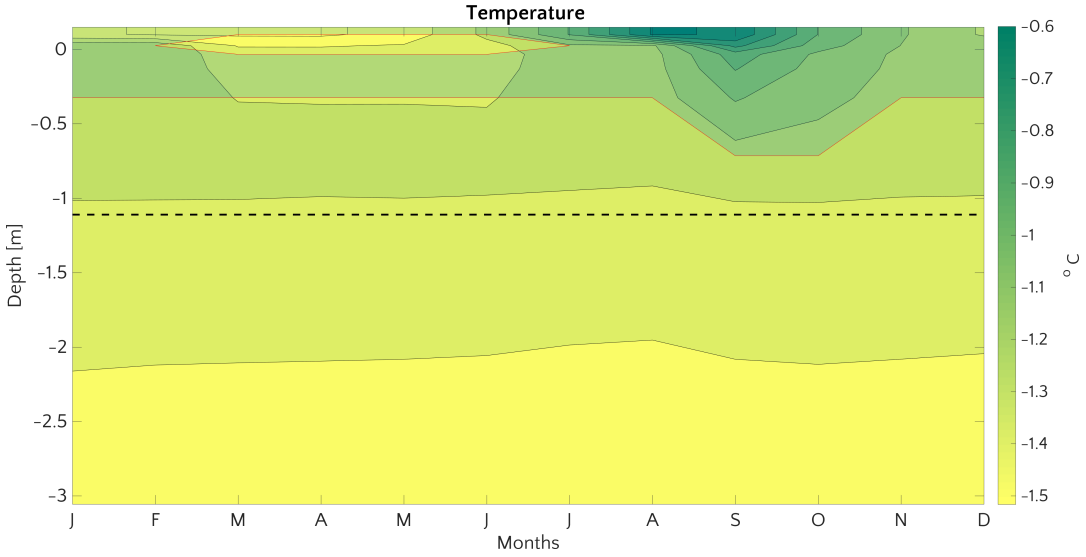

(a) The black dotted line represents the bedrock level and the blue shaded area represents the thawed levels. The uppermost layer, which is always thawed, is in contact with the seafloor. An ice-lens is present from February till July and defines the closed talik.

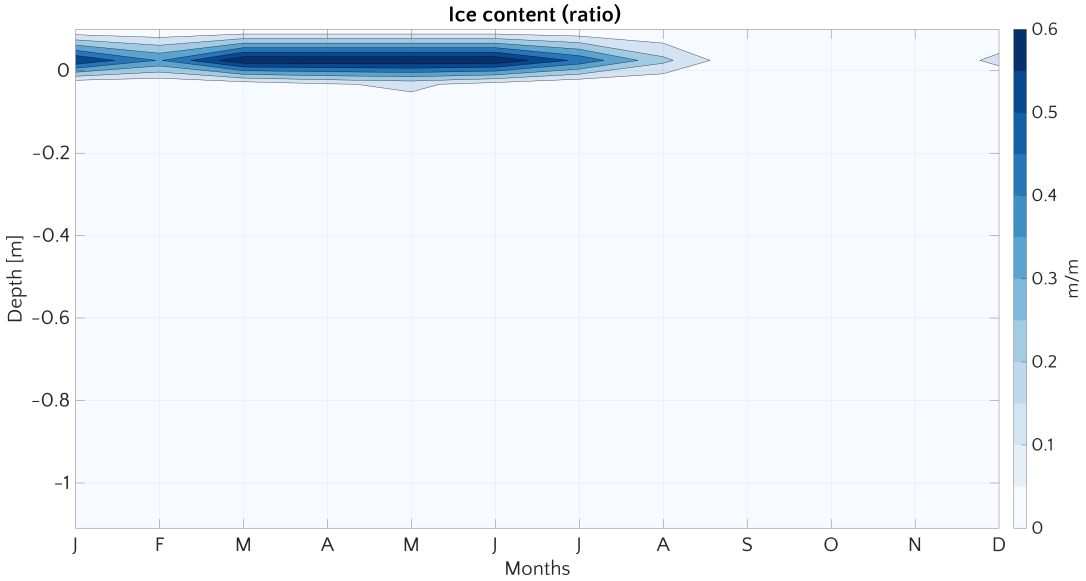

(b) The depth is reported down to the bedrock level.

Figure 3.17: Seasonal temperature (*a*) and ice (*b*) changes for simulation 5 of the set *A* for year 110 after inundation.

the SSPF table over the year. The seasonal dynamics resembles what has been modeled by Angelopoulos et al., 2019, although the size scale are different: the thawed portion in Angelopoulos et al., 2019 are larger (on the order of $1-2$ meters), but this difference can be ascribed to the geological constraints of JSBACH and to the differences in forcing used by CryoGRID2 (with summer sea water as warm as 7 °C). The ice content of the seasonal ice lenses simulated by JSBACH is

also in agreement with results by Angelopoulos et al., 2019, although the shape is different, as expected.

Therefore, the seasonal cycle and the ensuing thawing/freezing condition of the sediments appears to be influenced by two main factors: the ice and temperature state resulting from the previous year and the lag in time due to the typical time scale of heat transport in frozen soils.

Answering Q3.1, Q3.2, Q3.3 and Q3.5

3.3.5 *Exploring JSBACH sensitivity to bottom water temperature, phase change temperature, geothermal heat flux and temporal trend*

3.3.5.1 *Idealized experiments. How close to Stefan's problem?*

Usefulness of idealized experiments

Idealized experiments are generally useful tools to check the limits, internal processes and potential issues of models. Simplified setups are able to test the underlying basic mechanisms that a model is intended to reproduce and simulate, stripping it down to the bare bones and neglecting potential disturbances which may arise from details of boundary conditions, of initial conditions or of some parameters.

I ran some idealized scenarios with constant boundary conditions and some fixed model parameters in order to check how JSBACH modeling of the SSPF is affected by boundary conditions and to get an insight on model capabilities. These simplified runs enabled to investigate the main features of submergence, heat transfer and permafrost thawing.

+10 °C runs

BOTTOM WATER TEMPERATURE LARGER THAN THAWING/FREEZING TEMPERATURE An idealized set of simulations (set *B* of Section 3.2.2.2) is run as a copy of the experiment of the set *A* with temperature increased by 10 °C. Such forcing is comparable to what the forcing would be if it had been derived from MPI-OM results of the experiment of 1% CO_2 increase per year within CMIP5 (and CMIP6) or for year 2300 under RCP 8.5 (Giorgetta et al., 2013).

This set of experiments permits on one hand an immediate comparison with the outcomes which have been analyzed in the previous Sections of this chapter. On the other hand, it offers a view of how the system responds to a high temperature, much higher than inter- and infra-annual variability, or than the "critical" temperature that defines the setup: the thawing temperature of the layers.

Fig. 3.18 shows two main striking features: firstly a rapid reaction of the sediments to the high temperatures (both in terms of the top of the SSPF table and in term of the ice content) and secondly an almost identical behaviour for all the runs.

Quick thawing down to the base of the sediment column

The column thaws completely down to the lowest bottom of the sediment (99.8 m) in 270 years in an (almost) continuous manner, as the profile of the SSPF table (Fig. 3.18.*a*) shows. Pore ice melting occurs even faster (Fig. 3.18.*c*) and in only 2 years the ice, which is limited to

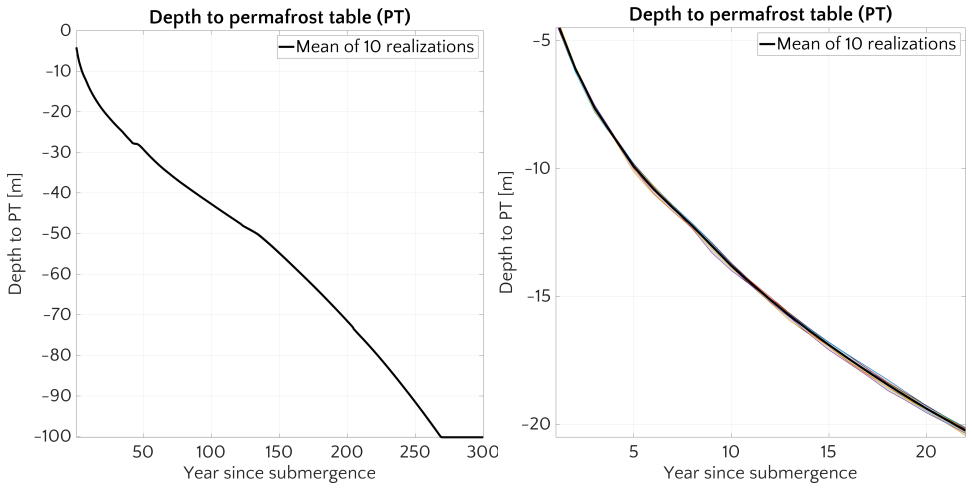

(a)

(b) Zoom-in of *a* to highlight the plots corresponding to different runs of the ensemble *B*.

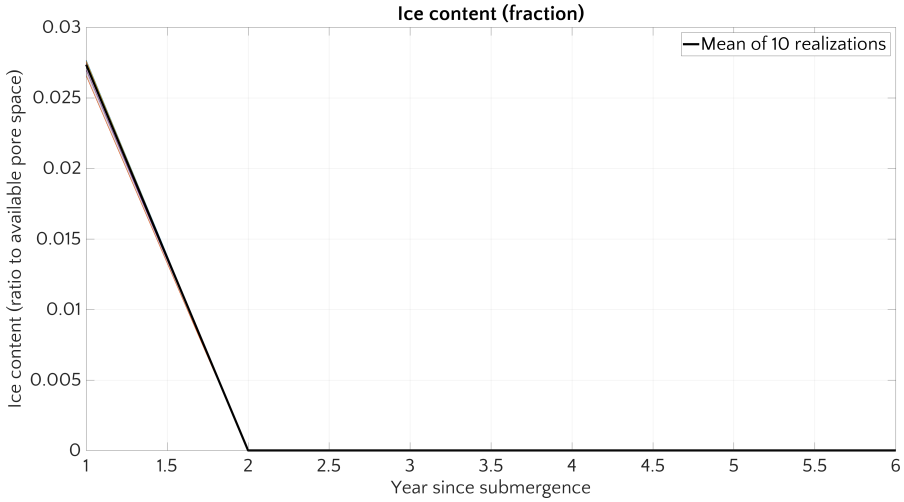

(c)

Figure 3.18: *a*. The depth to the top of the SSPF table over time for the set of runs with temperature increased by 10 °C (set *B*). The black line represents the average of the 10 runs. Individual results of each run are also plotted but practically overlap with the average value. Only a zoom-in (*b*) allows one to detect the presence of each run. *c*. shows the yearly averaged vertically integrated value of the ice content. Also in this case the ensemble mean (black line) coincides with the outcome of each run.

the first 1.11 m above the bedrock, melts away completely in a linear relationship with time.

The fact that the different runs overlap is expected: the +10 °C added on top of the original temperatures dwarfs the small differences due to randomization of the original forcing and the system reacts, on the first order, merely to this superimposed high temper-

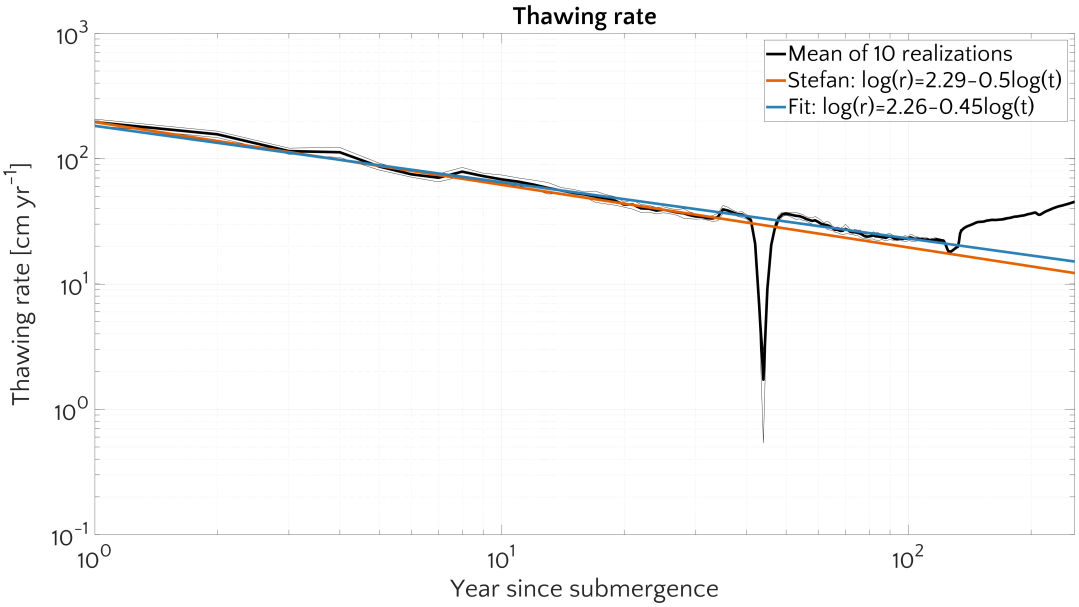

Figure 3.19: Mean value of the thawing rate for the +10 °C experiment (set *B*). The white interval around it delimits the standard deviation. A linear (blue) and Stefan's (red) fit is also shown. The time reported is until the full thawing of the sediment column: *i.e.* until the top of the SSPF table reaches the bottom of the sediments column itself after 273 years from inundation. Downward cusp at 45 year is an artifact.

ature. The fact that the simulations are consistently almost equal to each other is a good test for the model.

Meaningful comparison with Stefan's solution

Given the idealized conditions, the runs can be a test to check whether a Stefan-like solution applies and if the modeled system follows the expected result of a modified Stefan's problem. The submerged PF deviates indeed from a standard Stefan's problem because of salt penetration, the varying freezing temperature, accumulating sediments, porosity and in dishomonegeity of the medium. Since the main physical process driving the SSPF evolution is heat diffusion, a comparison with Stefan's problem is legitimate and can offer an idea of how close to idealized scenario the actual system is.

Stefan's solution partially holds

As apparent from Fig. 3.18.*a*, movement of the SSPF table only partially adhere to the theoretical Stefan's solution, which would predict a semi-parabolic downward trend. And the analysis of the thawing rate highlights this aspect. A log-log linear regression with slope -0.45 (while theoretical Stefan's rate would be -0.5) fits a relevant portion of the thawing regime. Two deviations from this quasi-Stefan behavior are an isolated cusp, which signals a decrease of thawing after about 45 years at a depth of 28 m, and a complicated pattern of decrease followed by a continuous increase of thawing starting at about $49 - 50$ m depth after 122 years.

The cusp and the the initial decrease at year 122 can be ascribed to the same cause as other anomalies above: the sudden adding of a layer of sediment (respectively the the first and the second one) on

top of the column, which a process that temporarily alters the temperature profiles. Thermal inertia increases slowing down the thawing, which would be otherwise undisturbed. Therefore these patterns can be just considered artifacts of the model and can be neglected.

In order to understand the variation (and increase) of the thawing rate of Fig. 3.19, the simulations of runs C.ii are useful. This setting is defined by a constant sea temperature ($T_w = 1$ °C) and thawing/freezing temperature has been set to $T_m = 0$ °C, a constant value $< T_w$. Thus constructed the experiment does not differentiate much from the runs of set B, except for the smaller difference between T_m and T_w[18], which simply imply a slower dynamic.

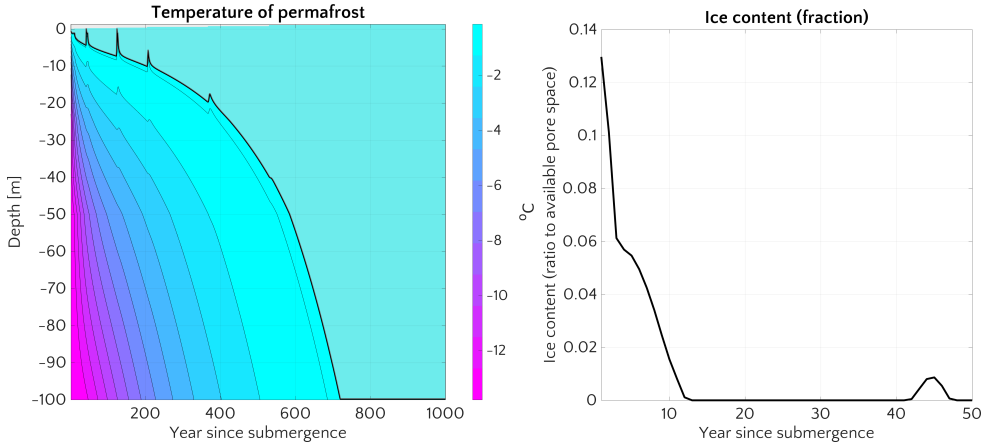

(a) September temperature evolution. The black line represents the top of the SSPF table and the shaded area the thawed portion.

(b) Evolution of the yearly averaged vertically integrated ice content

Figure 3.20: Results of run C.ii, with $T_w = 1$ °C and $T_m = 0$ °C.

Fig. 3.20 reports the main results of the simulation. The ice content also decreases rather quickly in this case, although not linearly and disappears completely after 12 years of submergence. It shows a sudden, spurious peak ($\sim 1\%$) at 41 years, after the second layer of sediments is added on top of the sediment column.

The temperature and SSPF evolution show the real striking features (Fig. 3.20.*a*), once the artificial peaks in correspondence of subsequent addition of sediment layers are neglected. As for runs of the set B, after the SSPF table has reached a certain depth, the thawing rate increases rather than decrease, as predicted by all the thawing regimes which have been proposed. Such a variation of slope is more pronounced and occurs later in time for runs of C.ii compared to the results of ensemble B. To understand this change, it must be considered that once that the SSPF table is deeply below the bedrock, the system is no longer comparable to a Stefan's problem. There is no more a

From a phase changing to a heat diffusion regime

18 As previously clarified, the fact that T_m and T_w are now constant has practically no importance

boundary moving because of the thawing and of internal effects of latent heat (which are at the basis of non-linearity of Stefan-like problem). The system is just a sediment column which warms up from the top with a zero-flux at the bottom. That is the reason why the SSPF table (defined by the 0 °C condition) deviates from Stefan's solution and just follows the trend of an isothermal line in a heat diffusion problem.

The change in regime of the moving boundary resulting from JSBACH simulations mirrors simply a change in the problem describing the system over time: at first from a phase boundary movement to a standard heat equation. This behavior is therefore linked to the geological structure and simulated water availability of the model.

IMPACTS OF THE DIFFERENCES OF THAWING/FREEZING TEMPERATURES The thawing/freezing temperature represents a critical quantity for the system. As shown, the connection between the thawing/freezing temperature and the salinity is crucial, and a substantial part of the code is written with the purpose of keeping track of the link between these two quantities. Given the heuristic approach I employed to implement transport of the freezing point depression, it is not surprising that its calculation can be affected by the parameters involved: a different value of tortuosity, of the salt diffusion coefficient or a variation of the layering scheme could determine a variation of the freezing point depression. A sensitivity study of the impact of the thawing/freezing temperature can offer an overview of their role and shed some light whether a precise estimation is needed, which would imply the necessity of a parallel salt transport implementation. In the following I will especially focus on the relative magnitude of the thawing/freezing temperature in SL, sediments and bedrock, on their relationship with the top boundary condition - which drives the thawing from above - and on how layering might modify the outcomes.

Motivation of a sensitivity study on thawing/freezing temperatures

Runs C.i and D considered

The settings of the runs C.i and D are very similar: in both case the thawing/freezing temperature of the SL and sediments has been set equal to -1.8 °C and sea water temperature temperature has been in both case > -1.8 °C: 0 °C for C.i and -0.7 °C for D. The experiment D enables an immediate comparison with CryoGRID2 simulation, since the top boundary condition corresponds to the yearly average temperature that has been considered for typical Arctic waters, while the phase change temperature correspond to the considered average salinity of 30 psu.

Fig. 3.21 compares results of C.i runs (top row: *a*, *b*, *c*) with results of D runs (bottom row: *d*, *e*, *f*).

Artificial step-like behavior

A step-like structure can be easily identified for the top of the SSPF table in correspondence of the addition of sediment layers on top of the sediment column (Fig. 3.21.*a*,*d*). A comparison with the value at

SWI(0) can clarify better how the PT has deepened into the sediments (Fig. 3.21.*b*,*e*). The artificial disturbances due to the increased thickness of the sediment layer are characterized by a peak followed by a recovery of a smooth profile. If the artifacts are neglected (dotted lines offer an interpolated plausible trend without disturbances), the difference in the movement of the SSPF for the two simulations is remarkable.

Different behavior

The SSPF table for simulation *D* only moves slowly downcore, approaching the top of bedrock with a rate decreasing over time. The results for C.i are instead much more diverse: after a period of about 380 year where the SSPF table settles around the top of the bedrock, it further moves more quickly downwards. The comparison with the ice content evolution (Fig. 3.21.*c*,*f*) offers an explanation of the different behaviour between the two runs, whose bottom line lies actually in the difference between the two sea water temperatures.

Origin of the different behavior

Because of the difference in the thawing/freezing temperature of the SL and 0 °C defining permafrost in bedrock, the layer of SL just in correspondence of the bedrock has a thawing/freezing temperature of about −0.2 °C. Considering that the top temperature is −0.7 °C, it means that the ice layer at −1.11 m in correspondence with the bedrock cannot melt away and this prevents further increase of temperature and consequent movement of the SSPF table. And this is exactly what occurs for runs *D* in the current implementation.

For runs *C*.i the ice layer in correspondence of the bedrock represents instead only a temporary slowing in further warming. After ice is consumed, the cold temperatures of the bedrock can still cause a lump of ice, as shown in the bulge of Fig. 3.21.*e* at about 366 years (corresponding to the sudden dip in SSPT table of Fig. 3.21.*c*). But once further heat transfer from warmer temperatures has melted it away, the warming can proceed downwards into the rock. This behavior is in line with the hypothesis that the thawing from top proceeds in two stages (Sharbatyan, 1974), the first of which consumes the "cold reserves" (Portnov et al., 2014) of the system.

Comparison of run D with CryoGRID2 is not meaningful

In the light of above explanation, it comes with no surprise that results of run *D*, designed to compare JSBACH outcome with CryoGRID2 simulations, leads to completely different results.

The outcomes of the runs *C*.iii, where thawing temperature and freezing temperature are not the same, was designed to reproduce the conditions of thawing and freezing as empirically implemented in MPI-OM. Fig. B.2 shows the main results, but decoupling the melting from freezing turns out to be highly flawed and I will not analyze this simulation.

Layering plays a role

In summary, this Section proves that the current JSBACH implementation is extremely sensitive to the layering and the associated freezing/thawing temperatures and that special attention must be given to avoid unphysical situations. Such a drawback could be overcome

by implementing salt transport and enforcing the dependence of the thawing/freezing temperatures from a more physical basis.

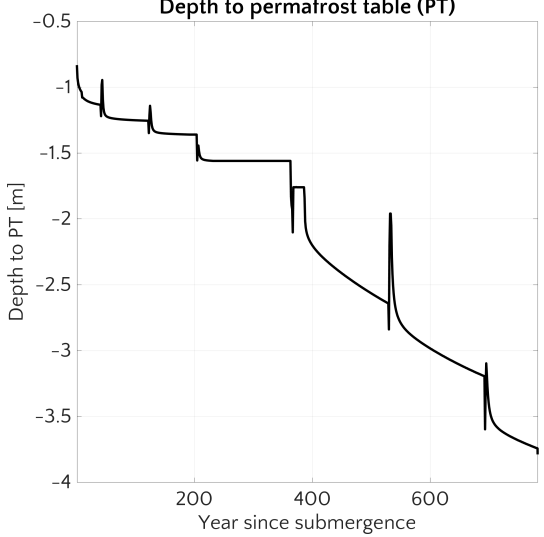

(a) C.i - Depth of the SSPF table

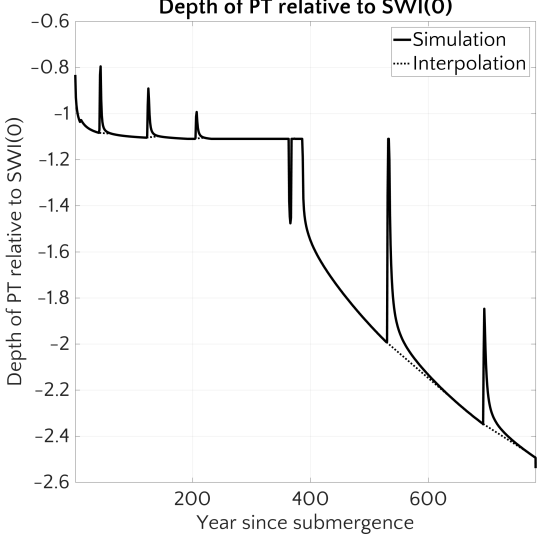

(b) C.i - Depth of the SSPF table with respect to SWI(0).

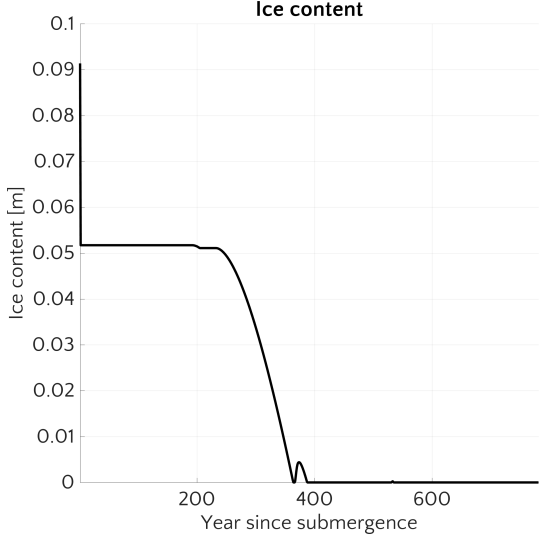

(c) C.i - Yearly mean of vertically integrated ice content

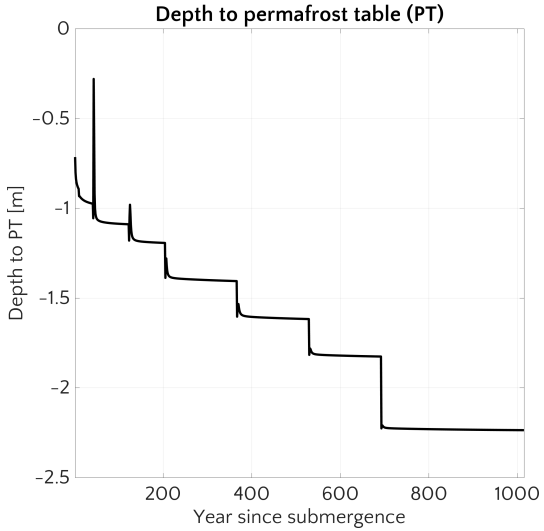

(d) D - Depth of the SSPF table

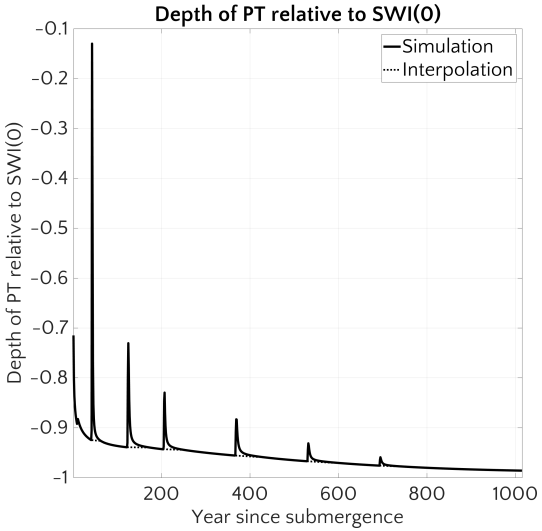

(e) D - Depth of the SSPF table with respect to SWI(0)

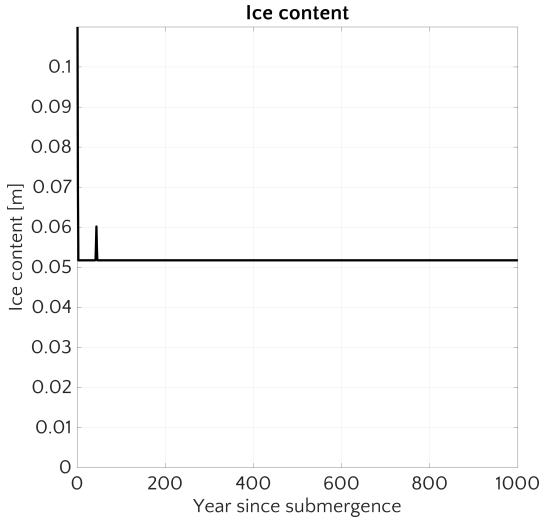

(f) D - Yearly mean of vertically integrated ice content

Figure 3.21: Comparison for runs C.i (*Top*) and runs D (*Bottom*), the latter imposing average boundary condition of "scenario C" of typical Arctic water condition in Angelopoulos et al., 2019. Dotted lines in (*c*) and (*d*) represents a plausible interpolated solution without the disturbance due to the addition of a sediment layer on top.

3.3.5.2 *Role of geothermal heat flux*

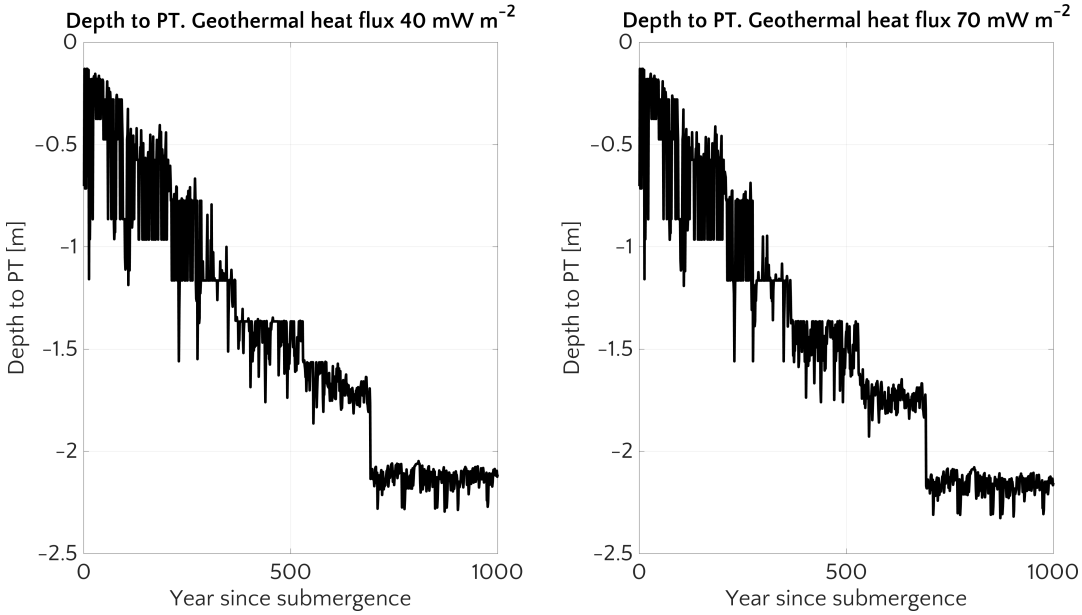

(a) Movement of the SSPF table

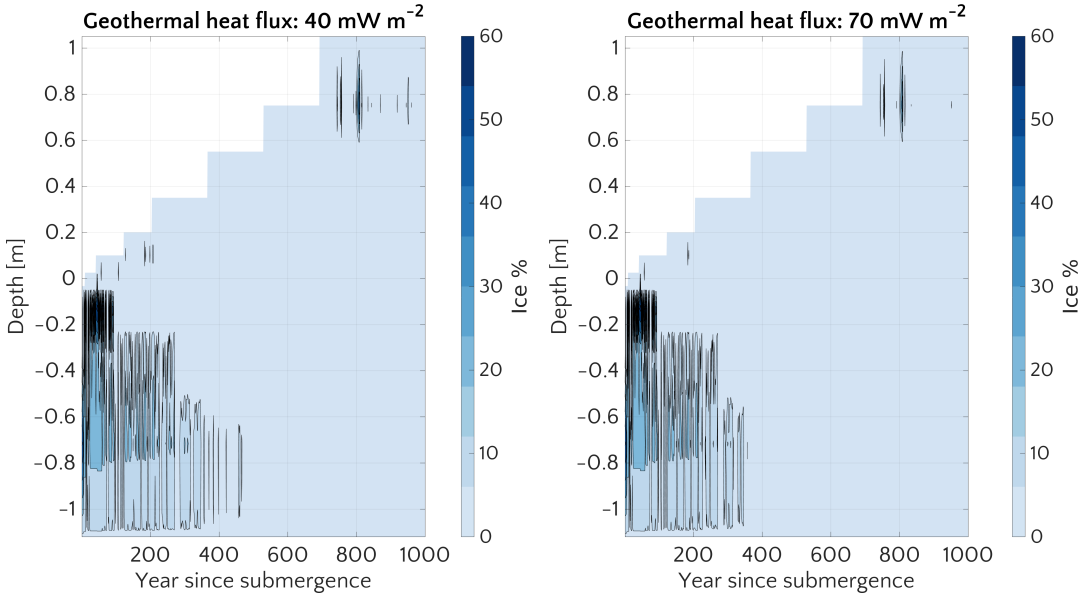

(b) September ice evolution

Figure 3.22: Movement of the SSPF table and evolution of ice content in simulations with imposed geothermal heat flux of 40 mW m^{-2} (*Left*) and 70 mW m^{-2} (*Right*).

Implementation of the geothermal flux in JSBACH

The implementation of the geothermal heat flux in JSBACH sets one of the necessary conditions for the development of the model, possibly in view of a simulation of the geological permafrost. Considered the low geothermal heat flux of most of the settings of the Arctic Sea (*e.g* the Siberian craton), the main results are no expected to change much. The addition of a more realistic lower boundary conditions

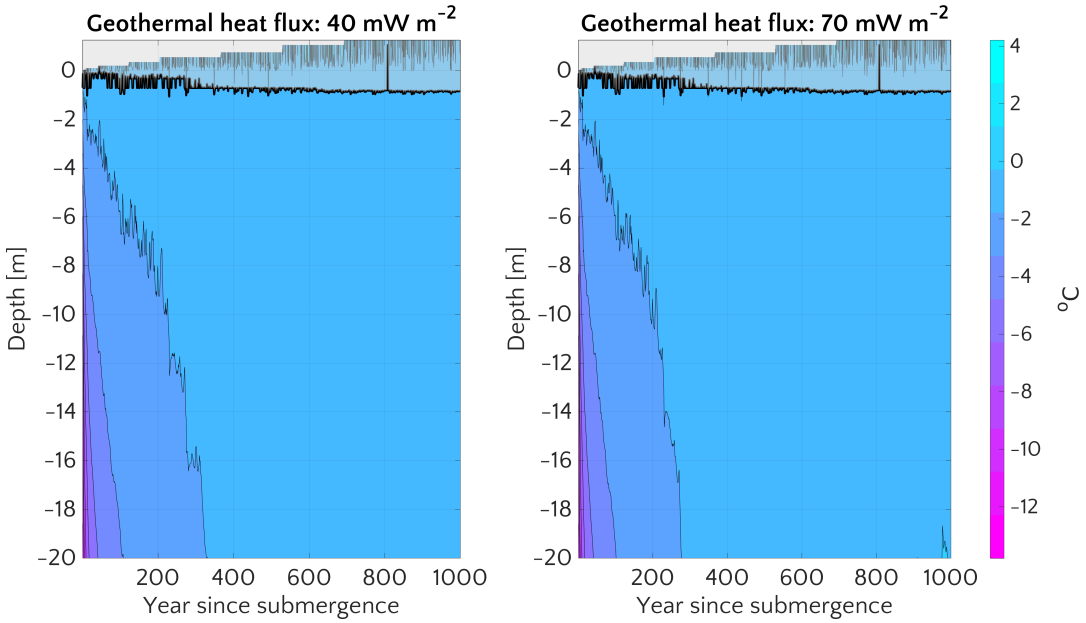

(a) Upper part of the sediment column

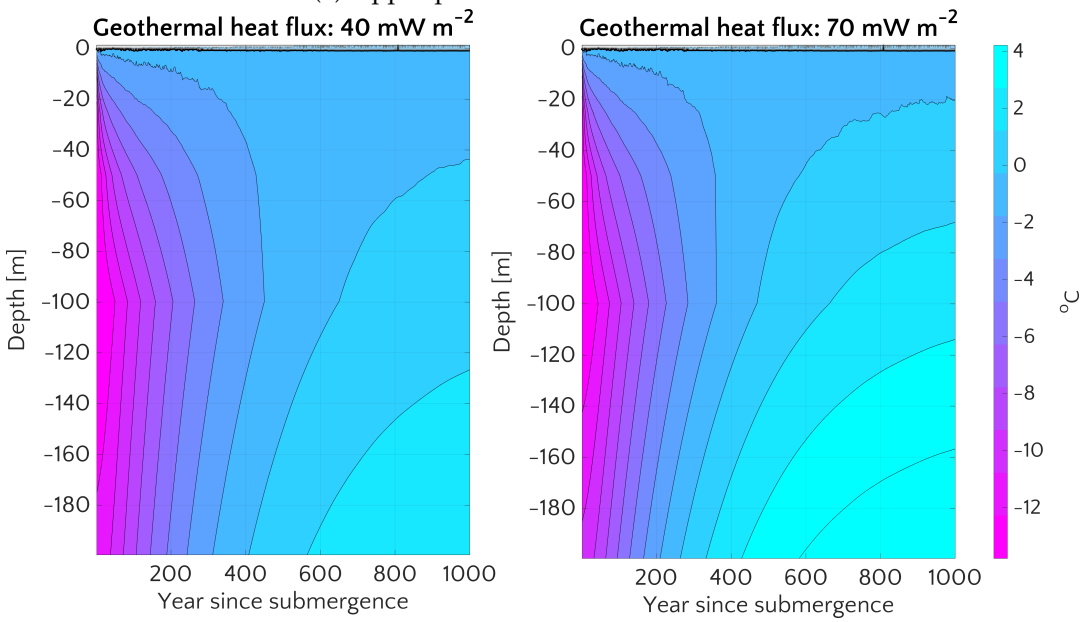

(b)

Figure 3.23: September temperature evolution for simulations with imposed geothermal heat flux of 40 mW m^{-2} (*Left*) and 70 mW m^{-2} (*Right*). Thick black lines represent the SSPF table and shaded area the thawed portion.

enables however the application of the model in more critical environments where heat flux is known to be paramount, like in the fault lines (Romanovskii et al., 2001; Romanovskii et al., 2005) and at the shelf break (Romanovskii et al., 2001). It would make possible the study of the thawing process in these settings.

Two simulation runs (*E*.i and *E*.ii) have been run to examine how the geothermal heat flux might alter the climate-affected portion of modeled SSPF (*i.e.* the upper part of the sediment column). To do so, the temperature gradient corresponding to two values of geothermal heat flux measured for the Siberian shelf has been imposed as the lowest boundary condition.

Little difference in thawing for the runs with geothermal flux

Fig. 3.22 shows that both the SSPF tables and the evolutions of September ice content show no alteration if compared with each other or with the reference value of null heat flux (Fig. 3.7 and Fig. 3.12). The only remarkable difference is the absence of formation of some ice lenses in the sediments in case of flux of 70 mW m^{-2} and the lack of late (after 500 years) and weak (ice content $< 10\%$) ice structures in both simulations compared to the case of a null flux. Such marginal variations were expected since ice is limited to the upper 1% of the sediments length, far from where heat enters the column.

Thermal state is slightly altered

Despite the fact that thawing of the upper part of the sediments is almost identical to reference simulation with zero heat flux, the thermal state is altered, as shown in Fig. 3.23 and warming occurs. The temperature at the end of the simulation ranges from -0.8 °C at the top, to 5.8 °C at the bottom.

The upward movement of the 0 °C isoline determines a tapering of the SSPF thickness which, in case of a flux of 70 mW m^{-2}, shrinks to the upper 20 m only after 1000 yr. If the 100 m depth is considered as reference, the SL ceases to be cryotic after about 600 yr (for 40 mW m^{-2} flux) and even less than 500 yr (for 70 mW m^{-2}). The overall temperature increase within the sediments, although not enough to determine a deeper thawing in the simulated time, is relevant and up to more than 6 °C in the lower part.

A general warming is an important point for two reasons: it is accompanied by a weakening of the sediment compactness and brings the SSPF sediments closer to the thawing, making them more vulnerable to perturbations and to the ensuing potential carbon release.

Simulations endowed with geothermal heat flux are thence generally recommended to get a better constraint on temperature state of the SSPF.

3.3.5.3 *Effect of summer increasing temperatures*

In order to shed some light on potential future evolution of the SSPF, a simulation (*F*) considering current trend in summer shallow water temperature of the Laptev Sea (Dmitrenko et al., 2011) was run. The - measured - summer temperature increase of 0.09 °C yr^{-1} was applied to the randomization of the forcing files (the same for simulation 1 of set *A*) derived from MPI-OM. The length of the simulation was limited to 200 years, to prevent an exaggerated and unrealistic temperature increment. The yearly average temperature at sea bottom is reported in Fig. 3.25.

Trend of increasing sea bottom water in summer

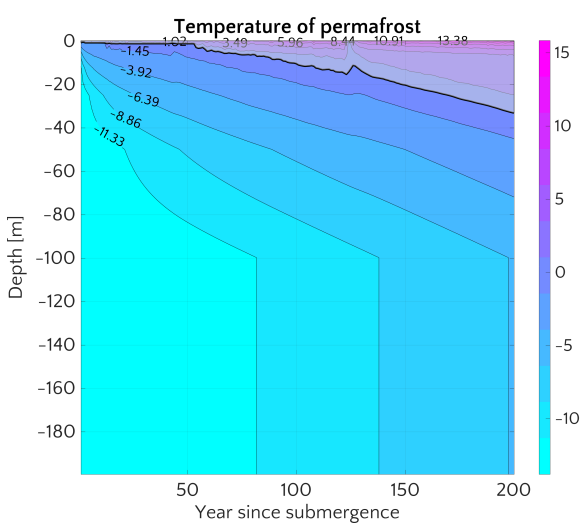

(a) September temperature evolution

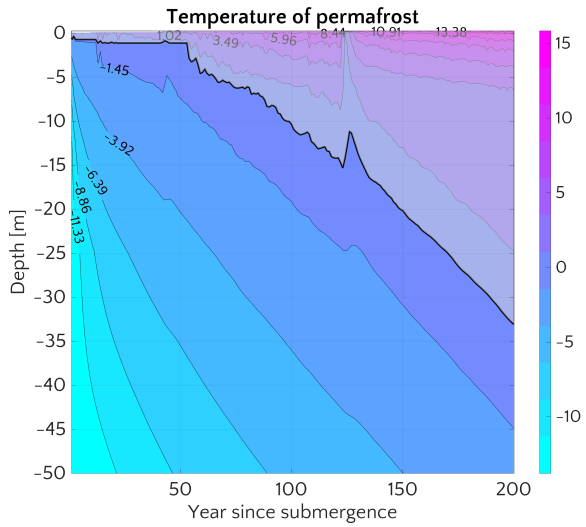

(b) September temperature evolution (zoom)

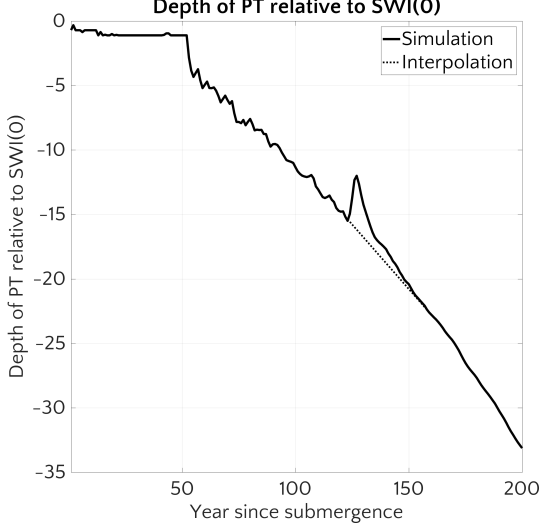

(c) Movement of SSPF table

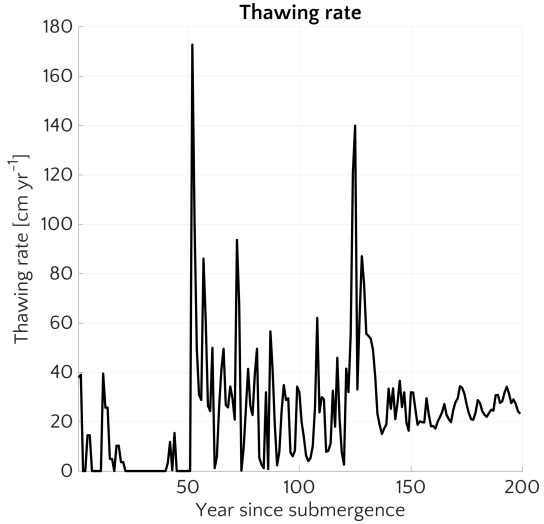

(d) Thawing rate

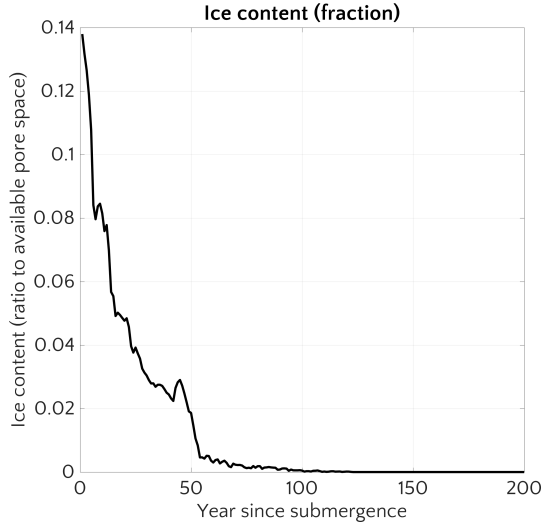

(e) Evolution of yearly mean of vertically integrated ice content

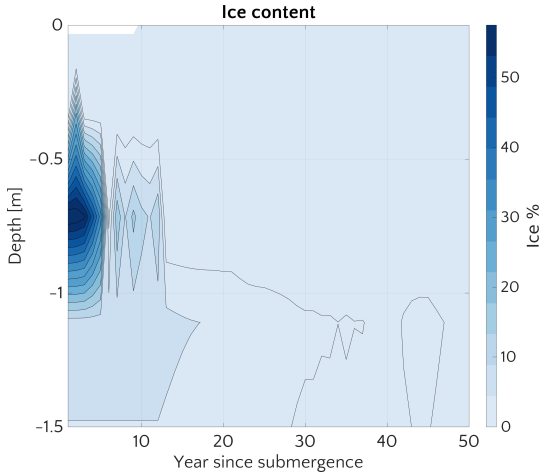

(f) Evolution of September ice content

Figure 3.24: Main results of the run *F*. Black lines in *a,b* represents the SSPF table and shaded area the thawed portion. Dotted line in *c* represents the interpolation of the trend neglecting the bump after 121 year following the addition of an extra sediment layer.

Movement of the SSPF table

The movement of the SSPF table (Fig. 3.24.*c*), as for results of run C.i (Fig. 3.21.*c*), can be split in two parts. A first quick drop down to the level of the bedrock where the SSPF lingers while the cold reservoirs of the ice are being consumed (as mirrored in panel *e,f*). While the SSPF table lines up at the bedrock, the thawing rate is almost zero (panel *d*) and the heat coming from above provides the latent heat needed to melt the ice. Once the pore ice is melted away (after 52 years), heat warms up the soil rapidly and the SSPF table, after a quick drop (and a brisk movement of even 1.7 m in a year), moves downcore linearly with time with a velocity of about 20 cm yr^{-1} and reaches the depth of 33.4 m. Around the end simulation (last 60 years) the thawing rate starts slowly increasing.

Modeled thawing rate compatible with observed high thawing rates

No theoretical model predicts such a behavior for movement of the SSPF table. The rapidly changing top boundary conditions however impedes a direct comparison with any proposed thawing regime and therefore the simulated behavior is likely to be legitimate and physically sound. Moreover the predicted average thawing rate of about 16 cm yr^{-1} is of the same order of the rate of about 14 cm yr^{-1} measured by (Shakhova et al., 2017) in the Buor Khaya bay.

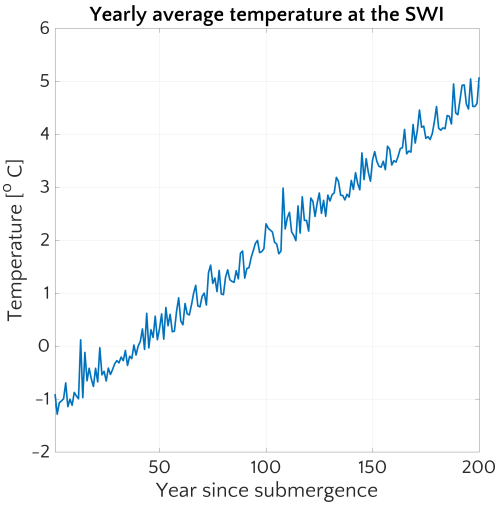

Figure 3.25: Yearly average temperature of the sea bottom waters under the steady temperature increase of 0.09 °C yr^{-1} of shallow Laptev Sea (Dmitrenko et al., 2011) in summer months (June-July-August). Upper boundary condition for simulation *F*.

At the end of simulation the highest temperature in the sediments is 18 °C and the lowest one is -6 °C (Fig. 3.24.*a,b*). These values give an idea of the strong thermal gradient which dominates the thawing from above.

3.4 CONCLUSIONS AND OUTLOOK

First implementation of the SSPF in an ESM

In the chapter I have presented the implementation of a scheme suitable to simulate the subsea permafrost in the process-oriented land surface model JSBACH. It represents the first study of the subsea permafrost performed with a model, part of a general Earth System Model. By including sediment accumulation, geothermal heat flux and a heuristic implementation for the transport of the salt-induced

freezing point depression, the model is capable of simulating in 1-D the permafrost submergence, subsea permafrost formation and the annexed processes.

Good site-level comparison for land PF

A site level comparison of the results of terrestrial permafrost prior to the submergence with some boreholes measurements shows a generally good agreement between the model and observations for the soil temperature in the upper 30 m. The temperature values, temperature gradient and the depth of seasonal fluctuations are also well reproduced. The ice content resulting from the spin-up phase is comparable with the high ice concentration that can be found in Yedoma affected soils.

SSPF thawing is slow

The submergence is modeled for a millennium by employing pre-industrial sea bottom water temperatures derived from the MPI-OM simulation. The top of subsea permafrost table is predicted to experience an overall downward movement of 2.05 ± 0.06 m: 1.23 m as a consequence of sediment accumulation and 0.82 m because of the thawing. Some simulations predict a thawing down to the top of the bedrock (1.11 m) but no further deepening with an ensuing overall preservation of the subsea permafrost on the long period. The time response to the change of boundary conditions in the aftermath of submergence is thus slow, both for the thawing boundary and for the temperature profile, in agreement with the long time response identified by Dmitrenko et al., 2011, Romanovskii et al., 2005 and Malakhova et al., 2017. The thawing rate in JSBACH simulations is generally slower than the thawing rate derived by Angelopoulos et al., 2019 with CryoGRID2, the only model of subsea permafrost explicitly resolving salt penetration in the submerged sediments. As already pointed out, the salt presence is the necessary condition to have a net thawing over time in JSBACH as well.

JSBACH models higher SSPF temperatures

A comparison of the modeled temperature profiles with boreholes measurements reveals that the model usually overestimates the temperatures: it could not be otherwise considering that the lowest temperature of the sea water modeled by MPI-OM is only -1.41 °C. The agreement of modeled with measured temperature profiles is better for the sediments which have been submerged for longer periods and which therefore have had more time to equilibrate to warmer conditions. This partial result consistency suggests that the heat conduction is the most relevant heat transfer mechanism on the longer time perspective and that JSBACH, neglecting other kind of heat transports, does not overlook relevant sizable processes.

A Stefan-like solution applies as long as the system is a phase-changing system

Even if the system of the subsea permafrost is far from being an idealized Stefan's problem, the predominance of heat conduction as the transfer mechanism is an indication that a quasi-Stefan regime might be valid. The movements of the subsea permafrost table in JSBACH simulations are however characterized by a continuous wavering trend of thawing and freezing. It prevents a simple comparison

with theoretically expected regimes described by Stefan's solution, approximately followed by CryoGRID2 simulations though.

Taliks are qualitatively well reproduced

The capability of qualitatively reproducing taliks represents a relevant achievement for JSBACH. The closed taliks which have been simulated are direct consequence of salt percolation into the sediments and they present a structure of frozen-unfrozen-frozen layers. These kind of formations had been observed in Arctic shelf and had been predicted by other *ad hoc* subsea permafrost models, although on different spatial scales.

The results of a sensitivity study and the comparison of the movement of the subsea permafrost table have enabled an understanding of i) the current limitations of the model, ii) the settings when JSBACH provides instead trustworthy results and consequently of iii) the conditions which are compatible to a large destabilization of the simulated subsea permafrost.

In the current setup, JSBACH gives results compliant with theoretical expectations of Stefan's problem when sea water temperature is higher than the phase change temperature of the sediments and of the bedrock. In this case the simplified premises of Stefan's solution are met and the model behaves accordingly.

High destabilization of the SSPF can be modeled

It is also one of the two circumstances which causes a massive destabilization of the subsea permafrost, the other one being the seasonal increase of sea water temperatures, as measured so far during summer in the shallowest waters of the Laptev sea (Dmitrenko et al., 2011).

Massive SSPF destabilization might occur before 2300

I have shown that the sea water temperature has to be even only one degree warmer than the phase change temperature to have a stark thawing of subsea permafrost, weakening the upper 20 m of sediments in less than 400 years and 100 m in less than a millennium. Considering that a severe warming of the Arctic waters (up to +10 °C) is projected for 2300 according to some pathways of CO_2 concentration in the atmosphere, it is logical to infer that a strong destabilization of the subsea permafrost might occur way before: as soon as Arctic waters average temperatures become positive. Modeled thawing rates derived from simulations forced with ongoing summer warming scenario are of about 16 cm yr^{-1}, in the range of [9.3 cm yr^{-1} – 18.3 cm yr^{-1}] measured in the Laptev Sea (Shakhova et al., 2017). Such rates suggest therefore a hefty loosening of the subsea permafrost in a couple of centuries and agree with the claim that Arctic frozen sediments might actually be responding to the ongoing climate change.

Limitations: shallow bedrock and no salt diffusion scheme

In the current configuration the main limitation for the applicability of JSBACH is caused by a combination of a (too) shallow bedrock and the absence of an explicit transport scheme for salt. The bedrock prevents ice formation and water percolation deeper in the sediments. Besides that, the temperature defining permafrost is set to 0 °C, higher than the sediments on top. As shown in this chapter, the downwards

movement of the subsea permafrost table proceeds in a reasonable way as long as the effects of the presence of the bedrock - ice formation on top and lack of water below it - do not affect the heat propagation scheme. In some cases the presence of a shallow bedrock completely alters the intrinsic nature of the system itself: from a phase change problem to a pure heat propagation problem.

Suggested improvements

The most physically sound solution would be the implementation of the salt transport in JSBACH. An alternative simpler way would be to change either the temperature defining the permafrost in the bedrock or to move the bedrock deeper down. Inconsistencies would also decrease if the temperature of the sea water were coupled to its salinity, a feature that is missing at the moment.

Another suggested improvement is the implementation of a finer and continuous sediment scheme accumulation since it would prevent spurious results, such as the ones analyzed in this chapter.

Such developments would finally allow a better and more trustworthy evaluation of key quantities like the thawing rate and temperature. This step represents a necessary preliminary condition for the intended and desired coupling of an Earth System Model with a reactive-transport model.

4

ASSESSING THE POTENTIAL FOR NON-TURBULENT METHANE ESCAPE FROM THE EAST SIBERIAN ARCTIC SHELF: THE EMPLOYMENT OF BRNS[1]

4.1 INTRODUCTION

The ESAS

The Siberian Shelf represents the largest shelf on Earth ($\sim$ 3 millions km^2, Wegner et al., 2015) and spreads from the Kara Sea to the Laptev, the East Siberian and the Chukchi Sea. The East Siberian Arctic Shelf (ESAS) corresponds to the broad area beneath the shallow ($\sim$ 45 m water depth, James et al., 2016) Laptev and East Siberian Arctic Sea (Romanovskii et al., 2004; Shakhova et al., 2010a) and represents the largest region on the Siberian Shelf (Romanovskii et al., 2005), covering about 25% of the total Arctic shelf (Shakhova et al., 2010a).

The SSPF: an important feature of the ESAS

Although similar in many aspects to other shelf environments, a distinguishing feature of the ESAS is the presence of subsea permafrost (SSPF) and associated gas hydrates buried in the sediment (Sloan Jr et al., 2007; Romanovskii et al., 2005). SSPF is a terrestrial relict that mainly formed during glacial periods, when Arctic shelves were exposed due to sea level retreating, down to a minimum of 120 m below the current level around the Last Glacial Maximum (Fairbanks, 1989; Bauch et al., 2001). Under these conditions, permafrost aggraded on the shelf and was subsequently submersed when rising sea level flooded the shelf during the Holocene sea transgression (12 and 5 kyr BP).

Uncertain C content

Little is known about the total amount of carbon stored in subsea permafrost, as well as its partitioning between subsea permafrost itself, gas hydrates and free gas. Published estimates of carbon reservoir sizes diverge by orders of magnitude. For instance Shakhova et al., 2010a estimate that 1175 PgC are locked in subsea permafrost on the ESAS alone, while McGuire et al., 2009 calculate that, across the entire Arctic shelf, 9.4 PgC reside in upper sediments and $1.5 - 49$ PgC ($2 - 65$ PgCH_4) in methane gas hydrates. Thus, the size of the Arctic subsea permafrost reservoir, its spatial distribution, as well as its biogeochemical and physical characteristics remain poorly known.

Polar amplification and oceanographic changes

These knowledge gaps are critical as climate change is amplified in polar regions. The Arctic is currently warming at a rate twice as fast as the global mean (Trenberth et al., 2007; Bekryaev et al., 2010; Jeffries

1 This chapter is amply based on the submitted paper Puglini, M., V. Brovkin, P. Regnier and S. Arndt (2019). "Assessing the potential for non-turbulent methane escape from East Siberian Arctic Shelf", *Biogeosciences discussions*, pp. 1-44, DOI:10.5194/BG-2019-264

et al., 2012; Christensen et al., 2013). Recent observations indicate that bottom water temperatures in the coastal and inner shelf regions of the ESAS (water depth < 30 m, Dmitrenko et al., 2011) are rising, while the central shelf sea may be subject to intense episodic warming (Janout et al., 2016). The increasing influx of warmer Atlantic water into the Arctic Ocean - the so-called Atlantification - will not only further enhance this warming, but will also influence circulation and salinity patterns on the shelf (Zhang et al., 1998; Biastoch et al., 2011; Polyakov et al., 2017).

The Arctic Ocean and CH_4

At the same time, it has been long recognized that the Arctic is a potential hotspot for methane emissions. Extensive methane gas bubbling has been observed in the Laptev Sea and has been directly linked to these environmental changes (Shakhova et al., 2010b; Shakhova et al., 2014). At present, a major unknown is the strength of methane sinks in Arctic sediments and waters and their influence on methane emissions (Ruppel et al., 2017). Therefore, improved assessments of the present and future climate impact of permafrost thaw and hydrate destabilization require not only a better knowledge of the Arctic subsea permafrost and hydrates distribution, reservoir size and characteristics, but also a better quantitative understanding of Arctic methane sinks.

CH_4 sinks need to be better understood

AOM and AeOM biofilters

In marine sediments, upward migrating methane is generally efficiently consumed by the anaerobic oxidation of methane (AOM) and, to a lesser extend, the aerobic oxidation of methane (AeOM) (Hinrichs et al., 2002; Reeburgh, 2007; Knittel et al., 2009). Although the exact AOM process has not been fully understood yet (James et al., 2016; McGlynn et al., 2015; Milucka et al., 2012; Wegener et al., 2015; Dean et al., 2018), it is thought that AOM is mediated by methane oxidizing archaea that use water (or bicarbonate) as electron acceptor (Hinrichs et al., 2002; Dale et al., 2006):

$$CH_4 + 3\,H_2O \longrightarrow 4\,H_2 + HCO_3^- + H^+ \tag{4.1}$$

The electrons are then shuttled (Krüger et al., 2003; Hinrichs et al., 2002), via H_2, to sulfate reducing bacteria (Eq. 4.2)

$$SO_4^{2-} + 4\,H_2 + H^+ \longrightarrow HS^- + 4\,H_2O \tag{4.2}$$

and the overall reaction is hence:

$$CH_4 + SO_4^{2-} \longrightarrow HCO_3^- + HS^- + H_2O. \tag{4.3}$$

The first catabolic step is thermodynamically favourable only under a limited range of environmental conditions, while the second step is subject to weaker thermodynamic constraints (LaRowe et al., 2008). The AOM usually takes places in a relatively narrow of the sediments, where counter-propagating fluxes of CH_4 and SO_4^{2-} converge, as they are both needed. This zone takes the name of Sulfate-Methane Transition Zone (SMTZ).

The SMTZ

AOM budget

A recent assessment indicates that, in global sediments, around 45-61 $TgCH_4\ yr^{-1}$ (Egger et al., 2018) are consumed by AOM, thus significantly reducing previously published estimates of $320 - 360\ PgCH_4\ yr^{-1}$ (Hinrichs et al., 2002; Reeburgh, 2007).

Despite a wealth of AOM-related research, a holistic, quantitative evaluation of the most important environmental controls on the efficiency of the AOM biofilter and its impact on methane escape from marine sediments is currently lacking. Thus our ability to understand and quantify AOM sink in ESAS sediments and thus the climate impact of subsea permafrost thaw and gas hydrate destabilization is seriously compromised.

A RTM to investigate the ESAS

We here use for the first time a reaction-transport model to investigate the ESAS sediments and its potential methane emission. The model has been developed to account for the most pertinent primary and secondary redox processes, as well as mineral precipitation, methane gas formation and fast equilibrium reactions that affect biogeochemical dynamics in both passive, as well as active sediments influenced by a deep methane source.

OAT sensitivity study

The model is forced with boundary conditions that are broadly representative of conditions encountered on ESAS. It is applied to conduct a comprehensive one-at-a-time, steady-state sensitivity study over the entire plausible range of 1) sedimentation rates, 2) active fluid flow velocities, 3) AOM rate constants, 4) organic matter reactivity and 5) nonlocal transport activity encountered on the ESAS. In addition, we also performed a two-level factorial all-at-a-time sensitivity analysis to investigate possible synergies among the drivers. Finally, we evaluated under transient conditions the influence of environmental change induced by 1) seasonal variability and 2) idealized climate change on the efficiency of the AOM-biofilter and non-turbulent methane escape at the seafloor. For this purpose, the model is extended by adopting an explicit description of AOM biomass dynamics and a bioenergetic rate law for AOM (Dale et al., 2006; Dale et al., 2008c; Dale et al., 2008b).

AAT sensitivity study

Transient analysis

Research questions of Chapter 4

In this chapter, the results of model simulations, will be used to address the following open questions.

Q4.1 How much methane could be emitted from Arctic sediments?
Shakhova et al., 2014 suggest that warming-induced subsea permafrost thaw and hydrate destabilization may support methane emissions of up to 17 $TgCH_4\ yr^{-1}$ from the ESAS alone. Projected climate change will further destabilize Arctic subsea permafrost together with gas hydrate reservoirs and might thus enhance further methane emissions (Piechura et al., 1995; Westbrook et al., 2009; Reagan et al., 2009; Biastoch et al., 2011; Hunter et al., 2013; Drake et al., 2015b; Ruppel et al., 2017). However, a number of recent studies have questioned the significance of subsea permafrost thaw and hydrate destabilization for methane efflux

from Arctic sediment (Thornton et al., 2016; Ruppel et al., 2017), for methane concentrations in Arctic Ocean waters (Overduin et al., 2015b; Sapart et al., 2017) and, ultimately, for methane emissions from the Arctic waters (Ruppel et al., 2017; Sparrow et al., 2018). Thus, the contribution of subsea permafrost thaw and gas hydrate destabilization to methane emissions from the warming Arctic shelf and, ultimately, methane-climate feedbacks remains poorly quantified (James et al., 2016; Saunois et al., 2016). In this chapter, the model results will then be used to quantitatively assess the potential for non-turbulent CH_4 escape from ESAS sediments and set some constraints on the Arctic methane budget.

Q4.2 *How efficient is the AOM biofilter? Which are the most important environmental controls on the efficiency of the AOM itself?*
AOM generally acts as a particularly efficient biofilter for upward migrating methane and oxidizes up to 100% of the methane flux coming from below (*e.g.* Regnier et al., 2011). However, a number of environmental conditions can reduce the efficiency of this AOM biofilter, allowing methane to escape from the sediment (Iversen et al., 1985; Piker et al., 1998; Jørgensen et al., 2001; Treude et al., 2005; Knab et al., 2008; Dale et al., 2008c; Thang et al., 2013; Egger et al., 2016). In this chapter we will investigate the significance of the main drivers of non-turbulent methane escape from marine sediments on the ESAS under present-day environmental conditions and in response to idealized environmental variability.

Q4.3 *Under which condition is a high methane escape possible?*
It has been shown that, in particular, high sedimentation rates (Egger et al., 2016), slow microbial growth (Dale et al., 2006; Dale et al., 2008c) or the accumulation of free gas can promote methane efflux from the sediment. These findings are particularly relevant for potential methane escape from Arctic shelf sediments. The Siberian shelf is in fact the largest sedimentary basin in the world (Gramberg et al., 1983) and shelf areas close to the large Arctic rivers reveal sedimentation rates than can be up to 5 times faster than rates that are typically observed in the ocean (Leifer et al., 2017). In addition, the Arctic shelf is subject to large seasonal, as well as climate-induced longterm, changes in environmental conditions that may influence the efficiency of the AOM biofilter through their effect on microbial biomass dynamics. In this chapter we will analyze the mechanisms behind a reduction of the efficiency of the AOM and an ensuing high CH_4 escape.

Bubble formation

It must be pointed out that several observations from the ESAS indicate that methane gas accumulates in the sediments, too. When free gas pockets grow enough, methane tends to migrate

upwards along pathways with higher permeability or where fractures occur (Yakushev, 1989; Boudreau et al., 2005; Wright et al., 2008; Shakhova et al., 2014; Shakhova et al., 2015; Shakhova et al., 2017; Leifer et al., 2017) and might even crack the sediments themselves (O'Connor et al., 2010; Overduin et al., 2016). We limit our model analysis however to non-turbulent methane efflux, because methane in gaseous form is not directly accessible for the AOM community. As a consequence, free gas bubbles are less prone to be consumed by AOM and methane gas either sits in the sediments or rapidly migrates upcore through cracks, faults or fractures (Boudreau, 2012), bypassing the AOM biofilter.

Only non-turbulent flux considered, i.e. no bubbles

Q4.4 How does the AOM affects the relation between CH_4 and SO_4^{2-} in the Arctic sediments?

A recent study (Egger et al., 2018) has highlighted that the ratio $CH_4 : SO_4^{2-}$ at the SMTZ is 1:1.4, although it is expected to be 1:1 according to the theoretical AOM formulation (see Eq. 4.3). Considering that this result emerge from a global collection of site-level measurements but that no sediments coming from the ESAS has been employed in its derivation, such finding is worth a further inquiry to check what the model predicts in the setting of the ESAS. The value of the ratio has been explained resorting to the role of sulfate reduction as a pathway of organic matter remineralization. This hypothesis can be put under exam in our scenario and analyzed with the tools of our simulations, shedding some light on this unexplored and novel aspect of the AOM.

4.2 METHODS

4.2.1 *BRNS: Reaction-transport model*

The RTM BRNS...

The Biogeochemical Reaction Network Simulator (BRNS) (Regnier et al., 2002; Aguilera et al., 2005; Centler et al., 2010) - an adaptive simulation environment suitable for simulating large, mixed kinetic-equilibrium reaction networks in porous media (*e.g.* Jourabchi et al., 2005; Thullner et al., 2005; Dale et al., 2009) - is used to quantitatively explore the fluxes and transformations of methane in ESAS sediments. For this purpose, we set-up a reaction network (Table C.3, C.4), model parameters (Table C.8), as well as boundary conditions (Table C.10) that are broadly representative for conditions encountered on the present-day Siberian shelf.

...applied to representative ESAS conditions

4.2.1.1 *From continuity equation to advection-diffusion-reaction equation*

In the BRNS, the general mass conservation for each solid and dissolved species is described by a a set of coupled advection-diffusion-reaction equations in porous media which are solved simultaneously (*e.g.* Berner, 1980; Boudreau, 1997).

The advection-diffusion-reaction equation

Each equation (one per species i) is a specific generalization of a continuity equation with fluxes F_i, related to the transport processes, and sources/sinks S_i related to the biogeochemical reactions. It reads:

$$\frac{\partial \xi(z) C_i(z,t)}{\partial t} = -\frac{\partial F_i(z,t)}{\partial z} + S_i(z,t). \tag{4.4}$$

Where $C_i(z,t)$ is the concentration of the species i (referred to pore-water volume if it is a dissolved species or solid matrix volume if it is a solid species) and $\xi(z)$ is the term accounting for this, *i.e.* the porosity $\xi = \varphi$ in case of a dissolved species or the solid fraction $\xi = \varphi_s = 1 - \varphi$ in case of a solid species.

Fluxes

The fluxes $F_i(z,t)$ consist of several components:

- $F_{D,i}(z,t)$: the molecular diffusive flux (only for dissolved species) is given by the Fick's law

$$F_{D,i}(z,t) = -D_i(z,t)\varphi(z)\frac{\partial C_i(z,t)}{\partial z} \tag{4.5}$$

  where $D_i(z,t)$ is the effective diffusion coefficient. The effective diffusion coefficients D_i is usually modeled as a time-independent variable and considered constant for each species. It is determined by correcting the diffusion coefficients in free solution D_i^0 (Boudreau, 1997) for tortuosity θ and temperature. Tortuosity is calculated by means of porosity φ according to a modified Weissberg relation (Boudreau, 1997): $\theta = 1 - \ln(\varphi^2)$. The relation between diffusion coefficient and salinity and temperature is provided in Table C.8. Note that the effective diffusion coefficients used in the model neglect pressure effects.

  The porosity φ follows an exponential decay with depth (Athy, 1930):

$$\varphi(z) = \varphi_0 e^{-c_0 z} \tag{4.6}$$

  with φ_0 porosity at the Sediment-Water Interface (SWI) and c_0 typical length scale for compaction (Table C.8).

- $F_{D_b,i}(z,t)$: the bioturbation flux, described as a diffusive flux (to be considered also for solid species), reads (Boudreau, 1986)

$$F_{D_b,i}(z,t) = -D_{b,i}(z,t)\xi(z)\frac{\partial C_i(z,t)}{\partial z} \tag{4.7}$$

with $D_b(z,t)$ bioturbation coefficient. Considering no time dependency, the latter is assumed to follow an exponential trend below a given $z_{bio} = 5$ cm depth (Boudreau, 1997), *i.e.* :

$$\begin{cases} D_b(z) = D_b^0 & 0 \leq z \leq 5 \text{ cm} \\ D_b(z) = D_b^0\, e^{-(z-5)} & 5 < z < 300 \text{ cm} \end{cases} \tag{4.8}$$

and D_b^0 given in Table C.8.

- $F_{v,i}(z,t)$: the advective flux is given by

$$F_{v,i}(z,t) = v(z,t)\xi(z)C_i(z,t) \tag{4.9}$$

where $v(z,t)$ is the sedimentation rate $v(z,t) = \omega(z,t)$ for solid species and the sum of sedimentation rate and possible advective flow velocity $v_{up}(z,t)$ for dissolved species, *i.e.* $v(z,t) = \omega(z,t) + v_{up}(z,t)$. If we assume steady state compaction then the burial velocity reads (Berner, 1980):

$$\omega(z) = \left(\frac{1-\varphi_0}{1-\varphi(z)}\right)\omega_0 \tag{4.10}$$

with ω_0 sedimentation rate at the SWI. A site where $v_{up} \neq 0$ is denominated as *active* while a site with null upward water velocity is defined as *passive*.

- $F_{NL,i}(z,t)$ represent any form of non-local transport. In its more classical form (Boudreau, 1997) it is given by the bioirrigation provided by irrigated furrows digged by benthic fauna and it reads

$$F_{irr}(z,t) = -\int_0^z \alpha_i(y)\varphi(y)[C_i(0,t) - C_i(y,t)]dy \tag{4.11}$$

where $\alpha_i(z)$ is the bioirrigation coefficient, $C_i(0,t)$ is the concentration of the species i at the SWI. It affects only the dissolved species and therefore only porosity φ enters the equation. The bioirrigation parameter α is modeled as (Thullner et al., 2009)

$$\alpha(z) = \alpha_0\, e^{-z/z_{irr}} \tag{4.12}$$

where α_0 is the bioirrigation coefficient, z_{irr} the bioirrigation attenuation depth (see Table C.8) and $\alpha = 0$ for solid species.

Bioirrigation is the only non-local flux considered

Yet other forms of non-local transport may be considered in the Arctic shelf scenario, such as ice scouring or bubble migration in sediments rich of free gas. These processes are even more difficult to be modeled and therefore are not included in the current version of BRNS.

With the fluxes described above equation 4.4 takes the form of a standard advection-diffusion-reaction which is the one implemented in BRNS or in any other reactive-transport diagenetic model (Berner, 1980; Boudreau, 1997) (dependencies on z and t has been omitted for simplicity):

$$\frac{\partial \xi C_i}{\partial t} = \frac{\partial}{\partial z}\left[(D_i + D_{b,i})\xi \frac{\partial C_i}{\partial z}\right] - \frac{\partial}{\partial z}(v\xi C_i) + \alpha_i \xi (C_i(0) - C_i) + S_i. \tag{4.13}$$

The reaction term S_i is written as

$$S_i = \sum_j \lambda_{ij} R_j \tag{4.14}$$

where λ_{ij} are the stoichiometric coefficients of all the reactions occurring with rate R_j that contribute in changing species i.

Movement of free gas is pseudo-diffusive

Finally, following Dale et al., 2008a, the migration of methane free gas is simply parameterized via a pseudo-diffusive term, with an apparent gas diffusion coefficient, $D_{CH_4(g)}$.

4.2.1.2 *Biogeochemical network*

The reaction network implemented here (33 species, 37 reactions) encompasses the most pertinent primary and secondary redox reactions, equilibrium reactions and mineral precipitation and adsorption reactions. A summary of the reactions, their stoichiometry and their rate formulations can be found in Table C.3 and Table C.4. The following section provides a description of the implemented reaction network, as well as of the reactions that affect the production/consumption of methane.

OM degradation and the redox ladder

PRIMARY REDOX REACTIONS Organic matter (OM) decomposition is a complex multi-step process (Arndt et al., 2013) carried out by micro-organism along a chain of enzyme-mediated biochemical redox reactions which exploits electronic cascades to provide energy. Carbon in the OM plays the role of electron donor, getting oxidized, and energy yield of the full redox reaction ultimately depends on the terminal electron acceptor (TEA) which overall acts as an oxidant, getting reduced. This entails a preferential sequence of how OM gets mineralized by microorganism along different metabolic pathways with different TEAs according to an energy gain ladder. Such a sequence determines the typical vertical zonation (Fig. 1.5) of the TEAs and byproducts of OM decomposition throughout the sediment column according to the redox sequence (Claypool et al., 1974; Froelich et al., 1979; Stumm et al., 1996).

The BRNS model accounts for the degradation of OM by aerobic degradation, denitrification, manganese oxide reduction, iron reduc-

tion, sulfate reduction (SR) and methanogenesis (Table C.3). The relative weight of each metabolic pathway is simulated through a series of kinetic limitation terms, enforcing their sequential utilization in the order of their decreasing Gibbs energy yields (Table C.2).

Primary reactions

OM degradation is modeled by a generalized first order kinetic equation, namely the decomposition rate is faster the more OM is present. The proportionality between organic carbon decay rate and organic carbon content is set by a degradability k which not necessarily has to be constant. We employed the reactive continuum model (RCM) (Aris, 1968; Ho et al., 1987; Boudreau et al., 1991) that describes compound-specific reactivities and, thus, captures the widely observed decrease in apparent organic matter reactivity with degradation state. In such model the degradability k is a continuous variable, whose distribution reads:

RCM

$$g(k) = \frac{g_0 k^{\nu-1} e^{-ak}}{\Gamma(\nu)} \tag{4.15}$$

where g_0 is a scale parameter, ν and a determine the shape of the distribution of k and $\Gamma(\nu)$ is the Gamma function[2].

The quantity a represents the average lifetime of the more reactive organic matter components in a reactive-continuum model (Boudreau et al., 1991) and the mean degradation constant $\langle k \rangle$ of the OM spectrum is given by $\langle k \rangle = \nu/a$. The choice of the RCM relies on the fact that it is considered more suitable for marine sediments than a discrete model (Aller et al., 2004; Arndt et al., 2013). It manages to encompass all the information about OM degradability in only two parameters, carriers of a theoretical meaning, instead of employing as many degradation constants as the number of carbon pools considered in a discrete model. Moreover the RCM is more flexible to account for the whole range of degradability that the Arctic OM shows, shifting its peak just by tweaking the parameters instead of changing the initial carbon content of each pool.

Motivation for the employment of a RCM

Another peculiarity of this formulation of the RCM is that, assuming distribution in Eq. 4.15, OM degradation S_{POC} can actually be rewritten as a first-order kinetic with the a degradability $K(t)$ dependent on the sediment age t (Boudreau et al., 1991), *i.e.*

RCM formulation as first-order kinetics

$$S_{POC} = \frac{dPOC(t)}{dt} = -K(t)POC(t) = -\frac{\nu}{a+t}POC(t) \tag{4.16}$$

where $POC(t)$ is the particulate organic carbon, *i.e.* the OM. $POC(t)$ in turns reads:

$$POC(t) = POC(0)\left(\frac{a}{a+t}\right)^{\nu} \tag{4.17}$$

2 $\Gamma(z) = \int_0^\infty t^{z-1}e^{-t}dt$.

$POC(0)$: the initial organic carbon concentration, which can be written in terms of the scale factor g_0 as

$$POC(0) = \frac{g_0}{a^\nu}. \tag{4.18}$$

This features allow one to estimate sediment age and POC vertical profile just coupling RCM and a discrete model as exposed in the following paragraph.

POC age is an important quantity

Estimate of sediment age t and POC content POC age and vertical profile are critical quantity to be evaluated. One approach would be performing *ab initio* simulations, but they would be difficult since a complete knowledge of past boundary conditions and how they evolved over time would be needed. Even when this knowledge is enough, simulation times are usually rather long and hence a different approach is generally used.

Age of non-bioturbated sediments

Using Eq. 4.10 and Eq. 4.6, in an unperturbed sediment setting, we find that the age at a certain depth z is provided by

$$t(z) = \int_0^z \frac{d\zeta}{\omega(\zeta)} = \frac{z + \frac{\varphi_0}{c_0}\left(e^{-c_0 z} - 1\right)}{\omega_0\left(1 - \varphi_0\right)}. \tag{4.19}$$

If another formulation for the porosity is employed, for instance:

$$\varphi(z) = \varphi_\infty + (\varphi_0 - \varphi_\infty)e^{-c_0 z} \tag{4.20}$$

where φ_∞ specifies the asymptotic value of the porosity, then the expression for the age $t(z)$ modifies as:

$$t(z) = \int_0^z \frac{d\zeta}{\omega(\zeta)} = \frac{(1 - \varphi_\infty)z + \frac{\varphi_0 - \varphi_\infty}{c_0}\left(e^{-c_0 z} - 1\right)}{\omega_0\left(1 - \varphi_0\right)}. \tag{4.21}$$

If the sediment column were not bioturbated, plugging Eq. 4.19 (or 4.21) into Eq. 4.17 would give the steady state profile of the organic matter throughout the whole sediments, with $POC(0)$ the POC concentration at the SWI (because considerations above legitimize a *space for time* substitution and initial time corresponds to the uppermost concentration).

Age of the bioturbated zone

The column is instead divided in bioturbated (the upper part) and not-bioturbated (below a certain depth). Because of bioturbation the upper layers are mixed, *i.e.* POC of different ages coexist at the same depth (Meile et al., 2005). This is actually the most difficult problem to be tackled to assign age to a certain sediment level. In order to deal with this issue, similarly to Dale et al., 2015, the POC in the bioturbated zone is modeled resorting to a multi-G approximation of the RCM. It means that, within the bioturbated region, the POC is represented by 500 distinct OM fractions, whose reactivity covers the spectrum $k = [k_{min} : 10^{-15}, k_{max} : -\log(a) + 2]$ yr^{-1} plus two extra fractions accounting for the reactivity $[0, k_{min}]$ and $[k_{max}, \infty]$. With these

Multi-G approximation of the RCM

considerations and considering constant porosity and sedimentation rate, Eq. 4.13 reads:

$$\varphi_s \frac{\partial POC_i(z,t)}{\partial t} = D_b \varphi_s \frac{\partial^2 POC_i(z,t)}{\partial z^2} - \omega \varphi_s \frac{\partial POC_i(z,t)}{\partial z} - \varphi_s k_i POC_i(z,t) \tag{4.22}$$

where $\varphi_s = 1 - \varphi$ and k_i is the reactivity of the i-th fraction of POC (*i.e.* POC_i) considered. Eq. 4.22 is an advective-diffusive-reactive equation which, in steady state, can be analytically solved for each fraction i, once the boundary conditions are provided. The general solution is:

$$POC_i(z) = Ae^{\lambda_1 z} + Be^{\lambda_2 z} \quad \text{where} \quad \begin{cases} \lambda_1 = \dfrac{\omega - \sqrt{\omega^2 + 4D_b k_i}}{2D_b} \\ \lambda_2 = \dfrac{\omega + \sqrt{\omega^2 + 4D_b k_i}}{2D_b}. \end{cases} \tag{4.23}$$

In this case the boundary conditions are given by

$$\begin{cases} POC_i(0) = POC_0 \cdot F_i & \text{at } z = 0 \\ D_b \frac{\partial POC}{\partial z} = 0 & \text{at } z = z_{bio} \end{cases} \tag{4.24}$$

where F_i is the fraction of initial POC_0 whose reactivity lies around k_i and z_{bio} is the depth of bioturbated zone where we impose that bioturbated flux shall be null. Bearing in mind Eq. 4.15 and Eq. 4.18, the distribution of the POC_0 lying around a certain value of $k = \bar{k}$ can be written as:

$$f(\bar{k}) = \frac{g(\bar{k})}{POC_0} = \frac{a^\nu \bar{k}^{\nu-1} e^{-a\bar{k}}}{\Gamma(\nu)}. \tag{4.25}$$

The initial fraction of POC_0 whose reactivity is within $[0, k_i]$, *i.e.* $F(k_i)$, can be obtained via integration of Eq. 4.25[3] and this allows to find finally the fraction F_i of POC_0 whose reactivity is in $[k_{i-1}, k_i]$ as

$$F_i = F(k_i) - F(k_{i-1}). \tag{4.26}$$

Enforcing boundary conditions (Eq. 4.24) for each of 502 fractions and summing up their solutions we find an approximate (numerical) solution of the RCM in the bioturbated layer. A comparison between the solution obtained in this way and what should be the RCM solution (Eq. 4.17) allows one to find the apparent age $t(z)$ of the sediments at each depth within the bioturbated zone and also at its bottom, *i.e.* $t(z_{bio})$. Below the bioturbated zone the apparent age is then found simply adding $t(z_{bio})$ and results of Eq. 4.19 (or 4.21).

The age profile and the POC profile found in this way is then calculated from BRNS at the very beginning of the simulation and imposed throughout the whole steady-state simulation.

3 And this brings into play the incomplete Gamma function $\gamma(s,z) = \int_0^s t^{z-1} e^{-t} dt$.

METHANOGENESIS AND METHANE CONSUMPTION Following the redox latter and the zonation of TEAs, after all the TEAs are consumed, the remaining organic matter may be degraded by methanogenesis (Table C.3, R6).

Formation of gaseous CH_4

If the concentration of dissolved methane exceeds the saturation concentration $[CH_4]^*$, methane free gas forms. The transfer rate of methane between the dissolved and gaseous phase is linearly controlled by the departure of the simulated dissolved methane concentration from the saturation concentration (Haeckel et al., 2004; Hensen et al., 2005; Tishchenko et al., 2005; Mogollón et al., 2009; Graves et al., 2017). $[CH_4]^*$ is calculated according to Dale et al., 2008a, derived from the formulation proposed by Duan et al., 1992 for which $[CH_4]^*$ depends on *in situ* salinity, pressure and temperature. Here, we assume that the formed methane gas is inaccessible to microbial activity and hence by-passes anaerobic and/or aerobic oxidation zones. In contrast, dissolved methane can be consumed by anaerobic (AOM) or aerobic oxidation of methane (AeOM). Free gas can re-dissolve into porewater once porewater methane concentration fall below the saturation level and may then become available to methanotrophs.

Bimolecular AOM formulation

AeOM rate is simply described by a bimolecular rate law (Table C.4, R14). The description of AOM depends on the model scenario. For steady state simulations, we apply a simple bimolecular rate:

$$\text{rate}_{AOM} = k_{AOM}[CH_4][{SO_4}^{2-}]. \tag{4.27}$$

It is the simplest and most commonly used formulation of the AOM rate in reaction-transport models (*e.g.* Regnier et al., 2011). It accounts for kinetic controls and assumes that, under steady state conditions, bioenergetic controls are negligible (Dale et al., 2006; Regnier et al., 2011).

Bioenergetic AOM formulation

For transient model simulations, we apply a bioenergetic rate law in combination with an explicit description of the AOM-performing biomass (Dale et al., 2006; Dale et al., 2008c). It has been shown that the rates of redox reactions, whose energy yield is used by microorganisms to grow, can be coupled to biomass growth rates via a kinetic Monod term and a thermodynamic Boltzmann term (*e.g.* Rittmann et al., 2019). Hence, the time derivative of AOM-performing biomass (B) can be written as:

Population dynamics for the AOM biomass

$$\frac{dB}{dt} = \mu_g B \cdot F_K \cdot F_T - \mu_d B^2 \tag{4.28}$$

where μ_g is the growth rate and μ_d is the decay rate. F_K is the kinetic constraint given by:

F_K: the kinetic constraint

$$F_K = \frac{[CH_4]}{K_m^{CH_4} + [CH_4]} \cdot \frac{[{SO_4}^{2-}]}{K_m^{{SO_4}^{2-}} + [{SO_4}^{2-}]} \tag{4.29}$$

with $K_m^{{SO_4}^{2-}}$ half saturation constant of ${SO_4}^{2-}$ and $K_m^{CH_4}$ half saturation constant of CH_4, according to a typical Michaelis-Menten for

enzymatically-catalyzed reactions. F_T represent the thermodynamic limitation and is given by

F_T: the thermodynamic constraint

$$\begin{cases} 1 - \exp\left(\frac{\Delta G_r + \Delta G_{BQ}}{\chi RT}\right), & \text{if } \frac{\Delta G_r + \Delta G_{BQ}}{\chi RT} < 0 \\ 0, & \text{if } \frac{\Delta G_r + \Delta G_{BQ}}{\chi RT} > 0 \end{cases} \tag{4.30}$$

where R is the gas constant, T is the absolute temperature, χ is the average number of electrons transferred per reaction per mole of ATP produced (Jin et al., 2005), ΔG_r is the Gibbs free energy of the reaction and $\Delta G_{BQ} = 20$ kJ (mol e^-)$^{-1}$ is the minimum energy needed to support synthesis of $\sim \frac{1}{3} - \frac{1}{4}$ mol ATP (Dale et al., 2008c). In order to be thermodynamically favorable the total energy $\Delta G_r + \Delta G_{BQ}$ has to be negative, meaning the that Gibbs free energy provided by the catabolic reaction is sufficient to sustain the microbial biomass growth. ΔG_r is given by

$$\Delta G_r = \Delta G_r^0 + RT \ln\left(\gamma \frac{[HS^-] \cdot [HCO_3{}^-]}{[CH_4] \cdot [SO_4{}^{2-}]}\right) \tag{4.31}$$

with ΔG_r^0: standard free energy of the reaction, the second term: deviations from standard conditions (temperature and reaction quotient) on Gibbs free energy and γ: a parameter representing departure from ideal behavior.

The link between substrate consumption and microbial growth (anabolism) is given by Dale et al., 2006:

Macrochemical anabolic reaction

$$\begin{aligned} 13.8SD \cdot SO_4{}^{2-} + 14.3SD \cdot CH_4 + 0.2SD \cdot NH_4{}^+ + \\ + 0.3SD \cdot H^+ \longrightarrow 0.2B + 13.3SD \cdot HCO_3{}^- + 13.8SD \cdot HS^- \end{aligned} \tag{4.32}$$

Assuming that the cellular composition of the biomass B is equal to $C_5H_7O_2N$ (Dale et al., 2006; Dale et al., 2008c; Rittmann et al., 2012). $SD = (1 - \varphi)/\varphi$ is the conversion factor between dissolved and solid species, here represented by microorganisms (which are assumed to be attached to the solid matrix). Catabolism is linked to biomass growth (anabolism) through the growth yield. We apply a yield of 0.0713 (Dale et al., 2006), which falls at the upper end of reported AOM growth yields, *i.e.* $0.05 - 0.07$ (Dale et al., 2006; Nauhaus et al., 2007).

Growth yield: 0.0713

OTHER REACTIONS The rates of secondary redox reactions (Table C.4), are described by bimolecular rate laws (*e.g.* Wang et al., 1996). Adsorption reactions are considered as fast equilibrium processes (Table C.4, R28-R30). Mineral precipitation rates are simulated according to kinetic-thermodynamic rate laws (Table C.4, R16-R24).

4.2.1.3 *Boundary conditions*

Boundary conditions place the model in its environmental context. For dissolved species, constant bottom water concentrations (Dirichlet boundary conditions) are applied at the SWI, while a known flux condition (Neumann boundary condition) are applied for solid species. At the lower boundary, a zero diffusive flux boundary condition ($\partial C/\partial z = 0$) is considered for all species except methane, for which a Dirichlet condition is specified to account for methane supplied from thawing permafrost and/or dissociating gas hydrates below.

4.2.2 *Model evaluation*

In order to evaluate the performance of the BRNS in capturing the main diagenetic patterns observed in Arctic marine sediments we perform two, steady state model case studies for two Arctic sites: 1) a cold seep site off Vesterålen (Norway), GC-51[4] and 2) a site (S23) on the ESAS, Laptev Sea[5].

1st case study: offshore the Versterålen (Norway)

Even though it is not located on the ESAS, the core offshore Norway (GC-51) is chosen because it was retrieved in the Hola trough, on the continental shelf of Vesterålen, and is thus representative for the type of shelf sediments considered in our study. In addition, porewater data reveals a well-developed SMTZ. The site has already been subject of a modeling analysis by Sauer et al., 2016, hence offering a benchmark for our simulation results. The Vesterålen site shows no sign of active water flow and, thus represents a passive setting ($v_{up} = 0$ cm yr^{-1}). Upper boundary conditions and model parameters are constrained on the basis of observations reported by Sauer et al., 2016 (Table C.6). In addition, we impose the POC depth-profile reported in Sauer et al., 2015 and evaluate the age of the organic matter using the sedimentology reported in Sauer et al., 2016.

2nd case study: passive core in the Laptev Sea (Russia)

The Laptev Sea core S23 has also been subject to a modeling study by Brüchert et al., 2018. Similar to core GC-51, this site also shows no active flow and the advective velocity v_{up} is thus set to zero. Upper boundary conditions and model parameters are constrained on the basis of the observations reported by Brüchert et al., 2018. Because Brüchert et al., 2018 do not report organic carbon profiles, the POC depth-profile is calculated through the RCM (described in Section 4.2.1.2 and 4.2.1.2) by assuming a OM content ($[CH_2O]$= 1.5 wt%) at the SWI that is broadly representative for Arctic shelf sediments.

NH_4^+ as proxy for OM degradation

When evaluating model performance, particular attention is given to sulfate, methane and ammonium (NH_4^+) depth profiles. While the former two species are of main interest for evaluating simulated AOM dynamics, NH_4^+ is a good indicator for OM degradation since it is produced by the degradation of organic matter (see Table C.3) and is

4 68.9179°N, 14.2858°E, 222 m water depth; Sauer et al., 2015; Sauer et al., 2016.
5 76.171°N, 129.333°E, 56 m water depth; Brüchert et al., 2018.

only affected by nitrification (Table C.4, R7) and adsorption (Table C.4, R28). The latter, although important, acts homogeneously throughout the sediments (considering the slight variation in sediment porosity, LaRowe et al., 2017). It can thus only cause uniform shifts in $[NH_4^+]$ profile, but does not affect the overall shape of the NH_4^+ depth profile.

For both case studies, OM reactivity parameters are varied to find the best fit between observed and simulated porewater profiles.

4.2.3 *Modeling strategy*

4.2.3.1 *Steady state sensitivity analysis*

To evaluate the main physical and biogeochemical controls on the efficiency of the AOM biofilter and non-turbulent methane emission from ESAS sediments, we conduct a comprehensive steady state sensitivity study. For this purpose, we design a set of two baseline scenarios:

Baseline simulations: passive and active sites

1. a passive case, *i.e.* $v_{up} = 0$ cm yr^{-1};
2. an active case, *i.e.* with $v_{up} = 1$ cm yr^{-1}, a value which falls within the range of fluid flow velocities $v_{up} = 0.005 - 30$ cm yr^{-1} observed across a wide range of different active environments (Regnier et al., 2011).

For both baseline scenarios, we assume a water depth of 30 m, which is similar to the average water depth of the ESAS ~45 m (James et al., 2016). Temperature is set equal to 0 °C, and thus similar to the yearly average of −0.79 °C observed in the Laptev Sea at a depth of about 30 m (Dmitrenko et al., 2011). The bioturbation coefficients D_b^0 and bioirrigation coefficients α_0 (Thullner et al., 2009) are then derived from global empirical relationships according to Middelburg et al., 1997 and Thullner et al., 2009, respectively. The methane saturation concentration $[CH_4]^*$ is calculated on the basis of the relationship proposed by Dale et al., 2008a assuming a soil matrix density of 2.8 g cm^{-3}. Values of φ_0 and c_0 (see Eq. 4.6) are determined based on LaRowe et al., 2017.

Boundary conditions are reported in Table C.10 and informed by observations. They are chosen to be broadly representative of the wider Siberian shelf environment. Each sensitivity study run is forced with a range of different dissolved $[CH_4]$ concentrations at the lower model boundary, mimicking different methane fluxes from thawing permafrost at depth. The applied set of methane concentrations at the lower boundary range from zero to the methane gas saturation concentration $[CH_4]_- = 0 - 20 - 100 - 330 - 1169 - 5455$ μM and also include the highest methane concentration in ESAS cores observed by Overduin et al., 2015b ($[CH_4]_- = 1.169$ mM).

Lower BC: $0 - [CH_4]^*$

Table 4.1: Model parameters changed in the OAT sensitivity studies. Reported values are for the baseline simulations.

Quantity	Meaning	Value	Units	Reference
ω	Sedimentation rate	0.123	cm yr^{-1}	Burwicz et al., 2011
a	Average lifetime of reactive OM	10	yr	This study
v_{up}	Upward water velocity	0, 1	cm yr^{-1}	This study
α_0	Bioirrigation coefficient	99.5	yr^{-1}	Thullner et al., 2009
k_{AOM}	AOM rate constant	$5.0 \cdot 10^3$	M^{-1} yr^{-1}	Regnier et al., 2011
$[CH_4]_-$	CH_4 lower boundary condition	0-5.455	mM	This study

Table 4.1 and Table C.8 summarize the parameters applied in the baseline simulation and Table C.10 provides an overview of the applied upper boundary conditions.

Design of the OAT sensitivity study

A set of five "one-at-a-time" (OAT) parameter variation experiments, encompassing the most important controls on benthic methane cycling (Regnier et al., 2011; Meister et al., 2013; Egger et al., 2018) is performed for both the passive as well as active baseline scenario:

1. Sedimentation rate ω. The sedimentation rate is varied over two orders of magnitude ($0.03 - 0.123 - 0.17 - 1.5$ cm yr^{-1}). Maximum values are comparable to terrestrial sediment accumulation rates in the Lena river delta (Bolshiyanov et al., 2015), fast marine sedimentation rates during the early Holocene sea transgression (Bauch et al., 2001) and marine accumulation on subsea permafrost deposit in Buor Khaya Bay (~ 1.1 cm yr^{-1}, inferred from Overduin et al., 2015b), while minimum values are representative of sedimentation rates found in the East Siberian Arctic Sea (Stein et al., 2001 in Levitan et al., 2009). The baseline value of ω is calculated based on the empirical global relationship proposed by Burwicz et al., 2011.

2. Active fluid flow v_{up}. Buoyancy-induced motion (Baker et al., 1988), water streams channeled through fault lines or groundwater discharge (Charkin et al., 2017) can cause active fluid flow in Arctic shelf sediments underlain by subsea permafrost or gas hydrates (Judd et al., 2009; Semenov et al., 2019). Therefore, v_{up} is varied from $0 - 0.3 - 0.5 - 1 - 3 - 7 - 10$ cm yr^{-1}. This interval falls in the range of reported upward advective water velocities in marine sediments $0.005 - 30$ cm yr^{-1} (Regnier et al., 2011).

3. AOM constant k_{AOM}. Rate constants implicitly account for factors that are not explicitly described in the model and thus tend

to show a strong variability between sites. A comprehensive compilation of published model AOM rate constants (Regnier et al., 2011) reveals a variability of over six orders of magnitudes [10 M^{-1} yr^{-1} – 10^7 M^{-1} yr^{-1}]. The AOM rate constant k_{AOM} (Eq. 4.27) is thus varied over the range $k_{AOM} = 5 \cdot 10^2 - 5 \cdot 10^3 - 5 \cdot 10^4 - 5 \cdot 10^5 - 5 \cdot 10^6 - 5 \cdot 10^7$ M^{-1} yr^{-1}.

4. Organic matter reactivity (i.e. a RCM parameter). Although the apparent OM reactivity is controlled by a combination of two parameters (a and ν), previous studies indicate a less pronounced variability in ν (Arndt et al., 2013; Sales de Freitas, 2018), as well as a strong control of a on the SMTZ depth (Regnier et al., 2011; Meister et al., 2013). Thus, ν was kept constant, while a was varied over the entire range of previously published values $a = 0.1 - 1 - 10 - 100 - 500 - 1000$ yr (Arndt et al., 2013).

5. Bioirrigation coefficient α_0. Bioirrigation activity remains largely unconstrained on the Siberian shelf due to the scarcity of observational data (Teal et al., 2008). However, environmental stressors, such as ice scouring (*e.g.* Shakhova et al., 2017 and references therein) and trawling are detrimental to the local fauna, thus suggesting a low bioirrigation intensity. Yet, observations from other polar sites indicate that although biological diversity and activity is often low, it might be locally enhanced (Clough et al., 1997). In addition, ice scouring might also seasonally boost the non-local transport. We therefore, varied α_0 over the entire range of plausible values : $0 - 33 - 66 - 99.5 - 120 - 240$ yr^{-1} (Thullner et al., 2009).

TWO-LEVEL FACTORIAL SENSITIVITY ANALYSIS In order to corroborate findings of the OAT sensitivity analysis and to put into perspective not only the role that one parameter has but also possible effect of interactions among factors, we performed an "all-at-a-time" (AAT) sensitivity analysis. Among the vast variety of procedures which could be employed for of global sensitivity analysis (Pianosi et al., 2016) we used a two-level factorial design (Box et al., 1978; Montgomery, 2007) and employed the Yates algorithm. This kind of sensitivity tests varies simultaneously all the factors and assigns to each factor only two values (see Table 4.2). It means that considering the 4 internal parameters and 2 environmental conditions already considered in the OAT sensitivity analysis, the test needs just $2^{(2+4)} = 64$ runs. Refer to Section C.3 in the appendix for a better understanding of this kind of sensitivity design.

Table 4.2: Model parameters changed in the OAT and AAT sensitivity studies. Reported values are the minimum and maximum value for the 2-level factorial sensitivity design.

Quantity	Meaning	Min - Max	Units	Reference
ω	Sedimentation rate	0.03 - 1.5	cm yr^{-1}	Burwicz et al., 2011
a	Average lifetime of reactive OM	0.1 - 1000	yr	This study
v_{up}	Upward water velocity	0 - 10	cm yr^{-1}	This study
α_0	Bioirrigation coefficient	0 - 240	yr^{-1}	Thullner et al., 2009
k_{AOM}	AOM rate constant	$5\,10^2$ - $5\,10^7$	M^{-1} yr^{-1}	Regnier et al., 2011
$[CH_4]_-$	CH_4 lower boundary condition	0 - 5.455	mM	This study

A previous example of such technique to investigate the response of a reactive-transport model is found in Dale et al., 2006.

We investigated the role that simultaneous change of the quantities have on four outputs: methane flux at the SWI, SMTZ depth, AOM filter efficiency and integrated AOM (ΣAOM).

4.2.3.2 *Transient Sensitivity Study*

Transient regime might affect CH_4 escape

Dale et al., 2008c showed that temporally varying environmental conditions may reduce the efficiency of the benthic AOM filter and facilitate methane escape due to the delayed response of the microbial community to changing conditions. Therefore, we also perform a series of transient simulations with a bioenergetic rate law for AOM (Eq. 4.28) and an explicit description of AOM biomass to explore the impacts of seasonal and climate change driven environmental activity on methane escape from the ESAS. Simulation results from the passive steady state baseline run with $[CH_4]_- = 0$ mM are used as initial conditions for the transient experiments. Four different transient environmental perturbation scenarios that reflect seasonal (1, 2), as well as idealized future (3, 4) environmental variability on the ESAS are run with three different values of $v_{up} = 0 - 1 - 5$ cm yr^{-1} over a period of 200 years:

Transient simulations

1. *Seasonal* CH_4: seasonal change of methane supply from permafrost thaw and/or hydrate destabilization. CH_4 concentration at the bottom of the sediment column: null for 6 months, then increasing up to a peak of $[CH_4]_-$ ($20 - 100 - 330 - 1169 - 5455$ μM) for the remaining 6 months of the year and again back to null concentration. See Fig. 4.1.*a*.

Seasonal trend

2. *Seasonal* $CH_4 + {SO_4}^{2-}$: seasonal freshening of waters due to riverine discharge and sea ice melt. During winter, higher bottom

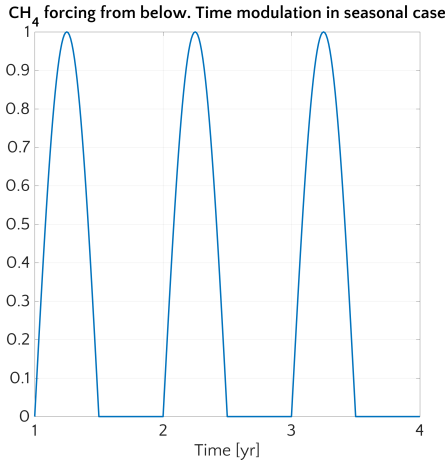

(a) Factor multiplying $[CH_4]_-$ in seasonal transient case

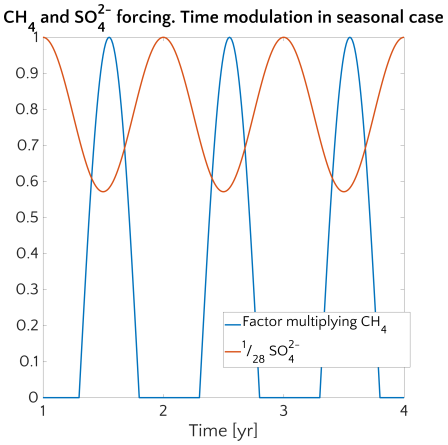

(b) Seasonal transient case: factor multiplying $[CH_4]_-$ (blue) and $1/28$ of $[SO_4^{2-}]_+$ upper boundary concentration (red, units: mM). The values of SO_4^{2-} follow a seasonal cycle according to salinity variation.

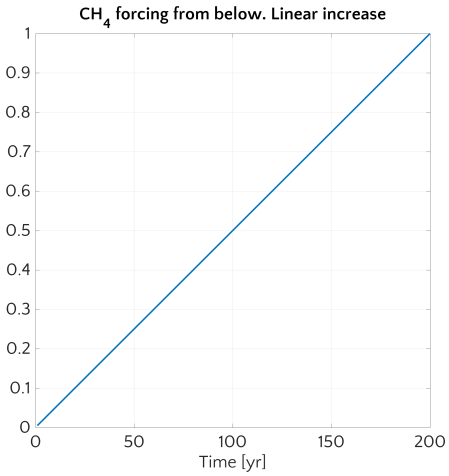

(c) Factor multiplying $[CH_4]_-$ in linear transient case.

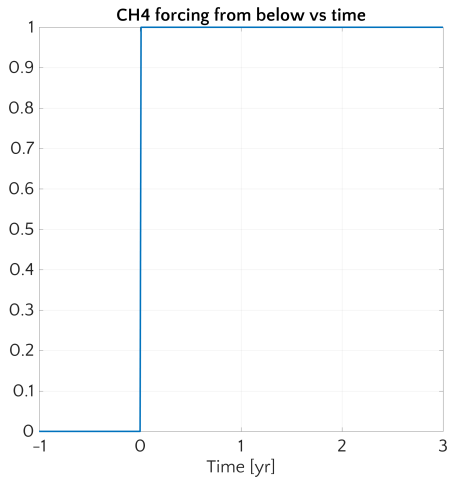

(d) Factor multiplying $[CH_4]_-$ in instantaneous transient case.

Figure 4.1: Forcing of CH_4 from below and SO_4^{2-} from above in case of different transient scenarios.

salinity (Dmitrenko et al., 2011) results in higher sulfate concentration (Dickson et al., 1994), while lower salinities and thus sulphate concentrations characterize the melt season. The bottom boundary condition for methane $[CH_4]_-$ follows an opposite trend: it is set to zero during the winter months and increases in Arctic summer. See Fig. 4.1.*b*.

3. *Linear* CH_4: slow increase in methane supply from permafrost thaw and/or hydrate destabilization. A linear increase of the

Long-term trend

bottom boundary methane concentration $[CH_4]_-$ (from 0 up to the peak) over 200 years is applied. See Fig. 4.1.*c*.

4. *Sudden* CH_4: abrupt increase of methane supply from permafrost thaw and/or hydrate destabilization. An instantaneous change of bottom boundary methane concentration - from 0 to one of the peak value $[CH_4]_-$ - is applied. See Fig. 4.1.*d*.

4.2.3.3 *Analyzed output*

For each simulation (steady state or transient) we evaluate the effect of the respective parameter change on:

1. the non-turbulent (i.e. not-ebullition driven) flux of methane from the sediments into the water column - in the following also called (CH_4) *efflux*;
2. the depth of the SMTZ;
3. the efficiency (η) of the AOM biofilter (see Appendix C.1 for the exact definition of η applied here).

In addition, fluxes of SO_4^{2-} and CH_4 at the SMTZ, the maximum and integrated AOM rate and the Damköhler number (D_a) for AOM and methanogenesis are also calculated. Damköhler number is defined as Eq. C.5 (see Appendix C.2) and sets the ratio between the typical transport time-scale and the typical reaction time-scale. If $D_a < 1$, the reaction time-scale is longer than transport time-scale (i.e. the reaction is slower) and the process is reaction-limited. If $D_a > 1$ the process is transport-limited. Finally, for transient simulations, the integrated AOM-performing biomass (ΣB) was also analyzed.

4.3 RESULTS AND DISCUSSION

4.3.1 *Case studies*

4.3.1.1 *Case study: Cold seep off Vesterålen, Norway*

Good agreement above the SMTZ

Fig. 4.2 compares simulated and observed depth profiles for site GC-51. The values of the model quantities employed in this simulations are reported in Table C.6. Simulation results show an overall satisfactory agreement with measurements. The general shape of the downward diffusing SO_4^{2-} and upward diffusing CH_4 depth profiles is similar to the profiles that are typically observed in passive sediments. In addition, the model reproduces the observed SMTZ depth, located at about 100 cm. Above the SMTZ, the simulated CH_4 concentrations closely agree with measurements, but simulated and observed depth profiles diverge significantly below the SMTZ. Such a discrepancy is common (*e.g.* Dale et al., 2008a; Sauer et al., 2016) and likely results

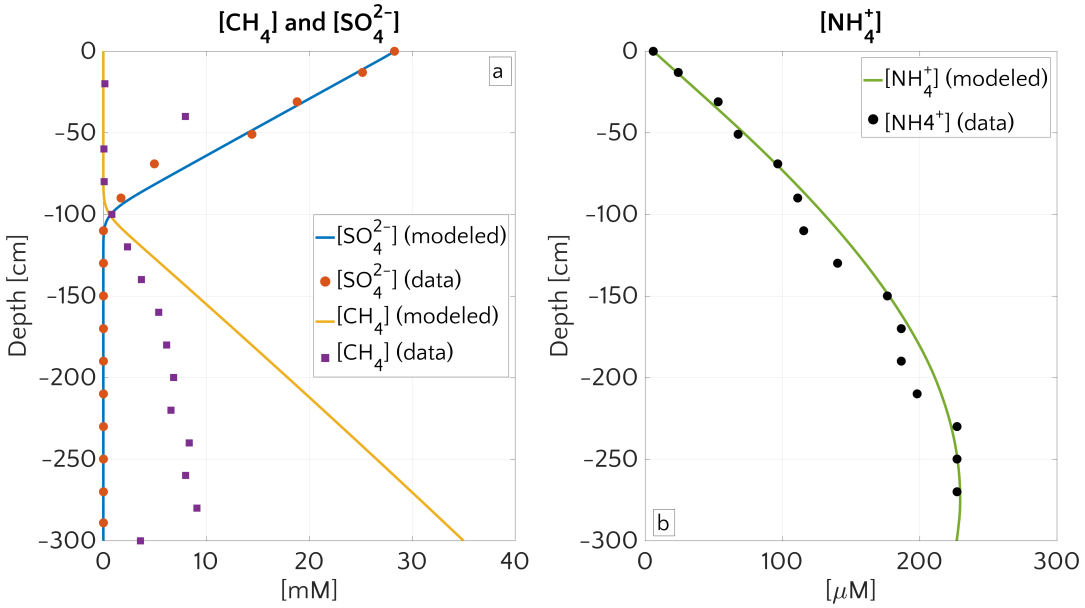

Figure 4.2: Pore water concentration profiles for CH_4, SO_4^{2-} (*a*) and NH_4^+ (*b*) at site GC-51 of Hola trough. Dots represents the measurements and continuous lines the simulated results. The boundary conditions employed in the model are reported in Table C.6.

from degassing during core extraction and recovery (Dickens et al., 2003). Yet, the simulated CH_4 concentration close to the lower model boundary (35 mM) is consistent with the values reported in Sauer et al., 2016 (30 mM) and is lower than the in-situ methane saturation concentration at that depth (39 mM).

Possible reasons of discrepancy below the SMTZ

Furthermore, the observed NH_4^+ profile is also well reproduced, suggesting that the model captures OM degradation dynamics well. Model derived organic matter degradation rate parameters of $a = 1100$ yr, $\nu = 0.100$ indicate a generally low reactivity of OM depositing at this site, which is in agreement with observations and low NH_4^+ concentrations.

Good agreement for NH_4^+

4.3.1.2 *Case study: sediment core on Laptev Sea shelf*

The sediment core S23 was collected during SWERUS-C3 campaign in summer 2004, at station n. 23. Brüchert et al., 2018 already performed a modeling of the porewater profile, which can be compared to our results. The sediments used to lie on the shelf of the Laptev Sea at 76.171° N, 129.333° E and at a water depth of 56 m. This point showed no indication of active methane bubble plumes, hence also in this case v_{up} was set to zero. For this simulations we employed the technique described in Section 4.2.1.2 to assign the OM vertical profile. We considered then, for the species indicated, the boundary conditions described in Brüchert et al., 2018 - see Table C.7. Varying then a and ν, as in the case of the seepage offshore Vesterålen archipelago, we reproduced POC, $[NH_4^+]$ and $[O_2]$ better

Good agreement for NH_4^+, O_2, Mn^{2+} and Fe^{2+}

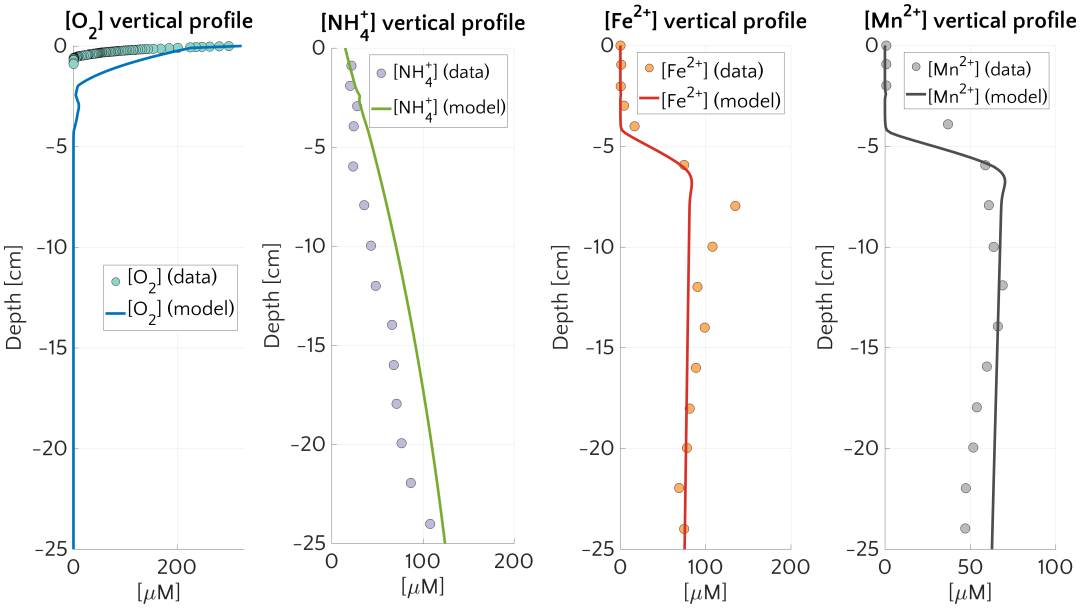

Figure 4.3: Pore water profiles reproducing O_2, NH_4^+, Fe^{2+}, Mn^{2+} resulting from model simulation and measurement at station n. 23 of the SWERUS-C3 campaign and analyzed by Brüchert et al., 2018

fitting the measurements. Modifying unconstrained boundary conditions for MnO_2 and $Fe(OH)_3$, the vertical profiles of Mn^{2+} and Fe^{2+} were then achieved. We aimed at modeling OM and reproducing O_2, NH_4^+, Mn^{2+} and Fe^{2+} (see Fig. 4.3). Our simulation is not able to well reproduce vertical profiles of SO_4^{2-} (not shown) and this is very likely ascribable to a jump in the age of OM material that our procedure does not take into account.

SO_4^{2-} is not well reproduced

4.3.2 *Main physical and biogeochemical controls on potential non-turbulent methane flux from ESAS sediments*

4.3.2.1 *General patterns of methane and sulfate cycling on the ESAS*

AOM is an efficient sink

The comprehensive ensemble of all sensitivity experiments allows exploring the general patterns of methane and sulfate cycling under a range of environmental conditions that is broadly representative for conditions encountered on the ESAS (Fig. 4.4). Model results confirm that AOM is an efficient sink for the diffusive CH_4 supply from below. For 95% of the runs and therefore for most of the investigated environmental conditions, $95 - 99.9\%$ of the upward diffusing CH_4 is consumed within the SMTZ, resulting in very small or negligible methane effluxes ($\leq 10^{-2}$ $\mu molCH_4$ cm^{-2} yr^{-1}) from the sediment. If upscaled to the total area of the ESAS ($\sim 1.485 \cdot 10^6$ km^2, Wegner et al., 2015) the smallest simulated non-turbulent methane flux (*i.e.* $1.4 \cdot 10^{-13}$ μmol cm^{-2} yr^{-1}, Fig. 4.4.*b*) would sum up to a total flux

of 2.1 mmolCH_4 yr^{-1} resulting in a negligible role of non-turbulent, benthic methane fluxes to the Arctic methane budget.

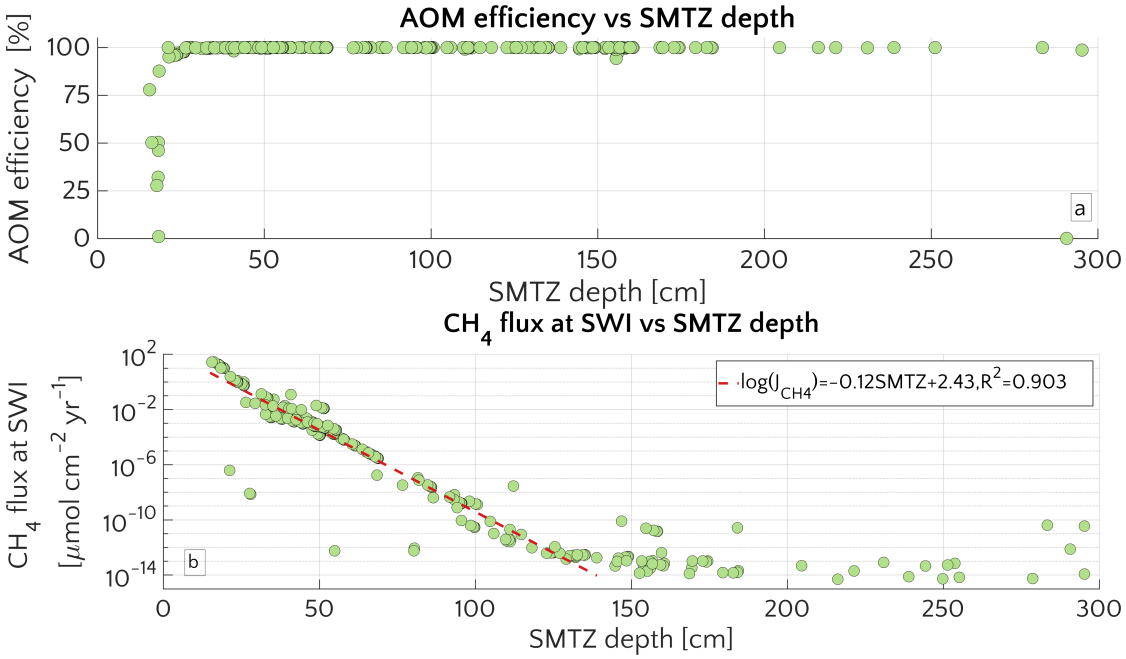

Figure 4.4: Aggregation of all the simulations performed for the OAT sensitivity study. *a*. AOM efficiency versus the depth of the SMTZ. *b*. Scatter plot and semi-log fit of the methane flux (J_{CH4}) at the SWI versus SMTZ depth.

Low AOM efficiency corresponds to a shallow SMTZ

Yet, model results also show that, under a specific set of environmental conditions that lower the efficiency of the AOM biofilter (see detailed discussion below), non-turbulent CH_4 escape from ESAS sediments can reach values up to 27 μmolCH_4 cm^{-2} yr^{-1}. Simulation results show that these high effluxes and, thus, low AOM biofilter efficiencies, are generally simulated for environmental conditions that cause a shallow location of the SMTZ ($<$ 18 cm) and that they are very sensitive to changes in environmental conditions that would cause a deepening of the SMTZ. For instance, a deepening of the SMTZ from 18 to 26 cm results in a rapid increase in AOM efficiency from 1% to 98% (Fig. 4.4.*a*). Furthermore, results indicate that, for SMTZ depths larger than 26 cm, AOM remains an efficient barrier across the full spectrum of investigated environmental conditions (Fig. 4.4). The observed link between AOM filter efficiency and SMTZ is reflected in the strong (semilog) linear relationship between methane flux at the SWI and the SMTZ depth (Fig.4.4.*b*). Such a relationship reveals the pivotal connections between these two quantities and mirrors the empirically found linear log-log relationship (Fig. 4.5) between measured CH_4 fluxes at the SMTZ and the SMTZ depths and identified at a global scale by Egger et al., 2018.

CH_4 flux at the SWI vs. SMTZ

High fluxes comparable to mud-volcanoes and coastal settings

Maximum simulated CH_4 effluxes are thus comparable in magnitude to fluxes reported from mud-volcanoes, *e.g.* in the Gulf of Cadiz 2.1 – 40.7 μmolCH_4 cm^{-2} yr^{-1} (Niemann et al., 2006a), Mosby

mud-volcano in the Barents Sea 0.03 μmolCH$_4$ cm^{-2} yr^{-1} (Niemann et al., 2006b). Other coastal settings (Dutch coastal reservoir 20 – 80 μmolCH$_4$ cm^{-2} yr^{-1}, Egger et al., 2016) or tidal flats (4 – 800 μmolCH$_4$ cm^{-2} yr^{-1},Dale et al., 2008b) show similar elevated values. Upscaling the highest simulated non-turbulent flux to the ESAS results in a total efflux of 0.408 TmolCH$_4$ yr^{-1} = 6.52 TgCH$_4$ yr^{-1} a value that equals ∼ 10% of global marine seepage at seabed level (Saunois et al., 2016) and similar in magnitude to the global methane efflux that has been estimated for upper continental slope sediments on a centennial timescale (4.73 TgCH$_4$ yr^{-1}, Kretschmer et al., 2015).

Upscale of the highest flux: 6.52 *TgCH$_4$ yr^{-1}*

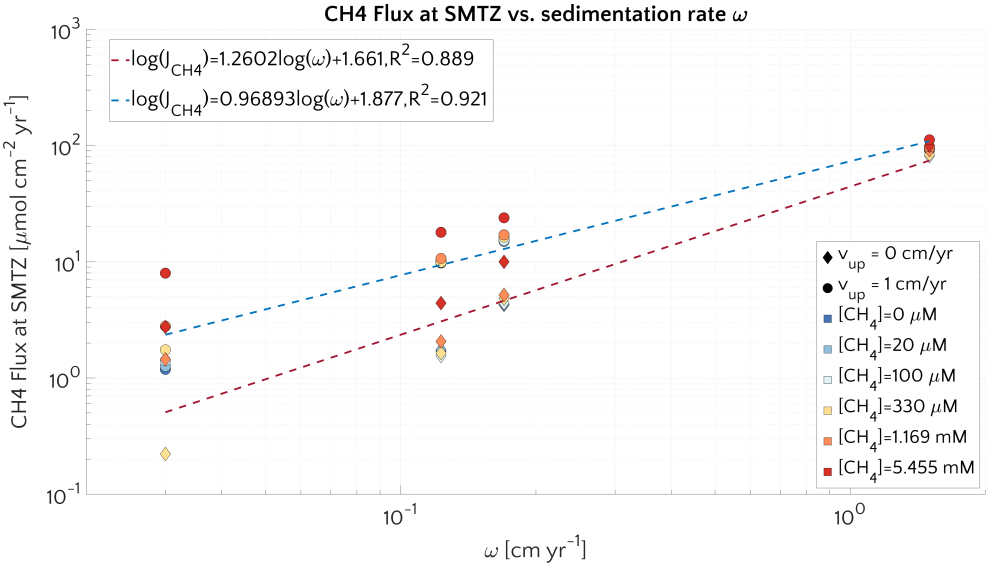

Figure 4.5: Methane flux at the centre of SMTZ versus ω for passive (diamonds) and active (circle) cases. Log-log fit is reported.

Further insights into the general drivers that control methane dynamics in ESAS sediments are provided by Damköhler numbers. Damköhler numbers for simulated methanogenesis ($D_{a_{MG}}$) and AOM ($D_{a_{AOM}}$) are reported in Fig. 4.6. $D_{a_{MG}}$ (purple circles) are < 1 , span a range of $\sim 0.0021 - 0.43$ and are thus comparable to previously reported $D_{a_{MG}}$ of 0.22 for methane gas hydrate bearing sites, such as the Hydrate Ridge and the Kithley Canyon (Chatterjee et al., 2011). They reveal that methanogenesis is always slower than methane transport and that CH_4 dynamics driven by methanogenesis are thus reaction-limited. This result is consistent with the fact that methanogenesis rates are merely supported by the slow influx and transport of OM by burial and bioturbation.

MG is reaction-limited

In contrast, high $D_{a_{AOM}}$ values ($D_{a_{AOM}} = 32 - 2.78 \cdot 10^5$ - Fig. 4.6, orange circles), show that AOM is transport-limited, suggesting a sensitive role of transport parameters in determining AOM efficiency and in controlling methane flux across the SMTZ and subsequently the SWI.

AOM is transport-limited

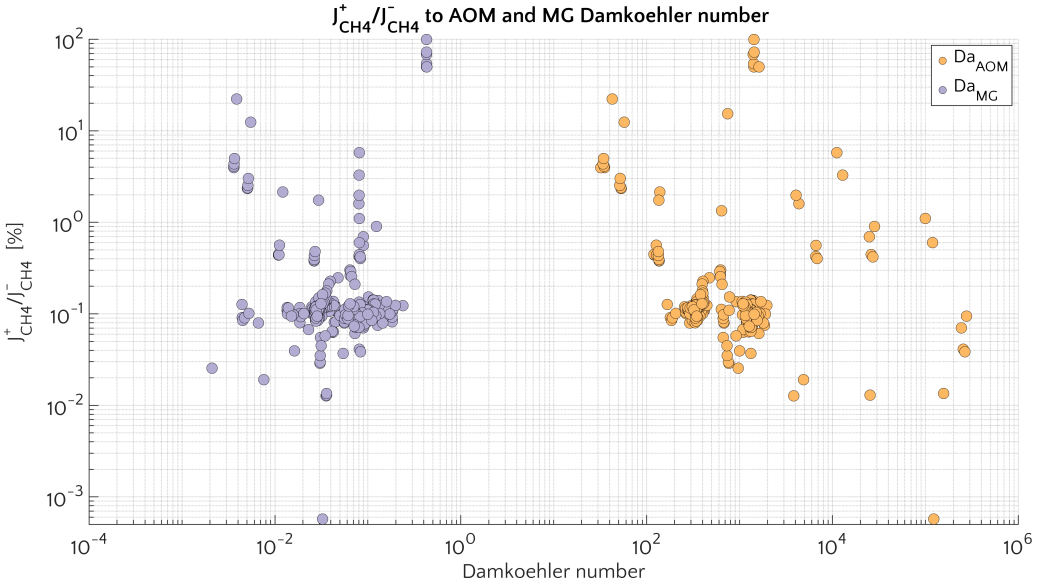

Figure 4.6: Ratio J^+_{CH4}/J^-_{CH4} (in %) as a function of the Damköhler numbers for AOM (orange) and for methanogenesis (purple)

4.3.2.2 *Environmental controls and mechanisms of methane escape from ESAS sediments*

Transport exerts the main control on CH_4 efflux

The simulated general patterns of methane and sulfate cycling on the ESAS thus broadly corroborate previous findings regarding the dominant environmental controls on AOM biofilter efficiency and SMTZ depth (Regnier et al., 2011; Egger et al., 2018; Meister et al., 2013; Winkel et al., 2018). Yet, they also challenge traditional views on the factors that favour high CH_4 escape through the SWI. In particular, they highlight the essential link between AOM efficiency and SMTZ depth, and as a consequence the central importance of environmental conditions that control the depth of the SMTZ. In addition, they suggest that transport processes play a dominant role for non-turbulent methane effluxes from ESAS sediments. The following sections explore the role of each of the investigated environmental conditions on methane efflux in more detail. They also shed light on the mechanisms behind non-turbulent methane escape from ESAS sediments.

ROLE OF ADVECTIVE TRANSPORT Fig. 4.7.*a* illustrates the effects of sedimentation rate ω on the flux of methane across the SWI. For both active ($v_{up} = 1$ cm yr^{-1}) and passive ($v_{up} = 0$ cm yr^{-1}) settings, simulated CH_4 effluxes increase exponentially with sedimentation rate (log-log linear, see Fig. 4.8.*a*) from $5.5 \cdot 10^{-15}$ μmolCH_4 cm^{-2} yr^{-1} for low sedimentation rates ($\omega = 0.03$ cm yr^{-1}) to values as high as 27.5 μmolCH_4 cm^{-2} yr^{-1} for high sedimentation rates ($\omega = 1.5$ cm yr^{-1}). Accordingly AOM acts as an efficient filter for upward diffusing methane (with $\eta \sim 100\%$, see Fig. C.5), in slowly accumulating sediments. Integrated AOM rates (ΣAOM), for both active and pas-

AOM is 100% efficient in slowly accumulating sediments

sive settings, are in agreement with these findings. They range from $0.04 - 3.7$ mol m^{-2} yr^{-1} and are, thus, comparable to values that are typically observed in sediments characterized by an efficient AOM biofilter (*e.g.* Albert et al., 1998; Martens et al., 1998; Regnier et al., 2011). In contrast, the efficiency of the AOM biofilter drops to $50 - 0\%$ for high sedimentation rates. The main driver behind the simulated high CH_4 fluxes and low AOM efficiencies in these rapidly accumulating sediments, are enhanced methanogenesis rates.

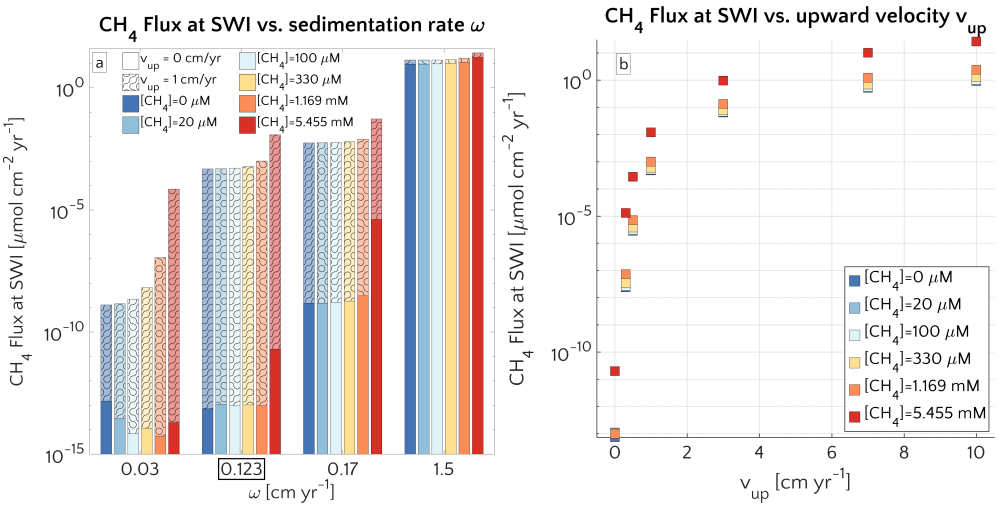

Figure 4.7: *a.* Barplot of the methane flux at the SWI versus ω for passive case (plain style) and active case (pattern style) and the $[CH_4]_-$ reported in the text. The squared value of ω is the reference value. *b.* Semilog plot of methane flux at SWI versus v_{up} for the different $[CH_4]_-$ reported in the text.

AOM is inefficient in fast accumulating sediment

High sedimentation rates facilitate not only the supply of organic matter to the methanogenic zone of the sediment, but also reduce residence times in the upper sediment layer, resulting in a lower OM age (see Eq. 4.19 and Eq. 4.21)/degradation state (see Eq. 4.16) within the methanogenic zone. The enhanced supply of reactive OM to anoxic sediment layers supports higher methanogenesis rates, resulting in higher methane porewater concentrations and an upward shift of the SMTZ.

v_{up} enhances CH_4 efflux

In addition, the presence of active fluid flow further enhances methane efflux. The CH_4 fluxes from below adds complexity to the overall methane dynamics and this effect is investigated further by contrasting Damköhler numbers for passive and active margins. Table 4.3 shows that for intermediate (or low) sedimentation rates, Da_{AOM} values significantly decrease with v_{up}, indicating that less and less methane consumption occurs within the typical transport time scale τ_T, thus, leading to a reduction in AOM biofilter efficiency. For instance, for $\omega = 0.123$ cm yr^{-1}, τ_T is about three orders of magnitude longer than τ_R without the presence of active fluid flow, while for $v_{up} = 10$ cm yr^{-1}, τ_T accelerates and is only one order of magnitude longer than τ_R, resulting in a reduced consumption within the

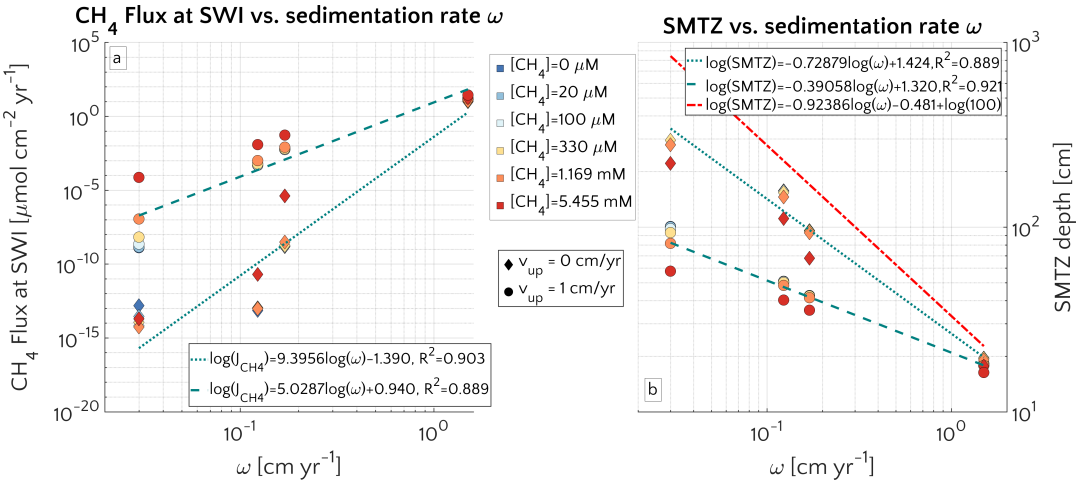

Figure 4.8: *a*. Log-log plot of methane efflux at SWI versus ω for passive case (diamonds) and active case (circle). The log-log fit is also displayed. *b*. Log-log plot of SMTZ depth versus ω for passive case (diamonds) and active case (circle) with log-log fit. The red line is the trend found by Egger et al., 2018 (the term log(100) is to take into account unit conversion).

SMTZ. Accordingly, the decrease in $D_{a_{AOM}}$ coincides with an increase in CH_4 effluxes (Fig. 4.7 and 4.8). The trend in $D_{a_{AOM}}$ is reversed for high sedimentation rates ($\omega > 1.5$) cm yr^{-1}, *i.e.* $D_{a_{AOM}}$ increases with increasing v_{up}, while CH_4 efflux remains constant. This increase in $D_{a_{AOM}}$ can be explained with a simple increase in AOM rates due to the build-up of methane gas in deeper sediment layers and its partial re-dissolution with in the AOM zone where porewater methane concentrations decrease (see Fig. 4.9).

Gaseous CH_4 formation with $\omega = 1.5$ cm yr^{-1}

Table 4.3: AOM Damköhler number for $\omega = 0.123$ cm yr^{-1} and $\omega = 1.5$ cm yr^{-1}. The two values reported for each v_{up} are the maximum and minimum values in the simulations with different bottom methane concentrations. Missing values are because simulations were not run with the corresponding pair of parameters.

		v_{up} [cm yr^{-1}]						
		0	0.3	0.5	1	3	7	10
ω	0.123	1206	1124	683	327	120	52	32
[cm yr^{-1}]		1521	1473	772	409	139	57	42
	1.5	470	-	-	1408	-	-	-
		518			1630			

Maximum simulated flux differences between active and passive settings can reach up to 10 orders of magnitude. Yet, flux differences quickly decrease with increasing sedimentation rates. Rapidly accumulating sediments show almost no difference in efflux between active and passive sites (Fig. 4.7.*a*). In contrast to sedimentation rates, the mechanism behind the control of v_{up} on non-turbulent methane efflux is straightforward and self-evident. Active flow enhances the

Advective transport does not keep up increase in $[CH_4]$

upcore transport of CH_4, shifting the SMTZ upcore and, thus, increasing CH_4 concentrations at shallow sediment depths (see Fig. 4.8.*b*). The apparent paradox of the CH_4 efflux insensitive to fluid flow in fast accumulating sediments can be resolved by examining the dissolved CH_4 depth profiles (Fig. 4.9). Simulated depth profiles are nearly identical and reveal CH_4 concentrations at or near the saturation concentration. In fast accumulating sediments, high methanogenesis rates result in an over-saturation of porewaters directly below the generally shallow SMTZ. High methanogenesis rates thus support the build up of methane gas. Methane gas formation also explains why, for these cases, integrated methanogenesis exceeds non-turbulent CH_4 fluxes by up to 6 times. In rapidly accumulating, active and passive sediments, non-turbulent CH_4 fluxes are thus essentially identical. However, active settings are characterized by the additional build-up of gaseous CH_4 and and by its potential escape through the SWI, a process not simulated in the present study.

Non-local transport dwarfs other transports

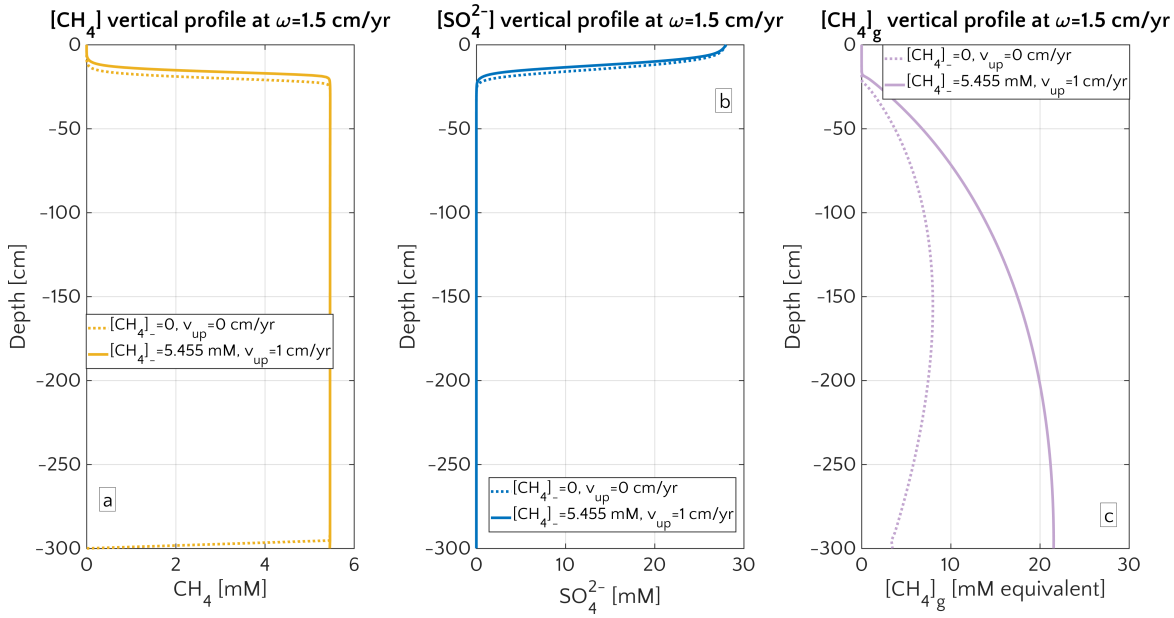

Figure 4.9: Porewater profiles in case of $\omega = 1.5$ cm yr^{-1} for CH_4 (*a*), SO_4^{2-} (*b*) and gaseous CH_4 (*c*). Dashed lines are simulation in passive scenario with $[CH_4]_- = 0$ mM, while continuous lines simulations display active scenario with $[CH_4]_- = 5.455$ mM, corresponding to the saturation concentration in the environmental conditions considered for the representative profile.

Model results thus show that the dominant mechanism behind the observed transport-control on non-turbulent CH_4 efflux is an overall increase in CH_4 concentration and an upcore shift of the SMTZ rather than an increasing relative contribution of advective transport processes to the total efflux. In fact, a comparison of the different methane transport processes across the SWI (Fig. 4.10) shows that the relative contribution of both the advection and molecular diffusion

flux to the total flux is small and further decreases with increasing v_{up}. High non-turbulent methane effluxes in rapidly accumulating and/or active settings are thus largely driven by the non-local irrigation flux (see Paragraph 4.3.2.2."Role of non-local transport" for more details on the role of irrigation). With increasing ω or v_{up}, the SMTZ shifts upcore, resulting in higher methane concentrations at shallow sediment depths and thereby reinforcing the relative contribution of non-local transport for CH_4 fluxes, as well as lowering the efficiency of the AOM barrier from $\eta \sim 100\%$ to $\eta \sim 78\%$.

Relation SMTZ vs. ω in agreement with global trend

The important role of the SMTZ location as a key control on CH_4 efflux is further confirmed by the observed exponential relationship between the location of the SMTZ and ω (Fig. 4.8.*b*). This result is qualitatively in agreement with the global compilation of empirical data by Egger et al., 2018, which reveals the same log-log decreasing trend between SMTZ and sedimentation rate. Our results are also consistent with observations from brackish sediments that show that sedimentation rates > 10 cm yr^{-1} give rise to high non-turbulent CH_4 fluxes ($20 - 80$ μmolCH_4 cm^{-2} yr^{-1}) and a high OM burial efficiency ($\sim 78\%$, Egger et al., 2016). Egger and co-workers explained these findings by the slow growth of AOM microorganisms and the resulting inability of the microbial community to consume all of the CH_4 produced. Yet, our results show that the same pattern can be observed without having to invoke a low efficiency of the AOM community. Our simulations thus indicate that the rapid burial of reactive organic matter to deeper sediment layers in rapidly accumulating sediments is sufficient to explain high CH_4 effluxes.

Comparison with Egger et al., 2016

Role of "a" as parameter describing the OM quality

ROLE OF ORGANIC MATTER QUALITY The quality of organic matter deposited onto the sediment exerts an additional control on CH_4 efflux. Fig. C.6 and C.7 show the effects of the organic matter quality only (as a function of OM degradation model parameter a, see Eq. 4.16) on CH_4 flux. But the real information is provided by Fig. 4.11, which illustrates the influence of the two quantities involved in the definition of OM flux (as Eq. 4.23 shows) namely the organic matter quality combined with sedimentation rate ω. The figure shows the joint effect of the two variables on non-turbulent methane efflux for both active and passive settings, as well as different methane fluxes from below. Results corroborate the dominant influence of sedimentation rates on methane efflux, while organic matter quality exerts a secondary control. Maximum fluxes are generally simulated for rapidly accumulating sediments $\omega > 0.5$ cm yr^{-1} that receive organic matter of intermediate quality ($a = 10 - 100$ yr), as the plot of the SMTZ (Fig. C.8.*a*) also shows.

Intermediate "a"s enhance $[CH_4]$ efflux

These findings are in agreement with previously published studies (Regnier et al., 2011; Meister et al., 2013) and can be explained with the fact that high methanogenesis rates require a supply of

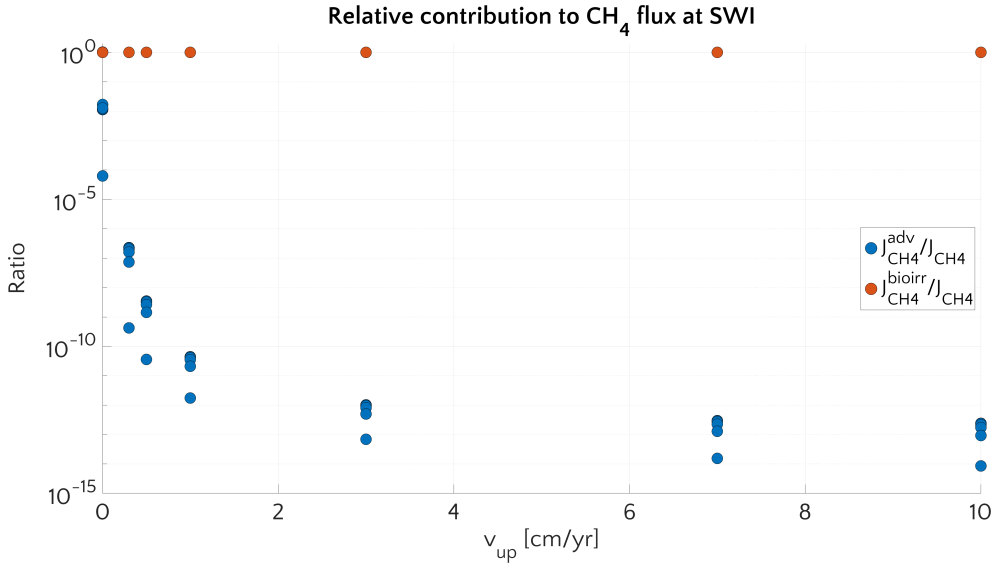

Figure 4.10: Relative contribution of transport processes to the CH_4 flux at the SWI: the advective component (blue) and the bioirrigation component (red). ω is set to the baseline value of 0.123 cm yr^{-1}. For each value of v_{up} and a specific flux component each dot corresponds to a simulation with a different value of bottom CH_4 concentration. Diffusive component of the flux is always $< 10^{-10}$ and therefore not shown.

reactive OM to the methanogenic zone. If organic matter quality is high ($a < 10$ yr), methanogenesis becomes substrate limited due to the rapid degradation of organic matter through energetically more favourable degradation pathways in the shallow sediments. In turn, if organic matter quality is low ($a > 100$ yr), methanogenesis becomes reactivity limited. The ideal combinations of organic matter reactivity and sedimentation rate that result in maximum methane effluxes correspond to conditions characterized by OM that is i) sufficiently reactive to support enhanced methanogenesis rates and thus an accumulation of CH_4 at depth, but ii) sufficiently unreactive (in comparison to the burial rate) to escape the complete degradation in non-methanogenic sediments.

Model results show that the onset of active fluid flow (Fig. 4.11.*c-d*) and an enhanced methane supply from below (i.e. higher CH_4 concentration at the lower boundary) increase the CH_4 efflux through the SWI without altering the overall patterns.

No evident relationship with OM fluxes

An investigation to find a potential trend between CH_4 efflux and the flux of OM at the SWI, at the SMTZ and the overall quantity of OM stored in the whole sediment column has been attempted. But no clear pattern emerged, as Fig. 4.12 highlights.

Bioirrigation enhances CH_4 effluxes in settings with shallow SMTZ

ROLE OF NON-LOCAL TRANSPORT Fig. 4.13 further investigates the influence of bioirrigation on non-turbulent CH_4 efflux from the ESAS. It enhances methane efflux in sediments that are characterized by a shallow SMTZ, for instance, due to high sedimentation rates, ac-

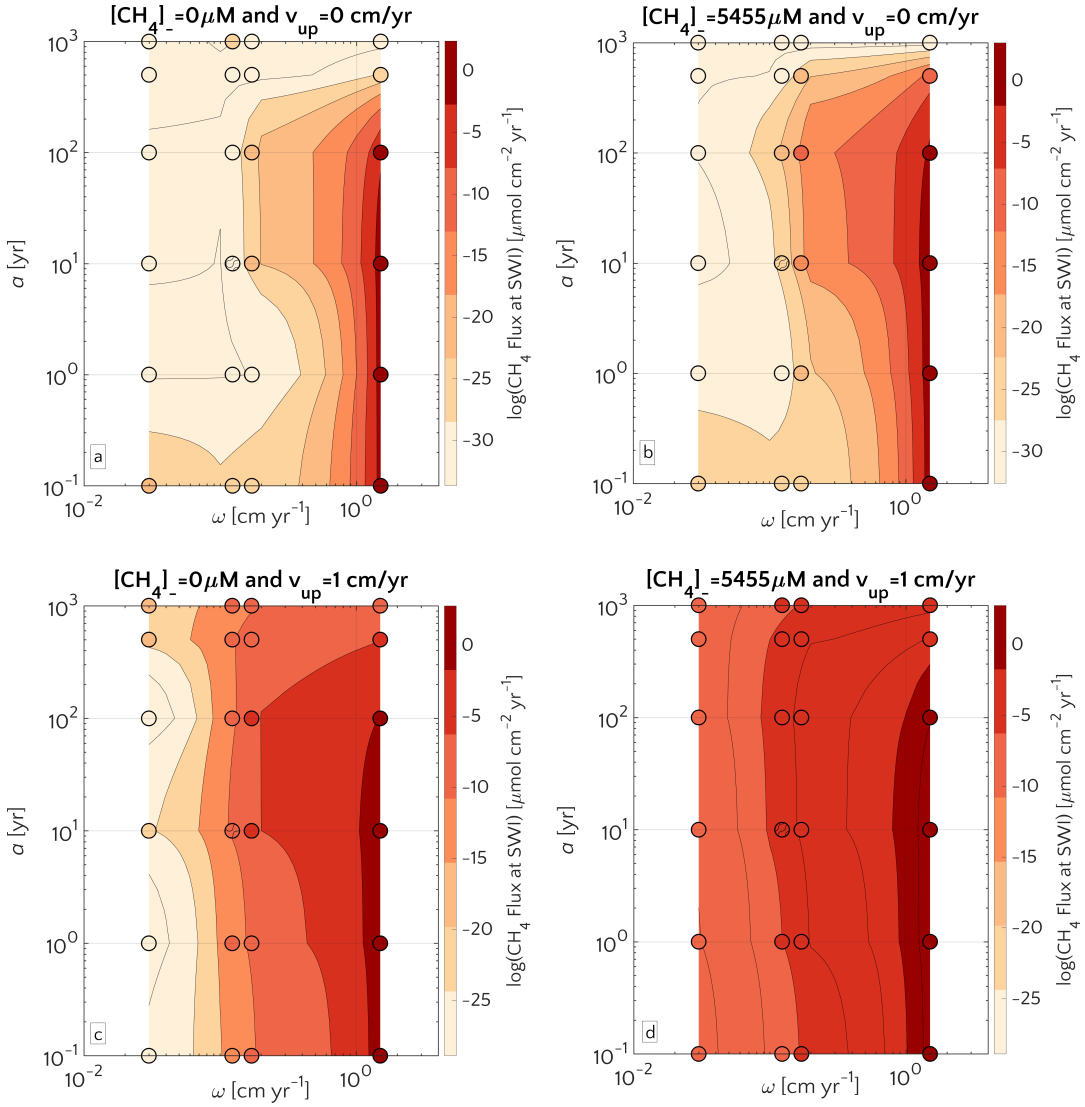

Figure 4.11: Flux of methane at the SWI as dependent on a and ω. For $[CH_4]_{=}0$ mM (*left*) and $[CH_4]_{=}5.455$ mM (*right*), and passive (*top*) and active (*bottom*) case. The circle with pattern corresponds to the baseline simulation.

tive fluid flow and/or methane flux from below. Yet, bioirrigation exerts a limited effect under a range of environmental conditions that favour a deep or shallow SMTZ location respectively.

Passive settings: limited influence of bioirrigation

In passive settings, changes in bioirrigation coefficient, α_0, exert a limited influence on CH_4 effluxes. For most model scenarios, the SMTZ is located well below the sediment layer affected by bioirrigation ($z_{irr} = 3.5$ cm, hence bioirrigation is strongly suppressed below 15 cm) and, thus, changes in α_0 have no effect on methane efflux. Changes in bioirrigation intensity only exert a noticeable effect on methane efflux when methane concentrations at the lower boundary exceed $[CH_4]_{-} = 5.455$ mM. Under these conditions, a decrease in methane efflux is observed with increasing α_0, because the increasing bioirrigation activity supports an enhanced downcore transport

Bioirrigation transports SO_4^{2-} deeper

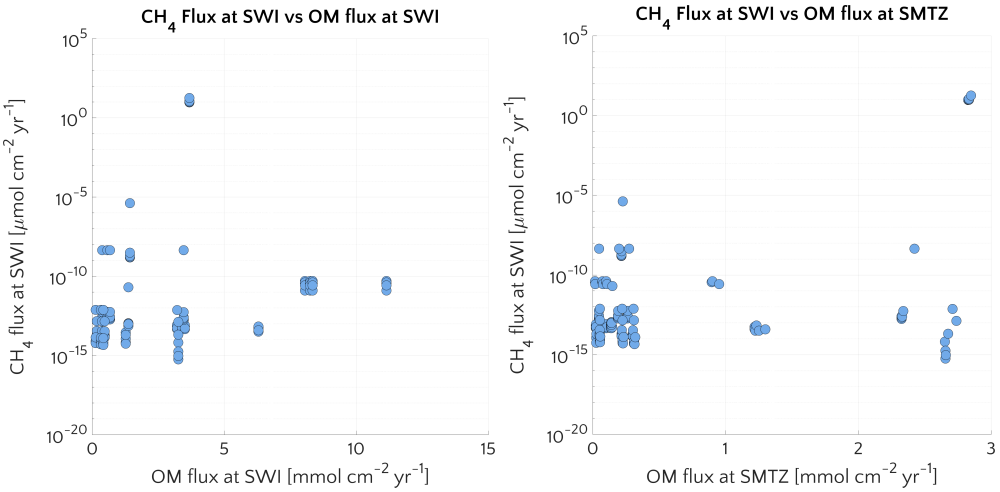

(a) Methane flux at SWI versus OM flux at SWI

(b) Methane flux at SWI versus OM flux at SMTZ

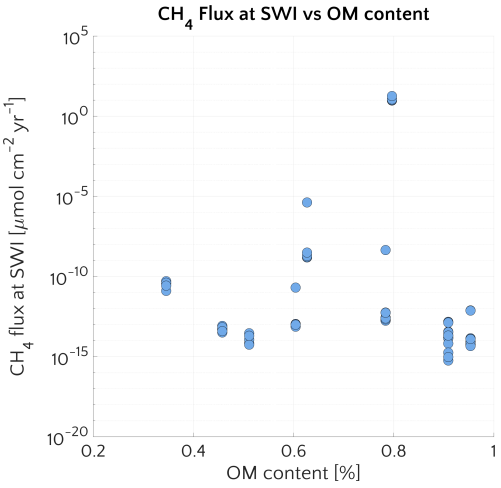

(c) Methane flux at SWI versus OM sediment content

Figure 4.12: Investigation of the dependencies of methane flux at SWI versus quantities involving the OM.

of SO_4^{2-}, leading to a deepening of the SMTZ and a reduction in methane efflux. Model results thus partly support previously published findings by Cordes et al., 2005 and Niemann et al., 2006a, who argued that bioirrigation increases methane consumption due to the enhanced downcore electron acceptors transport. However, model results also show that this effect is only observed under environmental conditions that result in a shallow SMTZ and that methane consumption and efflux remain largely unaffected by changes in bioirrigation intensity if the SMTZ is located deeper in the sediment.

Bioirrigation increases CH_4 efflux in active settings

In contrast to passive settings, active settings reveal a rapid increase in methane efflux with the onset of bioirrigation activity. Methane effluxes first increase by up to 5 orders of magnitude from $\alpha_0 = 0$

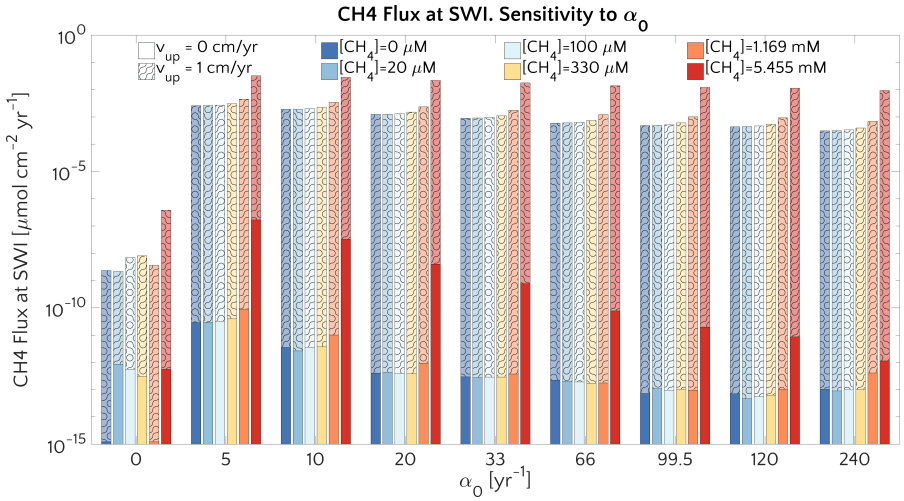

Figure 4.13: Barplot of the methane flux at the SWI versus α_0 for passive case (plain style) and active case (pattern style) and the $[CH_4]_-$ reported in the text.

yr^{-1} to $\alpha_0 = 5$ yr^{-1}, reaching maximum effluxes of ~ 0.02 $\mu molCH_4$ cm^{-2} yr^{-1}, before remaining almost constant with a further increase in bioirrigation coefficients (up to 240 yr^{-1}). The simulated increase in methane efflux is a direct effect of the transport process itself, which enhances the upcore transport of methane accumulating in the upper sediment layers, including layers below the generally shallow SMTZ. The subsequently simulated constant methane effluxes with increasing bioirrigation intensity in combination with the fact that bioirrigation represents the largest flux term at SWI (Fig.4.14) suggest that concentration differences close the the SWI remain broadly similar for all $\alpha_0 > 5$ yr^{-1}.

These results are corroborated by the concomitant analysis of CH_4 dynamics over the 3-dimensional transport coefficient ω, v_{up} and α_0 space shown in Fig.4.14.

A comparison between simulations with $\alpha_0 = 0$ yr^{-1} and $\alpha_0 \neq 0$ yr^{-1} ($\alpha_0 = 5$ yr^{-1}, $\alpha_0 = 10$ yr^{-1} and $\alpha_0 = 33$ yr^{-1}) shows that irrigation increases the CH_4 efflux at low to intermediate sedimentation rates and/or v_{up} (lower-left corner of the phase space in both plots). Yet, maximum methane effluxes that are simulated for high sedimentation rates or v_{up} are almost identical between bioirrigated and non-irrigated sites despite the differences in dominant transport mechanism (diffusion when $\alpha_0 = 0$ yr^{-1}; irrigation when $\alpha_0 \neq 0$ yr^{-1}). Under these conditions (i.e. high v_{up} and/or high ω), the SMTZ is located close to the SWI. Under these conditions, non-local transport becomes the dominant transport process in bioirrigated sediments (see Paragraph "Role of advective transport") because it weakens concentration gradients near the SWI and, thus, contributes to a substantial reduction in the gradient-driven, diffusive transport terms. As a consequence, simulated CH_4 efflux at the SWI are are broadly similar for all of the investigated $\alpha_0 \neq 0$ yr^{-1} (Fig. 4.14.*b,c,d*). It is worth noticing

Non-local transport weakens the diffusive transport

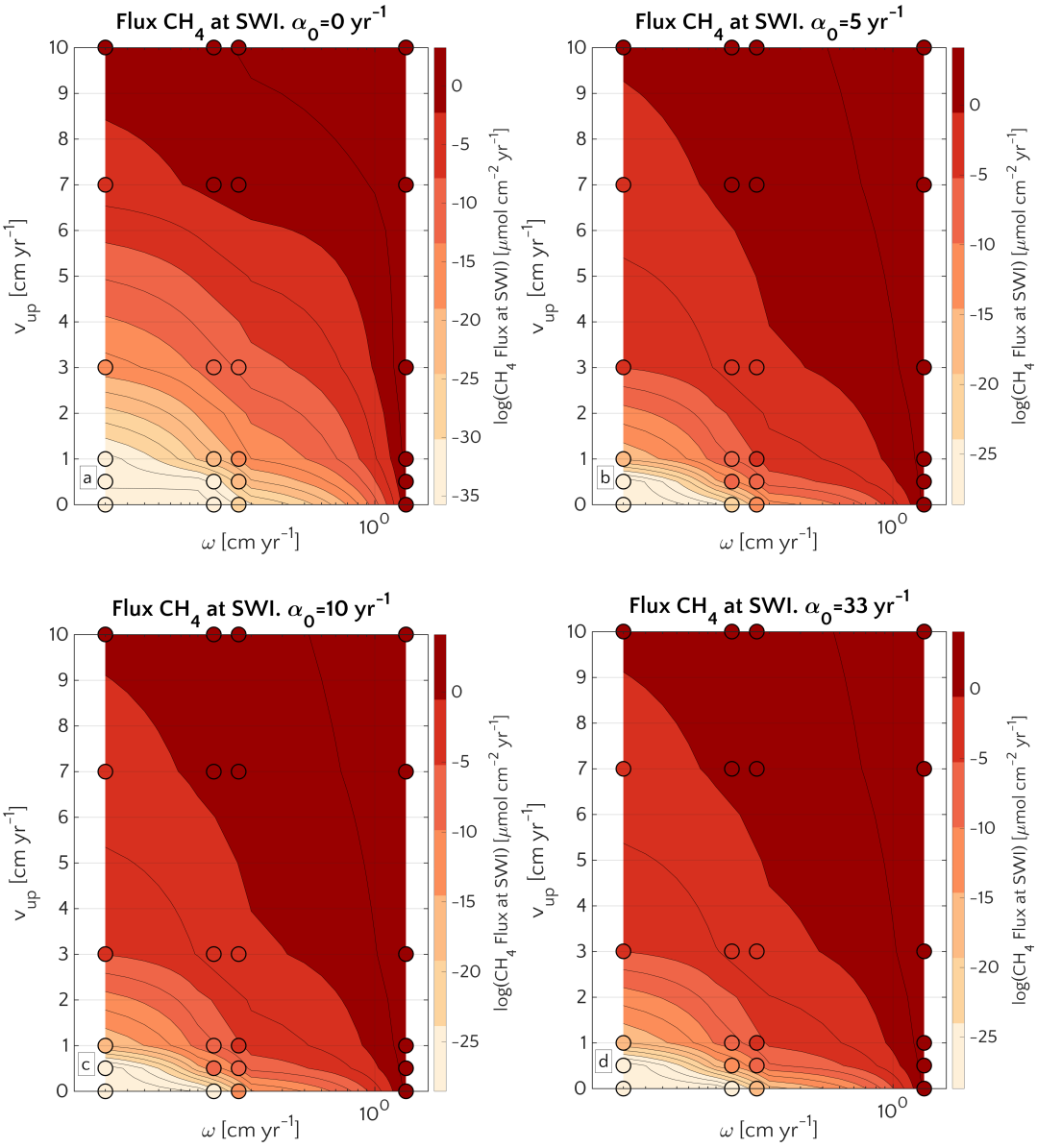

Figure 4.14: Efflux of methane at the SWI as dependent on v_{up} and ω for $\alpha_0 = 0$ yr^{-1} (*a*), $\alpha_0 = 5$ yr^{-1} (*b*), $\alpha_0 = 10$ yr^{-1} (*c*) and $\alpha_0 = 33$ yr^{-1} (*d*). Circles represent simulations outcomes. Results for $\alpha_0 \neq 0$ yr^{-1} are almost the same. The lower boundary condition for methane is $[CH_4]_- = 1.169$ mM.

that, independently on the α_0, CH_4 efflux for $\omega = 0.03$ cm yr^{-1} and $v_{up} = 10$ cm yr^{-1} is ~ 1 $\mu molCH_4$ cm^{-2} yr^{-1}- a value almost identical to the one reported in Luff et al., 2003 - 1.4 $\mu molCH_4$ cm^{-2} yr^{-1} - for a sediments characterized by $v_{up} = 10$ cm yr^{-1} and $\omega = 0.0275$ cm yr^{-1}.

Little influence of k_{AOM}

AOM RATE CONSTANT Given its crucial role in AOM biogeochemistry, one would expect a pronounced influence of the kinetic rates constant, k_{AOM}, on non-turbulent methane effluxes. However, simula-

tion results reveal that k_{AOM} only plays a minor role for non-turbulent methane fluxes across the SWI (see Fig. 4.15). An increase in k_{AOM} can reduce methane effluxes from passive shelf sediments by up to 5 order of magnitude. Still, its effect remains small compared, for instance, to the response to variations in sedimentation rate, which can change methane efflux by up to 14 orders of magnitude. The most important effect of increasing k_{AOM} is the increasing linearity of the $[CH_4]$ and $[SO_4^{2-}]$ profiles around the SMTZ and the concurrent narrowing and downcore movement of the SMTZ (Fig. C.9), which can result in a reduction in methane efflux. Model results thus show that the AOM biofilter and, as a consequence, non-turbulent methane effluxes from sediments are not affected by the exact value of the kinetic rate constant, at least in the range we analyzed.

Disagreement with previous study

This is in disagreement with results by Dale et al., 2008c, which show that, in dynamic settings subject to large methane fluxes, an increase of 3 orders of magnitude in k_{AOM} (from 10^2 M^{-1} yr^{-1} to 10^5 M^{-1} yr^{-1}) leads to a reduction in steady state methane fluxes below 10^{-2} $\mu molCH_4$ cm^{-2} yr^{-1}. However this discrepancy might be ascribable to the high water flow velocity employed in their simulation ($v_{up} = 10$ cm yr^{-1}), ten times higher than the one we considered in our active simulations. Finally, on the ESAS, dissolved methane concentrations are limited by the comparably low gas saturation concentration, resulting in lower methane fluxes (Fig. 4.15.*a*) limiting the influence of k_{AOM}. In addition, Luff et al., 2003 already showed that, as long as not null, the actual value of k_{AOM} plays only a secondary role for the precipitation of authigenic carbonate. Since this authigenic carbonate precipitation is largely driven by alkalinity produced during AOM, the observed independence precipitation rates from k_{AOM} supports our findings.

Indirect agreement from authigenic carbonates

4.3.2.3 *AAT sensitivity analysis*

AAT investigates synergies

In the following the results of the two-level factorial sensitivity analysis is presented. It allows a deeper investigation, not only of the results highlighted in the previous section, based on OAT sensitivity experiment, but also of interaction effects. In the plots showing the results of the factorial analysis the straight line correspond to the normal distribution. That means that effects (single-parameter or combined) lying on that line or its proximity are not significant since the variability can be explained in terms of stochastic behavior of the system. Effects which instead lie away from the straight line correspond to significant parameters (or combination of parameters) the model is sensitive to, since they cannot be explained resorting to normal stochasticity of the system. One of the major assumptions for this approach is that the outcome of the model, for not significant parameters, just follow a normal distribution, which is expected to be valid if we consider each simulation as a single realization of a process and

Normal plot representation

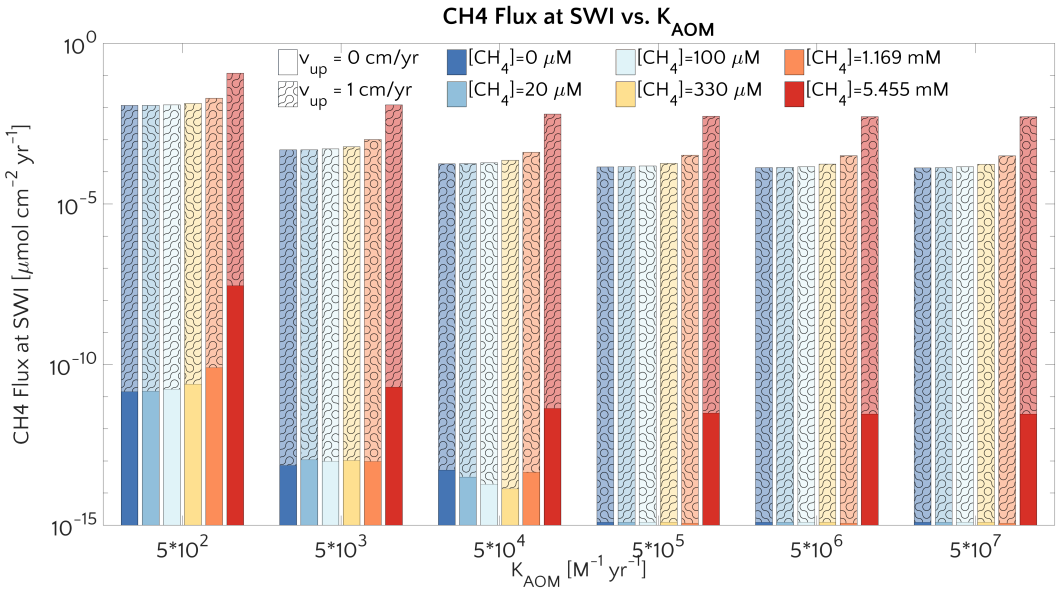

(a) Methane flux at SWI versus AOM reactivity constant k_{AOM}

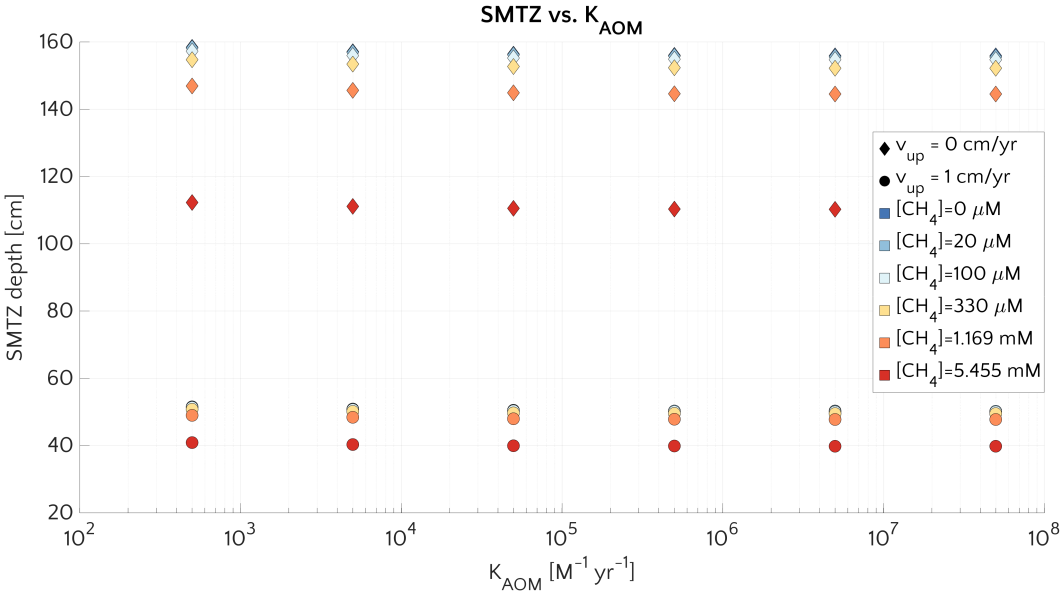

(b) SMTZ depth versus k_{AOM}. Passive (diamonds) and active (circle) cases for different $[CH_4]_-$.

Figure 4.15: Sensitivity of the model the reactivity constant k_{AOM}

in the limit of central limit theorem. A more detailed explanation of how to interpret the result of such a kind of sensitivity study is given in Section C.3.

EFFECTS ON CH_4 FLUX AT SWI Fig 4.16.*a* shows that most of the effects are not much distant from the normal distribution line. A hierarchy of the sensitivity of the main effects can be drawn according to the distance from the Gaussian distribution, showing again

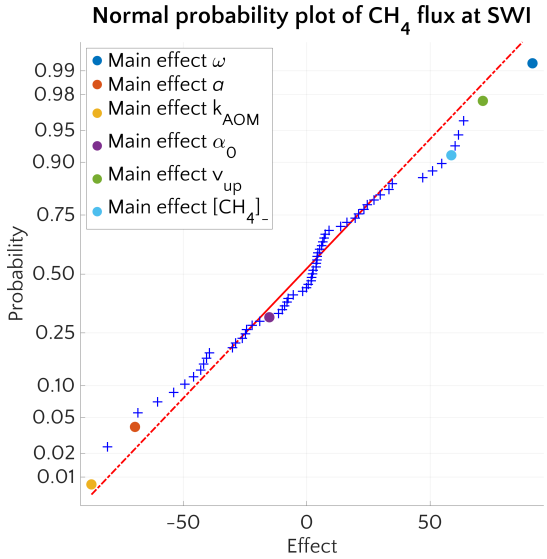

(a) Methane flux at the SWI (units: μmol cm^{-2} yr^{-1})

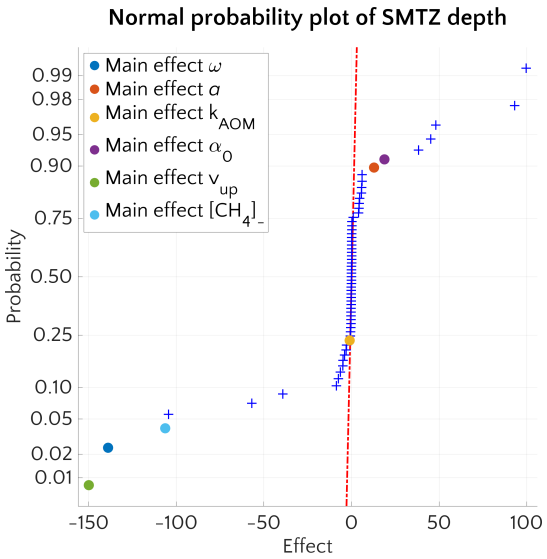

(b) SMTZ depth (units: m)

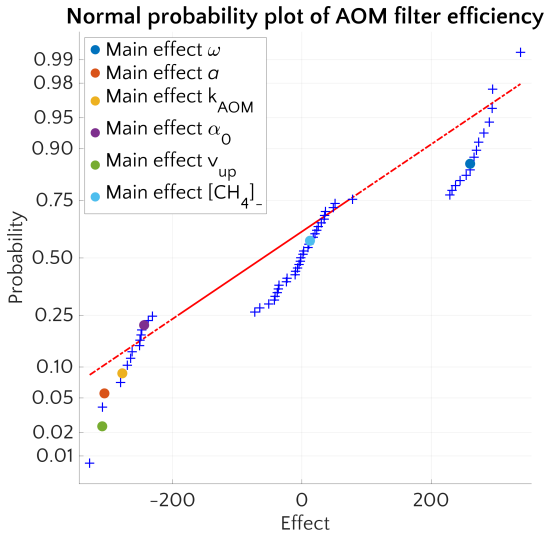

(c) AOM filter efficiency (no units)

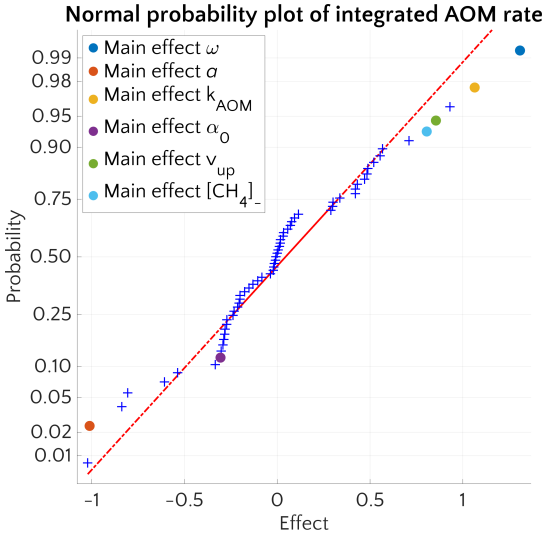

(d) Vertically integrated AOM rate (units: mol m^{-2} yr^{-1})

Figure 4.16: Results of the two-level factorial global sensitivity analysis for four quantities. The main effects of the 6 quantities which have been factorially combined are highlighted with colours. Straight line represents the normal distribution

that indeed ω is the single parameter whose variation the model is more responsive to. The effect is positive, which means that the average CH_4 flux when $\omega = 1.5$ cm/yr is higher then the average CH_4 flux when $\omega = 0.03$ cm/yr. The other main effects are, in order of importance, $[CH_4]_-$ (positive), a (negative), v_{up} (positive), α_0 (negative) and k_{AOM} (negative). But only ω and $[CH_4]_-$ appears to be significant enough. In the light previous considerations and results, a stronger main effect of v_{up} was expected. The study shows

however a relevant positive (synergetic) effect for the combinations $\omega - [CH_4]_-$, $v_{up} - [CH_4]_-$, $\omega - a - k_{AOM}$ and $\omega - v_{up} - k_{AOM}$. Apparently then k_{AOM} just plays a synergetic role: as pointed out in Paragraph "AOM rate constant", taken alone its role is secondary, but it enhances the flux considerably in combination with $\omega - v_{up}$ or $\omega - a$.

The model shows also a relevant antagonistic (negative) effect for the combinations $\omega - k_{AOM}$ and $\omega - a$. An antagonistic effect can be interpreted considering that, for instance, the average effect of ω at high k_{AOM} (or a) is less than the average effect of ω at small k_{AOM} (or a).

EFFECTS ON SMTZ DEPTH k_{AOM} plays basically no role in determining the SMTZ depth, while ω, $[CH_4]_-$ and v_{up} are paramount values (Fig. 4.16.*b*). Given the relation between flux of methane and SMTZ depth that we have found, this results is just a mirror of what described in the Paragraph "Role of advective transport". Combinations of $a - v_{up}$, $\omega - v_{up} - [CH_4]_-$ and $\omega - a - [CH_4]_-$ resulted in being significant and antagonist, while combined effect of $\omega - a$, $\omega - [CH_4]_-$, $\omega - v_{up}$, $a - [CH_4]_-$ and $a - v_{up} - [CH_4]_-$ resulted in being significant and synergetic. The synergy $\omega - a$ hints at a role that OM flux (determined by these two parameters) has in setting the SMTZ depth. Synergy $\omega - v_{up}$ underscores the relevance of the advective processes. Parameter a appears in so many significant effects because age of sediments at the SMTZ (directly connected to a) is linked to the SMTZ depth.

EFFECTS ON AOM FILTER EFFICIENCY AOM filter efficiency resulted in being the variable more difficult to determine since many effects appeared to be relevant (Fig. 4.16.c). The only negligible main effects are the ones linked to $[CH_4]_-$ and the bioirrigation factor. The fact that α_0 seems to play no role, unlike what shown in Paragraph "Role of non-local transport", is explainable considering that it is crucial in determining the transport of species out of the sediments but it is not expected to have a major role at the level of the SMTZ, where η is computed. v_{up} plays a big role. An explanation for such a diverse results compared to the other model outcomes may actually come from a definition of filter efficiency which is strictly valid and makes sense only in presence of a well-defined SMTZ, which is not always the case. That is why the integrated ΣAOM appears to be a better output (more constrained) to evaluate the capability of the model to account for methane consumption.

EFFECTS ON ΣAOM Fig. 4.16.d shows that the main effects of ω, a and k_{AOM} are relevant for the integrated AOM. It is not surprising that k_{AOM} is important as it determines the AOM rate, although it does not

appear to be significant for other quantities. And this is also not a contradiction since AOM is higher the higher is the simultaneous presence of sulfate and methane via the proportionality constant k_{AOM}. However the SMTZ position and the methane efflux have more to do with vertical profiles of the concentrations than with the value of the proportionality constant itself and this gives reason of the marginal role that k_{AOM} has for the other quantities we considered before. Even the negative effect of a can be explained considering that the ΣAOM at high values of a (more recalcitrant OM) is lower than ΣAOM at lower values of a (more reactive OM). A priori it could have been also the other way round since more recalcitrant OM implies also a deeper sulfate penetration depth, namely a higher SO_4^{2-} to appear in Eq. 4.27. But on the other hand it also means less methanogenesis and hence less methane than can be oxidized. Considering that SO_4^{2-}-CH_4 overlap is however inhibited (*i.e.* the product $[CH_4][SO_4^{2-}]$ of Eq. (4.27) is constrained), a change in sulfate penetration depth plays only a minor part. This means that for higher a, AOM rate is lower compared to the case of smaller a. Many other combined effects are relevant. All the synergetic ones are in combination with k_{AOM}. Among the four negative effects ($a - k_{AOM}$, $\omega - a - k_{AOM}$, $a - k_{AOM} - v_{up}$ and $\omega - k_{AOM}$) we want to focus on the last one. It supports what described in the Paragraphs "Role of advective transport" and "AOM rate constant". It means that the k_{AOM}-averaged ΣAOM at high ω is smaller than k_{AOM}-averaged ΣAOM at low ω. In other words even if ω is small the ΣAOM is large, so the system is able to cope with methane and hence a small flux at SWI is expected, and that is what we found. While if ω is large, independently on k_{AOM}, the AOM rate is smaller, thence less methane can be consumed and this leads to a higher methane outgoing flux.

4.3.2.4 *Summary of steady state experiments*

Intense advective flux promotes high CH_4 efflux

Bioirrigation and moderate "a" enhance the CH_4 efflux

Succinctly, the results of the steady state sensitivity study indicate that, under environmental conditions that are broadly representative for the ESAS, low AOM efficiencies and thus high non-turbulent CH_4 effluxes (larger than 4 $\mu molCH_4$ cm^{-2} yr^{-1}) are promoted by intense advective transport (sedimentation rate $\omega > 1$ cm yr^{-1}, active fluid flow $v_{up} > 7$ cm yr^{-1}). Under these conditions, CH_4 efflux can be further enhanced by moderate OM reactivity ($a = 10 - 10^2$ yr) and non-local transport processes, such as bioirrigation (irrigation constant $\alpha_0 > 0$ yr^{-1}). Overall, non-turbulent CH_4 fluxes appear to be mainly controlled by the concurrent effects of ω, v_{up} and α_0. In contrast, maximum AOM rates, k_{AOM}, exert no influence on the AOM filter efficiency.

ESTIMATE OF SSPF CONTRIBUTION TO CH_4 ESCAPE In consideration of the pivotal role that transport parameters have in controlling

Rough estimate of the contribution of JSBACH-modeled SSPF to CH_4 efflux

the carbon availability for the diagenesis and especially the AOM on the ESAS, it is meaningful giving a rough estimate of how eventually the degrading SSPF, making available old organic matter, might influence the methane efflux. As I performed no simulations coupling the thawing SSPF modeled in JSBACH (Chapter 3) with the biogeochemical network implemented in BRNS, I can only perform a *back of the envelope* calculation leaving a more refined and accurate estimate to future development.

The key quantities linking BRNS and JSBACH are: the carbon content (amount and quality) being released for the microbial activity at the thawing and the thawing rate. The latter is particularly important as it is plays the role of one of those advective quantities, like the sedimentation rate and the active fluid flow, the AOM is particularly sensitive to.

Assuming an organic carbon content in the degrading sediments ranging between $C[\%] = 0.7\% - 1.5\%$ (Mergelov et al., 2011; Wild et al., 2018) an average porosity of $\varphi = 0.45$, a methanogenic production coefficient[6] $\epsilon_{CH_4} = 0.5 - 0.7$ and a matric density $\rho = 2.7$ g cm^{-3}, the concentration of methane at the bottom is then given by:

$$[CH_4]_- = \frac{C[\%]}{100} \cdot \rho \cdot \frac{1-\varphi}{\varphi} \cdot \frac{1}{m_C} \cdot \epsilon_{CH_4} \cdot \frac{m_{CH_4}}{m_C} \tag{4.33}$$

with m_{CH_4}: molecular mass of methane and m_C: molecular mass of carbon. The resulting concentration is $[CH_4]_- = [1.28\text{ M} - 2.75\text{ M}]$, way above the saturation level in usual conditions (consider that the saturation concentration of methane at about 22 atm, *e.g.* 40 m water+100 m sediments, is $[CH_4]^* \sim 46$ mM, Dale et al., 2008a). It means that, for an approximate estimation, I can consider as bottom concentration the highest CH_4 concentration used in the sensitivity analysis ($[CH_4]^* = 5.46$ mM). The advection velocity has to be corrected for the thawing rate, as it contributes to deliver labile carbon. From results of Chapter 3, the (linearly) averaged thawing rate under mild assumptions and pre-industrial condition is $\omega_{SSPF} = 0.082$ cm yr^{-1}, a quantity which has to be added to the considered sedimentation rate ω. If I consider the results of Paragraph "Role of advective transport" (4.3.2.2) with an effective sedimentation rate increased of ω_{SSPF} and the bottom methane concentration at saturation, the results of emitted methane at the SWI basically do not change suggesting that, with modeled values, the direct impact of degrading SSPF on non-turbulent methane fluxes on the ESAS is actually secondary. It might however play a much prominent role if the not-dissolved methane fraction is considered, since the free gaseous methane represents reasonably most of the methane produced at the thawing boundary and its action throughout the sediment column, with movement and inter-

Marginal role of JSBACH-modeled SSPF to CH_4 efflux

JSBACH-modeled SSPF compatible with large gas content

6 The fraction of carbon which is ultimately transformed into methane and which takes into account in a simplified way of bacterial efficiency and quality of the OM.

woven dissolution/degassing along with methane consumption and depth change, has not been explored here.

4.3.2.5 *Geographic pattern and potential for non-turbulent methane emissions from Laptev Sea sediments*

CH_4 efflux based on ω

The results of the model sensitivity study provide a quantitative framework in which first-order estimates of potential non-turbulent methane escape from ESAS sediments can be derived. For instance, the functional relationship between sedimentation rate and methane flux across the SWI reported in Fig. 4.8.*a* allows estimating a potential non-turbulent methane efflux for a given sedimentation rate. Thus, if the spatial distributions of these environmental controls on methane efflux are known, a first-order geographical distribution of potential non-turbulent methane escape from the Siberian Shelf can be derived.

3D kriging to derive ω in the Laptev Sea

However, the availability of observational data from the Siberian Shelf is extremely scarce. Therefore, we here focus on the Laptev Sea - a comparable well studied part of the Siberian Shelf. The Laptev Sea is well-known for its subsea permafrost and gas hydrate content and subject to large riverine inputs from the Lena river. To derive a map of sedimentation rates for Laptev Sea shelf sediments, we use published linear sedimentation rates (Table C.12) and extrapolate these values to the entire region by applying a simple 3D kriging method (see Fig. 4.17.*a*), using the International Bathymetric Chart of Arctic Ocean (IBCAO) (Jakobsson et al., 2012) and employing longitude, latitude and water depth as predictors for ω.

ω in the Laptev Sea

Observations indicate that sedimentation rates are highest ($\omega = 0.45$ cm yr^{-1}) close to the mouth of the Lena river and Moustakh Island in the Buor-Khaya Gulf. As a consequence, the vicinity of the river mouth, as well as the area along the shallow bathymetric profile towards the NE of the Lena delta are characterized by comparably high sedimentation rates ($\omega = 0.27 - 0.42$ cm yr^{-1}). The relatively shallow areas (~ 10 m deep) around the New Siberian islands reveal intermediate values ($\omega = 0.06 - 0.12$), while minimum sedimentation rates ($\sim 0.002 - 0.03$ cm yr^{-1}) roughly follow the 55 m isobath down to the continental slope at 100m. Deeper shelf areas are characterized by a more homogeneous distribution of sedimentation rates with values around $0.03 - 0.06$ cm yr^{-1}.

Table 4.4: Estimated flux of CH_4 at SWI in mol yr^{-1} for different depth regions of Laptev Sea in a passive ($v_{up} = 0$ cm yr^{-1}) and active ($v_{up} = 1$ cm yr^{-1}) case.

	v_{up}	
Region (water depth, area)	0	1
$0 - 10$ m, $7.7 \cdot 10^4$ km^2	6.5	$8.9 \cdot 10^5$
$10 - 80$ m, $4.5 \cdot 10^5$ km^2	296.2	$8.5 \cdot 10^6$

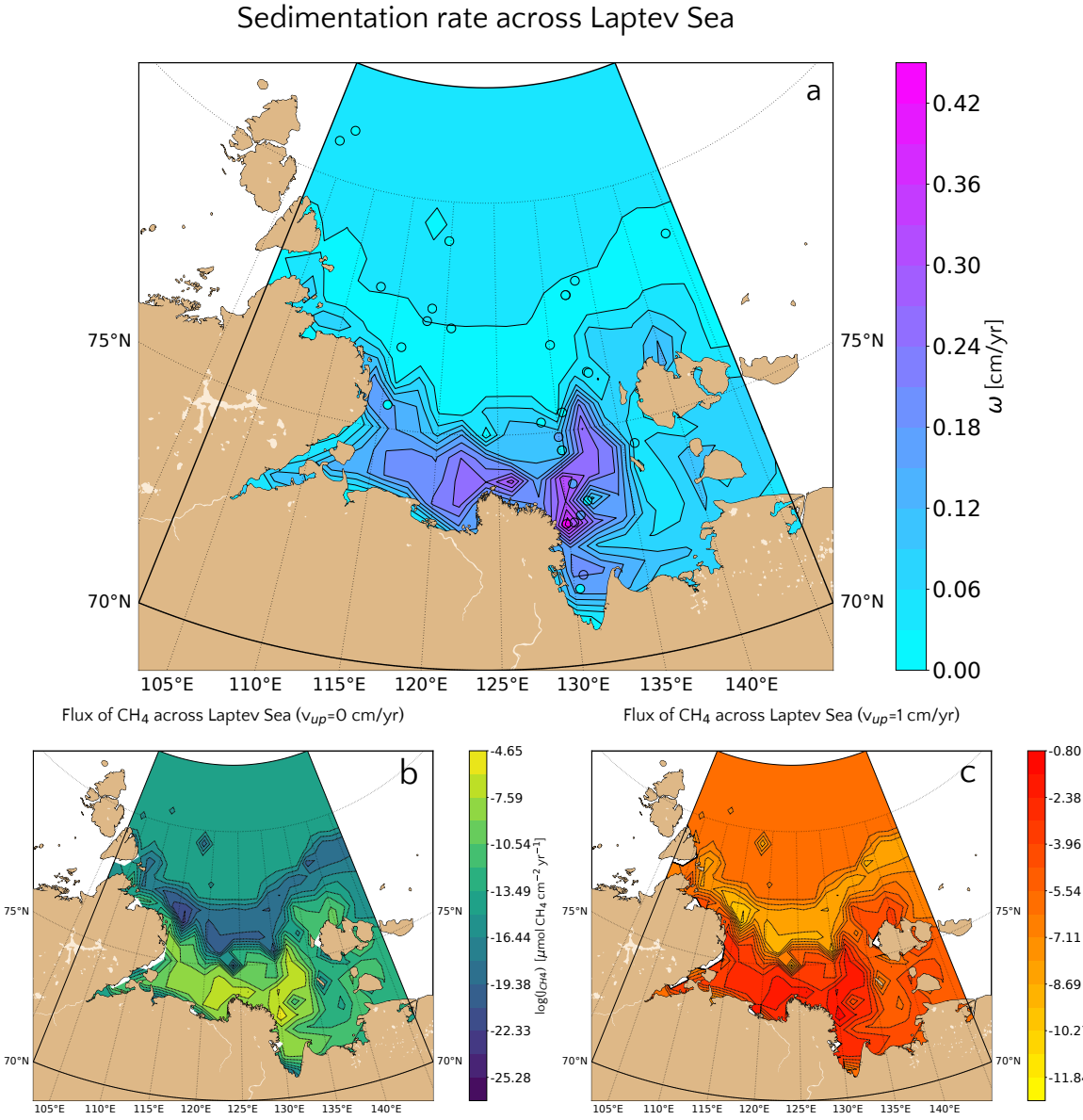

Figure 4.17: *a*. values of the sedimentation rate extrapolated for the whole Laptev Sea via a simple kriging method. The reference values (circles) are the ones reported in Table C.12. *Bottom* (Log) Values of the potential methane emissions at the SWI considering the relationship presented in Fig. 4.8.*a* for passive (*b*) and active (*c*) cases.

Estimated non-turbulent methane effluxes corresponding to the highest measured sedimentation rates close to the Lena mouth do not exceed $1.57 \cdot 10^{-1}$ μmolCH_4 cm^{-2} yr^{-1} assuming the presence of active fluid flow and $2.25 \cdot 10^{-5}$ μmolCH_4 cm^{-2} yr^{-1} for passive settings. These findings are not surprising as steady state sensitivity results indicate that high CH_4 efflux requires sedimentation rates of $\omega > 1$ cm yr^{-1}. The regional non-turbulent CH_4 efflux budget for different depth sections of the Laptev Sea assuming the absence of active fluid flow in Laptev Sea shelf sediments (see Table 4.4) thus indi-

cates that non-turbulent CH_4 efflux is negligible. Even if we assume the omnipresence of an active fluid flow of $v_{up} = 1$ cm yr^{-1}, the estimated non-turbulent methane efflux merely sums up to $9.39 \cdot 10^6$ $molCH_4$ yr^{-1} ($\sim$ 0.1 $GgCH_4$ yr^{-1}) over the entire Laptev Sea area of $527.4 \cdot 10^3$ km^2. Such small effluxes would most likely be subject to further oxidation in the water column, thus limiting any potential impact on atmospheric methane concentrations and climate.

Non-turbulent flux < 0.1 $GgCH_4$ yr^{-1}

Higher advective fluid flow velocities, intermediate organic matter reactivity and/or a more intense macrobenthic biological activity could increase these estimates of non-turbulent methane escape from the Laptev Sea shelf. Higher advective fluid flow velocities (i.e. $v_{up} >$ 1 cm yr^{-1}), possibly in connection with active seepages, groundwater discharges and fault lines (the latter follow parallel pattern in Laptev Sea Drachev et al., 1998 on the direction SW-NE from the west of Lena delta up to the little Lyakhovsky and Kotelny island), could result in methane effluxes of up to $10 - 10^{1.3}$ $\mu molCH_4$ cm^{-2} yr^{-1} (see Fig. 4.11 and Fig. 4.14). However, such high fluid flow velocities would be only found locally and would thus merely give rise to a number of methane emission hot spots that would not change the overall non-turbulent methane flux budget. In addition the intermediate organic matter reactivity could result in a higher estimated non-turbulent methane escape, in particular in the fast accumulating sediments close to the coastline and the Lena River Delta that receive more reactive organic carbon from thawing terrestrial permafrost (Wild et al., 2018) . However, our sensitivity study shows that OM reactivity merely plays a secondary role: for instance varying a of two orders of magnitude ($a = 1 - 100$ yr) affects the CH_4 efflux by less than an order of magnitude. Changes in bioirrigation intensity would exert merely a limited effect on efflux estimates, as bioirrigation has already been included in the estimate calculations. Additional physical reworking such as ice scouring or dredging, or the absence of bioirrigation, which is known to be patchy in Arctic sediments could even further reduce estimated non-turbulent methane efflux.

Spatial variability

Model results thus show that, under present-day, steady state environmental conditions, AOM acts as a general efficient biofilter for potential non-turbulent methane fluxes in Laptev Sea sediments. Such estimates cannot support previously estimated methane outgassing fluxes of few teragrams of CH_4 yr^{-1} (Berchet et al., 2016) or even tens of teragrams of CH_4 yr^{-1} (Shakhova et al., 2014). If such outgassing were to be sustained by methane efflux from the Laptev Shelf, it would require the build-up of CH_4 gas reservoirs in Laptev Sea sediments of at least similar or larger size than the evaded amount, accompanied by a rapid transport mechanism of this CH_4 gas to the atmosphere. Nevertheless, model results also suggest that projected trends of terrestrial permafrost thawing and coastal permafrost degradation (Vonk et al., 2012) might increase the importance of non-turbulent

Estimate of non-turbulent CH_4 *efflux does not support high* CH_4 *fluxes to th atmosphere*

Non-turbulent CH_4 *flux might increase in the future*

methane escape for the Artic's methane budget by potentially increasing sedimentation rates through coastal erosion and increased riverine inputs (Guo et al., 2007); active fluid flow through permafrost and methane gas hydrate degradation (James et al., 2016; Ruppel et al., 2017); organic matter reactivity through an enhanced delivery of more reactive permafrost organic matter (Wild et al., 2019) and/or a boosted macrobenthic activity through warming and Atlantification. However, the magnitude of these projected environmental changes and thus their effect on non-turbulent methane escape is difficult to assess.

4.3.3 *Methane efflux dynamics in response to seasonal and long term environmental variability*

Transient phenomena may reduce AOM efficiency

Although steady state sensitivity results revealed that AOM represents an efficient biofilter for upward migrating methane, transient dynamics induced by, for instance, seasonal variability or climate change may weaken the efficiency of the AOM biofilter. Therefore, we also explore the potential for non-turbulent methane escape from ESAS sediments under transient conditions. Table 4.5 summarizes maximum simulated, non-turbulent methane escape for two seasonal environmental change scenarios, as well as two longterm idealized environmental change scenarios.

Table 4.5: Maximum of methane fluxes (in μmol cm^{-2} yr^{-1}) at SWI for transient simulations. Values in round parenthesis indicate the year after the beginning of simulation corresponding to the reported maximum.

		1. Seasonal CH_4			1. Seasonal $CH_4 + SO_4^{2-}$		
		v_{up}			v_{up}		
		0	1	5	0	1	5
CH_4 (μM)	20	0.030 (200)	0.550 (50)	12.7 (17.5)	0.059 (200)	0.772 (51)	13.7 (18)
	100	0.029 (200)	0.550 (50)	12.7 (17.5)	0.058 (200)	0.753 (51)	13.7 (18)
	330	0.030 (200)	0.552 (49.5)	12.8 (18)	0.058 (200)	0.775 (51)	13.8 (18)
	1169	0.031 (200)	0.558 (49.5)	12.9 (18)	0.059 (200)	0.783 (51)	14.0 (18)
	5455	0.034 (200)	0.577 (49)	14.0 (19)	0.062 (200)	0.832 (50)	15.2 (19)
		3. Linear CH_4			4. Sudden CH_4		
		v_{up}			v_{up}		
		0	1	5	0	1	5
CH_4 (μM)	20	0.029 (200)	0.550 (50)	11.7 (20)	0.029 (200)	0.550 (50)	12.7 (18)
	100	0.030 (200)	0.550 (50)	11.7 (20)	0.030 (200)	0.552 (50)	12.7 (18)
	330	0.30 (200)	0.550 (50)	11.7 (20)	0.031 (200)	0.557 (50)	12.9 (18)
	1169	0.032 (200)	0.550 (50)	11.7 (20)	0.033 (200)	0.565 (49.5)	13.4 (18)
	5455	0.036 (200)	0.560 (50)	11.8 (20)	0.040 (200)	0.639 (47)	18.8 (23)

Interestingly, model results reveal that the temporal dynamics of simulated, non-turbulent methane fluxes does not depend on the spe-

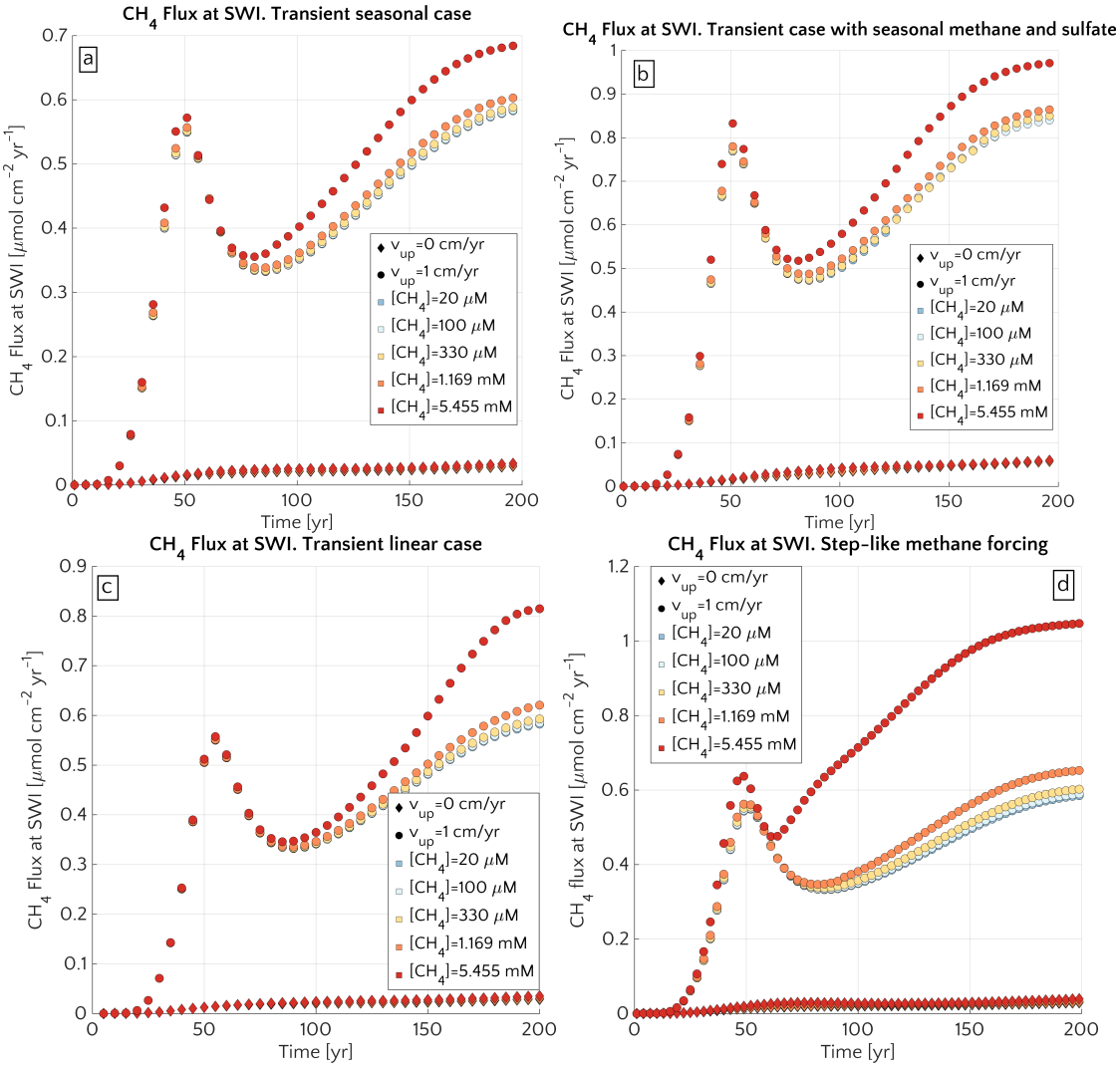

Figure 4.18: Flux of methane at SWI over time for passive (diamonds) and active (circle) setups and different $[CH_4]_-$. *a.* Seasonal methane forcing from below. *b.* Seasonal methane forcing from below and seasonal sulfate forcing from above. *c.* Linear methane forcing from below. *d.* Step-like methane forcing from below.

cific environmental scenario (*i.e.* fluxes respond in a similar way to all methane forcing scenarios), but is rather controlled by the presence/absence of active fluid flow (Table 4.5).

Transient CH_4 effluxes controlled by v_{up} not by details of BC

In passive settings, methane efflux monotonously increases to small maxima of $0.03 - 0.05$ $\mu molCH_4$ cm^{-2} yr^{-1}. At the same time, the SMTZ merely migrates $11.5 - 29$ cm upcore (Fig. 4.19). Over a period of 200 years, the non-turbulent methane escape from passive settings merely reaches $3 - 4$ $\mu molCH_4$ cm^{-2}. The transient simulations thus show that passive settings generally allow only for little methane escape (Fig. 4.18).

Passive settings in transient runs

Active settings, in turn, are characterized by an initial increase in CH_4 fluxes to maxima of $0.55 - 0.83$ $\mu molCH_4$ cm^{-2} yr^{-1} ca. 50 years

into the simulation (assuming a flow velocity of $v_{up} = 1$ cm yr^{-1}). During this initial time period, the SMTZ rapidly shifts upcore by 100 cm. While the SMTZ subsequently remains located in shallow sediment layers for the remaining simulation period, methane escape temporarily decreases by $17 - 20\%$ until year $70 - 75$, followed by a monotonous increase or the onset of a new steady-state until the end of the simulation, at year 200. For $v_{up} = 1$ cm yr^{-1}, the temporally integrated methane efflux (over 200 years) falls within the range $66 - 121$ μmolCH_4 cm^{-2}. For $v_{up} = 5$ cm yr^{-1}, the integrated efflux is 10- to 14-fold larger (i.e $\sim 0.95 - 1.154$ mmolCH_4 cm^{-2}). For $v_{up} = 1$ cm yr^{-1}, almost 30% of these emissions occurs in the first century after the perturbation. This fraction increases to $48 - 87\%$ for $v_{up} = 5$ cm yr^{-1}.

Temporal evolution of CH_4 efflux and SMTZ in active settings in transient runs

Time response of sediments is slower than seasonal variability

The similarity of the CH_4 efflux dynamics (Fig. 4.18) in response to different environmental scenarios (*i.e.* seasonal CH_4, seasonal CH_4 + SO_4^{2-}, linear CH_4 and sudden CH_4) as well as the smooth, continuous upcore movement of the SMTZ (Fig. 4.19) thus indicates that the time response of the biogeochemical process network that controls CH_4 dynamics and efflux (*i.e.* biomass growth, AOM rate, methanogenesis) is slower than the characteristic timescales of the investigated environmental variability. In addition, results show that a notable methane escape is only compatible with environmental conditions that enables the formation of a "window of opportunity" during which the efficiency of the AOM biofilter is temporarily weakened. The following sections explore the factors that control the creation of such a window of opportunity and discusses the mechanisms behind the simulated methane escape.

Window of opportunity for CH_4 escape

4.3.3.1 *Window of opportunity*

BC scenario considered: sudden change of $[CH_4]_-$

Given the broadly similar behaviour of methane fluxes with respect to the different environmental scenarios, we will focus the following discussion on scenario 4 (*i.e.* step-like CH_4 forcing) with $v_{up} = 1$ cm yr^{-1} and a specific bottom concentration, *e.g.* $[CH_4]_- = 1.169$ mM. In contrast to the other scenarios that are characterized by transient CH_4 supply from below, scenario 4 allows for a straightforward definition of initial and final state, which facilitates the attribution of a typical response timescale for the system.

No AOM, weak AeOM: CH_4 escapes at first

Fig. 4.20 illustrates the temporal evolution of the simulated filter efficiency and AOM rate (a), CH_4 flux (b), SMTZ depth (c) and AOM biomass (d) for scenario 4. During the initial 23 years, the AOM biomass is constant and thus the AOM rate and filter efficiency are zero. In addition, the AeOM represents a weak barrier since oxygen is merely present in the upper few centimetres and AeOM competes with aerobic organic matter degradation, as well as a number of additional secondary redox reactions (see Table C.4). As a consequence the CH_4 produced *in situ* as well as the one externally supplied diffuses up-

Escape of CH_4 produced in situ

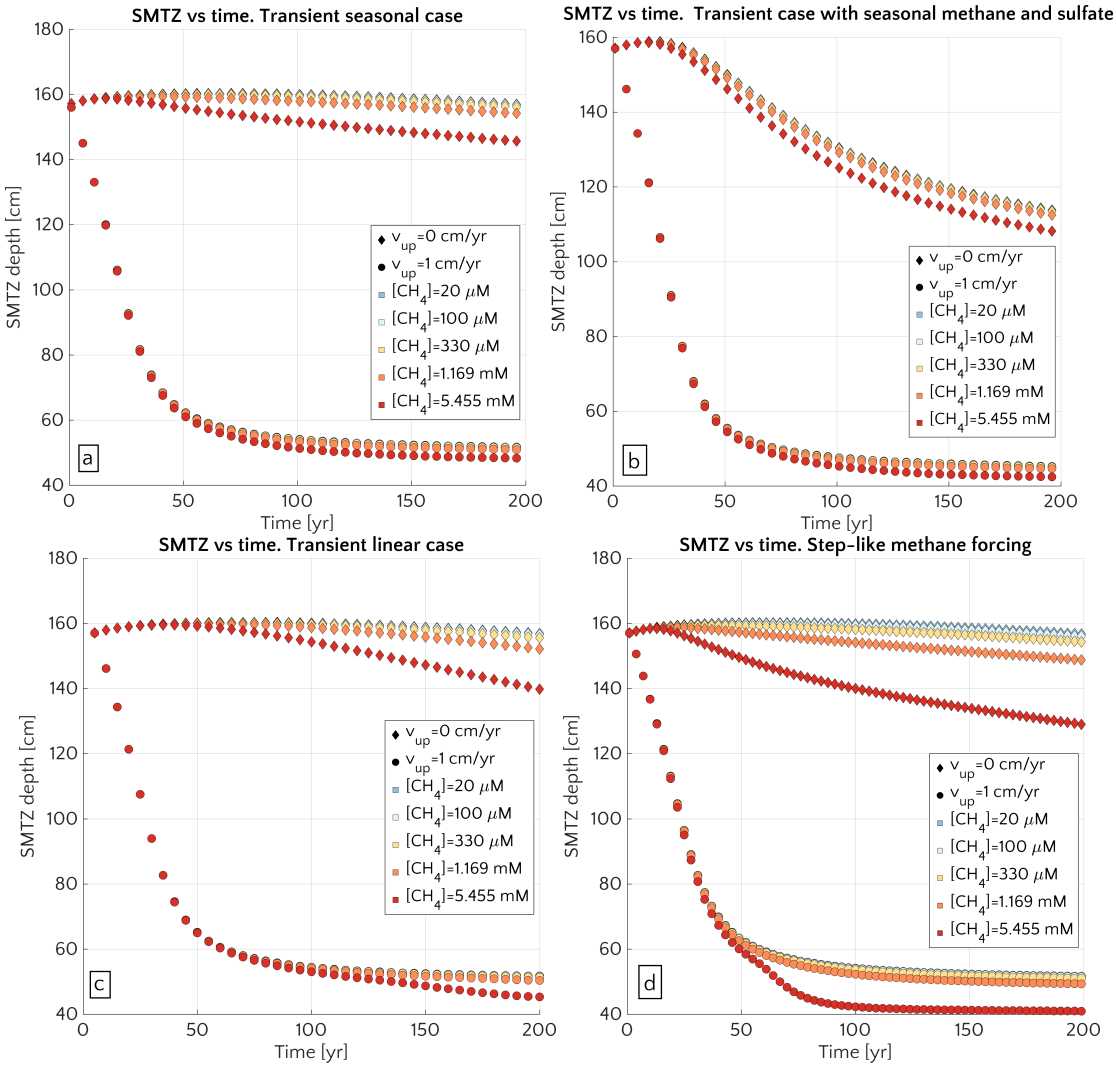

Figure 4.19: Movement of SMTZ over time for passive (diamonds) and active (circle) setups and different $[CH_4]_-$. *a.* Seasonal methane forcing from below. *b.* Seasonal methane forcing from below and seasonal sulfate forcing from above. *c.* Linear methane forcing from below. *c.* Step-like methane forcing from below.

ward and mostly escapes, leading to an increase in CH_4 efflux. A large fraction of this methane efflux is produced within the sediments since the average advective velocity of methane ($\bar{v} = v_{up} - \omega = 0.877$ cm yr^{-1}) merely covers 20.2 cm in 24 years. The dynamic is hence too slow to allow the methane from below the sediments to reach the SWI.

Rapid shift of SMTZ → window of opportunity

Transient model results thus reveal that the temporary perturbation of AOM and the consequent opening of a "window of opportunity" for methane escape require a significant upward shift of the SMTZ. Such a shift has moreover to be rapid enough to prevent the establishment of an efficient AOM community at the SMTZ level. In the passive settings, all the investigated environmental scenarios trigger a limited

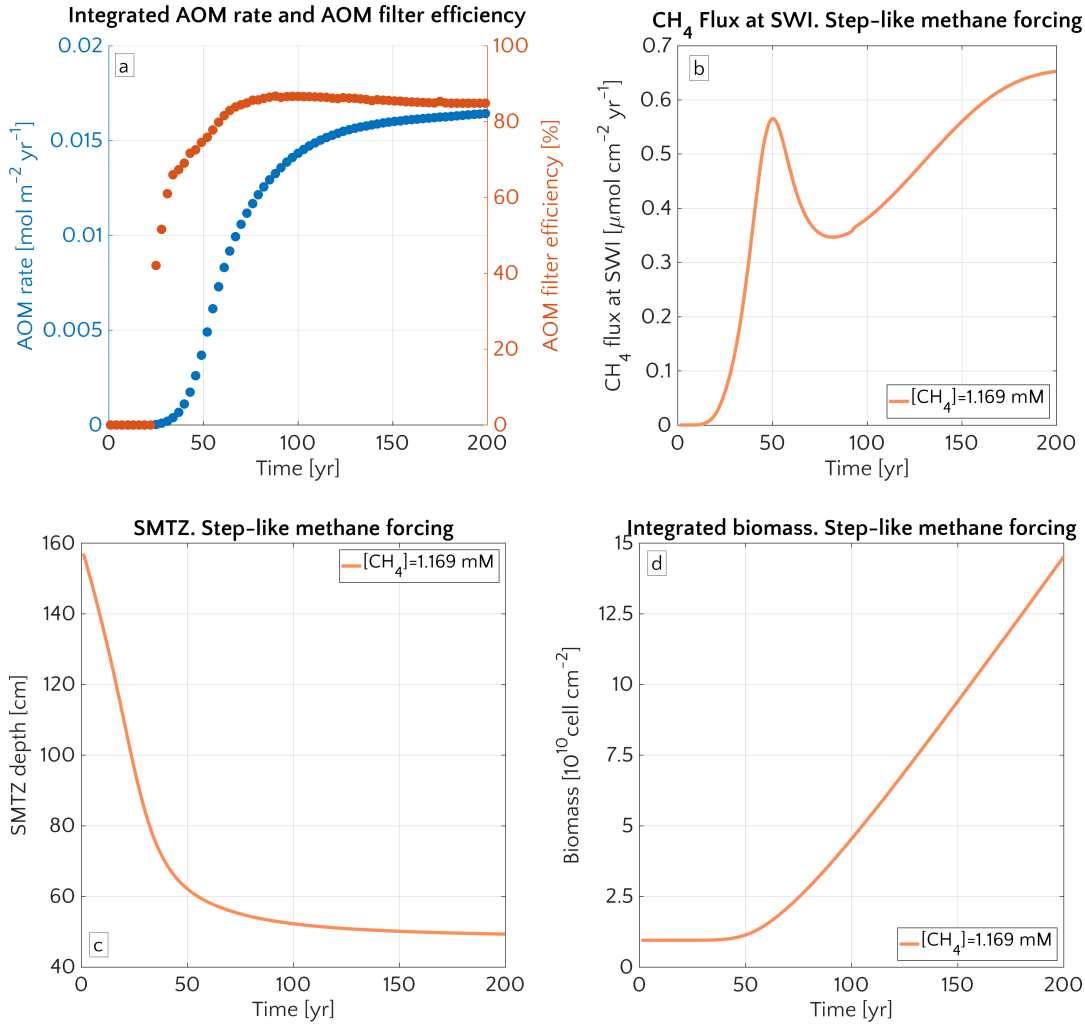

Figure 4.20: Time evolution over 200 years for the case of an active setup with $v_{up} = 1$ cm yr^{-1} and a step-like methane forcing from below from 0 to $[CH_4]_- = 1.169$ mM. *a.* AOM vertically integrated rate (blue) and AOM efficiency (red). *b.* CH_4 flux at SWI. *c.* SMTZ depth. *d.* Vertically integrated biomass (number of cells).

and comparably slow movement of the SMTZ (Fig. 4.19) thus allowing for the formation of an AOM community consuming methane and hindering the creation of such a window of opportunity. In contrast, active settings show a rapid and significant shift of the SMTZ in response to methane supply from below, which creates a window of opportunity for CH_4 escape, whose onset and duration is controlled by advective velocity v_{up} of the active fluid flow and the AOM biomass growth.

Maximal CH_4 emissions increase with v_{up}

Assuming typical values of v_{up} reported for active marine sediments ($0.5 - 5$ cm yr^{-1}), we show that methane from deep sources (ca. 3 m) reaches the sediment water interface within 7 to 20 years. Maximum CH_4 effluxes are typically simulated two-three decades after the onset of methane supply. Furthermore, simulations reveal

that the maximum magnitude of methane effluxes increases with v_{up} from $0.5 - 0.6$ μmolCH$_4$ cm^{-2} yr^{-1} for $v_{up} = 1$ cm yr^{-1} to $11 - 15$ μmolCH$_4$ cm^{-2} yr^{-1} for $v_{up} = 5$ cm yr^{-1}. In parallel, the duration of the window of opportunity for methane escape in turn decreases with increasing v_{up}. Values of methane fluxes for the maximum and for the new steady state fall in the range of other previous model results (Sommer et al., 2006; Dale et al., 2008c) but do not reach the high values measured in other active settings (Linke et al., 2005; Regnier et al., 2011).

Duration of window of opportunity decreases with v_{up}

An insight into the mechanism that drive the creation of this window of opportunity and control non-turbulent methane efflux under these conditions can be inferred by evaluating methane migration time scales within the sediments. After the first 23 years, the AOM begins to efficiently consume upward migrating methane (see Fig. 4.20.*a*) and reduces the methane flux by 40%. Because consumption occurs at SMTZ, it does not immediately affect the methane efflux at the SWI. The effect of this consumption on methane concentration first has to propagate upwards through the sediments till it reaches the SWI, and this results in a delayed response of the efflux to the onset of the AOM. The velocity of this propagation is given by $\bar{v} = v_{SMTZ} + v_{up} - \omega$, where v_{SMTZ} denotes the velocity at which the SMTZ (where consumption happens) moves upward. From Fig. 4.20.*c* and Fig. 4.19 we can infer that, initially, the SMTZ moves with a fairly constant velocity of about 2.46 cm yr^{-1} and, hence, $\bar{v} = 2.46 + 1 - 0.123 = 3.337$ cm yr^{-1}. At the onset of an efficient AOM barrier (i.e. after 23 years), the SMTZ is located at a sediment depth of 100.4 cm and the time required for the consumption signal to propagate to the SWI thus amounts to $\frac{100.4\,\text{cm}}{3.337\,\text{cm yr}^{-1}} = 30.1$ yr. After this initial period of 53.1 years, the effect of CH$_4$ consumption at the SMTZ starts to reduce the non-turbulent methane efflux (Fig. 4.20.*b*).

CH$_4$ consumption at depth has to propagate upwards: delayed effect on efflux

Velocity of propagation of CH$_4$ consumption

Simulations show that v_{SMTZ} is solely controlled by v_{up} and does not depend on additional environmental conditions, as revealed in Fig. 4.19 by the velocity with which the SMTZ moves upwards (~ 11.4 cm yr^{-1}) in case of $v_{up} = 1$ cm yr^{-1} and which is constant for all the transient scenarios. This also suggests that the methane efflux at the SWI is initially controlled by the velocity of the SMTZ, which is in turn is determined by the upward velocity v_{up}.

v_{SMTZ} controlled by v_{up}

CH$_4$ efflux initially controlled by v_{up}

The reduction in methane efflux after the onset an efficient AOM barrier lasts until the upward movement of the SMTZ slows down. At this point, the AOM filter efficiency reaches a quasi-stationary level of $\sim$85% (Fig. 4.20.*a*). Meanwhile, *in situ* methanogenesis continues to produce methane, which is not entirely consumed by the AOM community that already reached its full capacity. As a consequence, methane flux at SWI increases again until a new steady state is reached.

Drop in CH$_4$ efflux till v_{SMTZ} slows down

Such a pattern arises even more clearly in simulations with $v_{up} = 5$ cm yr^{-1} (see Fig. 4.21). Here, the onset of a new steady state occurs

Case $v_{up} = 5$ cm yr^{-1}

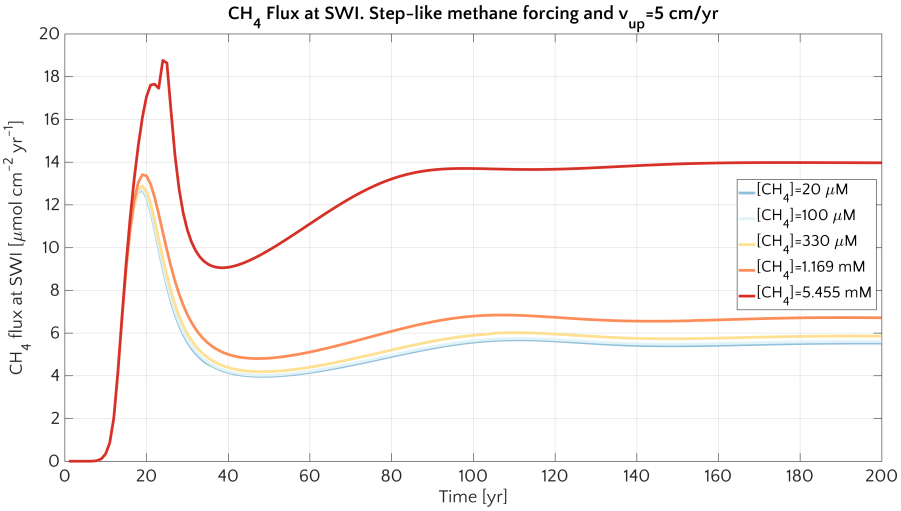

Figure 4.21: Flux of methane at SWI versus time for scenario 4 (step-like methane increase) and $v_{up} = 5$ cm/yr. Colours identify simulations with different CH_4 bottom concentrations.

earlier and AOM suppresses the non-turbulent methane efflux to the value of about 7 μmolCH$_4$ cm^{-2} yr^{-1} (Fig. 4.21). The comparison of such value with the simulated steady state efflux ($\sim$ 0.1 μmolCH$_4$ cm^{-2} yr^{-1} inferred from Fig. 4.14) under identical environmental conditions (i.e. $v_{up} = 5$ cm yr^{-1}, $\omega = 0.123$ cm yr^{-1} and $[CH_4]_- = 1.169$ mM) indicates that the final steady state flux observed in transient simulations (with a bioenergetic AOM formulation) is roughly two order of magnitude larger than the flux simulated with a bimolecular rate law. Bioenergetic findings are in agreement with Dale et al., 2008c, who reported an efflux of similar magnitude (3 μmolCH$_4$ cm^{-2} yr^{-1}) for the new steady state at the of a transient run with $v_{up} = 10$ cm yr^{-1} and $[CH_4]_- = 70$ mM. They also show that CH_4 efflux simulated with a bimolecular AOM rate law can vary from being higher to much smaller than the one estimated in the bioenergetic approach, depending on the value of k_{AOM}.

Bioenergetic CH_4 efflux >> bimolecular CH_4 efflux

Dale et al., 2008c: bimolecular CH_4 efflux depend on k_{AOM}

Such a conclusion seems to disagree with what we showed in Paragraph 4.3.2.2."AOM rate constant", where we deflated the role of k_{AOM}, but such a disagreement has to be put into perspective. Firstly it is actually expected even in our case that, with a bimolecular AOM implementation, CH_4 flux increases if k_{AOM} is further reduced down, and it could not be otherwise, considered that k_{AOM} controls the AOM rate. But the employment of values for k_{AOM} smaller than the ones we explored is not supported by any other previous study and would have then therefore rather arbitrary. Secondly some light should be shed on why the bimolecular and the bioenergetic AOM formulations give such different methane effluxes, under the same conditions.

Apparent k_{AOM} is small and spatial dependent

For this purpose we assessed an apparent k_{AOM}, *i.e.* how the k_{AOM} would look like if we wanted to describe the AOM rate at the end of the transient simulation by means of the bimolecular description of

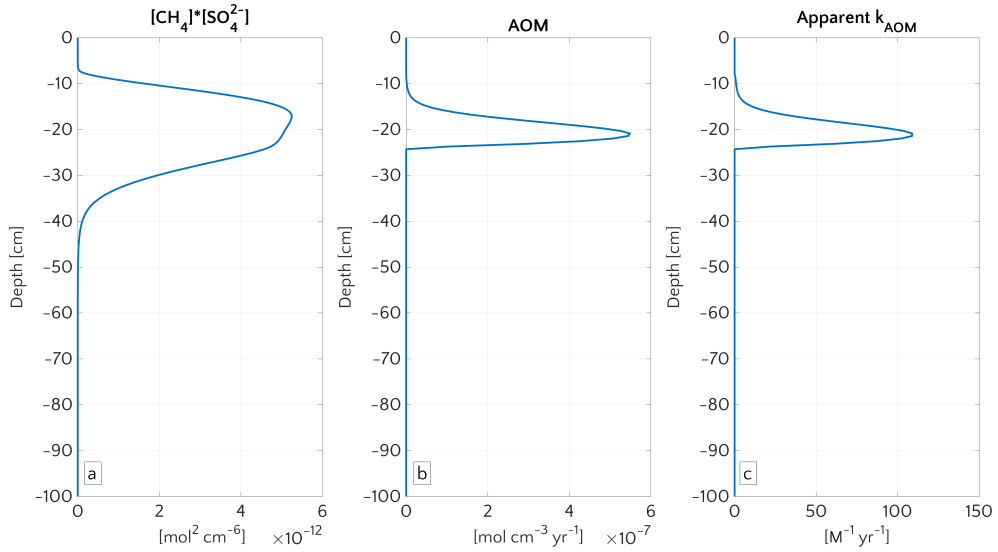

Figure 4.22: Vertical profiles at the end of transient simulation (after 200 years) with bioenergetic AOM formulation for the case $[CH_4]_- = 1.169$ mM and $v_{up} = 5$ cm yr^{-1}. *a.* Bimolecular product $[CH_4] \cdot SO_4^{2-}]$. *b.* AOM rate. *c.* Apparent k_{AOM}, estimated from Eq. 4.27.

Eq. 4.27. Results are shown in Fig. 4.22. Panel 4.22.*a* shows that the product $[CH_4] \cdot [SO_4^{2-}]$ is broader than the AOM profile (panel 4.22.*b*). It therefore means that the bioenergetic AOM is strongly limited by the thermodynamic constraint F_T (Eq. 4.30). Fig. 4.22.*c* also shows that the apparent k_{AOM} is not constant and never exceeds 109 M^{-1} yr^{-1}, being for the most of the depths well below 100 M^{-1} yr^{-1}. It confirms that AOM resulting from bioenergetic formulation cannot be trivially described by a simple bimolecular expression of the rate with a constant k_{AOM} value. This, combined to the low values of apparent k_{AOM}, gives reason of the difference in steady-state CH_4 effluxes.

Biomass controls: F_T and F_K temporal and spacial dynamics

The onset of an efficient AOM biofilter requires the establishment of an AOM community that is sufficiently large to consume upward migrating methane. Therefore, the AOM and its filter efficiency are controlled by AOM biomass dynamics, which in turn are determined by kinetic (F_K) and thermodynamic (F_T) constraints. Fig. 4.23 illustrates the depth profiles of the thermodynamical and kinetic terms in the bioenergetic AOM formulation (Eq. 4.28), as well as their evolution in response to the onset of a sudden methane flux from below. Initially, although kinetically possible (i.e. $F_K \neq 0$, Eq. 4.29), AOM is inhibited by thermodynamic constraints (i.e. $F_T = 0$, Eq. 4.30). These thermodynamic constraints ease when the SMTZ becomes stationary after the initial decades. At that point, favourable conditions are encountered over a horizon about 20 cm deep (for methane scenario 4 and $v_{up} = 5$ cm yr^{-1}) and the increasing AOM filter efficiency reduces methane efflux (Fig. 4.23.*b*). After 200 years (Fig. 4.23.*c*), a more uniform sulfide concentration in lower sediments together with the upward movement of the SMTZ pushes the maximum of F_T upwards,

F_T main constraint to AOM

thus limiting the zone where AOM is thermodynamically favourable ($\sim$ 13 cm deep). F_T remains the main constraint on AOM throughout the simulation.

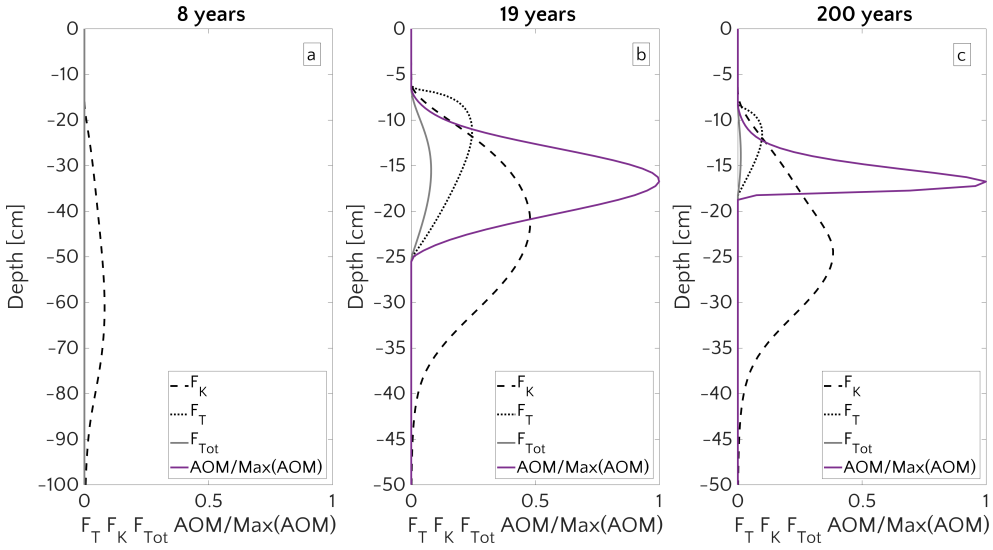

Figure 4.23: Vertical profile of F_T, F_K, $F_{Tot} = F_K \cdot F_T$ and the AOM (scaled to the maximum) for three instant in times. 8 years (*a*), 19 years (*b*)and 200 years ((*c*) of simulation, for the case $[CH_4]_- = 1.169$ mM and $v_{up} = 5$ cm yr^{-1}.

ΣB comparable with previous findings

Integrated biomass ΣB ranges from $\sim 1.2 \cdot 10^{10}$ to $3.5 \cdot 10^{11}$ cells cm^{-2} (except for simulation with $v_{up} = 5$ cm yr^{-1} and $[CH_4]_- = 5.455$ mM, whose $\Sigma B = 1.2 \cdot 10^{12}$). These values are comparable with AOM biomass reported in Treude et al., 2003 ($1.5 - 1.8 \cdot 10^{10}$ cells cm^{-2}) or with values simulated in Dale et al., 2008c ($3.7 \cdot 10^{11}$ cells cm^{-2} for $v_{up} = 5$ cm yr^{-1}). In addition, the maximum simulated biomass for active settings of $0.5 - 2.5 \cdot 10^{10}$ cells cm^{-3} well agrees with previously reported values, ranging from 0.27 to $7.4 \cdot 10^{10}$ cells cm^{-3} (Dale et al., 2008c).

ΣAOM smaller than previous findings

However, integrated AOM rates, ΣAOM, are instead smaller then previously published rates for shallow, active sites (Boetius et al., 2000; Haese et al., 2003; Luff et al., 2003; Linke et al., 2005; Wallmann et al., 2006b; Dale et al., 2008c), but comparable to those observed in active sites below the shelf break (Aloisi et al., 2004; Wallmann et al., 2006a; Maher et al., 2006) or in passive settings (Borowski et al., 1996; Martens et al., 1998; Fossing et al., 2000; Jørgensen et al., 2001; Dale et al., 2008c).

Reasons of discrepancy

The discrepancy is likely due to different environmental conditions encountered at these sites. For instance, Dale et al., 2008c applied an advective velocity of $v_{up} = 10$ cm yr^{-1} and $[CH_4]_- = 60$ mM. While differences in v_{up} affect the ΣAOM, their effect on ΣB is negligible since an efficient AOM microbial filter is known to account for at least $> 10^{10}$ cells cm^{-3} (Lösekann et al., 2007; Knittel et al., 2009).

Simulation results finally show that AOM biomass and, thus, AOM rate increase with an increase in methane supply from below (Fig.

C.12). The ratio between the flux of methane at the SWI and the advective methane flux at the bottom of the sediment column reflects this behaviour. It decrease from values > 1 to values < 1 with an increase in methane from below (Fig. C.11.*b*). This does not only mean that *in situ* methanogenesis rather than methane supply from below drives methane efflux for low methane supply scenarios, but also that the influence of methanogenesis on efflux decreases with an increase in methane supply. This shift is accompanied by a shift in the a diffusion-driven to a advection-driven influx (not shown). In addition, although absolute methane efflux is higher for higher $[CH_4]_-$, the smaller values of the efflux/influx ratio show that the system becomes much more efficient in removing methane when it is forced with a higher methane flux. Simulation results show that the AOM biofilter efficiency increases by 17% (49% in passive settings) over the increase of $[CH_4]_-$ from 20 μM to 5.455 mM in agreement with observations (Treude et al., 2003; Beer et al., 2006; Niemann et al., 2006a). However, although AOM becomes more efficient, it cannot keep up with increasing fluxes, indicating that the inability of the AOM biomass to completely consume higher CH_4 flux does not exclusively depend on the presence of methane bubbles, as previously stated (James et al., 2016).

AOM biomass and rate increase with $[CH_4]_-$

Higher AOM efficiency for high $[CH_4]_-$ but...

it does not keep up with increasing flux

4.3.4 *Relations between Anaerobic Oxidation of Methane and Sulfate Reduction*

AOM connection to SR in the Arctic shelves crucial: in terms of (i) relative proportions (Regnier et al., 2011; Egger et al., 2018), to understand what is the weight of AOM in sulfate reduction compared to organoclastic sulfate reduction. (ii) byproducts, considering that SR is associated with alkalinity and sulfides production (and the link to iron cycle, which is particularly crucial in Arctic setups). (iii) effects that some transport processes (*e.g.* explicit bubble movement) may have in biogeochemical ratios of methane and sulfate (Regnier et al., 2011).

Role of AOM-associated SR

To better understand this, let us look at what happens at the SMTZ, since it is the key zone where AOM occurs. Fig. 4.24 shows the flux of CH_4 and SO_4^{2-} at SMTZ and two features are striking: i) the overall broad symmetry between the two fluxes; ii) the exponential-like trend. On a log-log scale we find two similar linear trends both for methane (Fig. 4.25.*c*) and sulfate (Fig. 4.25.*d*). Such a relation had also been identified by Egger et al., 2018 (see Fig. 4.25.*a*,*b*), taking into consideration measurements at AOM sites on a global scale. BRNS appears hence to be able to qualitatively grasp this feature ($R^2 = 0.77$ not dissimilar from $R^2 = 0.81$ by Egger et al., 2018), which holds also at a regional scale and in an environment not sampled by the data used by Egger et al., 2018. Considering the maximum and minimum values

Symmetry of CH_4 and SO_4^{2-} fluxes at the SMTZ and exponential trend

Qualitative agreement with global relationship by Egger et al., 2018

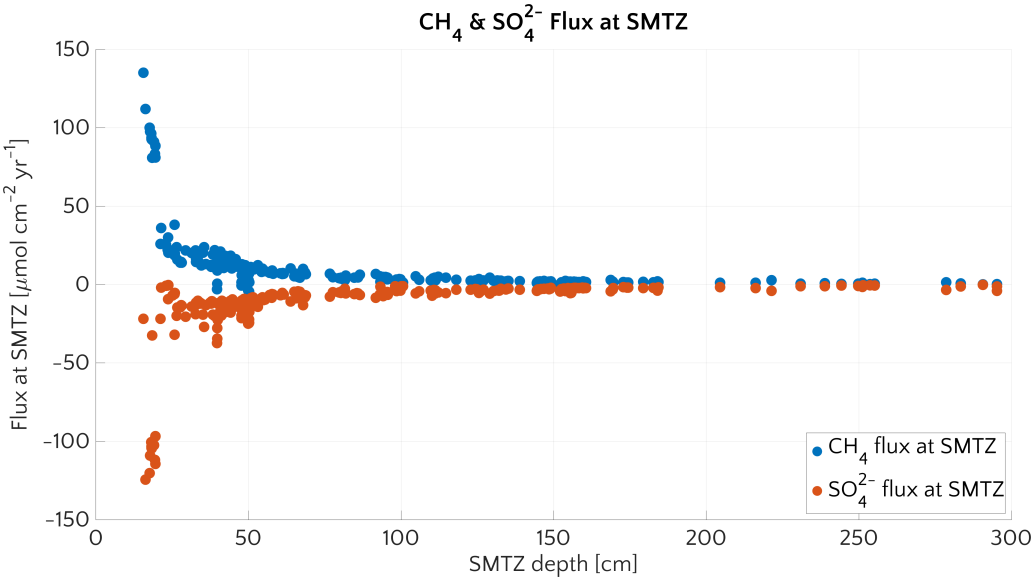

Figure 4.24: Methane (blue) and sulfate (red) fluxes at the SMTZ versus SMTZ depth. Positive values mean upward fluxes while negative values mean downward fluxes.

of SMTZ depth that we find in our analysis (compatible with typical values of other methane influenced setups, *e.g.* Niemann et al., 2006b) and computing corresponding fluxes at the SMTZ with the relationships we have found, we estimate variations of the fitted fluxes with respect to the values reported by Egger et al., 2018: they lie between 17%-93% for CH_4 and 67%-77% for SO_4^{2-}.

Theoretical SO_4^{2-} : $CH_4 = 1:1$

Fig. 4.26.a reports the ratios of the SO_4^{2-} to CH_4 fluxes at SMTZ. From the stoichiometry of AOM (Eq. 4.3), SO_4^{2-} : CH_4 is expected to be 1:1 in steady-state, but also organoclastic SR contributes to sulfate consumption. Moreover there is always a preferential vertical direction component of the flux, which is the advective one, even if it is generally small. For all these reasons ratio is not unitary. Nevertheless if AOM itself represents the main contribution to SR, then the SO_4^{2-} to CH_4 ratio at SMTZ is expected to be roughly unitary and should not depend on SMTZ. The more it diverts from 1 the higher is the influence of organoclastic SR, which depends instead on OM content and quality. The overall picture shows that the dependency of the ratio on SMTZ depth is weak and for most of the cases it lies in a narrow stripe between $0.8 - 4.4$. A ratio around 1 can also be inferred from Fig. 4.24.

Ratio SO_4^{2-} : $CH_4 = 0.8 - 4.4$

Average SO_4^{2-} : $CH_4 = 1.36$ *in agreement with Egger et al., 2018*

If we do not consider the 14 outliers whose ratio is larger than 10^7 in Fig. 4.26.*a*, we find an average value of the ratio which is 1.36, not different from the corresponding value of $\sim$ 1.4 reported in Egger et al., 2018. From this value one would infer that $\sim$ 70% of SO_4^{2-} is consumed in AOM. Nonetheless this quantity finds no confirma-

7 Usually or model artifacts or originating from a vague definition of the SMTZ.

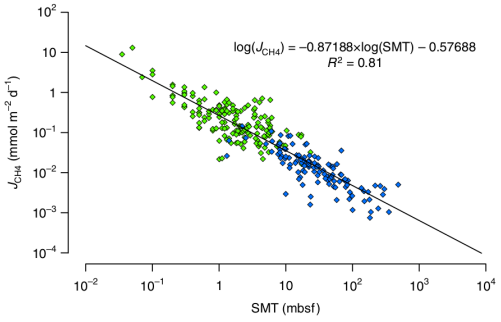

(a) Methane flux at the SMTZ versus SMTZ depth. From Egger et al., 2018.

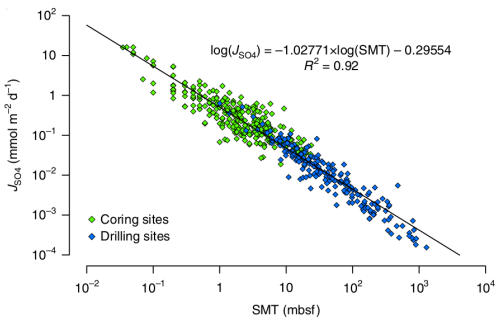

(b) Sulfate flux at the SMTZ versus SMTZ depth. From Egger et al., 2018.

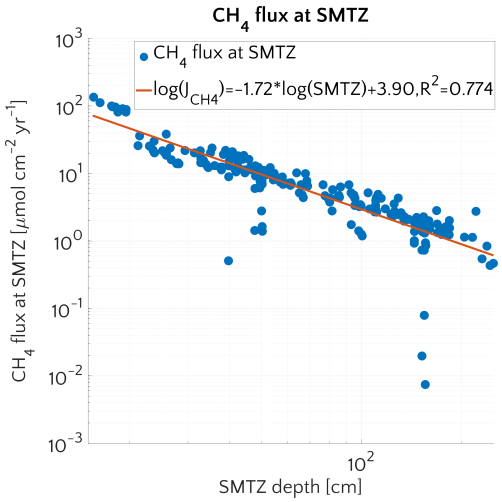

(c) Methane flux at the SMTZ versus SMTZ depth.

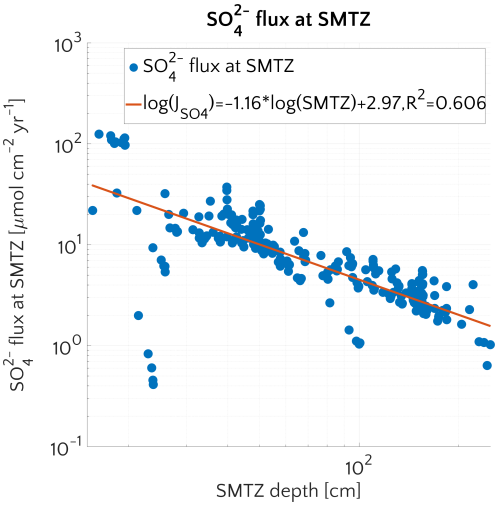

(d) Sulfate flux (absolute value) at the SMTZ versus SMTZ depth.

Figure 4.25: Methane and sulfate flux at the SMTZ versus SMTZ depth. Comparison with BRNS results and findings from Egger et al., 2018.

70% SO_4^{2-} consumed in AOM

tion if the ratio of integrated AOM (ΣAOM) to the integrated total SR (ΣSR as a sum of organoclastic SR and AOM-mediated SR) is considered (Fig. 4.26.*b*). In this case we see a decline of the role that AOM has in consuming sulfates with increasing SMTZ, suggesting that with deepening SMTZ, organoclastic SR does not decrease as fast as integrated AOM rate decreases. A deeper sulfate penetration may hence shift the weight that organoclastic SR has in comparison with AOM. The average value of ΣAOM/ΣSR is 0.30, which disagrees with the value of $\sim$ 70% previously found. It gives hence indication that the weight that contributions of bioirrigation and advection to fluxes at SMTZ must probably also be relevant. Considering in fact the ratios according to the upward water flow velocities we find that active sites have higher AOM contribution to total SR compared to passive sites (Regnier et al., 2011). Mean values augmented from 0.17 in passive setups, to 0.54 in active setups with the highest velocity v_{up} (and a mean value for active sites of 0.42).

Ratio ΣAOM: ΣSR= 0.3

Discrepancy probably due to transport processes

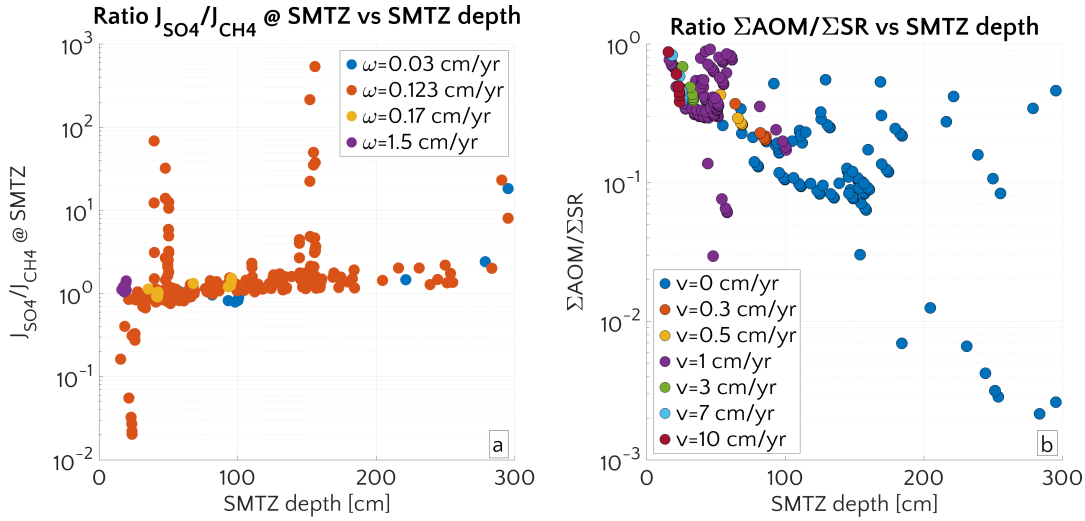

Figure 4.26: *a* Ratio of the flux of sulfate to the flux of methane at the SMTZ depth versus the SMTZ depth. From AOM stoichiometry it is expected to be 1. Colours identify simulations with dfferent ω. *b* Ratio of vertically integrated AOM rate to vertically integrated sulfate reduction rate. Scatter plot versus the depth of SMTZ. Colours identify simulations with different v_{up}.

Potential for AOM and SR in the Laptev Sea

We can also evaluate the range of SO_4^{2-} reduction and CH_4 oxidation capacity which can be attributed to ESAS by simply upscaling the punctual value (no more refined method like 3-D kriging). SO_4^{2-} ESAS reduction capacity would be between $0.114 - 11.82$ $TmolSO_4^{2-}$ yr^{-1}. As already mentioned before, both the lowest and upper results are extreme cases, also keeping in mind that Egger et al., 2018 estimated a global SO_4^{2-} reduction of 5.3 $TmolSO_4^{2-}$ yr^{-1}. CH_4 ESAS oxidation capacity would instead sum up to $0.12 - 87$ $TgCH_4$ yr^{-1}, where the global estimated values reported by Egger et al., 2018 are $45 - 61$ $TgCH_4$ yr^{-1}. Estimated values just for the subsea permafrost area ($\sim$ 3 million km^2) add up to $0.0001 - 1.1889$ $TgCH_4$ yr^{-1} (Winkel et al., 2018).

4.4 CONCLUSIONS

In this study, we evaluate the potential for non-turbulent methane escape from both passive as well as active East Siberian Arctic Shelf (ESAS) sediments that are affected by deep methane supply from, for instance, thawing subsea permafrost or methane gas hydrate dissociation. We identify the most important biogeochemical and physical controls on non-turbulent methane escape from those sediments under steady state conditions, as well as in response to environmental variability on seasonal and centennial timescales. Finally, we derive a first regional estimate of (not-turbulent) methane benthic-pelagic flux and of potential methane consumption in the Laptev Sea.

Model results reveal that AOM is an efficient sink for upward migrating dissolved methane in ESAS sediments. Simulated non-turbulent methane effluxes are negligible for a broad range of environmental conditions under both steady state and transient conditions. On the ESAS, AOM is a transport-limited process and transport parameters thus exert an important control on the efficiency of the AOM biofilter and, thus, on methane efflux. Both steady state and transient model results confirm the key role of advective transport (sedimentation and active fluid flow) in supporting methane escape from Arctic shelf sediments. Under steady state conditions, high methane effluxes (up to 27.5 μmol cm^{-2} yr^{-1}) are generally found for sediments that are characterized by high sedimentation rates and/or active fluid flow (sedimentation rate $\omega > 0.7$ cm yr^{-1}, active fluid flow $v_{up} > 6$ cm yr^{-1}). Under these conditions, methane efflux can be further enhanced by intermediate organic matter reactivity (RCM model parameter $a = 10 - 10^2$ yr) and intense local transport processes, such as bioirrigation (irrigation constant $\alpha_0 > 1$ yr^{-1}). Our results indicate therefore that present methane efflux from ESAS sediments can be supported by methane gas escape and non-turbulent CH_4 efflux from rapidly accumulating and/or active sediments (*e.g.* coastal settings, portions close to river mouths or submarine slumps). In particular, active sites sediments may release methane in response to the onset or increase of permafrost thawing or CH_4 gas hydrate destabilization.

AOM is an efficient biofilter

AOM is controlled by advective transport

Maximal CH_4 efflux in steady state

Supposed role of bubbles

High methane escape (up to $11 - 19$ μmolCH_4 cm^{-2} yr^{-1} corresponding to $2.6 - 4.5$ TgCH_4 yr^{-1} if upscaled to the ESAS) can occur during a transient period following the onset of methane flux from the deep sediments. Under these conditions, substantial methane escape from sediments requires the presence of active fluid flow that supports a significant and rapid upward migration of the SMTZ in response to the onset of CH_4 flux from below. Such rapid and pronounced movements create a window of opportunity for non-turbulent methane escape by inhibiting the accumulation of AOM-performing biomass within the SMTZ - mainly through thermodynamic constraints - thereby perturbing the efficiency of the AOM biofilter. The magnitude of methane effluxes, as well as the duration of this window of opportunity, is largely controlled by the active flow velocity. In addition, results of transient scenario runs indicated that the characteristic response time of the AOM biofilter is of the order of few decades ($20 - 30$ years), thus exceeding seasonal-interannual variability. Consequently, seasonal variation of bottom methane and sea water sulfates exert a negligible effect on methane escape through the SWI.

Maximal transient CH_4 escape

Window of opportunity for CH_4 escape

v_{up} dependency of window of opportunity

Characteristic time response: $20 - 30$ yr

The role that AOM has in consuming sulfate remains an open matter. On one hand our results for Arctic are quantitatively in agreement with some measurement-based world estimate (Egger et al., 2018). On

Role of AOM in SR is uncertain

the other hand the role that AOM turns out to have in reducing seawater sulfate depends actually on the method considered to assess it, ranging between $30 - 70\%$ (at least for the region considered). Uncertainty in the potential sulfate reducing power of sediments lying on East Siberian Arctic Shelf spans the range $0.114 - 11.82$ $TmolSO_4$ yr^{-1}.

AOM affects the biogeochemistry on the whole

AOM generally acts as an efficient biofilter for upward migrating CH_4 under environmental conditions that are representative for the present-day ESAS with potentially important, yet unquantified implications for the Arctic ocean's alkalinity budget and, thus, CO_2 fluxes. Our results thus suggest that previously published fluxes estimated from ESAS waters to atmosphere cannot be supported by non-turbulent methane efflux alone.

Laptev sea upscale of CH_4 efflux: ~ 0.1 $GgCH_4$ yr^{-1}

A regional upscaling of non-turbulent methane efflux for the Laptev Sea Shelf using a model-derived transfer function that relates sedimentation rate and methane efflux merely sums up to ~ 0.1 $GgCH_4$ yr^{-1}. Nevertheless, it also suggests that the evaluation of methane efflux from Siberian Shelf sediments should pay particular attention to the dynamic and rapidly changing Arctic coastal areas close to big river mouths, as well as areas that may favor preferential methane gas release (*e.g.* rapidly eroding coastlines, fault lines or shallow sea floors, *i.e* < 30 m). In addition, our findings call for more data concerning sedimentation and active fluid flow rates, as well as the reactivity of depositing organic matter and bioirrigation rates in Arctic shelf sediments.

Potentially sensitive environments

Perspectives

In conclusion , we argue that the evaluation of projected subsea permafrost thaw and/or hydrate destabilization impacts on the Arctic environment requires models that include an explicit description of 1) methane gas, 2) AOM biomass, as well as 3) the entire network of the most pertinent biogeochemical reactions. Such approaches, valid globally for all the shelves underlain by methane reservoirs (*e.g.* continental slopes), are even more recommended in order to enable a robust quantification of methane escape from the Arctic shelf to the Arctic ocean, settings even more sensible to the rapidly changing environmental conditions. Finally such refined modeling will also help evaluate the impact of subsea permafrost thaw and methane destabilization on Arctic alkalinity and biogeochemical cycling.

5 CONCLUSIONS

First comprehensive study of the SSPF and its potential impact on the Arctic carbon cycle

This dissertation presents the first comprehensive study of the ubsea permafrost (SSPF) with a focus on its possible impact on the carbon cycle of the Arctic region and its consequent climate impacts. Several problems relative to different aspects of the SSPF have been faced in a transversal approach: structural properties, thermal state and biogeochemical impact as a potential source of greenhouse gases, to the water column and, eventually, to the atmosphere.

Multi-sided approach

These aspects have been considered and dealt with in various and complementary ways both with experiments and with modeling, resorting to two types of models: i) a component of an Earth System Model (ESM) and ii) a diagenetic model, aiming at unraveling different questions about the subject. In light of such a diverse approach, the results of this study offer a rather comprehensive and many-sided view of the topic and its related problems.

SSPF hosts an unknown amount of carbon

The SSPF has been considered a reservoir of a potentially large amount of carbon and identified as a possible origin of the high methane concentration measured lately (Shakhova et al., 2010b; Shakhova et al., 2014; Shakhova et al., 2017) in the waters of the East Siberian Arctic Shelf (ESAS), especially in the Laptev Sea. These measurements and such interpretations have however originated a vivid debate about the validity of the measurements themselves (especially on the trustworthiness of their upscale), about the origin of methane (Overduin et al., 2015b; Sapart et al., 2017) and about the cause and extent of the SSPF thawing.

Research questions about the properties of the SSPF and about the AOM

I set up a research line consisting of multiples approaches with the goal to investigate the main properties of the SSPF and to fill some of the knowledge gaps about the Anaerobic Oxidation of Methane (AOM), the process which basically controls the emission of methane to the water column and sets the potential release of methane from the ESAS. This research strategy had the aim of making up for the lack of extensive, structural and planned observations of the SSPF condition, carbon content or specific studies on its impact on the carbon release in the Arctic. The topic lacks also a history of systematic modeling, with only spare simulations performed over time with models specifically tailored to address some problems but missing other aspects.

5.1 CHAPTER 2. THE SUBSEA PERMAFROST IN A BOX: LABORATORY EXPERIMENTS, MODELING RESULTS AND COMPARISON WITH STEFAN'S PROBLEM

Experimental setups

In Chapter 2 I describe the design and results of two experiments carried out in the sea ice laboratory[1]. These have been the first experiments performed to study the thawing of the SSPF in the controlled environment of a laboratory. In such experimental setups the SSPF was therefore simplistically as frozen porous medium overlain by salty water with a temperature higher than the thawing temperature.

The experiments enabled the investigation of the delicate moment of the submergence of permafrost and the study of how the thawing front evolves over time.

Is the numerical model able to reproduce the movement of the phase boundary?

Convective-corrected heat conduction scheme works well

The comparison of experimental results with the outcomes of a model developed on purpose has shown that the heat is transported by conduction and, at least in the constrained context of the laboratory, also by convection. Limiting the model scheme to a pure heat conduction is therefore a poor approximation which brings to wrong outcomes. However the conductive model can be properly modified to take convection into account and this results in a generally good agreement between experimental and model outcomes. *The capacity of the conductive model to reproduce the data suggests that heat conduction alone can be considered to be the main form of heat propagation in larger setups, such as the SSPF for real.*

How do the laboratory and model results compare to theoretical expectations?

Stefan-like parabolic solution reproduces the data

Conduction turns out to be enough to grasp the main features of the thawing, once the chemical effects of the salt are considered. For this reason an overall broad agreement emerges between the observed thawing profiles and a parabolic, theoretical Stefan-like profile. Since one of the main assumption behind the development of Stefan's problem is the purely conductive nature of the heat transfer, the fact that a parabolic solution fits well the experimental results is a confirmation about the reasonableness of this hypothesis. However it has been shown that the fully theoretically derived Stefan's solutions is not capable of reproducing the experimental results and therefore it cannot be used as a predictive tool in place of an experiment or of a model run.

1 Thanks to the supervision of Dr. Dirk Notz and the technical support of Niels-Jakob Fuchs

How do the model results compare with field observations?

First phases after submersion correspond to the fastest thawing

Laboratory results have finally confirmed with the experiments the *critical role of the first phases after the submergence* as those phases when the thawing rate is the fastest. This fact is qualitatively in agreement with the thawing rates measured in multiple locations with several methods and sets an emphasis on the importance of a good modeling the first phases of the thawing.

5.2 CHAPTER 3. THE SUBSEA PERMAFROST ENTERS AN EARTH SYSTEM MODEL: THE CASE OF JSBACH

Implementation of a SSPF module in JSBACH

The research presented in Chapter 3 ideally upscales the simple experimental setup described in Chapter 2 and loosens its artificial constraints taking the first step towards a consistent study of the real SSPF, the one spreading in the Arctic shelf. Unlike previous studies, the modeling tool chosen for my research has not been an *ad hoc* model but rather JSBACH, the land component of a larger ESM. *For the first time I implemented the submergence of the terrestrial permafrost and the consequent formation and evolution of the SSPF in a model developed for climate simulations*. Besides adding a novel feature to an ESM, such implementation has had also the advantage of relying on a process-based and physically-based model and therefore on a model potentially capable of keeping track of the complex and multiple phenomena occurring for real.

How does submergence affect the permafrost in JSBACH? What is the SSPF time response to change of upper boundary conditions from land to submarine?

Response time of modeled SSPF: millennia

As emerges from JSBACH simulations, the typical response time of the SSPF to the submersion is of the order of the millennia, in line with other previous findings (Romanovskii et al., 2005; Malakhova et al., 2017). It implies that, as long as the average sea bottom temperature is lower than the thawing temperature of the SSPF, the degradation from above proceeds at an extremely slow pace. Provided that the sea bottom water temperature is lower than 0 °C (as it is currently), the SSPF thawing temperature is set by the sluggish salinity penetration within the sediments, which is therefore the limiting factor for the thawing rate. In the simulations I performed using pre-industrial forcing, the thawing due to a combined temperature-chemical effect is only of 82 cm in 1000 years, and it poses therefore no significant threat to a massive destabilization of the SSPF and the carbon stored within in interglacial periods.

Salt drives th thawing in interglacial periods

Thawing rate is small in interglacial period: $\sim 0.8\ cm\ yr^{-1}$

How does the SSPF modeled in JSBACH compare to observations, other studies and to theoretical expectations?

Reasonable agreement with equilibrated profiles

The results of the 1-D site-level JSBACH simulations for the SSPF show a temperature profile usually a bit higher than the temperature profiles retrieved from cores, but compatible with the limitations imposed by the model itself (the temperature of the water set as upper boundary conditions never goes below -1.41 °C). *The agreement between modeled and measured temperature profiles is better for the sediments submerged for a longer period and which have therefore had more time to equilibrate to the new boundary conditions*. Simulations show a thawing which is not compliant with Stefan's theoretical solution expect for one idealized scenario, suggesting that the quickly varying boundary conditions might be the cause for a non-Stefan trend.

Under which conditions is an extensive destabilization of the SSPF possible?

Massive destabilization if summer temperatures continue increasing or in 2300 according to RCP 8.5

The slow temporal response and the little salt-induced thawing are valid in pre-industrial conditions and the situations drastically changes if the sea bottom water temperatures is even slightly larger than the thawing temperature of the SSPF. In this case the time needed to have a large destabilization is much smaller and of the order of few centuries. Such condition is compatible with two projections.

i The ongoing increase of the sea bottom temperatures during the summer in the Laptev Sea (Dmitrenko et al., 2011), if persistent, brings the yearly average temperature above the threshold of 0 °C in about four decades. In this case a net thawing occurs independently of the salt effects into the sediments. This would cause a thawing of more than 30 m in 200 years. It must also be stressed that the thawing rates simulated in this scenario do agree with the modern and high (up to 16 cm yr^{-1}) thawing rates recently measured in the Laptev Sea (Shakhova et al., 2017), suggesting therefore that the current climate might actually be the cause of an acceleration of the thawing, whereas the slow natural response to the submersion would on the contrary cause a slowing down.

ii An Arctic sea bottom water temperature which could be up to $+10$ °C higher than nowadays temperatures is projected in year 2300 according to the RCP 8.5 (Giorgetta et al., 2013), which is the concentration pathways that has been currently being followed. Simulations have shown that in this case the entire thickness of the modeled permafrost (100 m) would eventually thaw in 270 years.

Is JSBACH capable of modeling complex features like taliks?

JSBACH models the salinity-induced taliks

Simulations showed that *JSBACH is capable of reproducing, at least qualitatively, salinity-induced features like the taliks*, although in a reduced size compared to the observations (Osterkamp et al., 1989) or other model (Nicolsky et al., 2010). Taliks represent important SSPF characteristics because, being unfrozen throughout the year, they constitutes a place where carbon is available for biogeochemical processes and they can also serve as preferential pathway for migration of chemical species, enhancing the biogeochemical role of the SSPF.

What are the current limitations present in JSBACH for modeling the SSPF?

Main defects: bedrock level and lack of salt diffusive scheme

JSBACH simulations have also enabled a deep understanding of the current main limitations of the model itself. *The principal downside is the lack of an explicit scheme for the motion of the salt and the shallow position of the bedrock*. The latter has especially a relevant role in determining how the sediment column is affected from above because it sets the depth where the system changes its physical regime: from a phase-changing system above the bedrock to a simple warming system below the bedrock. These limitations hamper the use of JSBACH for a better understanding of the impact of the SSPF on the carbon cycle and on the climate system, and thwart its employment for hind- and fore-casting.

5.3 CHAPTER 4. ASSESSING THE POTENTIAL FOR NON-TURBULENT METHANE ESCAPE FROM THE EAST SIBERIAN ARCTIC SHELF: THE EMPLOYMENT OF BRNS

BRNS simulation of CH_4-affected sediments on the ESAS

Chapter 4 is devoted to the investigation of the potential contribution of the SSPF as source of greenhouse gases (mainly methane) and to its effects in the biogeochemistry of the Arctic shelf, especially the ESAS.

The quantity and the quality of the carbon stored in the SSPF and the efficiency of the biological filters consuming methane, especially the AOM, is largely uncertain. Such an uncertainty prevents a systematic understanding of the Arctic carbon cycle and an overview of the SSPF in the methane budget. For these reasons the role of the AOM and of the other biofilters, as well as their influence in the biochemistry of the sediments, has been investigated with a diagenetic model, BRNS, which includes the most important transport and reaction processes occurring during diagenesis. This model allows hence the theoretical exploration of the biogeochemical impact of the SSPF.

How efficient is the AOM biofilter? Which are the most important environmental controls on the efficiency of the AOM itself?

AOM is an efficient biofilter for CH_4

Results of 1-D simulations on a generic sediment column designed to be representative of the Arctic conditions show that, in many settings and in most of environmental conditions, *the AOM acts as a very efficient filter, consuming the dissolved methane almost completely before it reaches the water column*. As the AOM is transport-limited, it turns out that transport parameters are particularly important in determining the efficiency of the AOM, which decreases in presence of a high advective transport. The reason of such crucial role is that transport rules indeed the availability of the "fuel" of diagenetic process: the organic matter.

Under which condition is a high methane escape possible?

AOM efficiency is reduced if advective transport is high

In settings with high sedimentation rate and/or high active water flow, the local flux of methane at the Sediment-Water Interface (SWI) can be as high as in some mud volcanoes (up to 27.5 $\mu molCH_4\ cm^{-2}\ yr^{-1}$). It has also been shown that this efflux can be tellingly enhanced by the patchy bioirrigation proofing that, at least in the ESAS setting, this process indeed decreases the AOM efficiency and answering one of the open questions regarding the AOM (James et al., 2016). Other forms of non-local transport, like ice scouring, are also expected to increase methane efflux.

Bioenergetic modeling: AOM efficiency responds to perturbation of BC

Substantial methane escape (up to 19 $\mu molCH_4\ cm^{-2}\ yr^{-1}$) is also temporarily possible in case of a transient scenario, due to a change of the lower methane boundary conditions, for instance in the aftermath of destabilization of gas hydrates or thawing of the SSPF. This changes alter the steady state and efficient microbial community oxidizing methane, and *opens a "window of opportunity" for methane to escape the AOM filter, during the time that the AOM-performing biomass needs to adapt the new conditions*. The length of this period is controlled by the active flow velocity and lasts two-three decades, resulting therefore important mainly on a centennial time scale. The identification of such a peculiar behavior has been made possible thanks to the implementation of a bioenergetic formulation of the AOM, *i.e.* a formulation kinetically an thermodynamically coupling the AOM with the building up of the AOM-performing biomass itself. Although already used in other settings, this has been the first time it has been employed to study the biogeochemistry of the AOM in a critical setting like the ESAS.

How much methane could be emitted from Arctic sediments?

According to modeling results, the estimated regional upscale of the oxidation capacity of the ESAS is higher than the previous estimate (Winkel et al., 2018). Such a high value also reveals itself in the *rather low estimate of the upscaled non-turbulent methane efflux to the waters of the Laptev Sea:* 0.1 $GgCH_4\ yr^{-1}$. This amount of methane is expected to undergo further consumption in the sea water column (like via the aerobic oxidation of methane) and therefore the outgassing flux is thought to be even smaller. The non-turbulent methane flux at the SWI is hence not sufficient to explain the significant methane efflux from the ESAS waters ($0 - 17\ TgCH_4\ yr^{-1}$) estimated by a number of publications (Shakhova et al., 2010b; Shakhova et al., 2014; Shakhova et al., 2015; Shakhova et al., 2017; Shakhova et al., 2019). My modeling result, although only limited to the Laptev Sea, is up to three orders of magnitude lower than the revised and more recent estimates of fluxes from the ESAS area (Berchet et al., 2016; Lorenson et al., 2016; Thornton et al., 2016; Reum, 2019). However it is compatible with the low end of literature estimates and gives an extra confirmation of the actual small amount emitted. *Such a difference can be however explained reminding that in my research only non-turbulent methane fluxes were considered, i.e. bubbles were not taken into account*. It is well-known how ebullition may be a relevant component of methane fluxes, often being the largest one, although characterized by a patchy emission in space and irregular emission in time and therefore problematic to upscale. It is also well-known that gaseous methane is not accessible to AOM, the main process I investigate in this dissertation. Free gaseous methane sums up to a large quantity potentially capable of determining a strong revision of budget of the methane effluxes from the ESAS sediments.

CH_4 oxidation capacity of the Laptev Shelf is high → small non-turbulent regional flux

Regional CH_4 efflux does not back previous estimates of ESAS sea-air CH_4 flux

Potential role of bubbles, not included in my study

How does the AOM affects the relation between CH_4 and SO_4^{2-} in the Arctic sediments?

BRNS simulations have also allowed me to get insight on some unexplored aspects of the AOM, as the the role that the AOM has in consuming sulfate, brought up by a recent research based on global measurements (Egger et al., 2018). The ratio of modeled fluxes at the Sulfate-Methane Transition Zone (SMTZ) confirms locally the global estimate by Egger et al., 2018, namely that about that only about 70% of the sulfates is reduced in the AOM and the remainder is consumed in organoclastic Sulfate Reduction (SR). However the ratio of the integrated AOM to SR rates does not back this assessment. Such a discrepancy may be ascribable to the role of transport processes at the level of the SMTZ defining the fluxes and is the origin of *the uncertainty range*

Role of AOM in SR is uncertain: depends on the evaluation method

in the estimated potential for sulfate reduction in the ESAS which spans two orders of magnitude: $0.114 - 11.82\ Tmol SO_4\ yr^{-1}$.

5.4 OUTLOOK

This dissertation offers a first step in a comprehensive and multi-sided approach at the study of the SSPF and its biogeochemical importance in the Arctic carbon cycle. Many are the questions left open and the challenges that such an integrated study can face with future development.

Call for better data coverage and collaboration

My study advocates generally for a better, namely more numerous and more equally distributed, data coverage of the Arctic sediments. In a setting so prone to quick changes and more sensible than others to anthropogenic influence, only a well-planned and better integrated research activity, open to the positive influence of many groups and transparent in providing the data can offer an adequate overview of the evolution of the Arctic sediment and a sound term of comparison for any further model development.

Perspective for laboratory setups: limiting the spurious convective heat transport

The experimental setup I employed, as well as the model I developed, can surely be revised and used to explore more in detail some of the phenomena related to the SSPF evolution. For instance a larger tank with a larger amount of water could be used to minimize the temperature change of the water itself and simulate better the water overlying the sediments, whose temperature is roughly constant in reality of the Arctic Ocean. A larger tank with higher water temperature could also be of avail in order to speed up the thawing and enabling therefore more numerous experiments. As I showed, the numerical model is reliable and works with the same procedure on a reasonable range of water temperatures. If an improvement of the "ad hoc" model is of interest, the transport of salt should be implemented together with a more physically-based evaluation of instability and the onset of convection. This line of development is especially true if the model is to be used in a small scale setting, like the laboratory tank, where the boundaries introduce non-trivial spurious effects which cannot be neglected.

Perspective for JSBACH improvements to explore the SSPF: salt transport, realistic bedrock, 3D simulations

Concerning *JSBACH*, the most urgent changes needed for a better and more physically sound simulation of the SSPF and of its thawing rate, are: i) the implementation of a transport scheme for the salt, parallel to the heat conduction, based on the simplifying but reasonable assumption that salt moves via diffusion; ii) the introduction of a more realistic bedrock, surely deeper, since its shallowness introduces artificial effects like a "zero-curtain effect" which is merely due to its presence and prevents thawing from occurring; iii) a 3-D setup, ex-

tending the current 1-D vertical model and enabling hence the SSPF modeling on the overall regional setting.

Some of these points are already object of a preliminary work within the frame of the EU Horizon 2020 Project NUNATARYUK[2].

Perspective for BRNS improvements to explore the biogeochemistry of CH_4-affected sediments: AOM effects on carbonate system and on biomass

BRNS offers in its current setting already the chance to explore other aspects linked to the AOM, especially in the ESAS. The impact that AOM has on the carbonate system of the sediments has been left completely unexplored, even if it is known that the alkalinity production associated with AOM is extremely relevant, especially in an iron-rich environment. The study of the effects of the AOM on DIC, alkalinity and carbonate saturation profile (Ω) is therefore a research area extremely promising. The effects of the AOM on carbonate system have been overlooked for long, especially in a regional setting, and the analysis of benthic-pelagic fluxes in response of the AOM could offer a deeper insight on methane-affected sediments and on the repercussions on the carbon cycle.

Another encouraging research branch would be exploring, with the current model, the behavior of AOM-performing biomass. If improvements in its implementation are actually needed (Regnier et al., 2011), it is also true that the biological response to AOM has not been deepened as worth.

Need of a component bubble

An issue of the biogeochemical modeling of methane which has been recalled many times in this dissertation and which is also regularly suggested in literature, is the lack of a bubble component in the models. It is widely acknowledged that bubble modeling is tricky, difficult to implement and especially problematic to coupled to a more general reactive-transport diagenetic model, but this represents by far one of the biggest challenge that modeling community has to face in the future.

Call for a coupling between RTM and ESM

The coupling of a sediment reactive-transport model like BRNS with a regional or global ESM like JSBACH has been advocated for long (Regnier et al., 2011) by the biogeochemical community. A new generation of models, the well-balanced trade off between physics and biogeochemistry, is expected to be developed in the future. The research presented in this dissertation and the technical work behind it represents a first step in this direction. Only such kind of models would allow the researches to state more clearly the role of the Arctic SSPF in the carbon cycle and, eventually on the climate. Coupled models would enable to overcome the approximative calculation I carried out in this chapter to rely on coupled simulations able to properly frame each component of the complicate picture presented in this study. They could be used to investigate paleo scenarios as well a future projections, in an integrated way which needs less and less

2 https://nunataryuk.org/

prescribed inputs but relies more and more on a coherent simulation, with an obvious scientific and technical improvement. The development of 3-D JSBACH coupled with BRNS is one of the main goals of the interdisciplinary EU H2020 project NUNATARYUK, currently in its second year.

APPENDIX

APPENDIX TO CHAPTER 2

A.1 DERIVATION OF NEUMANN SIMILARITY SOLUTION FOR THE STEFAN'S PROBLEM

The derivation of the solution for the Stefan's problem, and so for a system of differential equations like Eq. 2.13 or Eq. 2.25, relies on the scale invariance of the system itself (GFD, 2006) and in the derivation of the so called Neumann solution (Alexiades et al., 1993).

An intrinsic scale length is missing

Let us first show that no intrinsic length emerge in the system and that, therefore, a self-similar solution is legitimate. Let us rewrite Eq. 2.13a and Eq. 2.13c in an dimensionless form, introducing appropriate scales for temperature ($\mathcal{T}$), length ($\mathcal{L}$) and time (t). It means:

$$\frac{\mathcal{T}}{t} \sim \alpha_L \frac{\mathcal{T}}{\mathcal{L}^2} \tag{A.1}$$

which implies $\mathcal{L} \sim \sqrt{\alpha_L t}$. Eq. 2.13c becomes:

$$L\rho \frac{\mathcal{L}}{t} \sim k_L \frac{\mathcal{T}}{\mathcal{L}} = \alpha_L \rho c \frac{\mathcal{T}}{\mathcal{L}} \tag{A.2}$$

which implies $\mathcal{L} \sim \sqrt{St}\sqrt{\alpha_L t}$, with St: Stefan's number $c\mathcal{T}/L$.

The scaling analysis shows that the scale length $\mathcal{L}$ follows, in both cases, the same dependence on the time scale t and that, because of it, no intrinsic, constant, length emerge. This is the requirement for the validity of a similarity solution, which therefore can be written in terms of a new similarity variable.

Let us define this new variable as:

$$\sigma = \frac{x}{\sqrt{t}} \tag{A.3}$$

and the solution of the Stefan problem will be then given in the form

$$T(x,t) = F(\sigma). \tag{A.4}$$

Given the scaling reasoning, the position of the interface is expected to be in the form:

$$Z(t) = A\sqrt{t}. \tag{A.5}$$

In the new variable, Eq. 2.13a reads:

$$-\frac{F'(\sigma)\sigma}{2\alpha_L} = F''(\sigma) \tag{A.6}$$

whose integration yields:

$$F'(\sigma) = Ae^{-\frac{\sigma^2}{4\alpha_L}} \tag{A.7}$$

. Another integration gives:

$$F(\sigma) = A\int_0^\sigma e^{-\frac{s^2}{4\alpha_L}}ds + C = B\sqrt{\pi\alpha_L}\,\mathrm{erf}\,\frac{\sigma}{2\sqrt{\alpha_L}} + C \tag{A.8}$$

having employed the definition of error function:

$$\mathrm{erf}\,z = \frac{2}{\sqrt{\pi}}\int_0^z e^{-s^2}ds. \tag{A.9}$$

Enforcing the boundary conditions, for instance Eq. 2.13e, one gets:

$$C = T_L \quad \text{and} \quad B = \frac{T_m - T_L}{\sqrt{\pi\alpha_L}\,\mathrm{erf}\,(A/\sqrt{\alpha_L})}.$$

Calling

$$\lambda = \frac{A}{2\sqrt{\alpha_L}} \tag{A.10}$$

and plugging it into Stefan's condition (Eq. 2.13c), the similarity solution and the Stefan's implicit equation is derived.

Since the well-posedness of Stefan systems like this has been proofed, the Neumann solution is not only one solution but the only solution that this kind of problem might have and is the prototype form of the solution of Stefan's problems, whenever an analytical is actually possible.

A.2 SENSITIVITY STUDY ON KT AND h

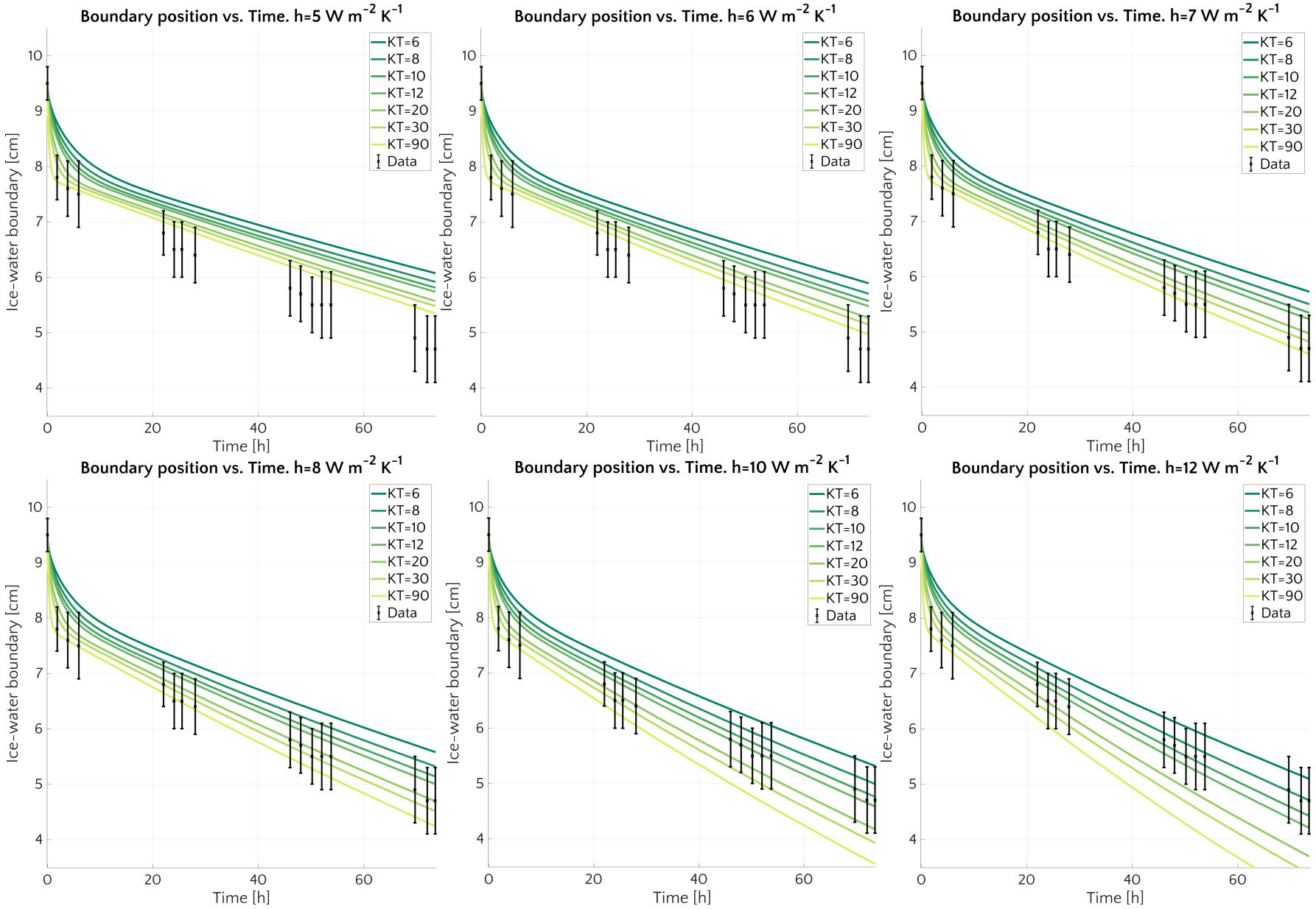

Figure A.1: Sensitivity runs with fixed value of the heat transfer coefficient h and varying constant value of the coefficient KT.

B

APPENDIX TO CHAPTER 3

B.1 EXAMPLE OF TEMPERATURE AND ICE CONTENT EVOLUTION FOR ANOTHER SIMULATION OF THE SET *a*

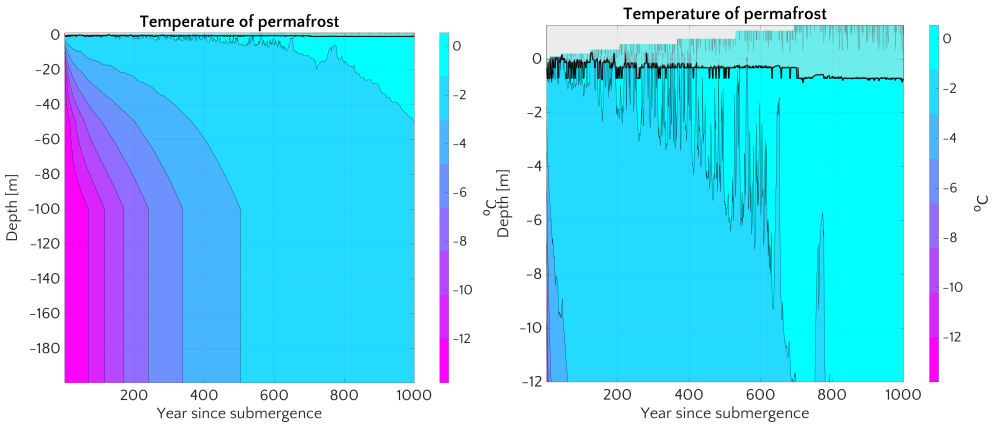

(a) Evolution of September temperature profile. The black line represents the top of the SSPF table while area shaded in gray represents average thawed portion.

(b) Zoom from the SWI(1000) down to 12 m depth

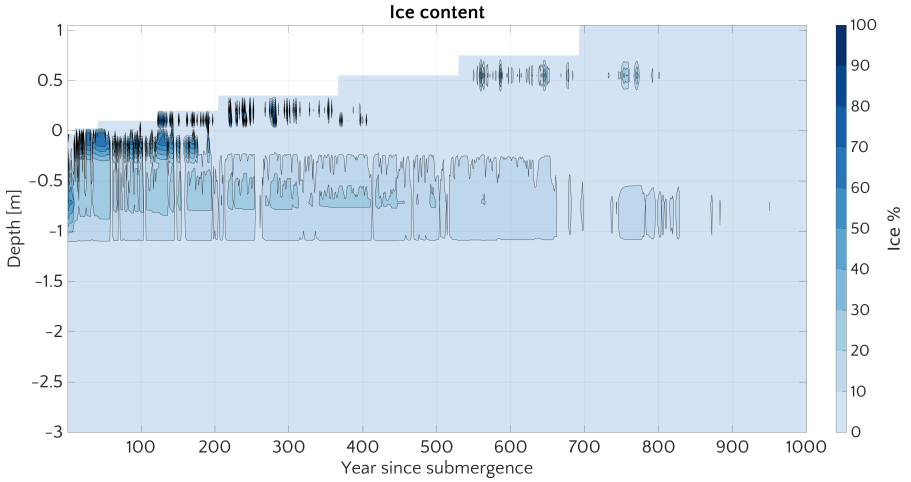

(c) Evolution of September ice content for the top layers

Figure B.1: Temperature and ice content evolution for simulation 4 of the set *A*.

B.2 RESULTS OF THE SIMULATION IN WHICH THE FREEZING TEMPERATURE DIFFERS FROM THE THAWING TEMPERATURE.

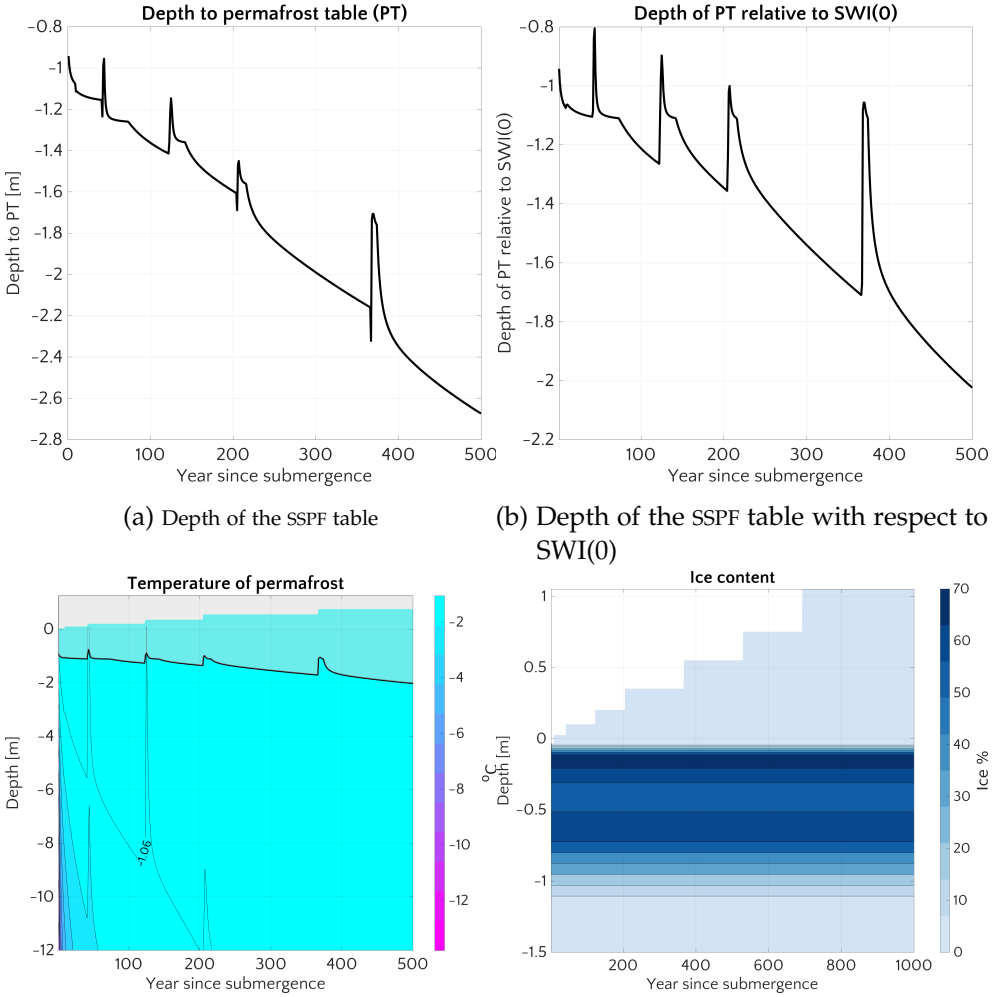

(a) Depth of the SSPF table

(b) Depth of the SSPF table with respect to SWI(0)

(c) Temperature evolution

(d) Ice content evolution

Figure B.2: Results for simulation C.iii, where thawing temperature is set to $T_m = 0$ °C and freezing temperature $T_f = -1.8$ °C. The outcomes are artificial and shed no further light on the physical behavior of the SSPF or on JSBACH. Results are shown here for the sake of completeness.

C

APPENDIX TO CHAPTER 4

C.1 AOM EFFICIENCY η

If we identify the SMTZ region as the portion of the sediment column where the rate of AOM is 1% of the maximum, we can define the efficiency of the AOM filter η as

$$\eta(\%) = \left(1 - \frac{J^{+}_{CH4}}{J^{-}_{CH4}}\right) \cdot 100 \tag{C.1}$$

where J^{+}_{CH4} is the methane flux at the shallowest point where the AOM rate is 1% of the maximum (upper dashed line in Fig. C.1), and J^{-}_{CH4} is methane flux at the deepest point where the AOM rate is 1% of the maximum (lower dashed line in Fig. C.1).

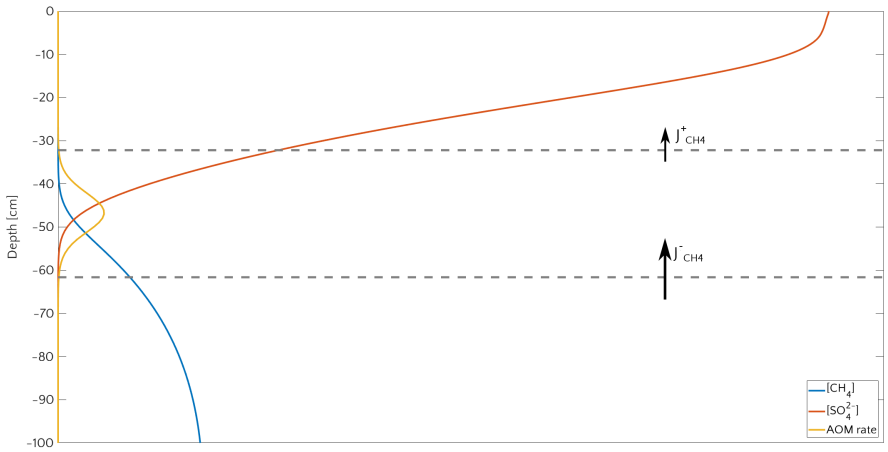

Figure C.1: Typical sediment profile of $[SO_4^{2-}]$, $[CH_4]$ and AOM rate. Units are mM for concentration and mM yr^{-1} for rate. The region between the two dashed lines represents the zone where AOM rate is larger than 1% of it its maximum and defines the Sulfate Methane Transition Zone (SMTZ). The fluxes J^{-}_{CH4} and J^{+}_{CH4} are the fluxes used in the definition of η of eq. (C.1).

C.2 DAMKÖHLER NUMBER

The Damköhler number D_a is a dimensionless quantity which relates time scales typical of transport processes to time scales typical of chemical reactions. It compares the consumption (or production) rate with the advective transport and is defined as

$$D_a = \tau_T / \tau_R \tag{C.2}$$

where τ_T is the advective timescale and τ_R is the reaction timescale. τ_R is defined as $1/K_R$ where K_R is the reaction rate of AOM or methanogenesis. If we call R the reaction rate then K_R reads:

$$K_R = \frac{1}{\mathcal{L}} \int_{\mathcal{L}} \frac{R}{[CH_4]} dz \tag{C.3}$$

where $\mathcal{L}$ is the width where the reaction rate is larger than 1% of the maximum rate. τ_T is instead defined as

$$\tau_T = \frac{\mathcal{L}}{|v_{up} - \omega|} \tag{C.4}$$

where $v_{up} - \omega$ is the effective advective velocity. D_a can be the expressed by:

$$D_a = \frac{\tau_T}{\tau_R} = \frac{1}{|v_{up} - \omega|} \int_{\mathcal{L}} \frac{R}{[CH_4]} dz. \tag{C.5}$$

C.3 2-LEVEL FACTORIAL SENSITIVITY ANALYSIS[1]

A two-level factorial sensitivity analysis (or experiment) is a kind of "all-at-a-time" (AAT) sensitivity study, *i.e.* where the output variation of the system under investigation are induced by varying all the input factors simultaneously. In such a way, with a proper procedure, it is possible to investigate how the variation of the outputs of the numerical model under exam can be attributed to the input factors, also considering their synergetic influence due to interaction.

"Cheap" AAT sensitivity design

It is a simplified form of AAT as each input factor, *i.e.* each model parameter/quantity which can change and whose role we want to assess, can only take two levels: its minimum value (usually just referred to as $-$) and its maximum value (usually just referred to as $+$). In this section I will quickly describe how a two-level factorial sensitivity analysis is performed and how to interpret its outcomes, but I will leave the interested reader to refer to a more appropriate literature (Box et al., 1978; Montgomery, 2007).

Number of runs needed

The two possible values for each input factor are used together and the model is run for each possible combination providing a result. It means that a full 2-level factorial with n factors requires 2^n runs. In case of the application to BRNS the input factors are 6 (ω, a, v_{up}, α_0, k_{AOM}, $[CH_4]_-$) and the considered outputs are 4 (CH_4 flux at SMTZ, SMTZ depth, AOM filter efficiency, ΣAOM).

Example with 3 factors: $2^3 = 8$ runs

For the sake of illustration and simplicity let us consider a two-level factorial with 3 factors and only one output. In order not to mix up with anything even slightly related to area of research of this dissertation the example is taken from an example of chemical vapor deposition (CVD) to produce a semiconductor. The 3 factors considered are

1 The writing of this section is amply based on the section 7.3.1 of the book "Fundamentals of semiconductor manufacturing and process control" by May et al., 2006

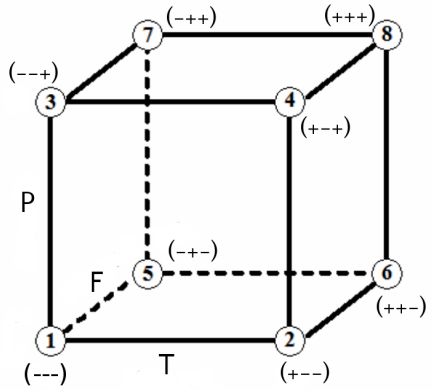

Figure C.2: Cube representing the two-level factorial design of the experiment with 3 varying factors or parameters: the temperature (T), gas flow (F) and the pressure (P). The highest value is indicated by a + the lowest value by a −. Redrawn from May et al., 2006.

temperature (T), the gas flow rate (F) and pressure (P) and while the response being measured is the deposition rate (D). For each combination of the 2 possible values of 3 factors a semiconductor is produced and the deposition rate is measured. This can be pictorially described by a cube (see Fig. C.2) and results are reported in Table C.1.

Table C.1: Example of the results of the $2^3 = 8$ runs for the two-level factorial design of a CVD experiment taken as example. From May et al., 2006 .

Run	P	T	F	D (Å/min)
1	−	−	−	$d_1 = 94.8$
2	+	−	−	$d_2 = 110.96$
3	−	+	−	$d_1 = 214.12$
4	+	+	−	$d_1 = 255.82$
5	−	−	+	$d_1 = 94.14$
6	+	−	+	$d_1 = 145.92$
7	−	+	+	$d_1 = 286.71$
8	+	+	+	$d_1 = 340.25$

Definition of main effect

From the outcomes of factorial design we can draw the so called *main effects* (ME), which quantify the effect of a factor on the outcomes independently on the other two factors. The main effect of factor is defined as the averaged difference between all the outputs when the factor takes the highest value and all the outputs when the factor takes the lowest value. For instance for the pressure P, it is the difference between the average deposition rate when pressure is high (runs 2, 4, 6 and 8) and the average deposition rate when the pressure is low (runs 1, 3, 5 and 7). It reads:

$$ME_P = \langle d_{P+} \rangle - \langle d_{P-} \rangle = \frac{1}{4}[(d_2 + d_4 + d_6 + d_8) + -(d_1 + d_3 + d_5 + d_7)] = 40.86 \tag{C.6}$$

It means that the average effect of increasing pressure is increasing the deposition of 40.86 Å/min. If the ME_P were null, it meant that pressure alone would play no role.

Definition of interaction effect

The design allows one also to derive the so called *interaction effects*. it allows to check the relative importance of a factor, when the other or the others are high or low. For instance it might happen that the pressure effect is much greater at high temperatures than it is at low temperatures. A way of quantify this interaction effect (PT) would be the difference between the average pressure effect at high temperature and the average pressure effect at low temperature. In order to evaluate this factor one need to check the runs where the two possible values for the P and the T are concordant (runs 1, 4, 5 and 8) and when they are discordant (runs 2, 3, 6 and 7), so that the effect reads:

$$(PT) = \langle d_{(PT)+} \rangle - \langle d_{(PT)-} \rangle = \frac{1}{4}[(d_1 + d_4 + d_5 + d_8) + \\ -(d_2 + d_3 + d_6 + d_7)] = 6.89 \tag{C.7}$$

and it means that, on average, temperature and pressure contributes concordantly to the deposition.

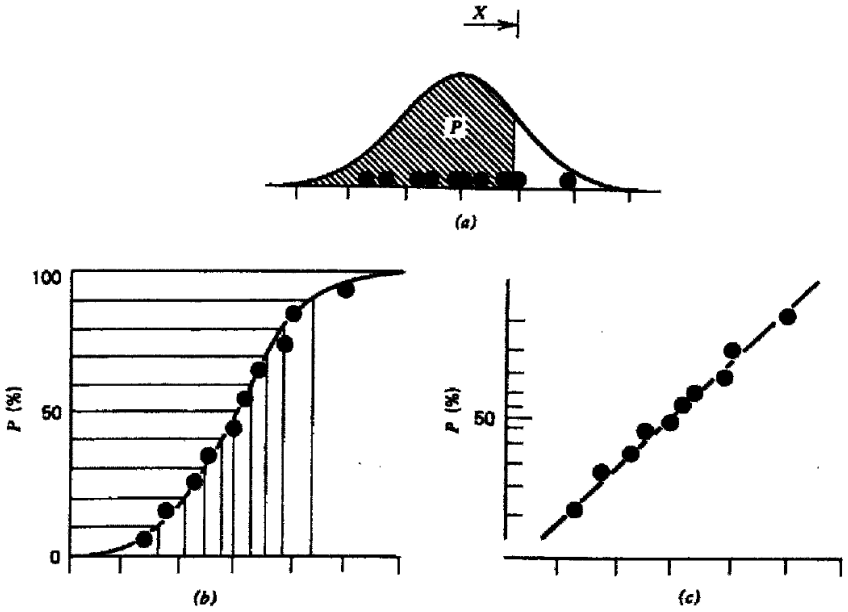

Figure C.3: Normal probability plot concepts. *a* A normal distribution with some sampling (dots). *b* The cumulative normal distribution on ordinary graph paper with the corresponding sampling. *c* A normal probability plot and the corresponding sampling lying on the straight line. From May et al., 2006.

A three-factor interaction PTF can be derived as well, again evaluating the difference between the average deposition when the product

of all the factor is concordant (runs 2, 3, 5 and 8) and discordant (runs 1, 4, 6 and 7) so that:

$$PTF = \langle d_{PTF+} \rangle - \langle d_{PTF-} \rangle = \frac{1}{4}[(d_2 + d_3 + d_5 + d_8) + \\ -(d_1 + d_4 + d_6 + d_7)] = -5.88 \tag{C.8}$$

which can be interpreted that the three factor contributes discordantly to the deposition, namely that for instance, on average, if both temperature and pressure are high, the gas flow should be low to have a higher deposition rate since a high gas flow reduces it.

Normal plot representation to check significance

This is the definition of effects but then one needs to ask whether these effects are actually statistically meaningful or not. It might occur that some of the interactions, of the effects, actually are simply occasional and just chance occurrences due to the internal variability, the "noise" of the system. An immediate way to check for significant outcomes is plotting the effects on a normal probability plot (see fig. C.3.*c*): a graph whose Y axis is scaled to reproduce in a straight line the cumulative normal distribution curve. If the effects are plotted in a normal probability graph, with on the X axis the value of the effect and on the Y axis its cumulative distribution, the not significant effects will lie on a straight line. This because each effects is given by a combination of observations and, for the central limit theorem, a linear combination of random variable is distributed according to a normal distribution. In other words, if the effects are negligible and just a product of the internal noise they are distributed according to a Gaussian and line up along a straight line in the normal probability graph, while if significant they are outliers. Because of their definition describing multiple interaction, four- or more factor interaction usually belongs to the normal population of trivial effects and therefore are rarely to be considered.

This is the rationale behind the two-level factorial analysis performed in section 4.3.2.3 and displayed in fig. 4.16.

C.4 BIOGEOCHEMICAL NETWORK: TABLES

Table C.2: The 6 inhibition factors ruling the onset of metabolic pathways according to the succession of the redox ladder.

f_{O_2}	$\begin{cases} 1 & \text{if } [O_2] > K_{O_2} \\ \frac{[O_2]}{K_{O_2}} & \text{if } [O_2] < K_{O_2} \end{cases}$
$f_{NO_3^-}$	$\begin{cases} 0 & \text{if } [O_2] > K_{O_2} \\ \left(1 - \frac{[O_2]}{K_{O_2}}\right) \frac{NO_3^-}{K_{NO_3^-}} & \text{if } [O_2] < K_{O_2} \end{cases}$
f_{MnO_2}	$\begin{cases} 0 & \text{if } [NO_3^-] > K_{NO_3^-} \\ \left(1 - \frac{[O_2]}{K_{O_2}} - \frac{[NO_3^-]}{K_{NO_3^-}}\right) \frac{MnO_2}{K_{MnO_2}} & \text{if } [NO_3^-] < K_{NO_3^-} \end{cases}$
$f_{Fe(OH)_3}$	$\begin{cases} 0 & \text{if } [MnO_2] > K_{MnO_2} \\ \left(1 - \frac{[O_2]}{K_{O_2}} - \frac{[NO_3^-]}{K_{NO_3^-}} - \frac{[MnO_2]}{K_{MnO_2}}\right) \frac{Fe(OH)_3}{K_{Fe(OH)_3}} & \text{if } [MnO_2] < K_{MnO_2} \end{cases}$
$f_{SO_4^{2-}}$	$\begin{cases} 0 & \text{if } [Fe(OH)_3] > K_{Fe(OH)_3} \\ \left(1 - \frac{[O_2]}{K_{O_2}} - \frac{[NO_3^-]}{K_{NO_3^-}} - \frac{[MnO_2]}{K_{MnO_2}} - \frac{[Fe(OH)_3]}{K_{Fe(OH)_3}}\right) \frac{SO_4^{2-}}{K_{SO_4^{2-}}} & \text{if } [Fe(OH)_3] < K_{Fe(OH)_3} \end{cases}$
f_{CH_4}	$\begin{cases} 0 & \text{if } [SO_4^{2-}] > K_{SO_4^{2-}} \\ \left(1 - \frac{[O_2]}{K_{O_2}} - \frac{[NO_3^-]}{K_{NO_3^-}} - \frac{[MnO_2]}{K_{MnO_2}} - \frac{[Fe(OH)_3]}{K_{Fe(OH)_3}} - \frac{[SO_4^{2-}]}{K_{SO_4^{2-}}}\right) \frac{CH_4}{K_{CH_4}} & \text{if } [SO_4^{2-}] < K_{SO_4^{2-}} \end{cases}$

Table C.3: The 6 primary redox reactions involved in the degradation of OM. The coefficients x, y and z, enforce Redfield ratio ($x = 106$, $y = 16$ and $z = 1$). SD stands for the conversion factor between solid and liquid volume, i. e.$SD = \varphi_s / \varphi$. For the expression of the inhibition factors f see Table C.2. $[CH_2O]$ is a shortcut for $(CH_2O)(NH_3)_{\frac{y}{x}}(H_3PO_4)_{\frac{z}{x}}$, to take into account nutrients.

#	Reaction	Rate expression
R1	$[CH_2O] + \left(\frac{x+2y}{x}\right) SD \cdot O_2 + \left(\frac{y+2z}{x}\right) SD \cdot HCO_3^- \longrightarrow \left(\frac{x+y+2z}{x}\right) SD \cdot CO_2 + \left(\frac{y}{x}\right) SD \cdot NO_3^- + \left(\frac{z}{x}\right) SD \cdot HPO_4^{2-} + \left(\frac{x+2y+2z}{x}\right) SD \cdot H_2O$	$\frac{\nu}{a+t}[CH_2O] \cdot f_{O_2}$
R2	$[CH_2O] + \left(\frac{4x+3y}{5x}\right) SD \cdot NO_3^- \longrightarrow \left(\frac{x-3y+10z}{5x}\right) SD \cdot CO_2 + \left(\frac{4x+3y-10z}{5x}\right) SD \cdot HCO_3^- + \left(\frac{z}{x}\right) SD \cdot HPO_4^{2-} + \left(\frac{3x+6y+10z}{5x}\right) H_2O + \left(\frac{2x+4y}{5x}\right) N_2$	$\frac{\nu}{a+t}[CH_2O] \cdot f_{NO_3^-}$
R3	$[CH_2O] + 2\,MnO_2 + \left(\frac{3x+y-2z}{x}\right) SD \cdot CO_2 + \left(\frac{x+y-2z}{x}\right) SD \cdot H_2O \longrightarrow 2SD \cdot Mn^{2+} + \left(\frac{y}{x}\right) SD \cdot NH_4^+ + \left(\frac{4x+y-2z}{x}\right) SD \cdot HCO_3^- + \left(\frac{z}{x}\right) SD \cdot HPO_4^{2-}$	$\frac{\nu}{a+t} \cdot [CH_2O] \cdot f_{MnO_2}$
R4	$[CH_2O] + 4\,Fe(OH)_3 + \left(\frac{7x+y-2z}{x}\right) SD \cdot CO_2 \longrightarrow 4SD \cdot Fe^{2+} + \left(\frac{8x+y-2z}{x}\right) SD \cdot HCO_3^- + \left(\frac{y}{x}\right) SD \cdot NH_4^+ + \left(\frac{z}{x}\right) SD \cdot HPO_4^{2-} + \left(\frac{3x-y+2z}{x}\right) H_2O$	$\frac{\nu}{a+t} \cdot [CH_2O] \cdot f_{Fe(OH)_3}$
R5	$[CH_2O] + \frac{1}{2}SD \cdot SO_4^{2-} + \left(\frac{y-2z}{x}\right) SD \cdot CO_2 + \left(\frac{y-2z}{x}\right) SD \cdot H_2O \longrightarrow \left(\frac{x+y-2z}{x}\right) SD \cdot HCO_3^- + \left(\frac{y}{x}\right) SD \cdot NH_4^+ + \frac{1}{2}SD \cdot H_2S + \left(\frac{z}{x}\right) SD \cdot HPO_4^{2-}$	$\frac{\nu}{a+t} \cdot [CH_2O] \cdot f_{SO_4^{2-}}$
R6	$[CH_2O] \longrightarrow \left(\frac{x-2y+4z}{2x}\right) SD \cdot CO_2 + \left(\frac{y-2z}{x}\right) SD \cdot HCO_3^- + \left(\frac{y}{x}\right) SD \cdot NH_4^+ + \frac{1}{2}SD \cdot CH4 + \left(\frac{z}{x}\right) SD \cdot HPO_4^{2-}$	$\frac{\nu}{a+t} \cdot [CH_2O] \cdot f_{CH_4}$

Table C.4: The secondary redox, precipitation, absorption and equilibrium reactions

#	Reaction	Rate expression
R7	$2\,O_2 + NH_4{}^+ + 2\,HCO_3{}^- \longrightarrow NO_3{}^- + 2\,CO_2 + 3\,H_2O$	$k_7[O_2][NH_4{}^+]$
R8	$\frac{1}{2}O_2 + Mn^{2+} + 2\,HCO_3{}^- \longrightarrow \frac{MnO_2}{SD} + 2\,CO_2 + H_2O$	$k_8[O_2][Mn^{2+}]$
R9	$MnO_2 + 2SD \cdot Fe^{2+} + 2SD \cdot HCO_3{}^- + 2SD \cdot H_2O \longrightarrow$ $2\,Fe(OH)_3 + SD \cdot Mn^{2+} + 2SD \cdot CO_2$	$k_9[Fe^{2+}][MnO_2]$
R10	$\frac{1}{4}O_2 + Fe^{2+} + 2\,HCO_3{}^- + \frac{1}{2}\,H_2O \longrightarrow \frac{Fe(OH)_3}{SD} + 2\,CO_2$	$k_{10}[O_2][Fe^{2+}]$
R11	$2\,O_2 + H_2S + 2\,HCO_3{}^- \longrightarrow SO_4{}^{2-} + 2\,CO_2 2\,H_2O$	$k_{11}[O_2]\left([H_2S] + [HS^-]\right)$
R12	$MnO_2 + SD \cdot H_2S + 2SD \cdot CO_2 \longrightarrow$ $S^0 + SD \cdot Mn^{2+} + 2SD \cdot HCO_3{}^-$	$k_{12}[MnO_2]\left([H_2S] + [HS^-]\right)$
R13	$2Fe(OH)_3 + SD \cdot H_2S + 4SD \cdot CO_2 \longrightarrow$ $S^0 + 2\,SD \cdot Fe^{2+} + 4SD \cdot HCO_3{}^-$	$k_{13}[Fe(OH)_3]\left([H_2S] + [HS^-]\right)$

R14	$CH_4 + 2\,O_2 \longrightarrow CO_2 + 2\,H_2O$	$k_{14}[CH_4][O_2]$
R15	$FeS + SD \cdot O_2 \longrightarrow S^0 + SD \cdot Fe^{2+} + SD \cdot {SO_4}^{2-}$	$k_{15}[FeS][O_2]$
R16	$Mn^{2+} + 2HCO_3^- \longrightarrow \frac{MnCO3}{SD} + CO_2 + H_2O$	$\begin{cases} k_{16}\left(\frac{[Mn^{2+}][{CO_3}^{2-}]}{K_{sMnCO_3}} - 1\right) & \text{if } [Mn^{2+}][{CO_3}^{2-}] > K_{sMnCO_3} \\ 0 & \text{if } [Mn^{2+}][{CO_3}^{2-}] < K_{sMnCO_3} \end{cases}$
R17	$Fe^{2+} + H_2S + 2HCO_3^- \longrightarrow \frac{FeS}{SD} + 2CO_2 + 2H_2O$	$\begin{cases} k_{17}\left(\frac{[Fe^{2+}][HS^-]}{[H^+]K_{sFeS}} - 1\right) & \text{if } \frac{[Fe^{2+}][HS^-]}{[H^+]} > K_{sFeS} \\ 0 & \text{if } \frac{[Fe^{2+}][HS^-]}{[H^+]} < K_{sFeS} \end{cases}$
R18	$\frac{FeS}{SD} + 2\,CO_2 + 2H_2O \longrightarrow Fe^{2+} + H_2S + 2HCO_3^-$	$\begin{cases} k_{18}\left(1 - \frac{[Fe^{2+}][HS^-]}{[H^+]K_{sFeS}}\right) & \text{if } \frac{[Fe^{2+}][H_2S]}{[H^+]} < K_{sFeS} \\ 0 & \text{if } \frac{[Fe^{2+}][H_2S]}{[H^+]} > K_{sFeS} \end{cases}$
R19	$Fe^{2+} + 2HCO_3^- \longrightarrow FeCO_3 + CO_2 + H_2O$	$\begin{cases} k_{19}\left(\frac{[Fe^{2+}][{CO_3}^{2-}]}{K_{sFeCO_3}} - 1\right) & \text{if } [Fe^{2+}][{CO_3}^{2-}] > K_{sFeCO_3} \\ 0 & \text{if } [Fe^{2+}][{CO_3}^{2-}] < K_{sFeCO_3} \end{cases}$
R20	$FeS + SD \cdot H_2S \longrightarrow FeS_2$	$k_{20}[FeS]\left([H_2S] + [HS^-]\right)$

R21	$3\,FeS + SD \cdot S^0 \longrightarrow Fe_3S_4$	$k_{21}[FeS][S^0]$
R22	${PO_4}^{3-} \longrightarrow CFA$	$\begin{cases} k_{22}\left([{PO_4}^{3-}] - [{PO_4}^{3-}]^*\right) & \text{if } [{PO_4}^{3-}] > [{PO_4}^{3-}]^* \\ 0 & \text{if } [{PO_4}^{3-}] < [{PO_4}^{3-}]^* \end{cases}$
R23	$CaCO_3 + SD \cdot H^+ \longrightarrow SD \cdot Ca^{2+} + SD \cdot {HCO_3}^-$	$\begin{cases} k_{23}\left(1 - \frac{[Ca^{2+}][{CO_3}^{2-}]}{K_{sCaCO_3}}\right) & \text{if } [Ca^{2+}][{CO_3}^{2-}] < K_{sCaCO_3} \\ 0 & \text{if } [Ca^{2+}][{CO_3}^{2-}] > K_{sCaCO_3} \end{cases}$
R24	$Ca^{2+} + {HCO_3}^- \longrightarrow \frac{CaCO3}{SD} + H^+$	$\begin{cases} k_{24}\left(\frac{[Ca^{2+}][{CO_3}^{2-}]}{K_{sCaCO_3}} - 4.5\right) & \text{if } \frac{[Ca^{2+}][{CO_3}^{2-}]}{K_{sCaCO_3}} > 4.5 \\ 0 & \text{if } \frac{[Ca^{2+}][{CO_3}^{2-}]}{K_{sCaCO_3}} < 4.5 \end{cases}$
R25	$CH_4(g) \longrightarrow CH_4(aq)$	$\begin{cases} k_{25}[CH_4(g)]\left([CH_4]^* - [CH_4]\right) & \text{if } [CH_4] < [CH_4]^* \\ 0 & \text{if } [CH_4] > [CH_4]^* \end{cases}$
R26	$CH_4(aq) \longrightarrow CH_4(g)$	$\begin{cases} k_{26}\left([CH_4] - [CH_4]^*\right) & \text{if } [CH_4] > [CH_4]^* \\ 0 & \text{if } [CH_4] < [CH_4]^* \end{cases}$
R27	$4\,S^0 + 4\,H_2O \longrightarrow {SO_4}^{2-} + 3H_2S + 2H^+$	$k_{27}[S^0]$

R28	$NH_4{}^+(aq) \longrightarrow NH_4{}^+(ads)$	$k_{28}^f[NH_4{}^+(aq)]\varphi - k_{28}^b[NH_4{}^+(ads)]\varphi_s$
R29	$PO_4{}^{3-}(aq) \longrightarrow PO_4{}^{3-}(ads)$	$k_{29}^f[PO_4{}^{3-}(aq)]\varphi - k_{29}^b[PO_4{}^{3-}(ads)]\varphi_s$
R30	$Fe^{2+}(aq) \longrightarrow Fe^{2+}(ads)$	$k_{30}^f[Fe^{2+}(aq)]\varphi - k_{30}^b[Fe^{2+}(ads)]\varphi_s$
R31	$FeOH_3 + PO_4{}^{-3} \longrightarrow PO_4(ads_{Fe(OH)3})$	$k_{31}^f[PO_4{}^{3-}][Fe(OH)_3] - k_{31}^b[PO_4(ads_{Fe(OH)3})]$
R32	$CO_2 + H_2O \longrightarrow H^+ + HCO_3{}^-$	k_{32} thermodynamic equilibrium
R33	$HCO_3{}^- \longrightarrow H^+ + CO_3{}^{2-}$	k_{33} thermodynamic equilibrium
R34	$H_2S \longrightarrow H^+ + HS^-$	k_{34} thermodynamic equilibrium
R35	$B(OH)_3 \longrightarrow B(OH)_4{}^- + H^+$	k_{35} thermodynamic equilibrium

C.5 MODEL VALIDATIONS

C.5.1 *Sediment core offshore Vesterålen Archipelago*

Table C.6: Model boundary parameters and boundary conditions for the case study of a cold seep GC-51 off Vesterålen, Norway. Values with $*$ are set for this study. All the other variables are as in Sauer et al., 2015 and Sauer et al., 2016. $[\ ]_-$ stands for lower boundary conditions, while $[\ ]_+$ stand for upper boundary conditions.

Quantity	Value	Units
$a*$	1100	yr
$\nu*$	100	-
v_{up}	0	cm yr^{-1}
$C/N*$	14.8	-
$[SO_4^{2-}]_+$	28.3	mM
$[SO_4^{2-}]_-$	0.0	mM
$[CH_4]_+$	42	nM
$[CH_4]_-*$	35	mM
$[NH_4^+]_+$	9.1	μM
$[NH_4^+]_-$	0.227	mM

C.5.2 *Sediment core on Laptev Sea shelf*

Table C.7: Model boundary parameters and boundary conditions for the case study of a passive station on the Laptev shelf (S23). Values with $*$ are set for this study. All the other variables are as in Brüchert et al., 2018. $[\,]_-$ stands for lower boundary conditions, while $[\,]_+$ stand for upper boundary conditions.

Quantity	Value	Units
$a*$	3	yr
$\nu*$	0.2	-
ω	0.8	mm yr^{-1}
v_{up}	0	cm yr^{-1}
$POC(0)*$	1.5	%
$\rho*$	2.41	g cm^{-3}
$[O_2]_+$	325	μM
$[SO_4{}^{2-}]_+$	28	mM
$[Mn^{2+}]_+$	0.21	μM
$[Mn^{2+}]_-$	47.2	μM
$[Fe^{2+}]_+$	0.37	μM
$[Fe^{2+}]_-$	74.9	μM
$[Fe(OH)_3]_+*$	1.645	μmol cm^{-2} yr^{-1}
$[MnO_2]_+*$	0.018	%

C.6 SENSITIVITY STUDY: MODEL PARAMETERS AND MODEL BOUNDARY CONDITIONS. TABLES

Table C.8: Generic BRNS parameters. The parameters below the dashed line at the bottom are the quantities involved in the bioenergetic formulation of AOM. Diffusion coefficients depends on temperature $T(°C)$, salinity S and porosity φ according to the relation $D(T,S,\varphi) = \frac{D(1+\mu T(°C))}{1-\ln(\varphi^2)}$.

Quantity	Value	Units	Reference
ν	0.125	-	This study
SD	φ_s/φ	-	-
S	20	psu	This study
ρ	2.41	g cm^{-3}	Berg et al., 2003
D_b^0	29.8	cm^2 yr^{-1}	Middelburg et al., 1997
z_{bio}	5	cm	Boudreau, 1997
z_{irr}	3.5	cm	Thullner et al., 2009
T	0, 273.15	°C, K	This study
C:N	106:16	-	Redfield ratio
C:P	106:1	-	Redfield ratio
D_{O_2}, μ_{O_2}	380.45, 0.06	cm^2 yr^{-1}, T^{-1}	Dale et al., 2012
$D_{NO_3^-}$, $\mu_{NO_3^-}$	394.59, 0.038	cm^2 yr^{-1}, T^{-1}	Van Cappellen et al., 1996
$D_{SO_4^{2-}}$, $\mu_{SO_4^{2-}}$	173.92, 0.045	cm^2 yr^{-1}, T^{-1}	Dale et al., 2012
D_{CH_4}, μ_{CH_4}	263.94, 0.052	cm^2 yr^{-1}, T^{-1}	Van Cappellen et al., 1996
$D_{NH_4^+}$, $\mu_{NH_4^+}$	395.87, 0.041	cm^2 yr^{-1}, T^{-1}	Van Cappellen et al., 1996
$D_{PO_4^{3-}}$, $\mu_{PO_4^{3-}}$	112.36, 0.054	cm^2 yr^{-1}, T^{-1}	Van Cappellen et al., 1996
$D_{Mn^{2+}}$, $\mu_{Mn^{2+}}$	123.39, 0.05	cm^2 yr^{-1}, T^{-1}	Van Cappellen et al., 1996
$D_{Fe^{2+}}$, $\mu_{Fe^{2+}}$	136.24, 0.044	cm^2 yr^{-1}, T^{-1}	Dale et al., 2012
D_{H_2S}, μ_{H_2S}	331.61, 0.06	cm^2 yr^{-1}, T^{-1}	Van Cappellen et al., 1996
D_{HS^-}, μ_{HS^-}	392.02, 0.031	cm^2 yr^{-1}, T^{-1}	Van Cappellen et al., 1996
$D_{CH_4(g)}$, $\mu_{CH_4(g)}$	5000.0, 0.0	cm^2 yr^{-1}, T^{-1}	Van Cappellen et al., 1996

$D_{H_2CO_3}$, $\mu_{H_2CO_3}$	320.04, 0.06	$cm^2\ yr^{-1}$, T^{-1}	Van Cappellen et al., 1996
$D_{HCO_3^-}$, $\mu_{HCO_3^-}$	217.22, 0.048	$cm^2\ yr^{-1}$, T^{-1}	Van Cappellen et al., 1996
$D_{CO_3^{2-}}$, $\mu_{CO_3^{2-}}$	176.09, 0.047	$cm^2\ yr^{-1}$, T^{-1}	Van Cappellen et al., 1996
$D_{B(OH)_3}$, $\mu_{B(OH)_3}$	110.05, 0.054	$cm^2\ yr^{-1}$, T^{-1}	Van Cappellen et al., 1996
$D_{B(OH)_4^-}$, $\mu_{B(OH)_4^-}$	96.30, 0.041	$cm^2\ yr^{-1}$, T^{-1}	Van Cappellen et al., 1996
D_{H^+}, μ_{H^+}	600.0, 0.05	$cm^2\ yr^{-1}$, T^{-1}	Van Cappellen et al., 1996
$D_{Ca^{2+}}$, $\mu_{Ca^{2+}}$	150.38, 0.045	$cm^2\ yr^{-1}$, T^{-1}	Van Cappellen et al., 1996
D_{S^0}, μ_{S^0}	173.92, 0.045	$cm^2\ yr^{-1}$, T^{-1}	Van Cappellen et al., 1996
φ_0	0.45	-	LaRowe et al., 2017
c_0	$0.5 \cdot 10^{-3}$	m^{-1}	LaRowe et al., 2017
φ_∞	0.35	-	This study
K_{O_2}	8	μM	Thullner et al., 2009
$K_{NO_3^-}$	5	μM	Van Cappellen et al., 1996
K_{MnO_2}	2	$\mu mol/g_d$	Thullner et al., 2009
$K_{Fe(OH)_3}$	5	$\mu mol/g_d$	Thullner et al., 2009
$K_{SO_4^{2-}}$	100	μM	Dale et al., 2006
k_7	$1.0 \cdot 10^7$	$cm^3\ mol^{-1}\ yr^{-1}$	Van Cappellen et al., 1996
k_8	$2.0 \cdot 10^9$	$M^{-1}\ yr^{-1}$	Thullner et al., 2009
k_9	$2.0 \cdot 10^8$	$M^{-1}\ yr^{-1}$	Thullner et al., 2009
k_{10}	$1.0 \cdot 10^{11}$	$cm^3\ mol^{-1}\ yr^{-1}$	Van Cappellen et al., 1996
k_{11}	$1.0 \cdot 10^9$	$cm^3\ mol^{-1}\ yr^{-1}$	Van Cappellen et al., 1996
k_{12}	$1.0 \cdot 10^4$	$M^{-1}\ yr^{-1}$	Thullner et al., 2009
k_{13}	$1.0 \cdot 10^4$	$M^{-1}\ yr^{-1}$	Thullner et al., 2009
k_{14}	$1.0 \cdot 10^{13}$	$cm^3\ mol^{-1}\ yr^{-1}$	Van Cappellen et al., 1996
k_{15}	$1.0 \cdot 10^9$	$cm^3\ mol^{-1}\ yr^{-1}$	Van Cappellen et al., 1996

k_{16}	$1.0 \cdot 10^{-8}$	$\frac{\text{mol}}{\text{yr}^{-1}}$	cm^{-3}	Van Cappellen et al., 1996
k_{17}	$5 \cdot 10^{-9}$	$\frac{\text{mol}}{\text{yr}^{-1}}$	cm^{-3}	Van Cappellen et al., 1996
k_{18}	$1.0 \cdot 10^{-3}$	$\frac{\text{mol}}{\text{yr}^{-1}}$	cm^{-3}	Van Cappellen et al., 1996
k_{19}	$1.0 \cdot 10^{-9}$	$\frac{\text{mol}}{\text{yr}^{-1}}$	cm^{-3}	Van Cappellen et al., 1996
k_{20}	$6.0 \cdot 10^{7}$	$\frac{\text{cm}^3}{\text{yr}^{-1}}$	mol^{-1}	Van Cappellen et al., 1996
k_{21}	$2.4 \cdot 10^{4}$	$\frac{\text{cm}^3}{\text{yr}^{-1}}$	mol^{-1}	Van Cappellen et al., 1996
k_{22}	1	yr^{-1}		Van Cappellen et al., 1996
k_{23}	0.1	$\frac{\text{mol}}{\text{yr}^{-1}}$	cm^{-3}	Van Cappellen et al., 1996
k_{24}	24.16	$\text{M}^{-1}\ \text{yr}^{-1}$		Wallmann et al., 2006a
k_{25}	$1.0 \cdot 10^{9}$	$\frac{\text{cm}^3}{\text{yr}^{-1}}$	mol^{-1}	Van Cappellen et al., 1996
k_{26}	$7.89 \cdot 10^{2}$	yr^{-1}		Pauss et al., 1990
k_{27}	$1.0 \cdot 10^{-3}$	yr^{-1}		Van Cappellen et al., 1996
k_{28}^{f}	1.6	yr^{-1}		Van Cappellen et al., 1996
k_{28}^{b}	1.0	yr^{-1}		Van Cappellen et al., 1996
k_{29}^{f}	1.8	yr^{-1}		Van Cappellen et al., 1996
k_{29}^{b}	1.0	yr^{-1}		Van Cappellen et al., 1996
k_{30}^{f}	400	yr^{-1}		Van Cappellen et al., 1996
k_{30}^{b}	1.0	yr^{-1}		Van Cappellen et al., 1996
k_{31}^{f}	100	yr^{-1}		Van Cappellen et al., 1996
k_{31}^{b}	1.0	yr^{-1}		Van Cappellen et al., 1996
k_{32}	$8.470 \cdot 10^{-7}$	M		Millero, 1995
k_{33}	$4.300 \cdot 10^{-10}$	M		Millero, 1995

k_{34}	$1.602 \cdot 10^{-7}$	M	Millero, 1995
k_{35}	$1.318 \cdot 10^{-9}$	M	Millero, 1995
$[CH_4]^*$	5.46	mM	Dale et al., 2008a
$[PO_4^{3-}]^*$	10	μM	Van Cappellen et al., 1996
K_{sMnCO_3}	$3.2 \cdot 10^{-9}$	M^2	Van Cappellen et al., 1996
K_{sFeCO_3}	$4.0 \cdot 10^{-9}$	M^2	Van Cappellen et al., 1996
K_{sFeS}	$8.2 \cdot 10^{-4}$	M	Van Cappellen et al., 1996
K_{sCaCO_3}	$3.8 \cdot 10^{-7}$	M^2	Mucci, 1983; Millero, 1995
μ_g	18.3	yr^{-1}	Dale et al., 2006; Dale et al., 2008c
μ_d	0.1	yr^{-1}	Dale et al., 2006; Dale et al., 2008c
γ	2.48	-	Dale et al., 2006; Dale et al., 2008c
χ	8.0	-	Dale et al., 2006; Dale et al., 2008c
ΔG_{BQ}	20	kJ/mol e^-	Dale et al., 2006; Dale et al., 2008c
ΔG_r^0	-29.92	kJ/mol e^-	Regnier et al., 2011
$K_m^{CH_4}$	$1.5 \cdot 10^{-3}$	M	Dale et al., 2006; Dale et al., 2008c
$K_m^{SO_4^{2-}}$	$1.0 \cdot 10^{-3}$	M	Dale et al., 2006; Dale et al., 2008c

Table C.10: Generic BRNS upper boundary conditions. The boundary condition for biomass is applied only in the bioenergetic formulation of AOM

Species	Value @ SWI	Units	Reference
POC	1.04	%	This study
O_2	306.98	μM	Garcia et al., 2010
NO_3^-	11.51	μM	Garcia et al., 2010
MnO_2	2.18	μmol cm^{-2} yr^{-1}	Glasby, 2006; Dale et al., 2015
$Fe(OH)_3$	7.09	μmol cm^{-2} yr^{-1}	Glasby, 2006; Dale et al., 2015
SO_4^{2-}	28.0	mM	Thullner et al., 2009
CH_4	0.0	mM	This study
NH_4^+	0.0	mM	This study
PO_4^{3-}	1.0	μM	Sales de Freitas, 2018
Mn^{2+}	1.0	μM	Sales de Freitas, 2018
Fe^{2+}	1.0	pM	Sales de Freitas, 2018
H_2S	0.835	nM	Sales de Freitas, 2018
HS^-	9.17	nM	Sales de Freitas, 2018
$CH_4(g)$	o.o	nM	This study
H_2CO_3	39	μM	Sales de Freitas, 2018
HCO_3^-	2150	μM	Sales de Freitas, 2018
CO_3^{2-}	15.3	μM	Sales de Freitas, 2018
$B(OH)_3$	363.6	μM	Sales de Freitas, 2018
$B(OH)_4^-$	61.4	μM	Sales de Freitas, 2018
H^+	6.31	μM	Sales de Freitas, 2018
$CaCO_3$	23	μmol cm^{-2} yr^{-1}	Sales de Freitas, 2018
Ca^{2+}	9.7	mM	Sales de Freitas, 2018
$NH_4^+(ads)$	o	mM	Sales de Freitas, 2018
$PO_4^{3-}(ads)$	o	mM	Sales de Freitas, 2018
FeS	o	μmol cm^{-2} yr^{-1}	Sales de Freitas, 2018
$FeCO_3$	o	mM	Sales de Freitas, 2018
S^0	o	mM	Sales de Freitas, 2018
FeS_2	o	μmol cm^{-2} yr^{-1}	Sales de Freitas, 2018
$Fe^{2+}(ads)$	o	mM	Sales de Freitas, 2018

$PO_{4Fe(OH)_3}$	0	mM	Sales de Freitas, 2018
B	$1\,10^8$, $3.158\,10^7$	mol cm^{-3}, cells cm^{-3}	This study

Table C.12: Name, location, water depth and linear sedimentation rate for cores used to inter- and extra-polate the sedimentation rates to the whole Laptev sea area via simple 3D kriging.

Core name	Lon (°)	Lat (°)	Water depth (m)	ω (cm/yr)	Reference
KD9502-14	133.117	76.192	46	0.003	Bauch et al., 2001
PM9462-4	136.005	74.503	27	0.05	Bauch et al., 2001
PM9499-2	115.545	75.501	48	0.004	Bauch et al., 2001
PS51/080-13	131.638	73.459	21	0.028	Bauch et al., 2001
PS51/092-13	130.136	74.594	32	0.07	Bauch et al., 2001
PS51/092-12	130.138	74.593	32	0.041	Bauch et al., 2001
PS51/118-2	132.237	77.892	114	0.002	Bauch et al., 2001
PS51/118-3	132.199	77.892	122	0.008	Bauch et al., 2001
PS51/135-4	133.243	76.165	51	0.031	Bauch et al., 2001
PS51/141-2	128.641	75.227	42	0.011	Bauch et al., 2001
PS51/154-11	120.610	77.276	270	0.012	Bauch et al., 2001
PS51/159-10	116.032	76.767	60	0.011	Bauch et al., 2001
PS2458-4	133.398	78.167	983	0.027	Bauch et al., 2001
L13-09-2	129.895	73.018	10	0.45	Han, 2014
L13-14-2	130.695	73.857	25	0.16	Han, 2014
L13-18-2	130.479	73.032	16	0.3	Han, 2014
L13-04-2	130.690	71.902	15	0.2	Han, 2014
C-37	130.367	71.617	10	0.024	Stein et al., 2000
C-4	131.000	73.167	26	0.17	Stein et al., 2000

C-7	129.983	74.883	37	0.159	Stein et al., 2000
C-8	130.500	75.400	48	0.015	Stein et al., 2000
C-11	130.083	76.867	66	0.011	Stein et al., 2000
PS2725-5	144.135	78.656	77	0.013	Stein et al., 2001
PS2778-2	113.065	77.978	341	0.038	Stein et al., 2001
PS2476-4	118.193	77.39	521	0.05	Stein et al., 2001
PS2742-5	103.815	80.788	1890	0.022	Stein et al., 2001
PS2474-3	118.575	77.67	1494	0.02	Stein et al., 2001
PS2741-1	105.395	81.105	2400	0.012	Stein et al., 2001
PS2471-4	119.793	79.152	3047	0.002	Stein et al., 2001

C.6.1 *Sensitivity study: model parameters and model boundary conditions. Figures*

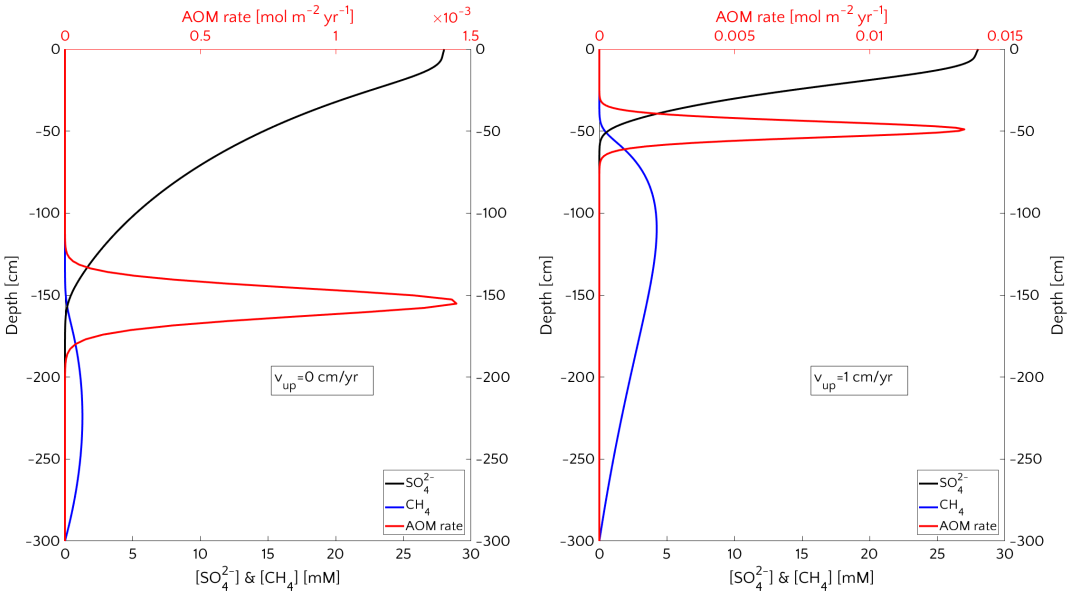

Figure C.4: Outcomes for the baseline simulations at steady state. Passive case (left) and active case with $v_{up} = 1$ cm/yr (right). Typical SMTZ shoaling (from 155.2 cm to 48.9 cm) and squeezing (from 65 cm to 38 cm) from passive to active case.

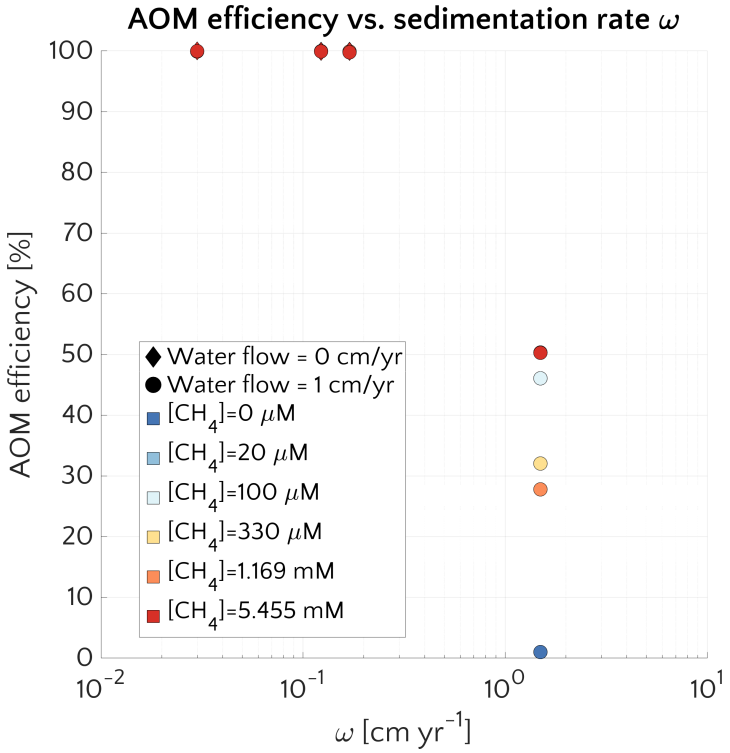

Figure C.5: AOM filter efficiency η versus ω for passive cases (diamonds) and active cases (circles).

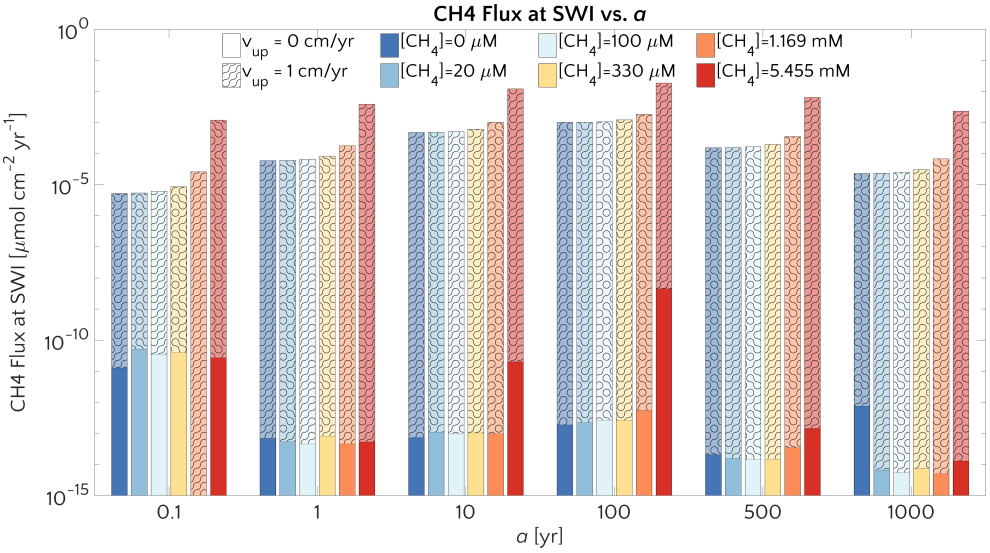

Figure C.6: Barplot of the methane flux at the SWI versus a for passive case (plain) and active case (pattern) and the $[CH_4]_-$ reported in the text.

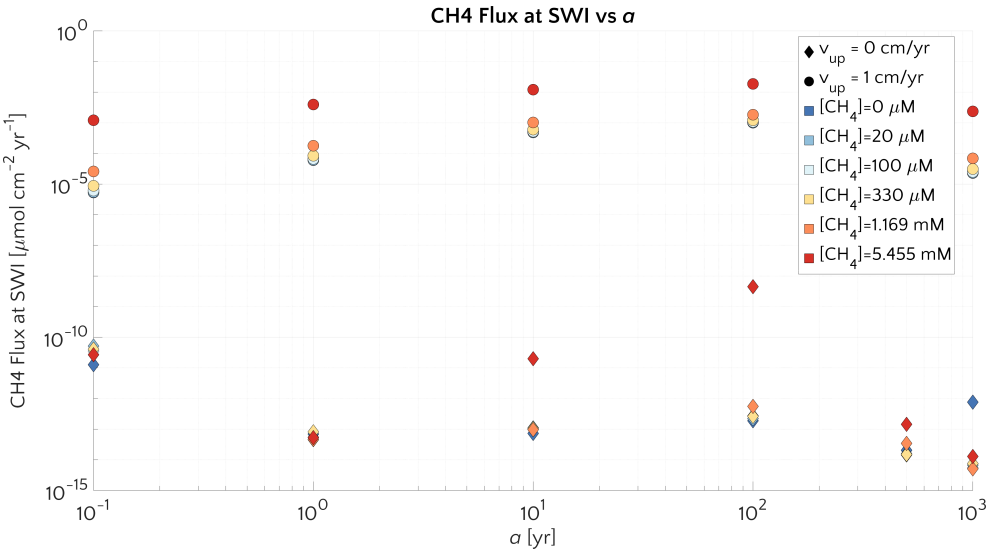

Figure C.7: Methane flux at SWI versus a for passive (diamonds) and active (circle) cases.

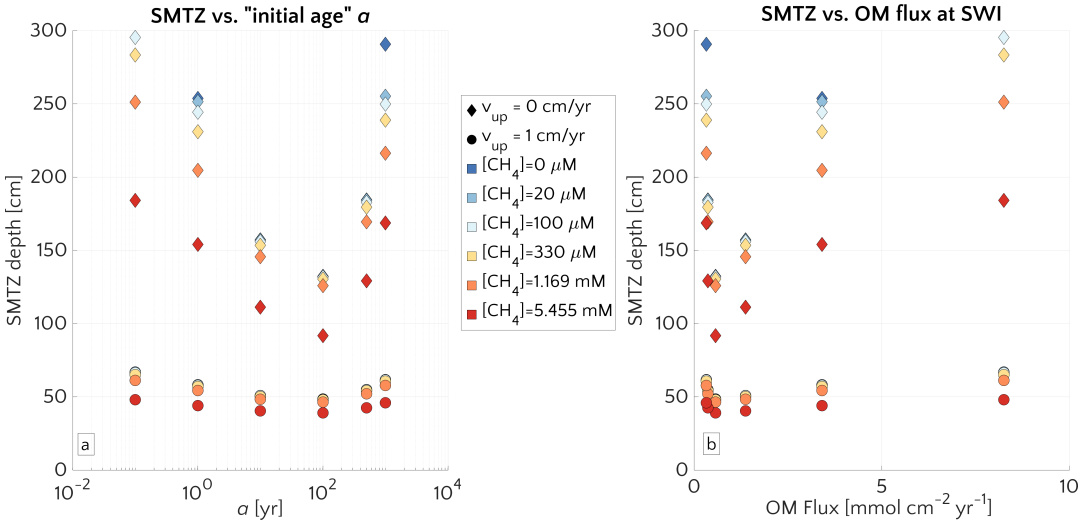

Figure C.8: (a) SMTZ depth versus a. Passive (diamonds) and active (circle) cases for different $[CH_4]_-$. (b) SMTZ depth versus OM flux entering the system at the SWI.

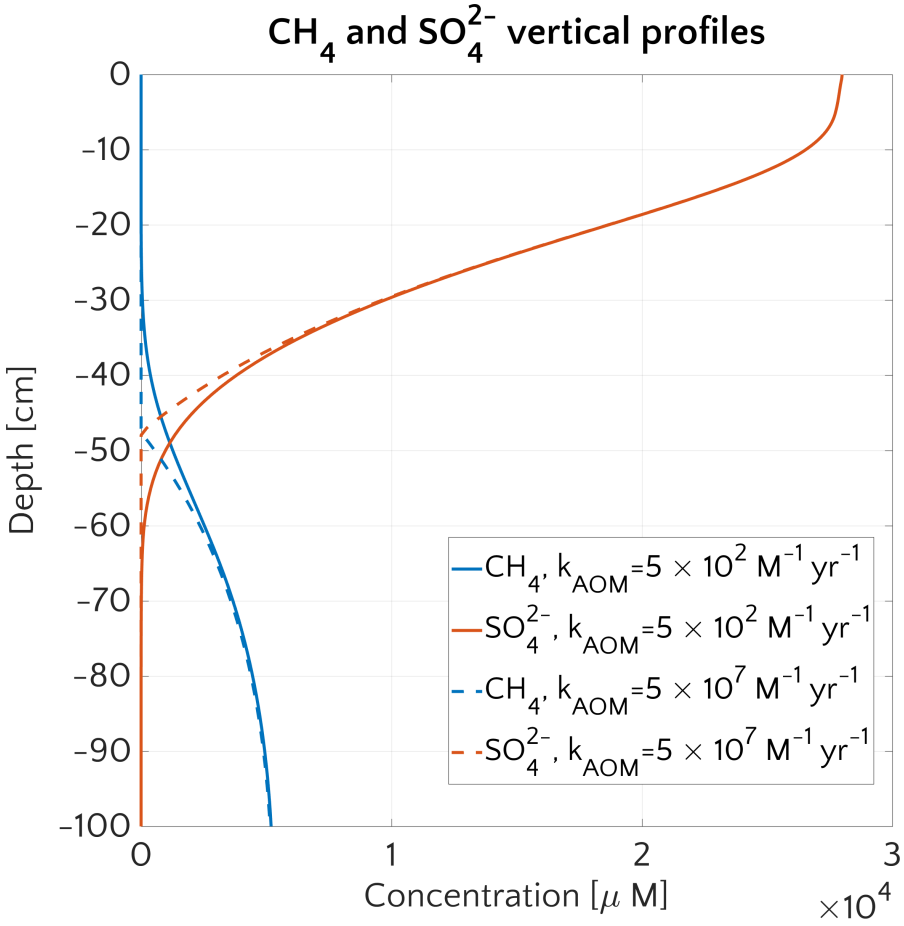

Figure C.9: Example of the effect of changing k_{AOM} on CH_4 and SO_4^{2-} vertical profile. The plot is for the active ($v_{up} = 1$ cm yr^{-1}) baseline simulation with the lowest ($5 \cdot 10^2$ M^{-1} yr^{-1}) and highest ($5 \cdot 10^7$ M^{-1} yr^{-1}) value for k_{AOM}.

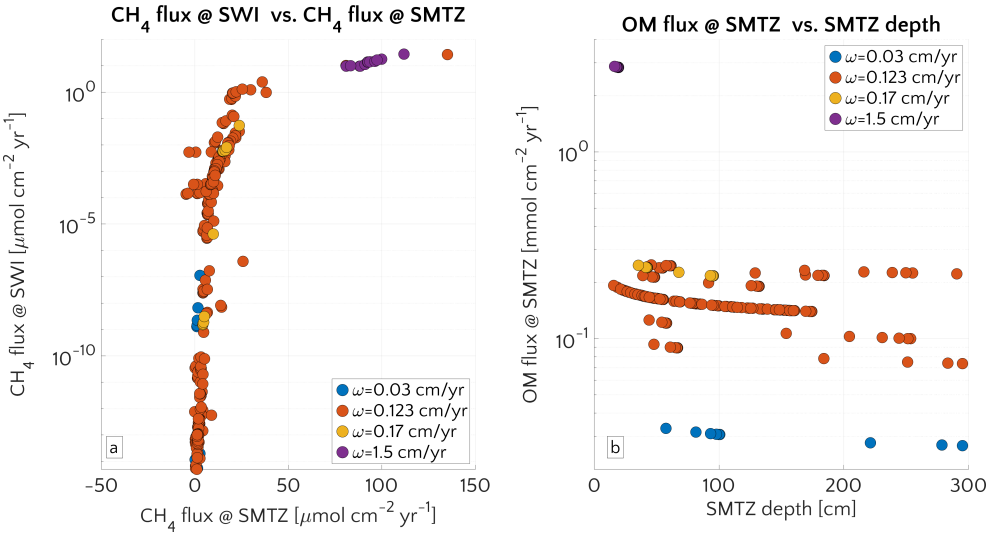

Figure C.10: *a.* Flux of methane at SWI versus flux of methane at the SMTZ depth. *b.* OM flux at the SMTZ depth versus SMTZ depth itself. Colours identify simulations with different ω.

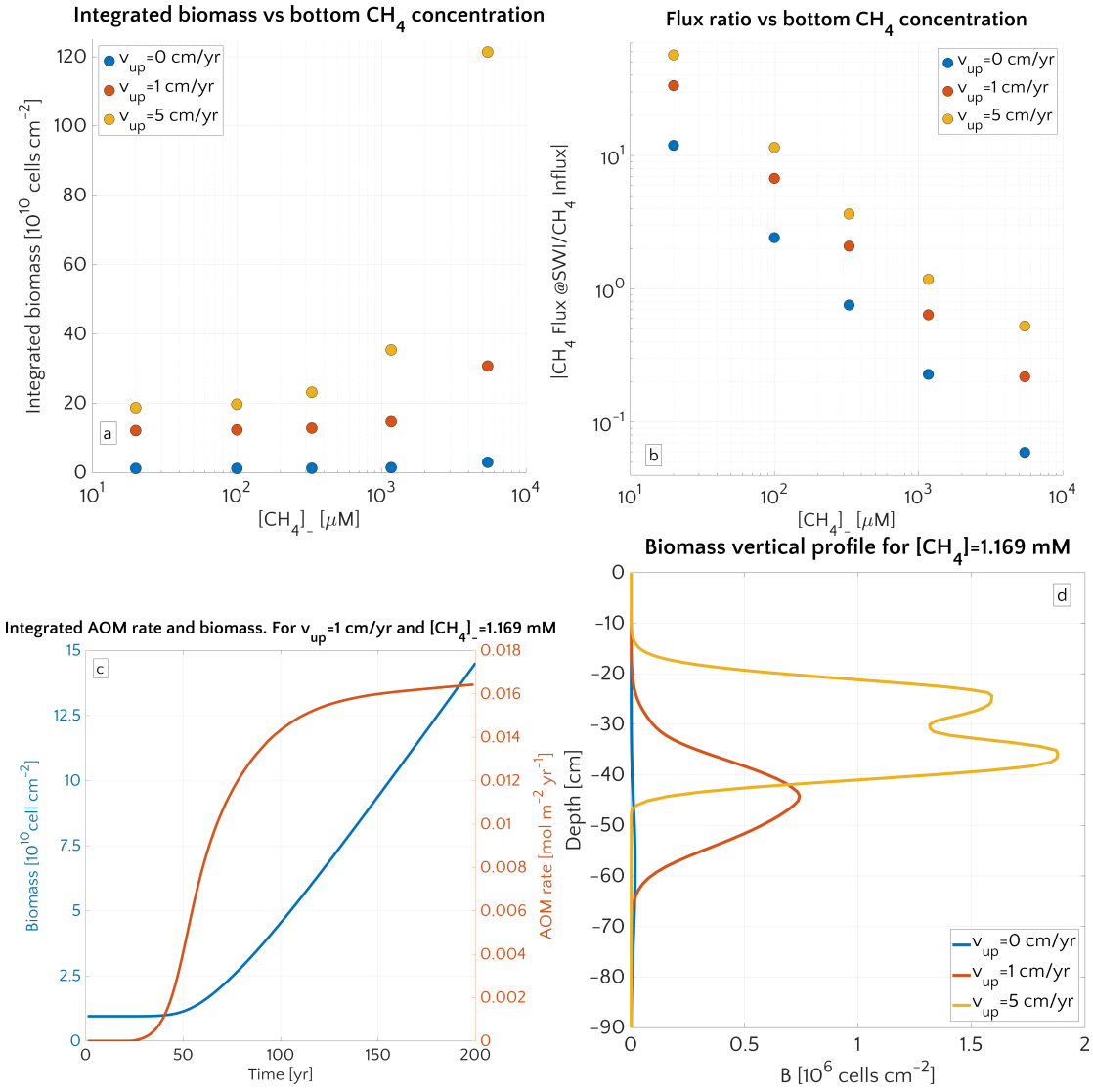

Figure C.11: *a.* Vertically integrated biomass after 200 years *vs* the bottom methane concentration $[CH_4]_-$ for three different v_{up}. *b.* Absolute value of the ratio of the methane flux at the SWI to the advective methane flux at the base of sediment column *vs* the bottom methane concentration $[CH_4]_-$ for three different v_{up}. *c.* Time evolution of the vertically integrated AOM biomass (blue) and vertically integrated AOM rate (red) for the step-like simulation with $[CH_4]_- = 1.169$ mM and $v_{up} = 1$ cm/yr. *d.* AOM biomass vertical profile after 200 years for three different v_{up} in case of step-like simulation with $[CH_4]_- = 1.169$ mM.

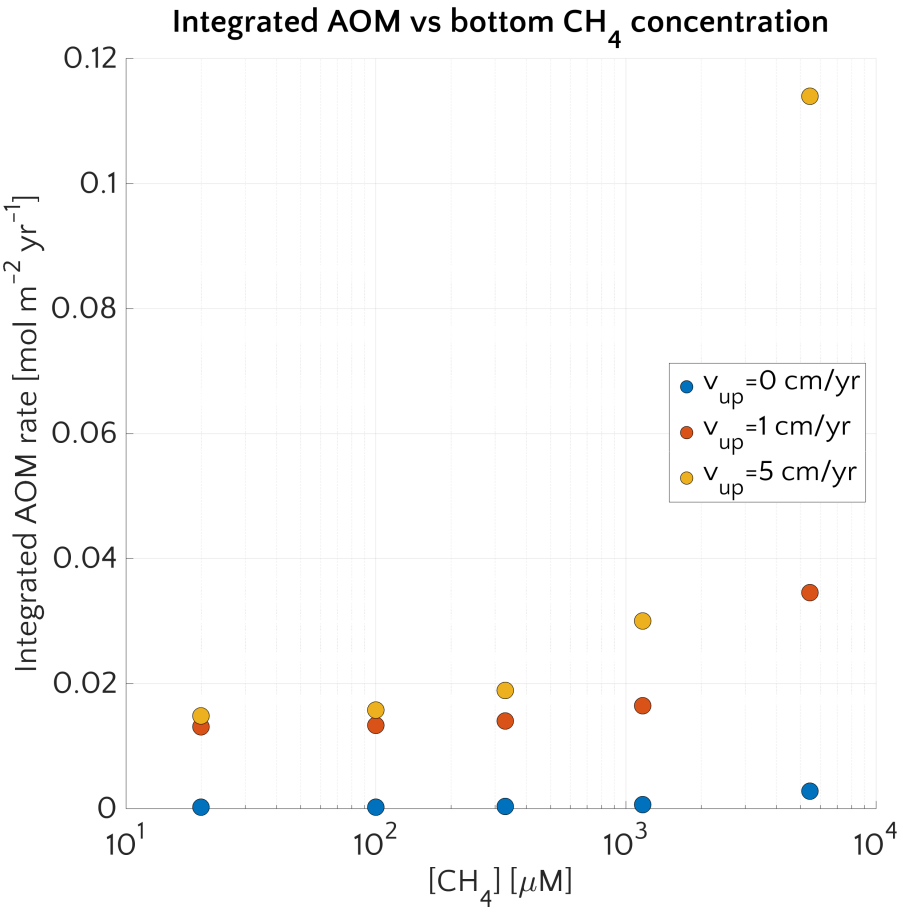

Figure C.12: Vertically integrated AOM *versus* the bottom methane concentration $[CH_4]_-$ for three different v_{up}.

BIBLIOGRAPHY

ACIA, Arctic Climate Impact Assessment (2005). *Arctic climate impact assessment*. Cambridge University Press.

Aguilera, DR, P Jourabchi, C Spiteri, and P Regnier (2005). "A knowledge-based reactive transport approach for the simulation of biogeochemical dynamics in Earth systems." *Geochemistry, Geophysics, Geosystems* 6.7.

Albert, Daniel B, Christopher S Martens, and Marc J Alperin (1998). "Biogeochemical processes controlling methane in gassy coastal sediments—part 2: Groundwater flow control of acoustic turbidity in Eckernförde Bay Sediments." *Continental Shelf Research* 18.14-15, pp. 1771–1793.

Alexiades, V and A. D. Solomon (1993). *Mathematical Modeling of Melting and Freezing Processes*. Hemisphere Publishing Corporation.

Alexiades, V, RD Solomon, and DG Wilson (1981). "Modleing of phase change processes with time-varying critical temperature."

Aller, Robert C and Neal E Blair (2004). "Early diagenetic remineralization of sedimentary organic C in the Gulf of Papua deltaic complex (Papua New Guinea): net loss of terrestrial C and diagenetic fractionation of C isotopes." *Geochimica et Cosmochimica Acta* 68.8, pp. 1815–1825.

Aloisi, Giovanni, Catherine Pierre, Jean Marie Rouchy, Jean Paul Foucher, and John Woodside (2000). "Methane-related authigenic carbonates of Eastern Mediterranean Sea mud volcanoes and their possible relation to gas hydrate destabilisation." *Earth and Planetary Science Letters* 184.1, pp. 321–338.

Aloisi, Giovanni, Klaus Wallmann, RR Haese, and J-F Saliege (2004). "Chemical, biological and hydrological controls on the 14C content of cold seep carbonate crusts: numerical modeling and implications for convection at cold seeps." *Chemical Geology* 213.4, pp. 359–383.

AMAP (2015). *AMAP Assessment 2015: Methane as an Arctic Climate Forcer*.

Anderson, Brian, Karen B Bartlett, Steve Frolking, Katharine Hayhoe, Jennifer C Jenkins, and William A Salas (2010). "Methane and nitrous oxide emissions from natural sources."

Anderson, Dale, John C. Tannehill, and Richard H. Pletcher (2016). *Computational fluid mechanics and heat transfer, Third edition*, pp. 1–740.

Angelis, Marie A de and Cindy Lee (1994). "Methane production during zooplankton grazing on marine phytoplankton." *Limnology and Oceanography* 39.6, pp. 1298–1308.

Angelopoulos, Michael, Sebastian Westermann, Paul Overduin, Alexey Faguet, Vladimir Olenchenko, Guido Grosse, and Mikhail N Grigoriev (2019). "Heat and salt flow in subsea permafrost modeled with CryoGRID2." *Journal of Geophysical Research: Earth Surface* 124.4, pp. 920–937.

Anisimov, OA, Yu G Zaboikina, VA Kokorev, and LN Yurganov (2014). "Possible causes of methane release from the East Arctic seas shelf." *Ice and Snow* 54.2, pp. 69–81.

Archer, D (2007). "Methane hydrate stability and anthropogenic climate change." *Biogeosciences* 4.4, pp. 521–544.

Archer, David (2015). "A model of the methane cycle, permafrost, and hydrology of the Siberian continental margin." *Biogeosciences* 12.10, pp. 2953–2974.

Archer, David, Bruce Buffett, and Victor Brovkin (2009). "Ocean methane hydrates as a slow tipping point in the global carbon cycle." *Proceedings of the National Academy of Sciences of the United States of America* 106.49, pp. 20596–20601.

Are, Felix E (2003). "Shoreface of the Arctic seas - a natural laboratory for subsea permafrost dynamics." In: *Permafrost: Proceedings of the 8th International Conference on Permafrost*. Zurich, Switzerland.

Aris, Rutherford (1968). "Prolegomena to the rational analysis of systems of chemical reactions II. Some addenda." *Archive for Rational Mechanics and Analysis* 27.5, pp. 356–364.

Arndt, Sandra, Bo Barker Jørgensen, Douglas E LaRowe, JJ Middelburg, RD Pancost, and Pierre Regnier (2013). "Quantifying the degradation of organic matter in marine sediments: a review and synthesis." *Earth-science reviews* 123, pp. 53–86.

Athy, Lawrence Ferdinand (1930). "Density, porosity, and compaction of sedimentary rocks." *AAPG Bulletin* 14.1, pp. 1–24.

Bai, Dongsheng, Diwei Zhang, Xianren Zhang, and Guangjin Chen (2015). "Origin of Self-preservation Effect for Hydrate Decomposition: Coupling of Mass and Heat Transfer Resistances." *Scientific Reports* 5.

Baker, GC and TE Osterkamp (1988). "Implications of salt fingering processes for salt movement in thawed coarse-grained subsea permafrost." *Cold regions science and technology* 15.1, pp. 45–52.

— (1989). "Salt redistribution during freezing of saline sand columns at constant rates." *Water Resources Research* 25.8, pp. 1825–1831.

Barton, Benjamin I, Yueng-Djern Lenn, and Camille Lique (2018). "Observed Atlantification of the Barents Sea causes the Polar Front to limit the expansion of winter sea ice." *Journal of Physical Oceanography* 48.8, pp. 1849–1866.

Bastviken, David, Lars J Tranvik, John A Downing, Patrick M Crill, and Alex Enrich-Prast (2011). "Freshwater methane emissions offset the continental carbon sink." *Science* 331.6013, pp. 50–50.

Bates, NR and JT Mathis (2009). "The Arctic Ocean marine carbon cycle: evaluation of air-sea CO 2 exchanges, ocean acidification impacts and potential feedbacks." *Biogeosciences* 6.11, pp. 2433–2459.

Bauch, Henning A, Thomas Mueller-Lupp, Ekaterina Taldenkova, Robert F Spielhagen, Heidemarie Kassens, Peter M Grootes, Jörn Thiede, J Heinemeier, and VV Petryashov (2001). "Chronology of the Holocene transgression at the North Siberian margin." *Global and Planetary Change* 31.1-4, pp. 125–139.

Beal, Emily J, Christopher H House, and Victoria J Orphan (2009). "Manganese-and iron-dependent marine methane oxidation." *Science* 325.5937, pp. 184–187.

Beer, Dirk de, Eberhard Sauter, Helge Niemann, Norbert Kaul, Jean-Paul Foucher, Ursula Witte, Michael Schlüter, and Antje Boetius (2006). "In situ fluxes and zonation of microbial activity in surface sediments of the Håkon Mosby Mud Volcano." *Limnology and Oceanography* 51.3, pp. 1315–1331.

Bekryaev, Roman V, Igor V Polyakov, and Vladimir A Alexeev (2010). "Role of polar amplification in long-term surface air temperature variations and modern Arctic warming." *Journal of Climate* 23.14, pp. 3888–3906.

Berchet, Antoine, Philippe Bousquet, Isabelle Pison, Robin Locatelli, Frédéric Chevallier, Jean-Daniel Paris, Ed J Dlugokencky, Tuomas Laurila, Juha Hatakka, Yrjo Viisanen, et al. (2016). "Atmospheric constraints on the methane emissions from the East Siberian Shelf." *Atmospheric Chemistry and Physics* 16.6, pp. 4147–4157.

Berg, Peter, Søren Rysgaard, and Bo Thamdrup (2003). "Dynamic modeling of early diagenesis and nutrient cycling. A case study in an artic marine sediment." *American journal of science* 303.10, pp. 905–955.

Berger, WH, VS Smetacek, and Gerold Wefer (1989). "Ocean productivity and paleoproductivity—an overview." In: *Productivity of the ocean: present and past*. Vol. 44. Wiley New York, pp. 1–34.

Berner, Robert A (1980). *Early diagenesis: a theoretical approach*. 1. Princeton University Press.

Beulig, F, H Røy, C. Glombitza, and B. B. Jørgensen (2017). "Control on rate and pathway of anaerobic organic carbon degradation in the seabed." *Proceedings of the National Academy of Sciences of the United States of America* 115.2, pp. 367–372.

Biastoch, Arne, Tina Treude, Lars H Rüpke, Ulf Riebesell, Christina Roth, Ewa B Burwicz, Wonsun Park, Mojib Latif, Claus W Böning, Gurvan Madec, et al. (2011). "Rising Arctic Ocean temperatures cause gas hydrate destabilization and ocean acidification." *Geophysical Research Letters* 38.8.

Black, Robert F (1957). "Some problems in engineering geology caused by permafrost in the Arctic Coastal Plain, northern Alaska." *Arctic* 10.4, pp. 230–240.

Boetius, Antje, Katrin Ravenschlag, Carsten J Schubert, Dirk Rickert, Friedrich Widdel, Armin Gieseke, Rudolf Amann, Bo Barker Jørgensen, Ursula Witte, and Olaf Pfannkuche (2000). "A marine microbial consortium apparently mediating anaerobic oxidation of methane." *Nature* 407.6804, p. 623.

Boetius, Antje and Frank Wenzhöfer (2013). "Seafloor oxygen consumption fuelled by methane from cold seeps." *Nature Geoscience* 6.9, p. 725.

Bogorodskii, Peter V., Andrey V. Pnyushkov, and Vasilii Yu. Kustov (2018). "Seasonal Freezing of a Subwater Ground Layer at the Laptev Sea Shelf." In: pp. 611–625.

Bolshiyanov, D, A Makarov, and L Savelieva (2015). "Lena River delta formation during the Holocene." *Biogeosciences* 12.2, pp. 579–593.

Borges, Alberto and Gwenaël Abril (2011). "5.04-Carbon dioxide and methane dynamics in estuaries." *Treatise on Estuarine and Coastal Science, Volume 5: Biogeochemistry*, pp. 119–161.

Borowski, Walter S, Charles K Paull, and William Ussler III (1996). "Marine pore-water sulfate profiles indicate in situ methane flux from underlying gas hydrate." *Geology* 24.7, pp. 655–658.

Boswell, Ray and Timothy S Collett (2011). "Current perspectives on gas hydrate resources." *Energy & environmental science* 4.4, pp. 1206–1215.

Boudreau, Bernard P (1986). "Mathematics of tracer mixing in sediments: I. Spatially-dependent, diffusive mixing." *Am. J. Sci* 286.3, pp. 161–198.

— (1997). *Diagenetic models and their implementation*. Vol. 505. Springer Berlin.

Boudreau, Bernard P. (2012). "Boudreau, Bernard P. "The physics of bubbles in surficial, soft, cohesive sediments." *Marine and Petroleum Geology* 38.1, pp. 1–18.

Boudreau, Bernard P, Chris Algar, Bruce D Johnson, Ian Croudace, Allen Reed, Yoko Furukawa, Kelley M Dorgan, Peter A Jumars, Abraham S Grader, and Bruce S Gardiner (2005). "Bubble growth and rise in soft sediments." *Geology* 33.6, pp. 517–520.

Boudreau, Bernard P., Yiming Luo, Filip J.R. Meysman, Jack J. Middelburg, and Gerald R. Dickens (2015). "Gas hydrate dissociation prolongs acidification of the Anthropocene oceans." *Geophysical Research Letters* 42.21, pp. 9337–9344.

Boudreau, Bernard P and Barry R Ruddick (1991). "On a reactive continuum representation of organic matter diagenesis." *American Journal of Science* 291.5, pp. 507–538.

Bowles, Marshall W, José M Mogollón, Sabine Kasten, Matthias Zabel, and Kai-Uwe Hinrichs (2014). "Global rates of marine sulfate re-

duction and implications for sub–sea-floor metabolic activities." *Science* 344.6186, pp. 889–891.

Box, George EP, William Gordon Hunter, J Stuart Hunter, et al. (1978). "Statistics for experimenters."

Brewer, MC (1975). "The seaward extension of permafrost off the northern Alaska coast." *Proceedings of the Third Internationa| | oonference on Port and ocean Engineering under Arctic Conditions, University of Alaska, to be published*.

Brigham, JK and GH Miller (1983). "Paleotemperature estimates of the Alaskan Arctic Coastal Plain during the last 125,000 years." In: *Proceedings of the Fourth International Conference on Permafrost*. National Academy Press Washington, DC, pp. 80–85.

Brooks, LD (1974). "Ice score on Northern continental shelf of Alaska." In: *The coast and shelf of the Beaufort Sea: proceedings of a Symposium on Beaufort Sea Coast and Shelf Research*. Arctic Institute of North America, pp. 355–366.

Brothers, Laura L, Patrick E Hart, and Carolyn D Ruppel (2012). "Minimum distribution of subsea ice-bearing permafrost on the US Beaufort Sea continental shelf." *Geophysical Research Letters* 39.15.

Brothers, Laura L, Bruce M Herman, Patrick E Hart, and Carolyn D Ruppel (2016). "Subsea ice-bearing permafrost on the US Beaufort Margin: 1. Minimum seaward extent defined from multichannel seismic reflection data." *Geochemistry, Geophysics, Geosystems* 17.11, pp. 4354–4365.

Brouchkov, Anatoli (2000). "Salt and water transfer in frozen soils induced by gradients of temperature and salt content." *Permafrost and Periglacial Processes* 11.2, pp. 153–160.

Brovkin, V., L. Boysen, T. Raddatz, V. Gayler, A. Loew, and M. Claussen (2013a). "Evaluation of vegetation cover and land-surface albedo in MPI-ESM CMIP5 simulations." *Journal of Advances in Modeling Earth Systems* 5.1, pp. 48–57.

Brovkin, V. et al. (2013b). "Effect of anthropogenic land-use and land-cover changes on climate and land carbon storage in CMIP5 projections for the twenty-first century." *Journal of Climate* 26.18, pp. 6859–6881.

Brown, Jerry, OJ Ferrians Jr, JA Heginbottom, and ES Melnikov (1997). *Circum-Arctic map of permafrost and ground-ice conditions*. US Geological Survey Reston, VA.

Brüchert, Volker, Lisa Bröder, Joanna E Sawicka, Tommaso Tesi, Samantha P Joye, Xiaole Sun, Igor P Semiletov, and Vladimir A Samarkin (2018). "Carbon mineralization in Laptev and East Siberian sea shelf and slope sediment." *Biogeosciences* 15.2, pp. 471–490.

Burwicz, E B, L H Rü, and K Wallmann (2011). "Estimation of the global amount of submarine gas hydrates formed via microbial methane formation based on numerical reaction-transport mod-

eling and a novel parameterization of Holocene sedimentation." *Geochimica et Cosmochimica Acta* 75, pp. 4562–4576.

Caldwell, Sara L, James R Laidler, Elizabeth A Brewer, Jed O Eberly, Sean C Sandborgh, and Frederick S Colwell (2008). "Anaerobic oxidation of methane: mechanisms, bioenergetics, and the ecology of associated microorganisms." *Environmental science & technology* 42.18, pp. 6791–6799.

Caleman, Carl and David Van Der Spoel (2008). "Picosecond melting of ice by an infrared laser pulse: A simulation study." *Angewandte Chemie - International Edition* 47.8, pp. 1417–1420.

Cannon, John R., Daniel B. Henry, and Daniel B. Kotlow (1974). "Continuous differentiability of the free boundary for weak solutions of the stefan problem." *Bulletin of the American Mathematical Society* 80.1, pp. 45–48.

— (1975). "Classical solutions of the one-dimensional, two-phase Stefan problem." *Annali di Matematica Pura ed Applicata, Series 4* 107.1, pp. 311–341.

Carini, Paul, Angelicque E White, Emily O Campbell, and Stephen J Giovannoni (2014). "Methane production by phosphate-starved SAR11 chemoheterotrophic marine bacteria." *Nature communications* 5, p. 4346.

Carmack, Eddy C, Robie W Macdonald, Ronald G Perkin, Fiona A McLaughlin, and Richard J Pearson (1995). "Evidence for warming of Atlantic water in the southern Canadian Basin of the Arctic Ocean: Results from the Larsen-93 expedition." *Geophysical Research Letters* 22.9, pp. 1061–1064.

Centler, Florian, Haibing Shao, Cecilia De Biase, Chan-Hee Park, Pierre Regnier, Olaf Kolditz, and Martin Thullner (2010). "GeoSysBRNS—A flexible multidimensional reactive transport model for simulating biogeochemical subsurface processes." *Computers & Geosciences* 36.3, pp. 397–405.

Charkin, Alexander N, Michiel Rutgers van der Loeff, Natalia E Shakhova, Örjan Gustafsson, Oleg V Dudarev, Maxim S Cherepnev, Anatoly N Salyuk, Andrey V Koshurnikov, Eduard A Spivak, Alexey Y Gunar, et al. (2017). "Discovery and characterization of submarine groundwater discharge in the Siberian Arctic seas: a case study in the Buor-Khaya Gulf, Laptev Sea." *The Cryosphere* 11.5, pp. 2305–2327.

Chatterjee, Sayantan, Gerald R Dickens, Gaurav Bhatnagar, Walter G Chapman, Brandon Dugan, Glen T Snyder, and George J Hirasaki (2011). "Pore water sulfate, alkalinity, and carbon isotope profiles in shallow sediment above marine gas hydrate systems: A numerical modeling perspective." *Journal of Geophysical Research: Solid Earth* 116.B9.

Chen, Jing, Zhichao Zhou, and Ji-Dong Gu (2015). "Complex community of nitrite-dependent anaerobic methane oxidation bacteria in

coastal sediments of the Mai Po wetland by PCR amplification of both 16S rRNA and pmoA genes." *Applied microbiology and biotechnology* 99.3, pp. 1463–1473.

Cherkis, MD, MD Max, A Midthasse, K Crane, E Sundvor, and P Vogt (1992). "Deep ice scour and mass-wasting features on the northern Svalbard insular shelf and slope." In: *Proceedings International Conference on Arctic Margins*. Anchorage, Alaska, pp. 333–338.

Christensen, JH, K Krishna Kumar, E Aldrian, SI An, IFA Cavalcanti, M de Castro, W Dong, A Goswami, A Hall, JK Kanyanga, et al. (2013). "Climate phenomena and their relevance for future regional climate change." In: *Climate Change 2013-The Physical Science Basis: Contribution of Working Group I to the Fifth Assessment Report of the Intergovernmental Panel on Climate Change*. Cambridge University Press, pp. 1217–1308.

Chuvilin, Evgeny M., Vladimir S. Yakushev, and Elena V. Perlova (2000). "Gas and possible gas hydrates in the permafrost of bovanenkovo gas field, Yamal Peninsula, West Siberia." *Polarforschung* 68.1-3, pp. 215–219.

Chuvilin, Evgeny, Boris Bukhanov, Dinara Davletshina, Sergey Grebenkin, and Vladimir Istomin (2018). "Dissociation and self-preservation of gas hydrates in permafrost." *Geosciences (Switzerland)* 8.12.

Chuvilin, Evgeny, Olga Guryeva, and Boris Buhanov (2011). "Experimental Study of Self-Preservation Mechanisms during Gas Hydrate Decomposition In Frozen Sediments." *Proceedings of the 7th International Conference on Gas Hydrates* 7.495, p. 92102.

Ciais, P et al. (2013). "Carbon and other biogeochemical cycles." In: *Climate change 2013: the physical science basis. Contribution of Working Group I to the Fifth Assessment Report of the Intergovernmental Panel on Climate Change*. Cambridge: Cambridge University Press, pp. 465–570.

Cicerone, R. J. and R. S. Oremland (1988). "Biogeochemical aspects of atmospheric methane." *Global Biogeochemical Cycles* 2.4, pp. 299–327.

Clapp, Roger B. and George M. Hornberger (1978). "Empirical equations for some soil hydraulic properties." *Water Resources Research* 14.4, pp. 601–604.

Clark, JI, R Phillips, and MJ Paulin (1998). "Ice scour research for safe design of pipelines." In: *Proceedings of the 13th International Symposium on Okhotsk Sea & Sea Ice*. Mombetsu, Japan, pp. 1–8.

Clark, Peter U and Alan C Mix (2002). "Ice sheets and sea level of the Last Glacial Maximum." *Quaternary Science Reviews* 21.1-3, pp. 1–7.

Claypool, George E and IR Kaplan (1974). "The origin and distribution of methane in marine sediments." In: *Natural gases in marine sediments*. Springer, pp. 99–139.

Clough, Lisa M, William G Ambrose Jr, J Kirk Cochran, Christina Barnes, Paul E Renaud, and Robert C Aller (1997). "Infaunal density, biomass and bioturbation in the sediments of the Arctic Ocean." *Deep Sea Research Part II: Topical Studies in Oceanography* 44.8, pp. 1683–1704.

Cohen-Adad, Roger. and John W. Lorimer (1991). *Alkali metal and ammonium chlorides in water and heavy water (binary systems)*, p. 533.

Collins, Matthew, Reto Knutti, Julie Arblaster, Jean-Louis Dufresne, Thierry Fichefet, Pierre Friedlingstein, Xuejie Gao, William J Gutowski, Tim Johns, Gerhard Krinner, et al. (2013). "Long-term climate change: projections, commitments and irreversibility." In: *Climate Change 2013-The Physical Science Basis: Contribution of Working Group I to the Fifth Assessment Report of the Intergovernmental Panel on Climate Change*. Cambridge University Press, pp. 1029–1136.

Cordes, Erik E, Michael A Arthur, Katriona Shea, Rolf S Arvidson, and Charles R Fisher (2005). "Modeling the mutualistic interactions between tubeworms and microbial consortia." *PLoS Biology* 3.3, e77.

Crémière, Antoine, Aivo Lepland, Shyam Chand, Diana Sahy, Daniel J. Condon, Stephen R. Noble, Tõnu Martma, Terje Thorsnes, Simone Sauer, and Harald Brunstad (2016a). "Timescales of methane seepage on the Norwegian margin following collapse of the Scandinavian Ice Sheet." *Nature Communications* 7.

Crémière, Antoine et al. (2016b). "Fluid source and methane-related diagenetic processes recorded in cold seep carbonates from the Alvheim channel, central North Sea." *Chemical Geology* 432, pp. 16–33.

Crowe, SA, Sergei Katsev, K Leslie, A Sturm, C Magen, S Nomosatryo, MA Pack, JD Kessler, WS Reeburgh, JA Roberts, et al. (2011). "The methane cycle in ferruginous Lake Matano." *Geobiology* 9.1, pp. 61–78.

Dale, Andrew W, Volker Brüchert, Marc Alperin, and Pierre Regnier (2009). "An integrated sulfur isotope model for Namibian shelf sediments." *Geochimica et Cosmochimica Acta* 73.7, pp. 1924–1944.

Dale, Andrew W, Stephen R Meyers, David R Aguilera, Sandra Arndt, and Klaus Wallmann (2012). "Controls on organic carbon and molybdenum accumulation in Cretaceous marine sediments from the Cenomanian–Turonian interval including Oceanic Anoxic Event 2." *Chemical geology* 324, pp. 28–45.

Dale, Andrew W, Levin Nickelsen, Florian Scholz, Christian Hensen, Andreas Oschlies, and Klaus Wallmann (2015). "A revised global estimate of dissolved iron fluxes from marine sediments." *Global Biogeochemical Cycles* 29.5, pp. 691–707.

Dale, Andrew W, P Regnier, and P Van Cappellen (2006). "Bioenergetic controls on anaerobic oxidation of methane (AOM) in

coastal marine sediments: a theoretical analysis." *American Journal of Science* 306.4, pp. 246–294.

Dale, Andy W, DR Aguilera, P Regnier, Henrik Fossing, NJ Knab, and Bo Barker Jørgensen (2008a). "Seasonal dynamics of the depth and rate of anaerobic oxidation of methane in Aarhus Bay (Denmark) sediments." *Journal of Marine Research* 66.1, pp. 127–155.

Dale, Andy W, Pierre Regnier, NJ Knab, Bo Barker Jørgensen, and Philippe Van Cappellen (2008b). "Anaerobic oxidation of methane (AOM) in marine sediments from the Skagerrak (Denmark): II. Reaction-transport modeling." *Geochimica et Cosmochimica Acta* 72.12, pp. 2880–2894.

Dale, Andy W, Philippe Van Cappellen, DR Aguilera, and Pierre Regnier (2008c). "Methane efflux from marine sediments in passive and active margins: Estimations from bioenergetic reaction–transport simulations." *Earth and Planetary Science Letters* 265.3-4, pp. 329–344.

Damm, Ellen, RP Kiene, J Schwarz, E Falck, and Gerhard Dieckmann (2008). "Methane cycling in Arctic shelf water and its relationship with phytoplankton biomass and DMSP." *Marine Chemistry* 109.1-2, pp. 45–59.

Dassargues, Alain (2018). *Hydrogeology: groundwater science and engineering*. CRC Press.

Dean, Joshua F, Jack J Middelburg, Thomas Röckmann, Rien Aerts, Luke G Blauw, Matthias Egger, Mike SM Jetten, Anniek EE Jong, Ove H Meisel, Olivia Rasigraf, et al. (2018). "Methane feedbacks to the global climate system in a warmer world." *Reviews of Geophysics*.

Deemer, Bridget R, John A Harrison, Siyue Li, Jake J Beaulieu, Tonya DelSontro, Nathan Barros, José F Bezerra-Neto, Stephen M Powers, Marco A Dos Santos, and J Arie Vonk (2016). "Greenhouse gas emissions from reservoir water surfaces: a new global synthesis." *BioScience* 66.11, pp. 949–964.

Delisle, G (2000). "Temporal variability of subsea permafrost and gas hydrate occurrences as function of climate change in the Laptev Sea, Siberia." *Polarforschung* 68, pp. 221–225.

Denisov, S. N., M. M. Arzhanov, A. V. Eliseev, and I. I. Mokhov (2011). "Assessment of the response of subaqueous methane hydrate deposits to possible climate change in the twenty-first century." *Doklady Earth Sciences* 441.2, pp. 1706–1709.

D'Hondt, Steven, Bo Barker Jørgensen, D Jay Miller, Anja Batzke, Ruth Blake, Barry A Cragg, Heribert Cypionka, Gerald R Dickens, Timothy Ferdelman, Kai-Uwe Hinrichs, et al. (2004). "Distributions of microbial activities in deep subseafloor sediments." *Science* 306.5705, pp. 2216–2221.

Dickens, Gerald R (2003). "Rethinking the global carbon cycle with a large, dynamic and microbially mediated gas hydrate capacitor." *Earth and Planetary Science Letters* 213.3-4, pp. 169–183.

Dickens, Gerald R., Maria M. Castillo, and James C.G. Walker (1997). "A blast of gas in the latest Paleocene: Simulating first-order effects of massive dissociation of oceanic methane hydrate." *Geology* 25.3, pp. 259–262.

Dickens, Gerald R., James R. O'Neil, David K. Rea, and Robert M. Owen (1995). "Dissociation of oceanic methane hydrate as a cause of the carbon isotope excursion at the end of the Paleocene." *Paleoceanography* 10.6, pp. 965–971.

Dickens, GR, D Schroeder, KU Hinrichs, and Leg 201 Scientific Party (2003). "The pressure core sampler (PCS) on Ocean Drilling Program Leg 201: general operations and gas release." In: *Proceedings ODP, Initial Reports 201*. Ocean Drilling Program College Station, TX, pp. 1–22.

Dickson, Andrew G and Catherine Goyet (1994). *Handbook of methods for the analysis of the various parameters of the carbon dioxide system in sea water. Version 2*. Tech. rep. Oak Ridge National Lab., TN (United States).

Dmitrenko, Igor A, Sergey A Kirillov, L Bruno Tremblay, Heidemarie Kassens, Oleg A Anisimov, Sergey A Lavrov, Sergey O Razumov, and Mikhail N Grigoriev (2011). "Recent changes in shelf hydrography in the Siberian Arctic: Potential for subsea permafrost instability." *Journal of Geophysical Research: Oceans* 116.C10.

Li-dong, Shen, Zhu Qun, Liu Shuai, Du Ping, Zeng Jiang-ning, Cheng Dong-qing, Xu Xiang-yang, Zheng Ping, and Hu Bao-lan (2014). "Molecular evidence for nitrite-dependent anaerobic methane-oxidising bacteria in the Jiaojiang Estuary of the East Sea (China)." *Applied microbiology and biotechnology* 98.11, pp. 5029–5038.

Drachev, Sergei S (2000). "Laptev Sea rifted continental margin: modern knowledge and unsolved questions." *Polarforschung* 68, pp. 41–50.

Drachev, Sergei S, Leonid A Savostin, Victor G Groshev, and Inna E Bruni (1998). "Structure and geology of the continental shelf of the Laptev Sea, Eastern Russian Arctic." *Tectonophysics* 298.4, pp. 357–393.

Drachev, SS, GL Johnson, SW Laxon, DC McAdoo, and Heidemarie Kassens (1999). "Main structural elements of Eastern Russian Arctic continental margin derived from satellite gravity and multichannel seismic reflection data." In: *Land-Ocean Systems in the Siberian Arctic*. Springer, pp. 667–682.

Drachev, SS, N Kaul, and VN Beliaev (2003). "Eurasia spreading basin to Laptev Shelf transition: structural pattern and heat flow." *Geophysical Journal International* 152.3, pp. 688–698.

Drachev, SS, LA Savostin, and IE Bruni (1995). "Structural pattern and tectonic history of the Laptev Sea region." *Rep. Polar Res* 176, pp. 348–366.

Drake, Henrik, Mats E. Aström, Christine Heim, Curt Broman, Jan Aström, Martin Whitehouse, Magnus Ivarsson, Sandra Siljeström, and Peter Sjövall (2015a). "Extreme 13 C depletion of carbonates formed during oxidation of biogenic methane in fractured granite." *Nature Communications* 6.

Drake, Travis W, Kimberly P Wickland, Robert GM Spencer, Diane M McKnight, and Robert G Striegl (2015b). "Ancient low–molecular-weight organic acids in permafrost fuel rapid carbon dioxide production upon thaw." *Proceedings of the National Academy of Sciences* 112.45, pp. 13946–13951.

Duan, Zhenhao, Nancy Møller, Jerry Greenberg, and John H Weare (1992). "The prediction of methane solubility in natural waters to high ionic strength from 0 to 250 C and from 0 to 1600 bar." *Geochimica et Cosmochimica Acta* 56.4, pp. 1451–1460.

Duchkuv, AD (1985). *Catalogue of geothermal heat flow data of Siberia (1966–1984)*. Tech. rep. Institute of Geology and Geophysics of Siberian Branch of USSR Academia of Science.

Duchkuv, AD and LS Sokolova (1985). "Temperature of the lithosphere of Siberia according to geothermal data." *Sovetskaia Geologi I Geophisika* 26, pp. 53–61.

Dunne, John P, Jorge L Sarmiento, and Anand Gnanadesikan (2007). "A synthesis of global particle export from the surface ocean and cycling through the ocean interior and on the seafloor." *Global Biogeochemical Cycles* 21.4.

Egger, Matthias, Wytze Lenstra, Dirk Jong, Filip JR Meysman, Célia J Sapart, Carina van der Veen, Thomas Röckmann, Santiago Gonzalez, and Caroline P Slomp (2016). "Rapid sediment accumulation results in high methane effluxes from coastal sediments." *PloS one* 11.8, e0161609.

Egger, Matthias, Natascha Riedinger, José M Mogollón, and Bo Barker Jørgensen (2018). "Global diffusive fluxes of methane in marine sediments." *Nature Geoscience* 11.6, p. 421.

Egger, Matthias, Olivia Rasigraf, Célia J Sapart, Tom Jilbert, Mike SM Jetten, Thomas Röckmann, Carina Van der Veen, Narcisa Banda, Boran Kartal, Katharina F Ettwig, et al. (2014). "Iron-mediated anaerobic oxidation of methane in brackish coastal sediments." *Environmental science & technology* 49.1, pp. 277–283.

Ehhalt, DH (1974). "The atmospheric cycle of methane." *Tellus* 26.1-2, pp. 58–70.

Ekici, Altug, Christian Beer, Stefan Hagemann, and C Hauck (2014). "Simulating high-latitude permafrost regions by the JSBACH terrestrial ecosystem model." *Geoscientific Model Development* 7, pp. 631–647.

Elliott, Scott, Mathew Maltrud, Matthew Reagan, George Moridis, and Philip Cameron-Smith (2011). "Marine methane cycle simulations for the period of early global warming." *Journal of Geophysical Research: Biogeosciences* 116.G1.

Elvert, Marcus, Erwin Suess, and Michael J Whiticar (1999). "Anaerobic methane oxidation associated with marine gas hydrates: superlight C-isotopes from saturated and unsaturated C20 and C25 irregular isoprenoids." *Naturwissenschaften* 86.6, pp. 295–300.

Epstein, M and F B Cheung (1983). "Complex Freezing-Melting Interfaces in Fluid Flow." *Annual Review of Fluid Mechanics* 15.1, pp. 293–319.

Etiope, Giuseppe (2015). "Natural gas seepage." *The Earth's Hydrocarbon De*.

— (2017). "Abiotic Methane in Continental Serpentinization Sites: An Overview." *Procedia Earth and Planetary Science* 17, pp. 9–12.

Ettwig, Katharina F, Daan R Speth, Joachim Reimann, Ming L Wu, Mike SM Jetten, and Jan T Keltjens (2012). "Bacterial oxygen production in the dark." *Frontiers in microbiology* 3, p. 273.

Ettwig, Katharina F, Margaret K Butler, Denis Le Paslier, Eric Pelletier, Sophie Mangenot, Marcel MM Kuypers, Frank Schreiber, Bas E Dutilh, Johannes Zedelius, Dirk de Beer, et al. (2010). "Nitrite-driven anaerobic methane oxidation by oxygenic bacteria." *Nature* 464.7288, p. 543.

Evans, Paul N, Donovan H Parks, Grayson L Chadwick, Steven J Robbins, Victoria J Orphan, Suzanne D Golding, and Gene W Tyson (2015). "Methane metabolism in the archaeal phylum Bathyarchaeota revealed by genome-centric metagenomics." *Science* 350.6259, pp. 434–438.

Everdingen, Robert O van, International Permafrost Association, et al. (1998). *Multi-language glossary of permafrost and related ground-ice terms in chinese, english, french, german...* Arctic Inst. of North America University of Calgary.

Fairbanks, Richard G (1989). "A 17,000-year glacio-eustatic sea level record: influence of glacial melting rates on the Younger Dryas event and deep-ocean circulation." *Nature* 342.6250, p. 637.

Fartyshev, AI (1993). "Peculiarities of the coastal-shelf cryolitozone of the Laptev Sea. Novosibirsk." *Nauka* 136.

Fichot, Cédric G, Karl Kaiser, Stanford B Hooker, Rainer MW Amon, Marcel Babin, Simon Bélanger, Sally A Walker, and Ronald Benner (2013). "Pan-Arctic distributions of continental runoff in the Arctic Ocean." *Scientific reports* 3, p. 1053.

Fleming, Kevin, Paul Johnston, Dan Zwartz, Yusuke Yokoyama, Kurt Lambeck, and John Chappell (1998). "Refining the eustatic sea-level curve since the Last Glacial Maximum using far-and intermediate-field sites." *Earth and Planetary Science Letters* 163.1-4, pp. 327–342.

Forbes, Donald L (2011). *State of the Arctic coast 2010: scientific review and outlook*. Land-Ocean Interactions in the Coastal Zone, Institute of Coastal Research.

Fortes, A Dominic and Mathieu Choukroun (2010). "Phase behaviour of ices and hydrates." *Space science reviews* 153.1-4, pp. 185–218.

Fortier, Richard, Michel Allard, and M-K Seguin (1994). "Effect of physical properties of frozen ground on electrical resistivity logging." *Cold Regions Science and Technology* 22.4, pp. 361–384.

Fossing, Henrik, Timothy G Ferdelman, and Peter Berg (2000). "Sulfate reduction and methane oxidation in continental margin sediments influenced by irrigation (South-East Atlantic off Namibia)." *Geochimica et Cosmochimica Acta* 64.5, pp. 897–910.

Franke, Dieter, Karl Hinz, and Onno Oncken (2001). "The Laptev Sea rift." *Marine and Petroleum Geology* 18.10, pp. 1083–1127.

Frederick, JM and BA Buffett (2014). "Taliks in relict submarine permafrost and methane hydrate deposits: Pathways for gas escape under present and future conditions." *Journal of Geophysical Research: Earth Surface* 119.2, pp. 106–122.

— (2015). "Effects of submarine groundwater discharge on the present-day extent of relict submarine permafrost and gas hydrate stability on the Beaufort Sea continental shelf." *Journal of Geophysical Research: Earth Surface* 120.3, pp. 417–432.

Frenzel, Burkhard (1992). "Atlas of paleoclimates and paleoenvironments of the Northern Hemisphere." *Geographical Research Institute, Hungarian Academy of SCiences, Budapest, Gustav Fischer Verlag, Stuttgart Jena New York*.

Froelich, PN, GP Klinkhammer, M Luedtke Bender, NA Luedtke, G Ross Heath, Doug Cullen, Paul Dauphin, Doug Hammond, Blayne Hartman, and Val Maynard (1979). "Early oxidation of organic matter in pelagic sediments of the eastern equatorial Atlantic: suboxic diagenesis." *Geochimica et cosmochimica acta* 43.7, pp. 1075–1090.

Gao, Xiang, C Adam Schlosser, Andrei Sokolov, Katey Walter Anthony, Qianlai Zhuang, and David Kicklighter (2013). "Permafrost degradation and methane: low risk of biogeochemical climate-warming feedback." *Environmental Research Letters* 8.3, p. 035014.

Garcia, Hernan E, Timothy P Boyer, Ricardo A Locarnini, John I Antonov, Alexey V Mishonov, Olga K Baranova, Melissa M Zweng, James R Reagan, Daphne R Johnson, and Sydney Levitus (2010). "World Ocean Atlas 2009, Volume 3: Dissolved Oxygen, Apparent Oxygen Utilization, and Oxygen Saturation."

Gavrilov, AV and VE Tumskoy (2003). "Model of mean annual temperature history for the Yakutian coastal lowlands and arctic shelf during the last 400 thousand years." In: *Permafrost, eight international conference on Permafrost*. Taylor and Francis Group plc London, UK, pp. 287–290.

GEOS (1997). *Baydaratskaya Bay environmental conditions. The basic result of studies for the pipeline "Yamal-Center" underwater crossing design*. Tech. rep. EPS "Eco-System Library".

GFD (2006). *Geophysical Fluid Dynamics lectures*. Woods Hole Oceanographic Institution.

Giorgetta, Marco A, Johann Jungclaus, Christian H Reick, Stephanie Legutke, Jürgen Bader, Michael Böttinger, Victor Brovkin, Traute Crueger, Monika Esch, Kerstin Fieg, et al. (2013). "Climate and carbon cycle changes from 1850 to 2100 in MPI-ESM simulations for the Coupled Model Intercomparison Project phase 5." *Journal of Advances in Modeling Earth Systems* 5.3, pp. 572–597.

Glasby, Geoffrey P (2006). "Manganese: predominant role of nodules and crusts." In: *Marine geochemistry*. Springer, pp. 371–427.

Goll, Daniel S., Victor Brovkin, Jari Liski, Thomas Raddatz, Tea Thum, and Kathe E.O. Todd-Brown (2015). "Strong dependence of CO2 emissions from anthropogenic land cover change on initial land cover and soil carbon parametrization." *Global Biogeochemical Cycles* 29.9, pp. 1511–1523.

Gramberg, I. S., Yu. N. Kulakov, Yu. E. Pogrebitsky, and D. S. Sorokov (1983). "Arctic oil and gas super basin." In: *X World Petroleum Congress*.

Grandpré, Isabelle de, Daniel Fortier, and Eva Stephani (2012). "Degradation of permafrost beneath a road embankment enhanced by heat advected in groundwater." *Canadian Journal of Earth Sciences* 49.8, pp. 953–962.

Graves, Carolyn A, Rachael H James, Célia Julia Sapart, Andrew W Stott, Ian C Wright, Christian Berndt, Graham K Westbrook, and Douglas P Connelly (2017). "Methane in shallow subsurface sediments at the landward limit of the gas hydrate stability zone offshore western Svalbard." *Geochimica et Cosmochimica Acta* 198, pp. 419–438.

Grigoriev, Mikhail N. and Volker Rachold (2003). "The degradation of coastal permafrost and the organic carbon balance of the Laptev and East Siberian Seas." *Permafrost: Proceedings of the 8th International Conference on Permafrost, 21-25 July 2003, Zurich, Switzerland* 1987, pp. 319–324.

Grigoriev, MN (2008). "Kriomorfogenez i litodinamika priberezhnoshel'fovoi zony morei vostochnoi Sibiri." *Habilitation thesis, Russian Academy of Sciences*.

Grigoriev, NF (1962). "Role of cryogenic factors in the formation of Yakutia shorelines." *Izd. AN SSSR*, pp. 68–78.

— (1966). *Perennial frozen rocks of the coastal zone of Yakutia*. Nauka.

— (1986). *Mnogoletnemerzlie porodi primorskoy zoni Yakutii*. Nauka.

Grosse, Guido, Joel E Robinson, Robin Bryant, Maxwell D Taylor, William Harper, Amy DeMasi, Emily Kyker-Snowman, Alexandra Veremeeva, Lutz Schirrmeister, and Jennifer Harden (2013).

"Distribution of late Pleistocene ice-rich syngenetic permafrost of the Yedoma Suite in east and central Siberia, Russia." *US Geological Survey Open File Report* 2013.1078, pp. 1–37.

Grosse, Guido, Vladimir Romanovsky, Torre Jorgenson, Katey Walter Anthony, Jerry Brown, and Pier Paul Overduin (2011). "Vulnerability and feedbacks of permafrost to climate change." *Eos, Transactions American Geophysical Union* 92.9, pp. 73–74.

Guinotte, John M and Victoria J Fabry (2008). "Ocean acidification and its potential effects on marine ecosystems." *Annals of the New York Academy of Sciences* 1134.1, pp. 320–342.

Gumerov, NA and CL Chahine (1998). "Dynamics of bubbles in conditions of gas hydrate formation." In: *8th International Offshore and Polar Engineering Conference*. Int. Soc. of Offshore and Polar Eng.

Günther, F, P. P. Overduin, I. A. Yakshina, T. Opel, A. V. Baranskaya, and M. N. Grigoriev (2015). "Observing Muostakh disappear: Permafrost thaw subsidence and erosion of a ground-ice-rich Island in response to arctic summer warming and sea ice reduction." *Cryosphere* 9.1, pp. 151–178.

Guo, Laodong, Chien-Lu Ping, and Robie W Macdonald (2007). "Mobilization pathways of organic carbon from permafrost to arctic rivers in a changing climate." *Geophysical Research Letters* 34.13.

Hachikubo, Akihiro, Satoshi Takeya, Evgeny Chuvilin, and Vladimir Istomin (2011). "Preservation phenomena of methane hydrate in pore spaces." *Physical Chemistry Chemical Physics* 13.39, pp. 17449–17452.

Haeckel, Matthias, Bernard P. Boudreau, and Klaus Wallmann (2007). "Bubble-induced porewater mixing: A 3-D model for deep porewater irrigation." *Geochimica et Cosmochimica Acta* 71.21, pp. 5135–5154.

Haeckel, Matthias, Erwin Suess, Klaus Wallmann, and Dirk Rickert (2004). "Rising methane gas bubbles form massive hydrate layers at the seafloor." *Geochimica et Cosmochimica Acta* 68.21, pp. 4335–4345.

Haese, Ralf R, Christof Meile, Philippe Van Cappellen, and Gert J De Lange (2003). "Carbon geochemistry of cold seeps: methane fluxes and transformation in sediments from Kazan mud volcano, eastern Mediterranean Sea." *Earth and Planetary Science Letters* 212.3-4, pp. 361–375.

Hagemann, Stefan and Tobias Stacke (2015). "Impact of the soil hydrology scheme on simulated soil moisture memory." *Climate Dynamics* 44.7-8, pp. 1731–1750.

Han, Pai (2014). "Characteristics and sedimentation rates at the shallow Laptev Sea." MA thesis. University of Bremen.

Handa, YP (1986). "Compositions, enthalpies of dissociation, and heat capacities in the range 85 to 270 K for clathrate hydrates of methane, ethane, and propane, and enthalpy of dissociation of isobu-

tane hydrate, as determined by a heat-flow calorimeter." *The Journal of chemical thermodynamics* 18.10, pp. 915–921.

Hanson, Richard S and Thomas E Hanson (1996). "Methanotrophic bacteria." *Microbiol. Mol. Biol. Rev.* 60.2, pp. 439–471.

Haroon, Mohamed F, Shihu Hu, Ying Shi, Michael Imelfort, Jurg Keller, Philip Hugenholtz, Zhiguo Yuan, and Gene W Tyson (2013). "Anaerobic oxidation of methane coupled to nitrate reduction in a novel archaeal lineage." *Nature* 500.7464, p. 567.

Harrison, WD and TE Osterkamp (1981). "Subsea permafrost: Probing, thermal regime and data analysis." *Environmental Assessment of the Alaskan Continental Shelf Annual Reports* 7, pp. 291–401.

Harrison, WD and Thomas E Osterkamp (1978). "Heat and mass transport processes in subsea permafrost 1. An analysis of molecular diffusion and its consequences." *Journal of Geophysical Research: Oceans* 83.C9, pp. 4707–4712.

Harvey, L. D.D. and Zhen Huang (1995). "Evaluation of the potential impact of methane clathrate destabilization on future global warming." *Journal of Geophysical Research* 100.D2, pp. 2905–2926.

Hedges, John I and Richard G Keil (1995). "Sedimentary organic matter preservation: an assessment and speculative synthesis." *Marine chemistry* 49.2-3, pp. 81–115.

Hensen, Christian and Klaus Wallmann (2005). "Methane formation at Costa Rica continental margin—constraints for gas hydrate inventories and cross-décollement fluid flow." *Earth and Planetary Science Letters* 236.1-2, pp. 41–60.

Hester, Keith C. and Peter G. Brewer (2009). "Clathrate Hydrates in Nature." *Annual Review of Marine Science* 1.1, pp. 303–327.

Hinrichs, Kai-Uwe, John M Hayes, Sean P Sylva, Peter G Brewer, and Edward F DeLong (1999). "Methane-consuming archaebacteria in marine sediments." *Nature* 398.6730, p. 802.

Hinrichs, K-U and Antje Boetius (2002). "The anaerobic oxidation of methane: new insights in microbial ecology and biogeochemistry." In: *Ocean margin systems*. Springer, pp. 457–477.

Hinz, K, G Delisle, and M Block (1998). "Seismic evidence for the depth extent of permafrost in shelf sediments of the laptev sea, russian arctic?" *Arctic* 55, pp. 453–457.

Ho, TC and R Aris (1987). "On apparent second-order kinetics." *AIChE journal* 33.6, pp. 1050–1051.

Hoegh-Guldberg, Ove and John F Bruno (2010). "The impact of climate change on the world's marine ecosystems." *Science* 328.5985, pp. 1523–1528.

Hoehler, Tori M, Marc J Alperin, Daniel B Albert, and Christopher S Martens (1994). "Field and laboratory studies of methane oxidation in an anoxic marine sediment: Evidence for a methanogen-sulfate reducer consortium." *Global Biogeochemical Cycles* 8.4, pp. 451–463.

— (1998). "Thermodynamic control on hydrogen concentrations in anoxic sediments." *Geochimica et cosmochimica acta* 62.10, pp. 1745–1756.
— (2001). "Apparent minimum free energy requirements for methanogenic Archaea and sulfate-reducing bacteria in an anoxic marine sediment." *FEMS Microbiology Ecology* 38.1, pp. 33–41.
Hoekstra, P (1967). "Moisture movement to a freezing front." *SYMP ON GEOCHEM, PRECIPITATION, EVAPORATION, SOIL MOISTURE, HYDOM, PROC GEN ASSEMBLY OF BERN*, pp. 411–417.
Hoekstra, Pieter (1966). "Moisture movement in soils under temperature gradients with the coldside temperature below freezing." *Water Resources Research* 2.2, pp. 241–250.
Holmes, RM, James W McClelland, Bruce J Peterson, Suzanne E Tank, Ekaterina Bulygina, Timothy I Eglinton, Viacheslav V Gordeev, Tatiana Y Gurtovaya, Peter A Raymond, Daniel J Repeta, et al. (2012). "Seasonal and annual fluxes of nutrients and organic matter from large rivers to the Arctic Ocean and surrounding seas." *Estuaries and Coasts* 35.2, pp. 369–382.
Hu, K, Z Issler, Z Chen, and TA Brent (2013). "Permafrost investigation by well logs, and seismic velocity and repeated shallow temperature surveys, Beaufort-Mackenzie Basin." *Geol. Surv. Can. Open File Rep* 6956, p. 228.
Hugelius, G. et al. (2014). "Estimated stocks of circumpolar permafrost carbon with quantified uncertainty ranges and identified data gaps." *Biogeosciences* 11.23, pp. 6573–6593.
Hunter, JA, KG Neave, HA MacAulay, and GD Hobson (1978). "Interpretation of sub-seabottom permafrost in the Beaufort Sea by seismic methods. Part I-seismic refraction methods." In: *Proceedings of the Third International Conference on Permafrost*. Vol. 1, pp. 514–520.
Hunter, JAM, Alan Stephen Judge, HA MacAulay, RL Good, RM Gagne, and RA Burns (1976). *The occurrence of permafrost and frozen sub-seabottom materials in the southern Beaufort Sea*. Beaufort Sea Project, Department of the Environment.
Hunter, SJ, DS Goldobin, AM Haywood, A Ridgwell, and JG Rees (2013). "Sensitivity of the global submarine hydrate inventory to scenarios of future climate change." *Earth and Planetary Science Letters* 367, pp. 105–115.
Hutter, Kolumban and Brian Straughan (1999). "Models for convection in thawing porous media in support for the subsea permafrost equations." *Journal of Geophysical Research: Solid Earth* 104.B12, pp. 29249–29260.
Istomin, VA (2006). "Gas hydrates in the permafrost zone." *Gas. Ind. Rus.* 4, pp. 16–27.

Ivanov, MS (1969). "Modern prennially frozen rocks in the coastal zone of the Yana Delta." *The problems of the Yakutia Geography* 5, pp. 138–148.

Iversen, Niels and Bo Barker Jorgensen (1985). "Anaerobic methane oxidation rates at the sulfate-methane transition in marine sediments from Kattegat and Skagerrak (Denmark) 1." *Limnology and Oceanography* 30.5, pp. 944–955.

Jackson, Bradley E and Michael J McInerney (2002). "Anaerobic microbial metabolism can proceed close to thermodynamic limits." *Nature* 415.6870, p. 454.

Jakobsson, Martin, Larry Mayer, Bernard Coakley, Julian A Dowdeswell, Steve Forbes, Boris Fridman, Hanne Hodnesdal, Riko Noormets, Richard Pedersen, Michele Rebesco, et al. (2012). "The international bathymetric chart of the Arctic Ocean (IBCAO) version 3.0." *Geophysical Research Letters* 39.12.

James, Rachael H, Philippe Bousquet, Ingeborg Bussmann, Matthias Haeckel, Rolf Kipfer, Ira Leifer, Helge Niemann, Ilia Ostrovsky, Jacek Piskozub, Gregor Rehder, et al. (2016). "Effects of climate change on methane emissions from seafloor sediments in the Arctic Ocean: A review." *Limnology and oceanography* 61.S1, S283–S299.

Janout, Markus, Jens Hölemann, Bennet Juhls, Thomas Krumpen, Benjamin Rabe, Dorothea Bauch, Carolyn Wegner, Heidemarie Kassens, and Leonid Timokhov (2016). "Episodic warming of near-bottom waters under the Arctic sea ice on the central Laptev Sea shelf." *Geophysical Research Letters* 43.1, pp. 264–272.

Jeffries, MO and J Richter-Menge (2012). "State of the climate in 2011: The Arctic." *Bull. Am. Meteorol. Soc* 93, S127–S148.

Jin, Qusheng and Craig M Bethke (2005). "Predicting the rate of microbial respiration in geochemical environments." *Geochimica et Cosmochimica Acta* 69.5, pp. 1133–1143.

Jørgensen, Bo Barker and Sabine Kasten (2006). "Sulfur cycling and methane oxidation." In: *Marine geochemistry*. Springer, pp. 271–309.

Jørgensen, Bo Barker, Andreas Weber, and Jakob Zopfi (2001). "Sulfate reduction and anaerobic methane oxidation in Black Sea sediments." *Deep Sea Research Part I: Oceanographic Research Papers* 48.9, pp. 2097–2120.

Jorgenson, MT and J Brown (2005). "Classification of the Alaskan Beaufort Sea Coast and estimation of carbon and sediment inputs from coastal erosion." *Geo-Marine Letters* 25.2-3, pp. 69–80.

Jourabchi, Parisa, Philippe Van Cappellen, and Pierre Regnier (2005). "Quantitative interpretation of pH distributions in aquatic sediments: A reaction-transport modeling approach." *American Journal of Science* 305.9, pp. 919–956.

Judd, Alan and Martin Hovland (2009). *Seabed fluid flow: the impact on geology, biology and the marine environment*. Cambridge University Press.

Kaiser, Sonja, Mathias Göckede, Karel Castro-Morales, Christian Knoblauch, Altug Ekici, Thomas Kleinen, Sebastian Zubrzycki, Torsten Sachs, and Christian Wille (2017). "Process-based modelling of the methane balance in periglacial landscapes (JSBACH-methane)." *Geoscientific Model Development* 10, pp. 333–358.

Kang, Mingu and J. S. Lee (2015). "Evaluation of the freezing-thawing effect in sand-silt mixtures using elastic waves and electrical resistivity." *Cold Regions Science and Technology* 113, pp. 1–11.

Karl, David M, Lucas Beversdorf, Karin M Björkman, Matthew J Church, Asuncion Martinez, and Edward F Delong (2008). "Aerobic production of methane in the sea." *Nature Geoscience* 1.7, p. 473.

Kelley, J.J. and D.F. Weaver (1969). "Physical Processes at the Surface of the Arctic Tundra." *ARCTIC* 22.4.

Kessler, John D, David L Valentine, Molly C Redmond, Mengran Du, Eric W Chan, Stephanie D Mendes, Erik W Quiroz, Christie J Villanueva, Stephani S Shusta, Lindsay M Werra, et al. (2011). "A persistent oxygen anomaly reveals the fate of spilled methane in the deep Gulf of Mexico." *Science* 331.6015, pp. 312–315.

Khain, VE, ID Polyakova, and NI Filatova (2009). "Tectonics and petroleum potential of the East Arctic province." *Russian Geology and Geophysics* 50.4, pp. 334–345.

Kholodov, Alexander L., Nikolai N. Romanovskii, Anatoli V. Gavrilov, Genady S. Tipenko, Sergei S. Drachev, Hans W. Hubberten, and Heidemarie Kassens (1999). "Modeling of the offshore permafrost thickness on the Laptev Sea shelf." *Polarforschung* 69.1-3, pp. 221–227.

Khutorskoy, MD and LV Podgornyh (2010). "Geothermics of the Arctic basin—The problems and solutions. Geothermal field and the Arctic shelf oil and gas bearing." *Monit. Sci. Technol* 1.1, pp. 6–26.

Kiene, Ronald P (1991). "Production and consumption of methane in aquatic systems." *Microbial Production and Consumption of Greenhouse Gases: Methane, Nitrogen Oxides, and Halomethanes*.

Kiene, Ronald P, Laura J Linn, and Jody A Bruton (2000). "New and important roles for DMSP in marine microbial communities." *Journal of Sea Research* 43.3-4, pp. 209–224.

Kim, B, G Grikurov, and V Soloviev (1999). "High resolution seismic studies in the Laptev Sea shelf: first results and future needs." In: *Land-Ocean Systems in the Siberian Arctic*. Springer, pp. 683–692.

Kirschke, Stefanie, Philippe Bousquet, Philippe Ciais, Marielle Saunois, Josep G Canadell, Edward J Dlugokencky, Peter Bergamaschi, Daniel Bergmann, Donald R Blake, Lori Bruhwiler, et al. (2013). "Three decades of global methane sources and sinks." *Nature geoscience* 6.10, p. 813.

Knab, NJ, Barry Andrew Cragg, ERC Hornibrook, L Holmkvist, C Borowski, RJ Parkes, and Bo Barker Jørgensen (2008). "Regulation of anaerobic methane oxidation in sediments of the Black Sea." *Biogeosciences Discussions* 5.3, pp. 2305–2341.

Knittel, Katrin and Antje Boetius (2009). "Anaerobic oxidation of methane: progress with an unknown process." *Annual review of microbiology* 63, pp. 311–334.

Komada, Tomoko, David J. Burdige, Huan Lei Li, Cédric Magen, Jeffrey P. Chanton, and Abraham K. Cada (2016). "Organic matter cycling across the sulfate-methane transition zone of the Santa Barbara Basin, California Borderland." *Geochimica et Cosmochimica Acta* 176, pp. 259–278.

Kort, EA, SC Wofsy, BC Daube, M Diao, JW Elkins, RS Gao, EJ Hintsa, DF Hurst, R Jimenez, FL Moore, et al. (2012). "Atmospheric observations of Arctic Ocean methane emissions up to 82 north." *Nature Geoscience* 5.5, p. 318.

Kretschmer, Kerstin, Arne Biastoch, Lars Rüpke, and Ewa Burwicz (2015). "Modeling the fate of methane hydrates under global warming." *Global Biogeochemical Cycles* 29.5, pp. 610–625.

Krüger, Martin, Anke Meyerdierks, Frank Oliver Glöckner, Rudolf Amann, Friedrich Widdel, Michael Kube, Richard Reinhardt, Jörg Kahnt, Reinhard Böcher, Rudolf K Thauer, et al. (2003). "A conspicuous nickel protein in microbial mats that oxidize methane anaerobically." *Nature* 426.6968, p. 878.

Kvenvolden, Keith A (1988). "Methane hydrate—a major reservoir of carbon in the shallow geosphere?" *Chemical geology* 71.1-3, pp. 41–51.

Kwon, Tae Hyuk, Gye Chun Cho, and J. Carlos Santamarina (2008). "Gas hydrate dissociation in sediments: Pressure-temperature evolution." *Geochemistry, Geophysics, Geosystems* 9.3, n/a–n/a.

Lachenbruch, Arthur H (1962). *Mechanics of thermal contraction cracks and ice-wedge polygons in permafrost*. Vol. 70. Geological Society of America.

Lachenbruch, Arthur H., J. H. Sass, B. V. Marshall, and T. H. Moses (1982). "Permafrost, heat flow, and the geothermal regime at Prudhoe Bay, Alaska." *Journal of Geophysical Research* 87.B11, pp. 9301–9316.

Lammers, Richard B, Alexander I Shiklomanov, Charles J Vörösmarty, Balázs M Fekete, and Bruce J Peterson (2001). "Assessment of contemporary Arctic river runoff based on observational discharge records." *Journal of Geophysical Research: Atmospheres* 106.D4, pp. 3321–3334.

Landau, H Go (1950). "Heat conduction in a melting solid." *Quarterly of Applied Mathematics* 8.1, pp. 81–94.

Lang, Kristina, Jörg Schuldes, Andreas Klingl, Anja Poehlein, Rolf Daniel, and Andreas Brune (2015). "New mode of energy metabolism

in the seventh order of methanogens as revealed by comparative genome analysis of "Candidatus Methanoplasma termitum"." *Appl. Environ. Microbiol.* 81.4, pp. 1338–1352.

Lantuit, Hugues, David Atkinson, Pier Paul Overduin, Mikhail Grigoriev, Volker Rachold, Guido Grosse, and Hans-Wolfgang Hubberten (2011). "Coastal erosion dynamics on the permafrost-dominated Bykovsky Peninsula, north Siberia, 1951–2006." *Polar Research* 30.1, p. 7341.

LaRowe, DE, Andy W Dale, and P Regnier (2008). "A thermodynamic analysis of the anaerobic oxidation of methane in marine sediments." *Geobiology* 6.5, pp. 436–449.

LaRowe, Douglas E, Ewa Burwicz, Sandra Arndt, Andrew W Dale, and Jan P Amend (2017). "Temperature and volume of global marine sediments." *Geology* 45.3, pp. 275–278.

Le Quéré, Corinne, Robbie M Andrew, Pierre Friedlingstein, Stephen Sitch, Judith Hauck, Julia Pongratz, Penelope A Pickers, Jan Ivar Korsbakken, Glen P Peters, Josep G Canadell, et al. (2018). "Global carbon budget 2018." *Earth System Science Data (Online)* 10.4.

Leifer, Ira, Denis Chernykh, Natalia Shakhova, and Igor Semiletov (2017). "Sonar gas flux estimation by bubble insonification: Application to methane bubble flux from seep areas in the outer Laptev Sea." *Cryosphere* 11.3, pp. 1333–1350.

Leighton, T. G. (2007). "Theory for acoustic propagation in marine sediment containing gas bubbles which may pulsate in a non-stationary nonlinear manner." *Geophysical Research Letters* 34.17, p. L17607.

Lessner, Daniel J (2009). "Methanogenesis Biochemistry." *e LS*.

Levitan, Mikhail Arkadevich and Yu A Lavrushin (2009). *Sedimentation history in the Arctic Ocean and Subarctic Seas for the last 130 kyr*. Vol. 118. Springer Science & Business Media.

Lewellen, Robert I (1974). "Offshore permafrost of Beaufort Sea, Alaska." *The Coast and Shelf of the Beaufort Sea. JC Reed and JE Sater (Eds.), Arctic Inst. North America, Arlington, Virginia*, pp. 417–461.

Linke, Peter, Klaus Wallmann, Erwin Suess, Christian Hensen, and Gregor Rehder (2005). "In situ benthic fluxes from an intermittently active mud volcano at the Costa Rica convergent margin." *Earth and Planetary Science Letters* 235.1-2, pp. 79–95.

Liski, Jari, Taru Palosuo, Mikko Peltoniemi, and Risto Sievänen (2005). "Carbon and decomposition model Yasso for forest soils." *Ecological Modelling* 189.1-2, pp. 168–182.

Lorenson, Thomas D, Jens Greinert, and Richard B Coffin (2016). "Dissolved methane in the Beaufort Sea and the Arctic Ocean, 1992–2009; sources and atmospheric flux." *Limnology and Oceanography* 61.S1, S300–S323.

Lösekann, Tina, Katrin Knittel, Thierry Nadalig, Bernhard Fuchs, Helge Niemann, Antje Boetius, and Rudolf Amann (2007). "Diversity

and abundance of aerobic and anaerobic methane oxidizers at the Haakon Mosby Mud Volcano, Barents Sea." *Applied and Environmental Microbiology* 73.10, pp. 3348–3362.

Lovley, Derek R and Steve Goodwin (1988). "Hydrogen concentrations as an indicator of the predominant terminal electron-accepting reactions in aquatic sediments." *Geochimica et cosmochimica acta* 52.12, pp. 2993–3003.

Luff, Roger, Jens Greinert, Klaus Wallmann, Ingo Klaucke, and Erwin Suess (2005). "Simulation of long-term feedbacks from authigenic carbonate crust formation at cold vent sites." *Chemical Geology* 216.1-2, pp. 157–174.

Luff, Roger and Klaus Wallmann (2003). "Fluid flow, methane fluxes, carbonate precipitation and biogeochemical turnover in gas hydrate-bearing sediments at Hydrate Ridge, Cascadia Margin: numerical modeling and mass balances." *Geochimica et Cosmochimica Acta* 67.18, pp. 3403–3421.

Lysak, SV (1988). *Geotermicheskii potok kontinental'nykh riftovykh zon (Geothermal Flux in Continental Rift Zones)*. Nauka.

MacAulay, HA, AS Judge, JA Hunter, VS Allen, RM Gagné, M Burgess, KG Neave, and J Collyer (1977). "A study of sub-seabottom permafrost in the Beaufort Sea - Mackenzie Delta by hydraulic drilling method." *Geological Survey of Canada Open file 472*.

MacDonald, Gordon J. (1990). "Role of methane clathrates in past and future climates." *Climatic Change* 16.3, pp. 247–281.

Mackay, J Ross (1972). "Offshore permafrost and ground ice, southern Beaufort Sea, Canada." *Canadian Journal of Earth Sciences* 9.11, pp. 1550–1561.

Maher, Kate, Carl I Steefel, Donald J DePaolo, and Brian E Viani (2006). "The mineral dissolution rate conundrum: Insights from reactive transport modeling of U isotopes and pore fluid chemistry in marine sediments." *Geochimica et Cosmochimica Acta* 70.2, pp. 337–363.

Maini, Brij B. and P. R. Bishnoi (1981). "Experimental investigation of hydrate formation behaviour of a natural gas bubble in a simulated deep sea environment." *Chemical Engineering Science* 36.1, pp. 183–189.

Makogon, Y. F., S. A. Holditch, and T. Y. Makogon (2007). "Natural gas-hydrates - A potential energy source for the 21st Century." *Journal of Petroleum Science and Engineering* 56.1-3, pp. 14–31.

Malakhova, Valentina V (2016). "On the thermal influence of thermokarst lakes on the subsea permafrost evolution." In: *22nd International Symposium on Atmospheric and Ocean Optics: Atmospheric Physics*. Vol. 10035. International Society for Optics and Photonics, 100355U.

Malakhova, Valentina V and Alexey V Eliseev (2017). "The role of heat transfer time scale in the evolution of the subsea permafrost

and associated methane hydrates stability zone during glacial cycles." *Global and Planetary Change* 157, pp. 18–25.

Marsland, Simon J, Helmuth Haak, Johann H Jungclaus, Mojib Latif, and Frank Röske (2003). "The Max-Planck-Institute global ocean/sea ice model with orthogonal curvilinear coordinates." *Ocean modelling* 5.2, pp. 91–127.

Martens, Christopher S, Daniel B Albert, and Marc J Alperin (1998). "Biogeochemical processes controlling methane in gassy coastal sediments—Part 1. A model coupling organic matter flux to gas production, oxidation and transport." *Continental Shelf Research* 18.14-15, pp. 1741–1770.

Maslowski, W, B Newton, Peter Schlosser, A Semtner, and D Martinson (2000). "Modeling recent climate variability in the Arctic Ocean." *Geophysical Research Letters* 27.22, pp. 3743–3746.

Masson-Delmotte, Valérie, M Kageyama, P Braconnot, S Charbit, G Krinner, C Ritz, E Guilyardi, Jean Jouzel, A Abe-Ouchi, M Crucifix, et al. (2006). "Past and future polar amplification of climate change: climate model intercomparisons and ice-core constraints." *Climate Dynamics* 26.5, pp. 513–529.

Matsuoka, Norikazu, Hanne H. Christiansen, and Tatsuya Watanabe (2018). "Ice-wedge polygon dynamics in Svalbard: Lessons from a decade of automated multi-sensor monitoring." *Permafrost and Periglacial Processes* 29.3, pp. 210–227.

May, Gary S and Costas J Spanos (2006). *Fundamentals of semiconductor manufacturing and process control*. Wiley Online Library.

McCalley, Carmody K, Ben J Woodcroft, Suzanne B Hodgkins, Richard A Wehr, Eun-Hae Kim, Rhiannon Mondav, Patrick M Crill, Jeffrey P Chanton, Virginia I Rich, Gene W Tyson, et al. (2014). "Methane dynamics regulated by microbial community response to permafrost thaw." *Nature* 514.7523, p. 478.

McClelland, James W, RM Holmes, Kenneth H Dunton, and RW Macdonald (2012). "The Arctic ocean estuary." *Estuaries and Coasts* 35.2, pp. 353–368.

McClelland, James W, RM Holmes, Bruce J Peterson, Peter A Raymond, RG Striegl, Alexander V Zhulidov, Sergey A Zimov, Nikita Zimov, Suzanne E Tank, Robert GM Spencer, et al. (2016). "Particulate organic carbon and nitrogen export from major Arctic rivers." *Global Biogeochemical Cycles* 30.5, pp. 629–643.

McGinnis, Daniel Frank, Jens Greinert, Yu Artemov, SE Beaubien, and ANDA Wüest (2006). "Fate of rising methane bubbles in stratified waters: How much methane reaches the atmosphere?" *Journal of Geophysical Research: Oceans* 111.C9.

McGlynn, Shawn E, Grayson L Chadwick, Christopher P Kempes, and Victoria J Orphan (2015). "Single cell activity reveals direct electron transfer in methanotrophic consortia." *Nature* 526.7574, p. 531.

McGuire, A David, Leif G Anderson, Torben R Christensen, Scott Dallimore, Laodong Guo, Daniel J Hayes, Martin Heimann, Thomas D Lorenson, Robie W Macdonald, and Nigel Roulet (2009). "Sensitivity of the carbon cycle in the Arctic to climate change." *Ecological Monographs* 79.4, pp. 523–555.

McGuire, AD, TR Christensen, DJ Hayes, Arnaud Heroult, E Euskirchen, Y Yi, John S Kimball, C Koven, P Lafleur, PA Miller, et al. (2012). "An assessment of the carbon balance of Arctic tundra: comparisons among observations, process models, and atmospheric inversions." *Biogeosciences Discussions* 9, p. 4543.

Meile, Christof and Philippe Van Cappellen (2005). "Particle age distributions and O2 exposure times: Timescales in bioturbated sediments." *Global biogeochemical cycles* 19.3.

Meister, Patrick, Bo Liu, Timothy G Ferdelman, Bo Barker Jørgensen, and Arzhang Khalili (2013). "Control of sulphate and methane distributions in marine sediments by organic matter reactivity." *Geochimica et Cosmochimica Acta* 104, pp. 183–193.

Mergelov, NS and VO Targulian (2011). "Accumulation of organic matter in the mineral layers of permafrost-affected soils of coastal lowlands in East Siberia." *Eurasian Soil Science* 44.3, pp. 249–260.

Mestdagh, Thomas, Jeffrey Poort, and Marc De Batist (2017). "The sensitivity of gas hydrate reservoirs to climate change: Perspectives from a new combined model for permafrost-related and marine settings." *Earth-science reviews* 169, pp. 104–131.

Middelburg, Jack J, Karline Soetaert, and Peter MJ Herman (1997). "Empirical relationships for use in global diagenetic models." *Deep Sea Research Part I: Oceanographic Research Papers* 44.2, pp. 327–344.

Milkov, Alexei V, George E Claypool, Young-Joo Lee, Wenyue Xu, Gerald R Dickens, and Walter S Borowski (2003). "In situ methane concentrations at Hydrate Ridge, offshore Oregon: New constraints on the global gas hydrate inventory from an active margin." *Geology* 31.10, pp. 833–836.

Millero, FJ (1978). "Freezing point of sea water." *eighth report of the Joint Panel of Oceanographic Tables and Standards, appendix* 6, pp. 29–31.

Millero, Frank J (1995). "Thermodynamics of the carbon dioxide system in the oceans." *Geochimica et Cosmochimica Acta* 59.4, pp. 661–677.

Milucka, Jana, Timothy G Ferdelman, Lubos Polerecky, Daniela Franzke, Gunter Wegener, Markus Schmid, Ingo Lieberwirth, Michael Wagner, Friedrich Widdel, and Marcel MM Kuypers (2012). "Zero-valent sulphur is a key intermediate in marine methane oxidation." *Nature* 491.7425, p. 541.

Mitchell, S. L. and T. G. Myers (2010). "Improving the accuracy of heat balance integral methods applied to thermal problems with time

dependent boundary conditions." *International Journal of Heat and Mass Transfer* 53.17-18, pp. 3540–3551.

Mogollón, José M, Ivan L'Heureux, Andrew W Dale, and Pierre Regnier (2009). "Methane gas-phase dynamics in marine sediments: A model study." *American Journal of Science* 309.3, pp. 189–220.

Molochushkin, EN (1973). "The effect of thermal abrasion on the temperature of the permafrost in the coastal zone of the Laptev Sea." In: *Proceedings of the Second International Conference on Permafrost, Takutsk, USSR*, pp. 90–93.

Montgomery, Douglas C (2007). *Introduction to statistical quality control*. John Wiley & Sons.

Mucci, Alfonso (1983). "The solubility of calcite and aragonite in seawater at various salinities, temperatures, and one atmosphere total pressure." *American Journal of Science* 283.7, pp. 780–799.

Myers, T. G., S. L. Mitchell, G. Muchatibaya, and M. Y. Myers (2007). "A cubic heat balance integral method for one-dimensional melting of a finite thickness layer." *International Journal of Heat and Mass Transfer* 50.25-26, pp. 5305–5317.

Myhre, C Lund, Benedicte Ferré, Stephen Matthew Platt, Anna Silyakova, Ove Hermansen, Grant Allen, Ignacio Pisso, N Schmidbauer, Andreas Stohl, J Pitt, et al. (2016). "Extensive release of methane from Arctic seabed west of Svalbard during summer 2014 does not influence the atmosphere." *Geophysical Research Letters* 43.9, pp. 4624–4631.

Myhre, G, D Shindell, FM Bréon, W Collins, J Fuglestvedt, J Huang, D Koch, JF Lamarque, D Lee, B Mendoza, et al. (2013). "Anthropogenic and natural radiative forcing." In: *Climate Change 2013-The Physical Science Basis: Contribution of Working Group I to the Fifth Assessment Report of the Intergovernmental Panel on Climate Change*. Cambridge University Press, pp. 659–740.

Naudts, Lieven, Jens Greinert, Yuriy Artemov, Peter Staelens, Jeffrey Poort, Pieter Van Rensbergen, and Marc De Batist (2006). "Geological and morphological setting of 2778 methane seeps in the Dnepr paleo-delta, northwestern Black Sea." *Marine Geology* 227.3-4, pp. 177–199.

Nauhaus, Katja, Melanie Albrecht, Marcus Elvert, Antje Boetius, and Friedrich Widdel (2007). "In vitro cell growth of marine archaeal-bacterial consortia during anaerobic oxidation of methane with sulfate." *Environmental Microbiology* 9.1, pp. 187–196.

Nicolsky, D. J., V. E. Romanovsky, N. N. Romanovskii, A. L. Kholodov, N. E. Shakhova, and I. P. Semiletov (2012). "Modeling sub-sea permafrost in the East Siberian Arctic Shelf: The Laptev Sea region." *Journal of Geophysical Research: Earth Surface* 117.3, n/a–n/a.

Nicolsky, D and N Shakhova (2010). "Modeling sub-sea permafrost in the East Siberian Arctic Shelf: the Dmitry Laptev Strait." *Environmental Research Letters* 5.1, p. 015006.

Niemann, H, J Duarte, Christian Hensen, E Omoregie, VH Magalhaes, Markus Elvert, LM Pinheiro, A Kopf, and Antje Boetius (2006a). "Microbial methane turnover at mud volcanoes of the Gulf of Cadiz." *Geochimica et Cosmochimica Acta* 70.21, pp. 5336–5355.

Niemann, Helge, Tina Lösekann, Dirk De Beer, Marcus Elvert, Thierry Nadalig, Katrin Knittel, Rudolf Amann, Eberhard J Sauter, Michael Schlüter, Michael Klages, et al. (2006b). "Novel microbial communities of the Haakon Mosby mud volcano and their role as a methane sink." *Nature* 443.7113, p. 854.

Niemann, H et al. (2009). "Biogeochemistry of a low-activity cold seep in the Larsen B area, western Weddell Sea, Antarctica." *Biogeosciences* 6.11, pp. 2383–2395.

Niu, Gou Yue and Zong Liang Yang (2006). "Effects of frozen soil on snowmelt runoff and soil water storage at a continental scale." *Journal of Hydrometeorology* 7.5, pp. 937–952.

Nixon, JF (1986). "Thermal simulation of subsea saline permafrost." *Canadian Journal of Earth Sciences* 23.12, pp. 2039–2046.

Norði, Katrin à, Bo Thamdrup, and Carsten J Schubert (2013). "Anaerobic oxidation of methane in an iron-rich Danish freshwater lake sediment." *Limnology and oceanography* 58.2, pp. 546–554.

Notz, Dirk, Miles G. McPhee, M. Grae Worster, Gray A. Maykut, K. Heinke Schlünzen, and Hajo Eicken (2003). "Impact of underwater-ice evolution on Arctic summer sea ice." *Journal of Geophysical Research C: Oceans* 108.7, pp. 16–1.

O'Connor, Fiona M, O Boucher, N Gedney, CD Jones, GA Folberth, R Coppell, P Friedlingstein, WJ Collins, J Chappellaz, J Ridley, et al. (2010). "Possible role of wetlands, permafrost, and methane hydrates in the methane cycle under future climate change: A review." *Reviews of Geophysics* 48.4.

Op den Camp, Huub J.M., Tajul Islam, Matthew B. Stott, Harry R. Harhangi, Alexander Hynes, Stefan Schouten, Mike S.M. Jetten, Nils Kåre Birkeland, Arjan Pol, and Peter F. Dunfield (2009). *Environmental, genomic and taxonomic perspectives on methanotrophic Verrucomicrobia*.

Orphan, Victoria J, Christopher H House, Kai-Uwe Hinrichs, Kevin D McKeegan, and Edward F DeLong (2001). "Methane-consuming archaea revealed by directly coupled isotopic and phylogenetic analysis." *science* 293.5529, pp. 484–487.

Orr, James C, Victoria J Fabry, Olivier Aumont, Laurent Bopp, Scott C Doney, Richard A Feely, Anand Gnanadesikan, Nicolas Gruber, Akio Ishida, Fortunat Joos, et al. (2005). "Anthropogenic ocean acidification over the twenty-first century and its impact on calcifying organisms." *Nature* 437.7059, p. 681.

Osterkamp, TE (2001). "Sub-sea permafrost." *Encyclopedia of ocean sciences* 5, pp. 2902–2912.

Osterkamp, TE, GC Baker, WD Harrison, and T Matava (1989). "Characteristics of the active layer and shallow subsea permafrost." *Journal of Geophysical Research: Oceans* 94.C11, pp. 16227–16236.

Osterkamp, TE and WD Harrison (1982). "Temperature measurements in subsea permafrost off the coast of Alaska." In: *4th Canadian Permafrost Conference*, pp. 238–248.

Osterkamp, Thomas E and WD Harrison (1976). "Subsea permafrost at Prudhoe Bay, Alaska: Drilling report and data analysis."

Overduin, Paul, Sebastian Wetterich, Frank Günther, Mikhail N Grigoriev, Guido Grosse, Lutz Schirrmeister, Hans-Wolfgang Hubberten, and Aleksandr S Makarov (2016). "Coastal dynamics and submarine permafrost in shallow water of the central Laptev Sea, East Siberia." *Cryosphere* 10, pp. 1449–1462.

Overduin, Pier P, Christian Haberland, Trond Ryberg, Fabian Kneier, Tim Jacobi, Mikhail N Grigoriev, and Matthias Ohrnberger (2015a). "Submarine permafrost depth from ambient seismic noise." *Geophysical Research Letters* 42.18, pp. 7581–7588.

Overduin, Pier Paul, Hans-W Hubberten, Volker Rachold, Nikolai Romanovskii, MN Grigoriev, and Maria Kasymskaya (2007). "The evolution and degradation of coastal and offshore permafrost in the Laptev and East Siberian Seas during the last climatic cycle." *Coastline changes: interrelation of climate and geological processes* 426, pp. 97–111.

Overduin, Pier Paul, Susanne Liebner, Christian Knoblauch, Frank Günther, Sebastian Wetterich, Lutz Schirrmeister, Hans-Wolfgang Hubberten, and Mikhail N Grigoriev (2015b). "Methane oxidation following submarine permafrost degradation: Measurements from a central Laptev Sea shelf borehole." *Journal of Geophysical Research: Biogeosciences* 120.5, pp. 965–978.

Overduin, Pier Paul, Volker Rachold, and M. N. Grigoriev (2008). "The State of Subsea Permafrost in the Western Laptev Nearshore Zone." In: *Proceedings of the 9th International Conference on Permafrost*. Fairbanks, Alaska.

Overduin, Pier Paul, Sebastian Westermann, Kenji Yoshikawa, Thomas Haberlau, Vladimir Romanovsky, and Sebastian Wetterich (2012). "Geoelectric observations of the degradation of nearshore submarine permafrost at Barrow (Alaskan Beaufort Sea)." *Journal of Geophysical Research: Earth Surface* 117.F2.

Overland, James E, Kevin R Wood, and Muyin Wang (2011). "Warm Arctic—cold continents: climate impacts of the newly open Arctic Sea." *Polar Research* 30.1, p. 15787.

Padilla, Cory C, Laura A Bristow, Neha Sarode, Emilio Garcia-Robledo, Eddy Gómez Ramírez, Catherine R Benson, Annie Bourbonnais, Mark A Altabet, Peter R Girguis, Bo Thamdrup, et al. (2016). "NC10 bacteria in marine oxygen minimum zones." *The ISME journal* 10.8, p. 2067.

Panganiban, ATjnr, TE Patt, W Hart, and RS Hanson (1979). "Oxidation of methane in the absence of oxygen in lake water samples." *Appl. Environ. Microbiol.* 37.2, pp. 303–309.

Parkes, R. John, Gordon Webster, Barry A. Cragg, Andrew J. Weightman, Carole J. Newberry, Timothy G. Ferdelman, Jens Kallmeyer, Bo B. Jørgensen, Ivano W. Aiello, and John C. Fry (2005). "Deep sub-seafloor prokaryotes stimulated at interfaces over geological time." *Nature* 436.7049, pp. 390–394.

Pauss, André, Gérald Andre, Michel Perrier, and Serge R Guiot (1990). "Liquid-to-gas mass transfer in anaerobic processes: inevitable transfer limitations of methane and hydrogen in the biomethanation process." *Appl. Environ. Microbiol.* 56.6, pp. 1636–1644.

Pianosi, Francesca, Keith Beven, Jim Freer, Jim W Hall, Jonathan Rougier, David B Stephenson, and Thorsten Wagener (2016). "Sensitivity analysis of environmental models: A systematic review with practical workflow." *Environmental Modelling & Software* 79, pp. 214–232.

Piechura, Jan and Waldemar Walczowski (1995). "The Arctic Front: structure and dynamics." *Oceanologia* 37.1, pp. 47–73.

Pierre, Catherine, Marie Madeleine Blanc-Valleron, Jérôme Demange, Omar Boudouma, Jean Paul Foucher, Thomas Pape, Tobias Himmler, Noemi Fekete, and Volkhard Spiess (2012). "Authigenic carbonates from active methane seeps offshore southwest Africa." *Geo-Marine Letters* 32.5-6, pp. 501–513.

Piker, Levent, Rolf Schmaljohann, and Johannes F Imhoff (1998). "Dissimilatory sulfate reduction and methane production in Gotland Deep sediments (Baltic Sea) during a transition period from oxic to anoxic bottom water (1993-1996)." *Aquatic Microbial Ecology* 14.2, pp. 183–193.

Piñero, E., M. Marquardt, C. Hensen, M. Haeckel, and K. Wallmann (2013). "Estimation of the global inventory of methane hydrates in marine sediments using transfer functions." *Biogeosciences* 10.2, pp. 959–975.

Ping, Chien-Lu, Gary J Michaelson, Laodong Guo, M Torre Jorgenson, Mikhail Kanevskiy, Yuri Shur, Fugen Dou, and Jingjing Liang (2011). "Soil carbon and material fluxes across the eroding Alaska Beaufort Sea coastline." *Journal of Geophysical Research: Biogeosciences* 116.G2.

Pithan, Felix and Thorsten Mauritsen (2014). "Arctic amplification dominated by temperature feedbacks in contemporary climate models." *Nature Geoscience* 7.3, p. 181.

Pollard, Wayne, Chris Omelon, Dale Andersen, and Chris McKay (1999). "Perennial spring occurrence in the Expedition Fiord area of western Axel Heiberg Island, Canadian High Arctic." *Canadian Journal of Earth Sciences* 36.1, pp. 105–120.

Polyakov, Igor V, Andrey V Pnyushkov, Matthew B Alkire, Igor M Ashik, Till M Baumann, Eddy C Carmack, Ilona Goszczko, John Guthrie, Vladimir V Ivanov, Torsten Kanzow, et al. (2017). "Greater role for Atlantic inflows on sea-ice loss in the Eurasian Basin of the Arctic Ocean." *Science* 356.6335, pp. 285–291.

Ponomarev, VM (1940). "On the history of the Kozhevnikov Bay region in the Quaternary period." *Soviet Geology* 11.

Portnov, Alexey, Jurgen Mienert, and Pavel Serov (2014). "Modeling the evolution of climate-sensitive Arctic subsea permafrost in regions of extensive gas expulsion at the West Yamal shelf." *Journal of geophysical research: Biogeosciences* 119.11, pp. 2082–2094.

Portnov, Alexey, Andrew J Smith, Jürgen Mienert, Georgy Cherkashov, Pavel Rekant, Peter Semenov, Pavel Serov, and Boris Vanshtein (2013). "Offshore permafrost decay and massive seabed methane escape in water depths> 20 m at the South Kara Sea shelf." *Geophysical Research Letters* 40.15, pp. 3962–3967.

Post, Vincent E.A., Jacobus Groen, Henk Kooi, Mark Person, Shemin Ge, and W. Mike Edmunds (2013). *Offshore fresh groundwater reserves as a global phenomenon*.

Prasad, Pinnelli S.R. and Burla Sai Kiran (2019). "Self-preservation and Stability of Methane Hydrates in the Presence of NaCl." *Scientific Reports* 9.1.

Pullan, SH and JAM MacAulay (1987). "Permafrost distribution determined from seismic refraction." *Geol. Surv. Can. Misc. Rep. 40*.

Qi, Di, Liqi Chen, Baoshan Chen, Zhongyong Gao, Wenli Zhong, Richard A Feely, Leif G Anderson, Heng Sun, Jianfang Chen, Min Chen, et al. (2017). "Increase in acidifying water in the western Arctic Ocean." *Nature Climate Change* 7.3, p. 195.

Rachold, Volker, Dmitry Yu Bolshiyanov, Mikhail N Grigoriev, Hans-Wolfgang Hubberten, Ralf Junker, Victor V Kunitsky, Franziska Merker, Paul Overduin, and Waldemar Schneider (2007). "Nearshore Arctic subsea permafrost in transition." *Eos, Transactions American Geophysical Union* 88.13, pp. 149–150.

Rachold, Volker, Hajo Eicken, VV Gordeev, Mikhail N Grigoriev, H-W Hubberten, Alexander P Lisitzin, VP Shevchenko, and Lutz Schirrmeister (2004). "Modern terrigenous organic carbon input to the Arctic Ocean." In: *The organic carbon cycle in the Arctic Ocean*. Springer, pp. 33–55.

Rachold, Volker, Mikhail N Grigoriev, Felix E Are, Steve Solomon, Erk Reimnitz, Heidemarie Kassens, and Martin Antonow (2000). "Coastal erosion vs riverine sediment discharge in the Arctic Shelf seas." *International Journal of Earth Sciences* 89.3, pp. 450–460.

Raghoebarsing, Ashna A, Arjan Pol, Katinka T Van de Pas-Schoonen, Alfons JP Smolders, Katharina F Ettwig, W Irene C Rijpstra, Stefan Schouten, Jaap S Sinninghe Damsté, Huub JM Op den Camp, Mike SM Jetten, et al. (2006). "A microbial consortium couples

anaerobic methane oxidation to denitrification." *Nature* 440.7086, p. 918.

Raiswell, Rob, Martyn Tranter, Liane G. Benning, Martin Siegert, Ros De'ath, Philippe Huybrechts, and Tony Payne (2006). "Contributions from glacially derived sediment to the global iron (oxyhydr)oxide cycle: Implications for iron delivery to the oceans." *Geochimica et Cosmochimica Acta* 70.11, pp. 2765–2780.

Raymond, Peter A, James W McClelland, RM Holmes, AV Zhulidov, K Mull, BJ Peterson, Robert G Striegl, GR Aiken, and TY Gurtovaya (2007). "Flux and age of dissolved organic carbon exported to the Arctic Ocean: A carbon isotopic study of the five largest arctic rivers." *Global Biogeochemical Cycles* 21.4.

Razumov, SO, VB Spektor, and MN Grigoriev (2014). "Model of the post-Cenozoic evolution of the cryolithozone of the shelf of the western part of the Laptev Sea." *Oceanology* 54.5, pp. 637–649.

Reagan, Matthew T. and George J. Moridis (2009). "Large-scale simulation of methane hydrate dissociation along the West Spitsbergen Margin." *Geophysical Research Letters* 36.23, p. L23612.

Reagan, Matthew T., George J. Moridis, Scott M. Elliott, and Mathew Maltrud (2011). "Contribution of oceanic gas hydrate dissociation to the formation of Arctic Ocean methane plumes." *Journal of Geophysical Research: Oceans* 116.9, p. C09014.

Reeburgh, William S (1976). "Methane consumption in Cariaco Trench waters and sediments." *Earth and Planetary Science Letters* 28.3, pp. 337–344.

— (2007). "Oceanic methane biogeochemistry." *Chemical reviews* 107.2, pp. 486–513.

Regnier, Pierre, Andy W Dale, S Arndt, DE LaRowe, J Mogollón, and P Van Cappellen (2011). "Quantitative analysis of anaerobic oxidation of methane (AOM) in marine sediments: a modeling perspective." *Earth-Science Reviews* 106.1-2, pp. 105–130.

Regnier, Pierre, JP O'kane, CI Steefel, and Jean-Pierre Vanderborght (2002). "Modeling complex multi-component reactive-transport systems: towards a simulation environment based on the concept of a Knowledge Base." *Applied Mathematical Modelling* 26.9, pp. 913–927.

Regnier, Pierre, Pierre Friedlingstein, Philippe Ciais, Fred T Mackenzie, Nicolas Gruber, Ivan A Janssens, Goulven G Laruelle, Ronny Lauerwald, Sebastiaan Luyssaert, Andreas J Andersson, et al. (2013). "Anthropogenic perturbation of the carbon fluxes from land to ocean." *Nature geoscience* 6.8, p. 597.

Rehder, Gregor, Peter W. Brewer, Edward T. Peltzer, and Gernot Friederich (2002). "Enhanced lifetime of methane bubble streams within the deep ocean." *Geophysical Research Letters* 29.15, pp. 1–4.

Reick, CH, Thomas Raddatz, Victor Brovkin, and Veronika Gayler (2013). "Representation of natural and anthropogenic land cover

change in MPI-ESM." *Journal of Advances in Modeling Earth Systems* 5.3, pp. 459–482.

Reum, Friedemann (2019). "Methane emissions from the East Siberian Arctic Shelf inferred from accurate observations of atmospheric methane mole fractions." PhD thesis. Department of Earth Sciences at Universität Hamburg.

Rhee, TS, AJ Kettle, and MO Andreae (2009). "Methane and nitrous oxide emissions from the ocean: A reassessment using basin-wide observations in the Atlantic." *Journal of Geophysical Research: Atmospheres* 114.D12.

Richtmyer, Robert D and KW Morton (1967). *Difference methods for initial-value problems*. Intersciences Publisher, John Wiley & Sons.

Rickard, David and George W. Luther (2007). *Chemistry of iron sulfides*.

Rittmann, Bruce E and Perry L McCarty (2012). *Environmental biotechnology: principles and applications*. Tata McGraw-Hill Education.

Rittmann, Bruce and Jeanne M VanBriesen (2019). "Microbiological processes in reactive modeling." In: *Reactive Transport in Porous Media*. Walter de Gruyter GmbH, pp. 311–334.

Roberts, Andrew P (2015). "Magnetic mineral diagenesis." *Earth-Science Reviews* 151, pp. 1–47.

Romanovskii, NN and Hans-W Hubberten (2001). "Results of permafrost modelling of the lowlands and shelf of the Laptev Sea region, Russia." *Permafrost and periglacial processes* 12.2, pp. 191–202.

Romanovskii, NN, H-W Hubberten, AV Gavrilov, AA Eliseeva, and GS Tipenko (2005). "Offshore permafrost and gas hydrate stability zone on the shelf of East Siberian Seas." *Geo-marine letters* 25.2-3, pp. 167–182.

Romanovskii, NN, H-W Hubberten, AV Gavrilov, VE Tumskoy, and AL Kholodov (2004). "Permafrost of the east Siberian Arctic shelf and coastal lowlands." *Quaternary Science Reviews* 23.11-13, pp. 1359–1369.

Romanovskii, NN, H-W Hubberten, AV Gavrilov, VE Tumskoy, GS Tipenko, MN Grigoriev, and Ch Siegert (2000). "Thermokarst and land–ocean interactions, Laptev Sea region, Russia." *Permafrost and Periglacial Processes* 11.2, pp. 137–152.

Rooze, Jurjen, Matthias Egger, Iana Tsandev, and Caroline P Slomp (2016). "Iron-dependent anaerobic oxidation of methane in coastal surface sediments: Potential controls and impact." *Limnology and Oceanography* 61.S1, S267–S282.

Ruppel, Carolyn (2011). "Methane hydrates and the future of natural gas." *MITEI natural gas Report, supplementary paper on Methane Hydrates* 4, p. 25.

Ruppel, Carolyn D and John D Kessler (2017). "The interaction of climate change and methane hydrates." *Reviews of Geophysics* 55.1, pp. 126–168.

Sales de Freitas, Felipe (2018). "Deciphering the relationships between reactivity and sources of organic matter in marine sediments: a coupled large-scale model and lipid biomarker analysis." PhD thesis. School on Earth Sciences, University of Bristol.

Sapart, Célia J, Natalia Shakhova, Igor Semiletov, Joachim Jansen, Sönke Szidat, Denis Kosmach, Oleg Dudarev, Carina Van Der Veen, Matthias Egger, Valentine Sergienko, et al. (2017). "The origin of methane in the East Siberian Arctic Shelf unraveled with triple isotope analysis." *Biogeosciences* 14.9, pp. 2283–2292.

Sauer, Simone, Jochen Knies, Aivo Lepland, Shyam Chand, Florian Eichinger, and Carsten J Schubert (2015). "Hydrocarbon sources of cold seeps off the Vesterålen coast, northern Norway." *Chemical Geology* 417, pp. 371–382.

Sauer, Simone, Wei-Li Hong, Jochen Knies, Aivo Lepland, Matthias Forwick, Martin Klug, Florian Eichinger, Soma Baranwal, Antoine Crémière, Shyam Chand, et al. (2016). "Sources and turnover of organic carbon and methane in fjord and shelf sediments off northern Norway." *Geochemistry, Geophysics, Geosystems* 17.10, pp. 4011–4031.

Saunois, Marielle, Philippe Bousquet, Ben Poulter, Anna Peregon, Philippe Ciais, Josep G Canadell, Edward J Dlugokencky, Giuseppe Etiope, David Bastviken, Sander Houweling, et al. (2016). "The global methane budget 2000–2012." *Earth System Science Data* 8.2, pp. 697–751.

Schaefer, Kevin, Hugues Lantuit, Vladimir E Romanovsky, Edward AG Schuur, and Ronald Witt (2014). "The impact of the permafrost carbon feedback on global climate." *Environmental Research Letters* 9.8.

Schink, Bernhard (1997). "Energetics of syntrophic cooperation in methanogenic degradation." *Microbiol. Mol. Biol. Rev.* 61.2, pp. 262–280.

— (2002). "Synergistic interactions in the microbial world." *Antonie Van Leeuwenhoek* 81.1-4, pp. 257–261.

Schirrmeister, Lutz, Duan Froese, Vladimir Tumskoy, Guido Grosse, and Sebastian Wetterich (2013). "Yedoma: Late Pleistocene ice-rich syngenetic permafrost of Beringia." In: *Encyclopedia of Quaternary Science. 2nd edition*. Elsevier, pp. 542–552.

Schirrmeister, Lutz, Guido Grosse, Sebastian Wetterich, Pier Paul Overduin, Jens Strauss, Edward AG Schuur, and Hans-Wolfgang Hubberten (2011). "Fossil organic matter characteristics in permafrost deposits of the northeast Siberian Arctic." *Journal of Geophysical Research: Biogeosciences* 116.G2.

Schneck, Rainer, Christian H. Reick, and Thomas Raddatz (2013). "Land contribution to natural CO<inf>2</inf> variability on time scales of centuries." *Journal of Advances in Modeling Earth Systems* 5.2, pp. 354–365.

Schneider von Deimling, Thomas, Guido Grosse, Jens Strauss, Lutz Schirrmeister, Anne Morgenstern, Sibyll Schaphoff, Malte Meinshausen, and Julia Boike (2015). "Observation-based modelling of permafrost carbon fluxes with accounting for deep carbon deposits and thermokarst activity." *Biogeosciences* 12.11, pp. 3469–3488.

Schneider Von Deimling, Thomas, Thomas Kleinen, Gustaf Hugelius, Christian Knoblauch, Christian Beer, and Victor Brovkin (2018). "Long-Term deglacial permafrost carbon dynamics in MPI-ESM." *Climate of the Past* 14.12, pp. 2011–2036.

Schremb, Markus, Ilia V. Roisman, and Cameron Tropea (2017). "Transient effects in ice nucleation of a water drop impacting onto a cold substrate." *Physical Review E* 95.2, p. 022805.

Schuur, Edward AG, A David McGuire, C Schädel, Guido Grosse, JW Harden, Daniel J Hayes, Gustaf Hugelius, Charles D Koven, Peter Kuhry, David M Lawrence, et al. (2015). "Climate change and the permafrost carbon feedback." *Nature* 520.7546, p. 171.

Screen, James A and Ian Simmonds (2010). "The central role of diminishing sea ice in recent Arctic temperature amplification." *Nature* 464.7293, p. 1334.

Sekretov, Sergej B. (2000). "Petroleum potential of laptev sea basins: Geological, tectonic and geodynamic factors." *Polarforschung* 68.1-3, pp. 179–186.

Sekretov, Sergey B. (1999). "Eurasian Basin - Laptev Sea geodynamic system: Tectonic and structural evolution." *Polarforschung* 69.1-3, pp. 51–54.

Sellmann, PV and EJ Chamberlain (1980). "Permafrost Beneath the Beaufort Sea: Near Prudhoe Bay, Alaska." *Journal of Energy Resources Technology* 102.1, pp. 35–48.

Semenov, Petr, Alexey Portnov, Alexey Krylov, Alexander Egorov, and Boris Vanshtein (2019). "Geochemical evidence for seabed fluid flow linked to the subsea permafrost outer border in the South Kara Sea." *Geochemistry*.

Semiletov, Igor P, Natalia E Shakhova, Valentin I Sergienko, Irina I Pipko, and Oleg V Dudarev (2012). "On carbon transport and fate in the East Siberian Arctic land–shelf–atmosphere system." *Environmental Research Letters* 7.1, p. 015201.

Semiletov, Igor Petrovich, Irina Ivanovna Pipko, Natalia Evgenievna Shakhova, Oleg Victorovich Dudarev, Svetlana Petrovna Pugach, Alexander Nikolaevich Charkin, CP McRoy, D Kosmach, and Örjan Gustafsson (2011). "Carbon transport by the Lena River from its headwaters to the Arctic Ocean, with emphasis on fluvial input of terrestrial particulate organic carbon vs. carbon transport by coastal erosion." *Biogeosciences* 8.9, pp. 2407–2426.

Semiletov, Igor, Irina Pipko, Örjan Gustafsson, Leif G Anderson, Valentin Sergienko, Svetlana Pugach, Oleg Dudarev, Alexander Charkin,

Alexander Gukov, Lisa Bröder, et al. (2016). "Acidification of East Siberian Arctic Shelf waters through addition of freshwater and terrestrial carbon." *Nature Geoscience* 9.5, p. 361.

Semiletov, IP (1999). "Aquatic sources and sinks of CO2 and CH4 in the polar regions." *Journal of the Atmospheric Sciences* 56.2, pp. 286–306.

Shakhova, N, I Semiletov, I Leifer, A Salyuk, P Rekant, and D Kosmach (2010a). "Geochemical and geophysical evidence of methane release over the East Siberian Arctic Shelf." *Journal of Geophysical Research: Oceans* 115.C8.

Shakhova, Natalia Evgenievna, VA Yusupov, AN Salyuk, Denis Alexeevich Kosmach, and Igor Petrovich Semiletov (2009). "Anthropogenic factor and methane emission on the East-Siberian shelf." In: *Doklady Earth Sciences*. Vol. 429. 2. Springer, pp. 1488–1491.

Shakhova, Natalia and Igor Semiletov (2007). "Methane release and coastal environment in the East Siberian Arctic shelf." *Journal of Marine Systems* 66.1-4, pp. 227–243.

Shakhova, Natalia, Igor Semiletov, and Evgeny Chuvilin (2019). "Understanding the Permafrost–Hydrate System and Associated Methane Releases in the East Siberian Arctic Shelf." *Geosciences* 9.6, p. 251.

Shakhova, Natalia, Igor Semiletov, Anatoly Salyuk, Vladimir Yusupov, Denis Kosmach, and Örjan Gustafsson (2010b). "Extensive methane venting to the atmosphere from sediments of the East Siberian Arctic Shelf." *Science* 327.5970, pp. 1246–1250.

Shakhova, Natalia, Igor Semiletov, Ira Leifer, Valentin Sergienko, Anatoly Salyuk, Denis Kosmach, Denis Chernykh, Chris Stubbs, Dmitry Nicolsky, Vladimir Tumskoy, et al. (2014). "Ebullition and storm-induced methane release from the East Siberian Arctic Shelf." *Nature Geoscience* 7.1, p. 64.

Shakhova, Natalia et al. (2015). "The East Siberian Arctic Shelf: Towards further assessment of permafrost-related methane fluxes and role of sea ice." *Philosophical Transactions of the Royal Society A: Mathematical, Physical and Engineering Sciences* 373.2052, p. 20140451.

Shakhova, Natalia, Igor Semiletov, Orjan Gustafsson, Valentin Sergienko, Leopold Lobkovsky, Oleg Dudarev, Vladimir Tumskoy, Michael Grigoriev, Alexey Mazurov, Anatoly Salyuk, et al. (2017). "Current rates and mechanisms of subsea permafrost degradation in the East Siberian Arctic Shelf." *Nature communications* 8, p. 15872.

Sharbatyan, AA (1974). *Extremal estimates in geothermy and geocryology*.

Sherman, Dallas, Peter Kannberg, and Steven Constable (2017). "Surface towed electromagnetic system for mapping of subsea Arctic permafrost." *Earth and Planetary Science Letters* 460, pp. 97–104.

Shiklomanov, Igor A, Alexander I Shiklomanov, Richard B Lammers, BJ Peterson, and Charles J Vorosmarty (2000). "The dynamics of

river water inflow to the Arctic Ocean." In: *The freshwater budget of the Arctic Ocean*. Springer, pp. 281–296.

Sidhu, PP (1991). "Classical analytical modelling of the offshore temperature profiles, Beaufort Shelf." *Geological Survey of Canada Open file 2338*.

Sivan, Orit, Michal Adler, Ann Pearson, Faina Gelman, Itay Bar-Or, Seth G John, and Werner Eckert (2011). "Geochemical evidence for iron-mediated anaerobic oxidation of methane." *Limnology and Oceanography* 56.4, pp. 1536–1544.

Slagoda, E.A. (2004). *Cryolithogenic Deposits of the Laptev Sea Coastal Lowland: Lithology and Micro-Morphology (Bykovsky Peninsula and Moustach Island)*.

Sloan Jr, E Dendy and Carolyn A Koh (2007). *Clathrate hydrates of natural gases*. CRC press.

Soloviev, V (1981). "Predicted distribution of relic submarine frozen zone (East Arctic seas example)." *Cryolithozone of the Arctic Shelf*, pp. 28–38.

Soloviev, VA, GD Ginzburg, EV Telepnev, and Yu N Mikhaluk (1987). "Cryothermia and gas hydrates in the Arctic Ocean." *Saint Petersburg, Russia: VNIIOkeangeologia, Leningrad*.

Soluri, EA and VA Woodson (1990). "World vector shoreline." *The International Hydrographic Review* 67.1.

Sommer, Stefan, Olaf Pfannkuche, Peter Linke, R Luff, Jens Greinert, Manuela Drews, S Gubsch, Martin Pieper, M Poser, and T Viergutz (2006). "Efficiency of the benthic filter: Biological control of the emission of dissolved methane from sediments containing shallow gas hydrates at Hydrate Ridge." *Global Biogeochemical Cycles* 20.2.

Sørensen, KB, K Finster, and NB Ramsing (2001). "Thermodynamic and kinetic requirements in anaerobic methane oxidizing consortia exclude hydrogen, acetate, and methanol as possible electron shuttles." *Microbial Ecology* 42.1, pp. 1–10.

Sparkes, Robert B, A Doğrul Selver, J Bischoff, HM Talbot, Örjan Gustafsson, IP Semiletov, OV Dudarev, and BE van Dongen (2015). "GDGT distributions in the East Siberian Sea: implications for organic carbon export, burial and degradation." *Biogeosciences Discussions* 12.

Sparrow, Katy J., John D. Kessler, John R. Southon, Fenix Garcia-Tigreros, Kathryn M. Schreiner, Carolyn D. Ruppel, John B. Miller, Scott J. Lehman, and Xiaomei Xu (2018). "Limited contribution of ancient methane to surface waters of the US Beaufort sea shelf." *Science Advances* 4.1.

Spencer, Robert GM, Paul J Mann, Thorsten Dittmar, Timothy I Eglinton, Cameron McIntyre, R Max Holmes, Nikita Zimov, and Aron Stubbins (2015). "Detecting the signature of permafrost thaw in Arctic rivers." *Geophysical Research Letters* 42.8, pp. 2830–2835.

Stefan, Johan (1891). "Über die Theorie der Eisbildung, insbesondere über die Eisbildung im Polarmeere." *Annalen der Physik* 278.2, pp. 269–286.

Stefels, J (2000). "Physiological aspects of the production and conversion of DMSP in marine algae and higher plants." *Journal of Sea Research* 43.3-4, pp. 183–197.

Stein, Rüdiger, B Boucsein, Kirsten Fahl, T Garcia de Oteyza, J Knies, and Frank Niessen (2001). "Accumulation of particulate organic carbon at the Eurasian continental margin during late Quaternary times: controlling mechanisms and paleoenvironmental significance." *Global and Planetary Change* 31.1-4, pp. 87–104.

Stein, Rüdiger and Kirsten Fahl (2000). "Holocene accumulation of organic carbon at the Laptev Sea continental margin (Arctic Ocean): sources, pathways, and sinks." *Geo-Marine Letters* 20.1, pp. 27–36.

Stein, Ruediger, Hannes Grobe, and Monika Wahsner (1994). "Organic carbon, carbonate, and clay mineral distributions in eastern central Arctic Ocean surface sediments." *Marine Geology* 119.3-4, pp. 269–285.

Stein, Ruediger, Robie W Macdonald, Ruediger Stein, and Robie W MacDonald (2004). "The organic carbon cycle in the Arctic Ocean."

Stevens, Christopher W., Brian J. Moorman, Steve M. Solomon, and Chris H. Hugenholtz (2009). "Mapping subsurface conditions within the near-shore zone of an Arctic delta using ground penetrating radar." *Cold Regions Science and Technology* 56.1, pp. 30–38.

Stock, Daniela, Andrew GW Leslie, and John E Walker (1999). "Molecular architecture of the rotary motor in ATP synthase." *Science* 286.5445, pp. 1700–1705.

Stocker, Thomas F, Dahe Qin, G-K Plattner, Melinda MB Tignor, Simon K Allen, Judith Boschung, Alexander Nauels, Yu Xia, Vincent Bex, and Pauline M Midgley (2013). *Climate Change 2013-The Physical Science Basis: Contribution of Working Group I to the Fifth Assessment Report of the Intergovernmental Panel on Climate Change*. Cambridge University Press.

Strauss, Jens, Lutz Schirrmeister, Guido Grosse, Daniel Fortier, Gustaf Hugelius, Christian Knoblauch, Vladimir Romanovsky, Christina Schädel, Thomas Schneider von Deimling, Edward AG Schuur, et al. (2017). "Deep Yedoma permafrost: A synthesis of depositional characteristics and carbon vulnerability." *Earth-Science Reviews* 172, pp. 75–86.

Stumm, Werner and James J Morgan (1996). *Aquatic Chemistry: Chemical Equilibria and Rates in Natural Waters {Environmental Science and Technology}*. Wiley.

Tanski, George, Nicole Couture, Hugues Lantuit, Antje Eulenburg, and Michael Fritz (2016). "Eroding permafrost coasts release low amounts of dissolved organic carbon (DOC) from ground ice into

the nearshore zone of the Arctic Ocean." *Global Biogeochemical Cycles* 30.7, pp. 1054–1068.

Tarnocai, Charles, JG Canadell, Edward AG Schuur, Peter Kuhry, G Mazhitova, and S Zimov (2009). "Soil organic carbon pools in the northern circumpolar permafrost region." *Global biogeochemical cycles* 23.2.

Taylor, Alan E, SR Dallimore, PR Hill, DR Issler, S Blasco, and F Wright (2013). "Numerical model of the geothermal regime on the Beaufort Shelf, arctic Canada since the Last Interglacial." *Journal of Geophysical Research: Earth Surface* 118.4, pp. 2365–2379.

Teal, LR, Mark T Bulling, ER Parker, and Martin Solan (2008). "Global patterns of bioturbation intensity and mixed depth of marine soft sediments." *Aquatic Biology* 2.3, pp. 207–218.

Terzaghi, Karl (1952). *Permafrost*. Harvard University.

Thang, Nguyen Manh, Volker Brüchert, Michael Formolo, Gunter Wegener, Livija Ginters, Bo Barker Jørgensen, and Timothy G Ferdelman (2013). "The impact of sediment and carbon fluxes on the biogeochemistry of methane and sulfur in littoral Baltic Sea sediments (Himmerfjärden, Sweden)." *Estuaries and Coasts* 36.1, pp. 98–115.

Thatcher, K. E., G. K. Westbrook, S. Sarkar, and T. A. Minshull (2013). "Methane release from warming-induced hydrate dissociation in the West Svalbard continental margin: Timing, rates, and geological controls." *Journal of Geophysical Research: Solid Earth* 118.1, pp. 22–38.

Thauer, Rudolf K and Seigo Shima (2008). "Methane as fuel for anaerobic microorganisms." *Annals of the New York Academy of Sciences* 1125.1, pp. 158–170.

Thiel, Volker, Jörn Peckmann, Hans Hermann Richnow, Ulf Luth, Joachim Reitner, and Walter Michaelis (2001). "Molecular signals for anaerobic methane oxidation in Black Sea seep carbonates and a microbial mat." *Marine chemistry* 73.2, pp. 97–112.

Thornton, Brett F, Marc C Geibel, Patrick M Crill, Christoph Humborg, and Carl-Magnus Mörth (2016). "Methane fluxes from the sea to the atmosphere across the Siberian shelf seas." *Geophysical Research Letters* 43.11, pp. 5869–5877.

Thullner, Martin, Andrew W Dale, and Pierre Regnier (2009). "Global-scale quantification of mineralization pathways in marine sediments: A reaction-transport modeling approach." *Geochemistry, geophysics, geosystems* 10.10.

Thullner, Martin, Philippe Van Cappellen, and Pierre Regnier (2005). "Modeling the impact of microbial activity on redox dynamics in porous media." *Geochimica et Cosmochimica Acta* 69.21, pp. 5005–5019.

Thum, T. et al. (2011). "Soil carbon model alternatives for ECHAM5/JSBACH climate model: Evaluation and impacts on global carbon cycle estimates." *Journal of Geophysical Research: Biogeosciences* 116.2, G02028.

Thuróczy, C. E., L. J A Gerringa, M. Klunder, P. Laan, M. Le Guitton, and H. J W De Baar (2011). "Distinct trends in the speciation of iron between the shallow shelf seas and the deep basins of the Arctic Ocean." *Journal of Geophysical Research: Oceans* 116.10.

Tien, R. H. and G. E. Geiger (1967). "A heat-transfer analysis of the solidification of a binary eutectic system." *Journal of Heat Transfer* 89.3, pp. 230–233.

Tishchenko, Pavel, Christian Hensen, Klaus Wallmann, and Chi Shing Wong (2005). "Calculation of the stability and solubility of methane hydrate in seawater." *Chemical geology* 219.1-4, pp. 37–52.

Topham, D. R. (1984). "The formation of gas hydrates on bubbles of hydrocarbon gases rising in seawater." *Chemical Engineering Science* 39.5, pp. 821–828.

Trenberth, KE, PD Jones, P Ambenje, R Bojariu, D Easterling, A Klein Tank, D Parker, F Rahimzadeh, JA Renwick, M Rusticucci, et al. (2007). "Observations: surface and atmospheric climate change. Chapter 3." *Climate change*, pp. 235–336.

Treude, Tina, Antje Boetius, Katrin Knittel, Klaus Wallmann, and Bo Barker Jørgensen (2003). "Anaerobic oxidation of methane above gas hydrates at Hydrate Ridge, NE Pacific Ocean." *Marine Ecology Progress Series* 264, pp. 1–14.

Treude, Tina, Martin Krüger, Antje Boetius, and Bo Barker Jørgensen (2005). "Environmental control on anaerobic oxidation of methane in the gassy sediments of Eckernförde Bay (German Baltic)." *Limnology and oceanography* 50.6, pp. 1771–1786.

Usov, VA (1965). "Cryogenic structure and composition of recent deposits in the lagoon shore near the Indigirka River delta." *Vest-Nik LAU* 18, pp. 49–59.

Vaksmaa, A, C Lüke, T Van Alen, G Valè, E Lupotto, MS Jetten, and KF Ettwig (2016). "Distribution and activity of the anaerobic methanotrophic community in a nitrogen-fertilized Italian paddy soil." *FEMS Microbiology Ecology* 92.12.

Valentine, David L, Douglas C Blanton, and William S Reeburgh (2000). "Hydrogen production by methanogens under low-hydrogen conditions." *Archives of Microbiology* 174.6, pp. 415–421.

Van Cappellen, Philippe and Yifeng Wang (1996). "Cycling of iron and manganese in surface sediments; a general theory for the coupled transport and reaction of carbon, oxygen, nitrogen, sulfur, iron, and manganese." *American Journal of Science* 296.3, pp. 197–243.

Van Everdingen, RO (1985). "Unfrozen permafrost and other taliks." In: *Proc. Workshop on Permafrost Geophysics*. 85-5. US Army, CRREL, Special Rept, pp. 101–105.

Van Walraven, Hendrika S, E Esther Hollander, Marijke JC Scholts, and Ruud Kraayenhof (1997). "The H+/ATP ratio of the ATP synthase from the cyanobacterium Synechococcus 6716 varies with growth temperature and light intensity." *Biochimica et Biophysica Acta (BBA)-Bioenergetics* 1318.1-2, pp. 217–224.

Van Walraven, Hendrika S, Heinrich Strotmann, Oliver Schwarz, and Bernd Rumberg (1996). "The H+/ATP coupling ratio of the ATP synthase from thiol-modulated chloroplasts and two cyanobacterial strains is four." *FEBS letters* 379.3, pp. 309–313.

Vanwonterghem, Inka, Paul N Evans, Donovan H Parks, Paul D Jensen, Ben J Woodcroft, Philip Hugenholtz, and Gene W Tyson (2016). "Methylotrophic methanogenesis discovered in the archaeal phylum Verstraetearchaeota." *Nature microbiology* 1.12, p. 16170.

Vigdorchik, Michael E (1980). *Arctic Pleistocene history and the development of submarine permafrost*. Westview Press.

Vize, V Yu (1946). "Sovietic arctic Seas and Islands." *Izd. Glavsevmorputy* 4.

Vonk, Jorien E and Örjan Gustafsson (2013). "Permafrost-carbon complexities." *Nature Geoscience* 6.9, p. 675.

Vonk, Jorien E, Igor P Semiletov, Oleg V Dudarev, Timothy I Eglinton, August Andersson, Natalia Shakhova, Alexander Charkin, Birgit Heim, and Örjan Gustafsson (2014). "Preferential burial of permafrost-derived organic carbon in S iberian-A rctic shelf waters." *Journal of Geophysical Research: Oceans* 119.12, pp. 8410–8421.

Vonk, Jorien E, Laura Sánchez-García, BE Van Dongen, Vanja Alling, D Kosmach, A Charkin, Igor Petrovich Semiletov, Oleg Victorovich Dudarev, Natalia Shakhova, P Roos, et al. (2012). "Activation of old carbon by erosion of coastal and subsea permafrost in Arctic Siberia." *Nature* 489.7414, p. 137.

Vrbka, Luboš and Pavel Jungwirth (2005). "Brine rejection from freezing salt solutions: A molecular dynamics study." *Physical Review Letters* 95.14, p. 148501.

Wåhlström, Iréne, Christian Dieterich, Per Pemberton, and HE Markus Meier (2016). "Impact of increasing inflow of warm Atlantic water on the sea-air exchange of carbon dioxide and methane in the Laptev Sea." *Journal of Geophysical Research: Biogeosciences* 121.7, pp. 1867–1883.

Walczowski, Waldemar and Jan Piechura (2006). "New evidence of warming propagating toward the Arctic Ocean." *Geophysical Research Letters* 33.12.

Wallmann, Klaus, Giovanni Aloisi, Matthias Haeckel, A Obzhirov, G Pavlova, and P Tishchenko (2006a). "Kinetics of organic matter degradation, microbial methane generation, and gas hydrate formation in anoxic marine sediments." *Geochimica et Cosmochimica Acta* 70.15, pp. 3905–3927.

Wallmann, Klaus, Manuela Drews, Giovanni Aloisi, and Gerhard Bohrmann (2006b). "Methane discharge into the Black Sea and the global ocean via fluid flow through submarine mud volcanoes." *Earth and Planetary Science Letters* 248.1-2, pp. 545–560.

Wallmann, Klaus, Elena Pinero, Ewa Burwicz, Matthias Haeckel, Christian Hensen, Andrew Dale, and Lars Ruepke (2012). *The global inventory of methane hydrate in marine sediments: A theoretical approach*.

Wang, S, D Bailey, K Lindsay, J. K. Moore, and M Holland (2014). "Impact of sea ice on the marine iron cycle and phytoplankton productivity." *Biogeosciences* 11.17, pp. 4713–4731.

Wang, Yifeng and Philippe Van Cappellen (1996). "A multicomponent reactive transport model of early diagenesis: Application to redox cycling in coastal marine sediments." *Geochimica et Cosmochimica Acta* 60.16, pp. 2993–3014.

Wegener, Gunter, Viola Krukenberg, Dietmar Riedel, Halina E Tegetmeyer, and Antje Boetius (2015). "Intercellular wiring enables electron transfer between methanotrophic archaea and bacteria." *Nature* 526.7574, p. 587.

Wegner, Carolyn, Katrina E Bennett, Anne de Vernal, Matthias Forwick, Michael Fritz, Maija Heikkilä, Magdalena Łącka, Hugues Lantuit, Michał Laska, Mateusz Moskalik, et al. (2015). "Variability in transport of terrigenous material on the shelves and the deep Arctic Ocean during the Holocene." *Polar Research* 34.1, p. 24964.

Weingartner, Thomas J, Stephen R Okkonen, Seth Lombard Danielson, and Alaska Outer Continental Shelf Region (2005). *Circulation and water property variations in the nearshore Alaskan Beaufort Sea*. US Department of Interior, Minerals Management Service.

Welte, Cornelia U, Olivia Rasigraf, Annika Vaksmaa, Wouter Versantvoort, Arslan Arshad, Huub JM Op den Camp, Mike SM Jetten, Claudia Lüke, and Joachim Reimann (2016). "Nitrate-and nitrite-dependent anaerobic oxidation of methane." *Environmental microbiology reports* 8.6, pp. 941–955.

Westbrook, Graham K. et al. (2009). "Escape of methane gas from the seabed along the West Spitsbergen continental margin." *Geophysical Research Letters* 36.15, n/a–n/a.

Westermann, S, M Langer, J Boike, M Heikenfeld, M Peter, B Etzelmüller, and G Krinner (2016). "Simulating the thermal regime and thaw processes of ice-rich permafrost ground with the land-surface model CryoGrid 3." *Geoscientific Model Development* 9.2.

Westermann, Sebastian, Maria Peter, Moritz Langer, Georg Schwamborn, Lutz Schirrmeister, Bernd Etzelmüller, and Julia Boike (2017). "Transient modeling of the ground thermal conditions using satellite data in the Lena River delta, Siberia." *The Cryosphere* 11.3, pp. 1441–1463.

Westermann, Sebastian, Thomas Schuler, Kjersti Gisnås, and Bernd Etzelmuller (2013). "Transient thermal modeling of permafrost conditions in Southern Norway." *The Cryosphere* 7.2, pp. 719–739.

Whitefield, Jonathan, Peter Winsor, James McClelland, and Dimitris Menemenlis (2015). "A new river discharge and river temperature climatology data set for the pan-Arctic region." *Ocean Modelling* 88, pp. 1–15.

Whiticar, Michael J (1999). "Carbon and hydrogen isotope systematics of bacterial formation and oxidation of methane." *Chemical Geology* 161.1-3, pp. 291–314.

Whiticar, Michael J, Eckard Faber, and Martin Schoell (1986). "Biogenic methane formation in marine and freshwater environments: CO2 reduction vs. acetate fermentation—isotope evidence." *Geochimica et Cosmochimica Acta* 50.5, pp. 693–709.

Wild, Birgit, August Andersson, Lisa Bröder, Jorien Vonk, Gustaf Hugelius, James W McClelland, Wenjun Song, Peter A Raymond, and Örjan Gustafsson (2019). "Rivers across the Siberian Arctic unearth the patterns of carbon release from thawing permafrost." *Proceedings of the National Academy of Sciences*, p. 201811797.

Wild, Birgit et al. (2018). "Organic matter across subsea permafrost thaw horizons on the East Siberian Arctic Shelf." *The Cryosphere Discussions*, pp. 1–26.

Williams, Gaynor P (1963). "Heat transfer coefficients for natural water surfaces." *International Association of Scientific Hydrology. Bulletin* 62, pp. 203–212.

Winkel, Matthias, Julia Mitzscherling, Pier P Overduin, Fabian Horn, Maria Winterfeld, Ruud Rijkers, Mikhail N Grigoriev, Christian Knoblauch, Kai Mangelsdorf, Dirk Wagner, et al. (2018). "Anaerobic methanotrophic communities thrive in deep submarine permafrost." *Scientific reports* 8.1, p. 1291.

Winterfeld, Maria, Lutz Schirrmeister, Mikhail N Grigoriev, Viktor V Kunitsky, Andrei Andreev, Andrew Murray, and Pier Paul Overduin (2011). "Coastal permafrost landscape development since the Late Pleistocene in the western Laptev Sea, Siberia." *Boreas* 40.4, pp. 697–713.

Woo, Ming-ko (2012). *Permafrost hydrology*. Springer Science & Business Media.

Wright, JF, AE Taylor, and SR Dallimore (2008). "Thermal Impact of Holocene Lakes on a Permafrost Landscape, Mackenzie Delta, Canada." In: *Proceedings of the Ninth international conference on Permafrost, Fairbanks, AK*.

Xu, Wenyue and Carolyn Ruppel (1999). "Predicting the occurrence, distribution, and evolution of methane gas hydrate in porous marine sediments." *Journal of Geophysical Research: Solid Earth* 104.B3, pp. 5081–5095.

Yakushev, V. S. (1989). "Gas hydrates in cryolithozone." 11, pp. 100–105.

Yamamoto, Akitomo, Yasuhiro Yamanaka, Akira Oka, and Ayako Abe-Ouchi (2014). "Ocean oxygen depletion due to decomposition of submarine methane hydrate." *Geophysical Research Letters* 41.14, pp. 5075–5083.

Yershov, ED, YR Lebedenko, EM Chuvilin, and VA Istomin (1991). "Features of gas hydrate occurrence in permafrost." *USSR Acad. Sci.* 321, pp. 788–791.

Yvon-Lewis, Shari A, Lei Hu, and John Kessler (2011). "Methane flux to the atmosphere from the Deepwater Horizon oil disaster." *Geophysical Research Letters* 38.1.

Zabel, Matthias and Christian Hensen (2006). "Quantification and regionalization of benthic reflux." In: *Marine Geochemistry*. Springer, pp. 429–456.

Zhang, Jinlun, D Andrew Rothrock, and Michael Steele (1998). "Warming of the Arctic Ocean by a strengthened Atlantic inflow: Model results." *Geophysical Research Letters* 25.10, pp. 1745–1748.

Zhang, Tingjun (2011). "Talik." *Encyclopedia of Snow, Ice and Glaciers*, pp. 1143–1144.

Zhang, Z (2015). "Heat transfer during the dissociation of hydrate in porous media." *Procedia Engineering* 126, pp. 502–506.

Zimov, SA, SP Davydov, GM Zimova, AI Davydova, EAG Schuur, K Dutta, and FS Chapin III (2006). "Permafrost carbon: Stock and decomposability of a globally significant carbon pool." *Geophysical Research Letters* 33.20.

ACKNOWLEDGEMENTS

I think that time has finally come to thank everyone who helped me to go through these not-always-easy last years and who, directly or indirectly, contributed to the present work and made all this possible.

First of all I would like to express my gratitude and appreciation to my supervisors, Prof. Sandra Arndt and Prof. Victor Brovkin. This thesis would have not seen the light of day without their invaluable contribution, their admirable patience, their recommendations and suggestions, their continuous human support and trust in my research as well as the insightful scientific discussions I had with them. I want to thank them for the knowledge and expertise they transmitted and the chances they offered me. Furthermore I need to thank them for their competent guidance, saving me from my own thoughts and tendency to get lost. Finally I would like to separately thank Victor for treating his group (including me) with Russian chocolates or other specialties, and Sandra for hosting me in Brussels with her family, where I got to know that ancient Romans and dinosaurs could have happily lived together.

I would also like to express my appreciation to Prof. Pierre Regnier and to Dr. Paul Overduin. Thanks to the interesting and enlightening discussions I had with them, they helped me to shape my research and gave fundamental contribution to harvest the fruits of my work, not last this thesis. Thanks also to Dr. Dirk Notz, who suggested the design of the experiments in the sea-ice lab and to Niels-Jakob Fuchs, who made them practically possible.

Un ringraziamento di cuore va ai miei genitori, Beatrice ed Enzo, per il loro immancabile supporto, la loro instancabile pazienza e il loro tremendo sforzo di comprensione umana che mi ha permesso di diventare ciò che sono. Un ringraziamento speciale va poi di diritto a Valentina, la mia ineguagliabile sorella, perché, nonostante la distanza e la vita personale ci abbia innegabilmente allontanati, non ha smesso un attimo di credere in me, di capirmi e di sostenermi. Probabilmente senza di lei non ce l'avrei fatta nel periodo piú nero della mia vita lontano da casa.

An open-hearted thanks cannot but go to Christel for the patience she had in sustaining me, supporting me, teaching me to listen to good music. Thanks for help me understand me better, for travelling together and for your generous and genuine friendship. Thanks for always being there in case I needed, for hosting me in Brussels and helping me survive its darkest aspects.

I would like to say thank to Alberto since he taught me how the scientific brilliance can come with a loyal friendship, a great under-

standing, humility and how it does grow with distance, instead of weakening. Thank you for your support, your help and your value.

Special thanks go to Guido, for sustaining my complaints and distracting me with concerts; to Jan-Niklas, for the coffees together and the discussions about German; to Beniamino, for having borne me for more than three years in our shared flat. Moreover they all three deserve a deep thank for their help in making this thesis a bit more readable and understandable. Deep gratitude goes also to Christopher, the poor good-hearted guy who had to defend his own language against my attempts to destroy it. He also has a great taste for pizzas and deserves to be mentioned for this. Thanks also to Fabio, who had the credit to introduce me to Hamburg. I would also like to thank all the other members of my enlarged international family in Hamburg: Bass, Camilla, Caterina, David, Federica, Gabriele, Giannina, Irina, Jessica, Lorenza, Marco, Miriam, Nasia and Roberta. Thanks also to Thibaut, especially in the last times.

I thank the entire CBI group in the Land department of the Max Planck Institute, all the researchers and all the other PhD students who, for years, shared with me that corridor and the magic view from the 17th floor of the Geomatikum. Especially I would like to thank Alex, Guilherme, Sabine, Sirisha and Sylvia for their friendly support; Tom, for the lunches together; and finally Dr. Veronika Gayler, Dr. Philipp de Vrese and Dr. Thomas Raddatz because without them, probably I would still be trying to compile JSBACH. Still at the institute I would like to express my gratitude towards Christina Rieckers and Sylvia Houston, who helped me surviving the German administration always with a smile.

I thank all of the C-CASCADES network for the human and scientific exchange. The events and trainings were inspiring and meaningful. Especially I'd like to thank Fabrice, for his loyal and careful support and for sharing with me the excitement and frustration of this PhD together with too many coffees; Philip, for sharing with me the frustration and (rare) excitement of a model as well as my office in Brussels; Simon, with whom I exchanged ideas and visions about the permafrost; Adam, for introducing me to Brussels; Domitille, for her energetic positivity; Anna C. who, as a true friend, has always found a way to get a smile out of me: I promise I'll come to Kiel one day. Thank also to Andreas, for his being spontaneously crazy and not snoring at night. Special thanks go to Dr. Emily Mainetti-Cloarec, for her professional and competent support related to almost any aspect of my life in Brussels and within C-CASCADES.

I would like to thank also the other members of the BGeoSys: Alizée, Dr. Goulven Laruelle, Dr. Ronny Lauerwald and Prof. Steeve Bonneville with whom I shared my days at the ULB.

Thank to Piero who had the bad luck of moving with me in the last months but who, stoically, supported my mess, my mood and who

has been always open for a talk. The conversations with him, from triviliaties to deep thoughts, have been a great source of energy as well as reflection.

Thanks from the bottom of my heart to the friends of a life time: Federico, Gianmarco, Giuseppe, Guglielmo e Matteo. Thanks for being understanding and supportive even from miles away. I do really consider myself lucky in having you as true friends. Special thanks go to Gabriele, who was there when "the night was dark and full of terror". I cannot express how grateful I am for those moments. Furthermore I would also like to thank Pippo, who has been way faster than me, Cristina, Sara and Silvia for their careful and constant support.

A special mention goes to the Grezzanesi who, from the remoteness of my village on the Tuscan Appenines, did not gave up on me. Warm thanks go therefore to Lorenzo, Elisabetta, Pietro and Conny.

Thanks to Giulia, for her indestructible support, for her friendship and for having accepted my hypochondria; to Leo, for the nice and motivating talks and walks we use to have; to Giuseppe M., for the hikes and the memories of them; to Nicola, who never let me down; to Altug, who put the basis of my research and I've always enjoyed meeting; to Alberto G. and Aurora, who never stopped considering me; to Claudia, my even too apprehensive cousin and to Maria, my dearest Italian grandma in Hamburg, whose brilliance always amazes and whose discrete support has been crucial.

I would like to thank Francesca and Matteo, who I met in the brightness of a cold midnight Sun and with whom I talked of methane. Thanks also to Prof. Michael Whiticar and Prof. Bernard Boudreau, whose lectures have been particularly inspiring and motivating.

I want to express my appreciation towards Kay-Dennis with whom, for a while, I shared the great time in "die Halle"; towards the whole training group of "Baristi Workout Hamburg" and towards Sascha, who, for some mysterious reasons, has always believed in my athletic skills. Thanks also to Dr. Anja Hüfner, who saved my mental health a couple of times.

I would like to express my gratitude to Amos, for the nice time spent together and having introduced me to a new world; to Jesús, for the movie evenings, the academic discussions and the second chance he offered me. Thanks to Genady, my Thracian warrior, for the hospitality and the support from far away. Special thanks go to Boštjan, for sharing his travel tales with me, for giving me a roof in Brussels and for his attentive interest, especially in the latest months. A big thank goes to Alexander, for the moments we enjoyed together, for his careful kindness and for having instilled a new interest in me. Thanks to Pierre and Stefan, who enlightened my stay in Brussels. Then thanks to Thiago, Russell, Tim, Jean, Ben, Friedrich, Danko and Guillermo for believing in me and making me believe in myself.

I would also like to say thank to people who probably are never going to read this, but whose little, daily and kind actions made so many of my days, especially during the gray and gloomy mornings that Hamburg can offer. A special mention goes to one of the shop assistant of the bakery "Daube" and to her contagious and radiant smile; to one of the caretaker of the Geomatikum, who never missed to wave his hand at me and to the smiling staff of the Mensa, whose joviality helped when food...could not.

Random and deep thanks go to the music of Ludovico Einaudi, Roberto Cacciapaglia, Astor Piazzolla, William Byrd, Antonio Vivaldi, Peer Kusiv, Tocotronic, Kaleo, Worakls, N'to, Yotto, Rüfüs du Sol and to the voice of Hannah Reid, John Grant, Alison Goldfrapp and Jakub Józef Orliński.

Thanks to the Facebook page "Non è successo niente" for its shrewd posts, which always offered me a chance to smirk, especially in the last months.

Thanks to Hamburg, to its sunsets over the Alster and to the stormy Elbe, the perfect settings for long, thoughtful runnings.

And of course a warm, intense and last thankful thought cannot but go to Andre, who made me completely new, who forced me to see the truth and whose fleeting presence in my life has altered notions and feelings, has subverted my priorities and has been the source of the strongest motivation as well as frustration. He made me discover the most secret corners of myself and stir me to find out "a passi tardi et lenti" the quiet and primordial remoteness that Germany has still to offer.

As you, reader, might have guessed I tend to be carried away. But this is the end, I swear.